

# **Determination of the chemical composition of cosmic rays in the energy region of 5 EeV with the AMIGA upgrade of the Pierre Auger Observatory**

Zur Erlangung des akademischen Grades eines  
**Doktors der Naturwissenschaften**  
von der KIT-Fakultät für Physik des  
Karlsruher Instituts für Technologie (KIT)  
und der  
Universidad Nacional de San Martín (UNSAM)

genehmigte

## **Dissertation**

von

**Lic. Ana Martina Botti**  
aus Buenos Aires

Tag der mündlichen Prüfung: 8. November 2019

Referent: Prof. Dr. A. Etchegoyen

Korreferent: Prof. Dr. J. Blümmer

Betreuer: Dr. M. A. Roth

Betreuer: Dr. F. A. Sánchez



# **Determination of the chemical composition of cosmic rays in the energy region of 5 EeV with the AMIGA upgrade of the Pierre Auger Observatory**

Tesis presentada para optar por el título de

**Doctora en Astrofísica**

del Instituto de Tecnología "Prof. Jorge A. Sábato" de la  
Universidad Nacional de San Martín (UNSAM)

y del  
Karlsruher Institut für Technologie (KIT)

por

**Lic. Ana Martina Botti**

Fecha de la defensa oral: 8 de Noviembre de 2019

Director: Prof. Dr. A. Etchegoyen

Co-director: Prof. Dr. J. Blümer

Colaborador: Dr. M. A. Roth

Colaborador: Dr. F. A. Sánchez



---

# Abstract

Ultra high energy cosmic rays are particles that arrive at the Earth with energies above  $10^{18}$  eV. When these particles interact with nuclei in the Earth's atmosphere, secondary particles are produced. These propagate towards the ground as extensive air showers. A number of questions remain open concerning these extremely energetic cosmic rays: the sources and acceleration mechanisms that give them origin, as well as their composition (the fraction of proton and of different nuclei type) and the nature of the suppression in their energy, among others, are still unknown. To shed light on these riddles, cosmic rays at the highest energies are studied at the Pierre Auger Observatory, in which a hybrid-detection technique, aiming to both enhance statistics and minimize systematic uncertainties, is implemented. Currently, the Pierre Auger Observatory is undergoing a major upgrade of its capabilities denominated AugerPrime. New detectors, such as radio antennas, surface scintillator detectors, and buried scintillator detectors are being deployed as part of this upgrade.

With the Auger Muons and Infill for the Ground Array (AMIGA) enhancement, it is aimed to both lower the detection threshold of the Pierre Auger Observatory down to energies of  $\sim 10^{16.5}$  eV and to directly measure the muon content of extensive air showers. AMIGA consists of an array of coupled water-Cherenkov and buried scintillation detectors deployed in two overlapped triangular grids of 433 m and 750 m spacings. Each underground detector has a total area of  $30\text{ m}^2$  and it is buried at a depth of 2.3 m to shield it from the electromagnetic component of showers. The scintillation plane is segmented in plastic-scintillator strips with embedded wavelength-shifting optical fibers coupled to an array of silicon photomultipliers (SiPMs). In this work, we present several studies on the AMIGA underground muon detector (UMD), which has two operating modes: the *counter*, designed to directly measure particles as they impinge on the detector and optimized to measure low muon densities and the *integrator*, which allows to estimate the muon content of extensive air showers by dividing the total signal charge by that of an average muon.

Firstly, we describe the current calibration for SiPMs and how the operation point of the *counter* mode is set. Using both laboratory and field data, we have performed studies to corroborate the SiPM gain stability under temperature fluctuations, thoroughly characterized its noise sources, and proposed a muon counting strategy that rejects the SiPM noise without significantly losing muon signal. We have also used laboratory and field data to extract the main features of the *integrator* mode and achieved an uncertainty model for its signal charge. We have also presented two possible calibration procedures for this mode: the first one based on shower events which can be performed offline, and the second one, based on background data that can be performed online.

Secondly, the AMIGA UMD simulations have been developed and implemented in the Auger data analysis and simulation software (Offline), as part of this thesis work. The code was developed and validated with laboratory data acquired using identical components as in the UMD final design. Both analog SiPM pulses and digital traces after the front-end board were acquired and compared to simulation outputs; the former using customized electronics and the latter with the same electronic kits as used in the UMD production. The main features of both *counter* and *integrator* channels relevant to the detector performance are discussed and the agreement between simulated and laboratory data is shown.

Finally, we used the recently implemented SiPM simulations in the Offline framework to study the bias sources of the *counter* mode and to propose corrections that remove its reconstruction biases. We also used simulations to test the calibration of the *integrator* mode and to compare both modes resolutions. We used these results to briefly study the sensitivity of the UMD to the composition of primary cosmic rays.

In this thesis work, we have made several contributions to AugerPrime: (i) studies to corroborate the stability of SiPMs, (ii) testing and tuning of the SiPM calibration procedure and the verification of its robustness, (iii) the characterization of UMD signals and noise sources, (iv) the determination of both efficiency and attenuation of scintillator strips with embedded optical fiber (v) a counting strategy for estimating the number of muons in air showers with the *counter* mode, (vi) the end-to-end calibration of the *integrator* mode using both online and offline data, (vii) the design, development, implementation and testing of SiPM and electronic simulations, (viii) the design, development, implementation and testing of the UMD event visualization in a graphic user interface, (ix) analyses on the effects of the soil in the UMD reconstruction, (x) a reconstruction bias correction for the *counter* mode with SiPMs, (xi) analyses to enhance the UMD capabilities to perform studies on the composition of cosmic rays. As such, the tools and methods described in this thesis work are of paramount importance for future analyses performed with the underground muon detector of AugerPrime.

---

# Zusammenfassung

Die ultra hochenergetische kosmisch Strahlung besteht aus Teilchen, die mit Energien von über  $10^{18}$  eV auf die Erde gelangen. Wenn diese auf Atomkerne in der Erdatmosphäre treffen, entstehen Sekundärteilchen. Diese propagieren als ausgedehnte Luftschauder bis zum Boden hin. Zu diesen extrem energiereichen kosmischen Strahlen gibt es noch eine Reihe von offenen Fragen: Was sind deren Quellen? Was sind die Beschleunigungsmechanismen, die ihnen den Ursprung geben, sowie ihre Zusammensetzung (der Anteil von Protonen und verschiedenen Kerntypen)? Welche Mechanismen sorgen für die Unterdrückung bei sehr hohen Energien. Um diese Fragen zu lösen, werden am Pierre Auger Observatorium kosmische Strahlen mit den höchsten Energien untersucht. Dafür wird eine Hybriddetektionstechnik verwendet, die darauf abzielt, sowohl die Teilchenstatistik zu verbessern als auch systematische Unsicherheiten zu minimieren. Derzeit werden die Messkapitäten vom Pierre Auger Observatorium, im Rahmen des AugerPrime Upgrades, verbessert. Dafür werden neue Detektoren wie Radioantennen, Oberflächen-Szintillatordetektoren und Untergrund-Szintillatordetektoren eingesetzt.

Das "Auger Muon and Infill for the Ground Array" (AMIGA) zielt darauf ab, sowohl die Nachweisgrenze des Pierre Auger Observatoriums auf Energien von  $\sim 10^{16.5}$  eV zu senken als auch den Myongehalt von ausgedehnten Luftschaubern direkt zu messen. AMIGA besteht aus einer Reihe von gekoppelten Wasser-Cherenkov- und vergraben Szintillatordetektoren, die in zwei überlappenden Dreiecksgittern im Abstand von 433 m und 750 m eingesetzt werden. Jeder Untergrunddetektor hat eine Gesamtfläche von  $30\text{ m}^2$  und ist 2,3 m unter der Erdoberfläche vergraben, um es vor der elektromagnetischen Komponenten der Schauer zu schützen. Die Szintillationsebene ist in Kunststoff-Szintillatorstreifen mit eingebetteten optischen Wellenlängenschieberfasern segmentiert, die mit einer Reihe von Silizium-Photomultiplier (SiPMs) gekoppelt sind. In dieser Arbeit stellen wir mehrere Studien über den AMIGA Untergrund-Myonendetektor (UMD) vor, der zwei Betriebsarten hat: den Zähler, der entwickelt wurde, um Myonen direkt zu messen, wenn sie auf den Detektor treffen, und optimiert ist, um niedrige Myondichten zu messen, und den Integrator, der es ermöglicht, den Myongehalt von ausgedehnten Luftschaubern zu schätzen, indem es die Gesamtladung durch die eines durchschnittlichen Myons teilt.

Zunächst beschreiben wir die aktuelle Kalibrierung für die SiPMs und wie der Arbeitsspunkt des Zählmodus eingestellt wird. Unter Verwendung von Labordaten und Messungen des Observatoriums haben wir Studien durchgeführt, um die Stabilität der SiPM-Verstärkung bei Temperaturschwankungen zu bestätigen. Wir haben deren Rauschquellen gründlich charakterisiert. Dazu haben wir auch eine Myon-Zählstrategie vorgeschlagen, die das SiPM-Rauschen minimiert, ohne signifikant an Myonsignalen zu verlieren. Wir haben

auch Daten aus dem Labor und dem Observatorium verwendet, um die Hauptmerkmale des Integrator-Modus zu extrahieren und ein Unsicherheitsmodell für die Signalladung zu erhalten. Zudem haben wir zwei mögliche Kalibrierungsverfahren für diesen Modus vorgestellt: das erste basiert auf Luftschaueereignissen, die offline durchgeführt werden können, und das zweite auf Hintergrunddaten, die online durchgeführt werden können.

Außerdem wurden als Teil dieser Arbeit die AMIGA UMD-Simulationen entwickelt und in die Auger Datenanalyse- und Simulationssoftware (Offline) implementiert. Der Code wurde mit Labordaten entwickelt und mit identischen Komponenten, wie die im UMD-Enddesign gemessen wurden, validiert. Sowohl analoge SiPM-Impulse als auch digitale Spuren nach der Frontend-Platine wurden erfasst und mit Simulationsergebnissen verglichen; erstere mit spezifischer Elektronik und letztere mit den gleichen elektronischen Bausätzen, die in der UMD-Produktion verwendet werden. Die Hauptmerkmale der Zähler- und Integratorkanäle sind relevant für die Detektorleistung und werden hier diskutiert. Deren Unterschiede und Übereinstimmungen zwischen Simulations- und Labordaten werden dargestellt. Schließlich haben wir die neulich implementierten SiPM-Simulationen im Offline-Framework verwendet, um die Quellen systematischer Fehler des Zähler-Modus zu untersuchen und Korrekturen vorzuschlagen, die etwaige Rekonstruktionsverzerrungen beseitigen. Wir haben die Simulationen auch verwendet, um die Kalibrierung des Integratormodus zu testen und die Auflösungen beider Modii zu vergleichen. Wir haben diese Ergebnisse verwendet, um die Empfindlichkeit der UMD gegenüber der kosmischen Strahlungsprimärmasse zu untersuchen.

Im Rahmen dieser Dissertation wurden mehrere Beiträge zum AugerPrime Upgrade erarbeitet. Unter anderem wurden: (i) Studien zur Bestätigung der Stabilität von SiPMs, (ii) die Prüfung und Abstimmung des SiPM-Kalibrierverfahrens und die Überprüfung seiner Robustheit, (iii) die Charakterisierung von UMD-Signalen und Rauschquellen, (iv) die Bestimmung der Effizienz und Dämpfung von Szintillatorstreifen mit eingebetteter Glasfaser (v) die Erreichung einer Zählstrategie zur Schätzung der Anzahl der Myonen in Luftschaubern mit dem Counter-Modus, (vi) die Kalibrierung des Integratormodus unter Verwendung von Online- und Offline-Daten, (vii) das Design, die Entwicklung, die Implementierung und das Testen von SiPM- und elektronischen Simulationen, (viii) das Design, die Entwicklung, die Implementierung und das Testen der UMD-Ereignisvisualisierung in einer grafischen Benutzeroberfläche, (ix) Analysen über die Auswirkungen des Bodens bei der UMD-Rekonstruktion, (x) das Erreichen einer Rekonstruktionsverzerrungskorrektur für den Counter-Modus mit SiPMs, (xi) Analysen zur Verbesserung der UMD-Fähigkeiten zur Durchführung von Studien über die Zusammensetzung der kosmischen Strahlung, durchgeführt.

Die in dieser Arbeit beschriebenen Werkzeuge und Methoden sind von größter Bedeutung für zukünftige Analysen mit dem unterirdischen AugerPrime Myonendetektor.

---

# Resumen

Los rayos cósmicos de ultra alta energía son partículas que llegan a la Tierra con energías superiores a  $10^{18}$  eV. Cuando estas partículas interactúan con núcleos en la atmósfera terrestre, se producen partículas secundarias que se propagan hacia el suelo en forma de lluvias atmosféricas extendidas. En la actualidad, varios interrogantes persisten respecto a los rayos cósmicos de ultra alta energía: las fuentes y mecanismos de aceleración que les dan origen, así como su composición (fracción de protones y/o diferentes tipos de núcleos) y la naturaleza de la supresión en el flujo de su espectro de energía, entre otros, aún son desconocidos. Para arrojar luz sobre estos acertijos, los rayos cósmicos de más altas energías se estudian en el Observatorio Pierre Auger donde se implementa una tecnología de detección híbrida con el objetivo de mejorar la estadística y minimizar las incertezas sistemáticas. Actualmente, el Observatorio Pierre Auger se encuentra atravesando una importante actualización de sus capacidades denominada AugerPrime. Nuevos detectores, como antenas de radio, detectores centelladores de superficie y detectores centelladores enterrados se están implementando como parte de esta actualización.

Con la extensión denominada “Auger Muons and Infill for the Ground Array (AMIGA)” se tiene como objetivo reducir el umbral de detección del Observatorio Pierre Auger a energías de  $\sim 10^{16.5}$  eV y realizar mediciones directas del contenido muónico de lluvias atmosféricas extendidas. AMIGA consiste en un arreglo de detectores de agua de Cherenkov y detectores centelladores enterrados. Éstos se disponen en dos grillas triangulares superpuestas de 433 m y 750 m de separación. Cada detector centellador tiene un área total de  $30 \text{ m}^2$  y está enterrado a una profundidad de 2.3 m para blindarlo de la componente electromagnética de las lluvias. El detector enterrado se segmenta en tiras de centellador plástico con fibras ópticas de desplazamiento de longitud de onda acopladas a una serie de fotomultiplicadores de silicio (SiPM). En este trabajo, presentamos varios estudios sobre el detector de muones subterráneo (UMD) de AMIGA, el cual tiene dos modos de funcionamiento: el *contador*, diseñado para medir directamente las partículas a medida que inciden en el detector y optimizado para medir bajas densidades de muones y el *integrador*, que permite estimar el contenido de muónico de las lluvias atmosféricas extendidas dividiendo la carga total de las señales por la carga media de un muón.

En primer lugar, describimos el procedimiento de calibración de los SiPMs de AMIGA y presentamos cómo se establece el punto de operación del modo *contador*. Utilizando datos de laboratorio y del campo, hemos realizado estudios para corroborar la estabilidad de ganancia de los SiPMs bajo fluctuaciones de temperatura. Se caracterizó además las fuentes de ruido que afectan al detector, y se propuso una estrategia de conteo de muones que reduce el ruido de los SiPMs sin perder significativamente señal de muones. También

hemos utilizado datos de laboratorio y del observatorio para extraer las principales características del modo *integrador* y lograr un modelo de incertezas para la carga de sus señales. También hemos presentado dos posibles procedimientos de calibración para este modo de funcionamiento: el primero basado en eventos de lluvias atmosféricas que se pueden realizar sin conexión, y el segundo, basado en datos de fondo que se pueden realizar en línea.

En segundo lugar, se describen las simulaciones del UMD que se han desarrollado e implementado en el Software de simulación y análisis de datos (*Offline*), como parte de este trabajo de tesis. El código fue desarrollado y validado con datos de laboratorio adquiridos utilizando componentes idénticos al diseño final de UMD. Pulsos analógicos de los SiPMs y sus trazas digitales se adquirieron y se compararon con las salidas de simulación; para los primeros se utilizó electrónica construida a tal fin mientras que para las trazas se utilizaron los mismos kits electrónicos utilizados en la producción de los UMDs. Las características principales de los canales *integrador* y *contador* relevantes para el rendimiento del detector se discuten y se muestra el acuerdo entre los datos simulados y los del laboratorio. Finalmente, utilizamos las simulaciones de SiPM implementadas recientemente en *Offline* para estudiar las fuentes de bias del modo *contador* y proponer correcciones que las eliminen de la reconstrucción. También utilizamos las simulaciones para probar la calibración del modo *integrador* y para comparar las resoluciones de ambos modos. Utilizamos estos resultados para estudiar brevemente la sensibilidad de los UMDs a la masa primaria de rayos cósmicos.

En este trabajo de tesis, hemos realizado varias contribuciones a AugerPrime: (i) estudios para corroborar la estabilidad de los SiPM, (ii) prueba y optimización de la calibración de SiPMs y la verificación de su robustez, (iii) caracterización de señales UMD y fuentes de ruido, (iv) determinación de la eficiencia y atenuación de los centelladores con fibra óptica incorporada (v) una estrategia de conteo para estimar el número de muones en chubásicos atmosféricos en el modo *contador*, (vi) calibración del *integrador* utilizando datos en y fuera de línea, (vii) diseño, desarrollo, implementación y prueba de simulaciones de SiPMs y electrónicas, (viii) diseño, desarrollo, implementación y prueba de la visualización de eventos UMDs en una interfaz gráfica de usuario, (ix) análisis de los efectos del suelo en la reconstrucción de UMD, (x) corrección del bias de reconstrucción para el modo *contador* con SiPMs, (xi) análisis para mejorar las capacidades de UMD en realizar estudios sobre la composición de los rayos cósmicos. Las herramientas y métodos descritos en este trabajo de tesis serán de suma importancia para los futuros análisis ha realizarse con el detector de muones subterráneo de AugerPrime.

---

# Contents

<b>1</b>	<b>Ultra High Energy Cosmic Rays</b>	<b>1</b>
1.1	Energy spectrum . . . . .	2
1.2	Chemical composition of primary cosmic rays . . . . .	4
1.3	Extensive Air Showers . . . . .	5
<b>2</b>	<b>The Pierre Auger Observatory</b>	<b>9</b>
2.1	Hybrid detection . . . . .	9
2.1.1	The Surface Detector . . . . .	10
2.1.2	The Fluorescence Detector . . . . .	13
2.2	Enhancements of the Observatory . . . . .	15
2.2.1	Auger Muon and Infill For the Ground Array . . . . .	15
2.2.2	High Elevation Auger Telescopes . . . . .	16
2.2.3	Auger Engineering Radio Array . . . . .	18
2.3	Published results highlights . . . . .	19
<b>3</b>	<b>AugerPrime</b>	<b>21</b>
3.1	Motivation and goals . . . . .	21
3.2	Scintillator Surface Detector . . . . .	23
3.3	Surface detector dynamic range . . . . .	23
3.4	Fluorescence detector duty cycle . . . . .	24
3.5	Radio Upgrade . . . . .	25
3.6	Underground Muon Detector . . . . .	25
3.6.1	Scintillators . . . . .	25
3.6.2	Optical fiber . . . . .	28
3.6.3	From photomultiplier tubes to silicon photomultipliers . . . . .	29
3.6.4	Silicon photomultipliers . . . . .	30
3.6.5	Read-out electronics . . . . .	34
<b>4</b>	<b>The Underground Muon Detector - Binary channel</b>	<b>37</b>
4.1	Calibration . . . . .	37
4.2	Temperature compensation . . . . .	43
4.3	Noise sources . . . . .	45
4.4	Signal characterization . . . . .	51
4.4.1	Counting strategy . . . . .	56
4.4.2	Counting efficiency . . . . .	57

4.4.3 Discussion . . . . .	58
4.5 Conclusions of this chapter . . . . .	59
<b>5 The Underground Muon Detector - ADC channel</b>	<b>61</b>
5.1 Signal characterization . . . . .	61
5.1.1 Timing . . . . .	62
5.1.2 Charge . . . . .	64
5.1.3 ADC signal model and field data . . . . .	67
5.2 Offline calibration with shower events . . . . .	72
5.2.1 Integration window . . . . .	72
5.2.2 The uncertainty model . . . . .	74
5.2.3 Calibration curves of the ADC channel . . . . .	75
5.2.4 Test and discussion . . . . .	80
5.2.5 Resolution . . . . .	84
5.2.6 Example of a calibrated event . . . . .	84
5.3 Online calibration with background events . . . . .	86
5.3.1 Data set selection . . . . .	86
5.3.2 Integration windows . . . . .	86
5.3.3 Mean charge and standard deviation . . . . .	92
5.3.4 Calibration stability . . . . .	94
5.3.5 Module-to-module optimization . . . . .	94
5.3.6 Comparison to offline calibration . . . . .	97
5.3.7 Implementation in the UMD electronics . . . . .	97
5.4 Conclusions of this chapter . . . . .	100
<b>6 SiPM and muon simulations</b>	<b>103</b>
6.1 Experimental setup and calibration . . . . .	103
6.2 Single-PE simulation . . . . .	104
6.2.1 Deconvolution algorithm . . . . .	105
6.2.2 Amplifier transfer function . . . . .	107
6.2.3 Single-PE model . . . . .	107
6.2.4 Single-PE pulse generator . . . . .	111
6.3 Muon pulse simulation . . . . .	111
6.3.1 Attenuation curve . . . . .	112
6.3.2 Simulated muons . . . . .	114
6.4 Conclusions of this chapter . . . . .	118
<b>7 Electronics simulation</b>	<b>119</b>
7.1 <i>Counter</i> mode simulation . . . . .	119
7.1.1 Model and transfer functions . . . . .	119
7.1.2 Validation of the <i>counter</i> mode simulation . . . . .	123
7.2 <i>Integrator</i> mode simulation . . . . .	125
7.2.1 Model and transfer functions . . . . .	125
7.2.2 Validation of the <i>integrator</i> mode simulation . . . . .	127
7.3 Implementation in <i>Offline</i> . . . . .	128
7.3.1 UMD SiPM simulations . . . . .	128
7.3.2 The UMD component in the EventBrowser . . . . .	131
7.4 Conclusions of this chapter . . . . .	135

<b>8 UMD optimization and Proton-Iron discrimination</b>	<b>137</b>
8.1 The simulation library . . . . .	137
8.2 <i>Counter</i> mode optimization . . . . .	139
8.2.1 Bias sources . . . . .	139
8.2.2 Inhibition window selection . . . . .	141
8.2.3 Geometric correction . . . . .	145
8.3 <i>Integrator</i> mode optimization . . . . .	147
8.3.1 Geometry dependence . . . . .	148
8.3.2 Calibration in simulation . . . . .	148
8.3.3 Bias and saturation . . . . .	148
8.4 <i>Counter</i> and <i>integrator</i> modes range and resolution . . . . .	155
8.5 Proton-Iron discrimination . . . . .	155
8.5.1 Muon densities . . . . .	157
8.5.2 Merit factor . . . . .	158
8.6 Conclusions of this chapter . . . . .	161
<b>9 Summary and conclusions</b>	<b>163</b>
<b>Appendix</b>	<b>166</b>
A Devoncolution algorithm in ROOT	167
Bibliography	168
Acronyms	178
List of Figures	181
List of Tables	194
Acknowledgments	196



---

---

# CHAPTER 1

---

## Ultra High Energy Cosmic Rays

Cosmic rays (CRs) are (mostly charged) particles that arrive at Earth in a wide range of energies: from less than a GeV up to energies of  $\sim 10^{20}$  eV. They arrive from different directions, and their origin may be either galactic or extra-galactic. These particles may interact (depending on their energy) with the nuclei of Earth's atmosphere producing a shower of secondary particles that propagate towards the ground.

Formally, it was believed that the ionizing radiation produced by CRs came from the Earth itself. In 1912 Victor Hess performed a series of measurements from a hot-air balloon and observed that the ionizing radiation increased in intensity as a function of the balloon height [1]. Later observations also proved that this radiation remains the same during solar eclipses, so the idea that CRs were originated in the Sun was rejected.

Robert Millikan introduced in 1925 the concept of "Cosmic Rays" [2] assuming that CR radiation was  $\gamma$  radiation, which was the most penetrating known at the time. Subsequently, it was determined that these "rays" were in fact charged particles and their energy was initially estimated at  $10^{10}$  eV. Furthermore, CRs allowed the study of processes with energies not reachable by accelerators, resulting in the discovery of new particles such as the muon [3].

The discovery of extensive air showers (EAS) is commonly attributed to the French physicist Pierre Auger, who initiated, in 1938, the study of extended atmospheric cascades [4]. His observations showed that by placing detectors 300 m away from each other, events were obtained in coincidence. These measurements allowed to extend the estimated range of cosmic-ray energies up to  $10^{15}$  eV. The temporal correlation among the arrivals is an effect of the secondary particles produced when a CR with energy above  $10^{14}$  eV interacts with nuclei of the Earth's atmosphere: these particles propagate to the ground as EAS.

Currently, there is general consensus regarding where CRs with energies up to  $10^{17}$  eV are originated and which are the processes that enable the production of these particles in our galaxy [5]. However, there is no solid background that explains how and in which astrophysical objects CRs with energy above  $10^{18}$  are produced [6, 7]. These CRs are of extra-galactic origin [8] and we refer to them as ultra-high energy cosmic rays (UHECRs). To explain the origin of UHECRs different mechanism were suggested [7], being the most accepted ones those based in the energy transfer from a macroscopic object to microscopic particles through repeated interactions. A common example is diffusive shock acceleration, also called "first-order Fermi acceleration" mechanism [9] proposed in 1949. It contends that irregularities in magnetic fields on both sides of an ultra-relativistic shock wave from supernova remnants can enclose charged particles. The energy of these particles is increased

when crossing back and forth the wave plane. Furthermore, the Fermi mechanism also predicted that the energy spectrum of cosmic rays follows an inverse power law [5].

With the discovery of the cosmic microwave background (CMB) radiation one of its theoretical predictions was first introduced: the GZK cut in the energy spectrum of protons formulated by Greisen [10] and, in parallel by Kuz'min and Zatsepin [11]. Protons with energies greater than  $5 \times 10^{19}$  eV interact with CMB photons and in this way, they slow down until their energy falls below the interaction range. This produces a decrease in the proton flux and consequently a spectrum suppression. However, it does not set a constrain on the energy that protons may have at their source.

Still, different experiments had previously not observed evidence of a spectrum cut-off [12–16]. This was originally one of the motivations that led to a new generation of UHECR experiments such as the Pierre Auger Observatory [17] and Telescope Array [18], none of which support these claims.

## 1.1 Energy spectrum

The cosmic-ray flux observed at Earth follows a decreasing power-law energy spectrum (see Fig. 1.1) with a spectral index that present small variations over more than 11 orders of magnitude in energy. The flux is a few hundred particles per  $\text{m}^2$  per second for the lowest energies ( $E \sim 10^9$  eV), until only a few per  $\text{km}^2$  per century for the highest energies observed ( $> 1 \text{ EeV} = 10^{18}$  eV). The high-energy spectrum has three main features in which the index of the flux power law changes slightly as seen in Fig. 1.1: the “knee” ( $\sim 10^{15}$  eV), where a sequential drop out of elements [19] seems to occur, the “ankle” ( $\sim 5 \times 10^{18}$  eV), where the transition from galactic to extra-galactic sources is historically assumed to take place [20] and the “spectrum suppression” ( $\sim 10^{19.5}$  eV), whose nature remains as an open question. Finally, a fourth feature (“second knee”) has also been reported at ( $\sim 10^{17}$  eV), which is assumed to be produced by a transition from light to heavier elements [21]. The interpretation of the spectrum features is still open, since these interpretations are strongly correlated to the choice of the astrophysical model used to describe the composition and origin of cosmic rays [22].

The decrease in the cosmic ray flux for  $E_{\text{GZK}} \sim 10^{19}$  eV is explained differently for each type of primary (protons, heavy nuclei or  $\gamma$ ). The suppression of the proton spectrum is expected to be originated by photo-pion production (through the  $\Delta$  resonance) when the energy of the proton exceeds the threshold to produce said particle. Through interaction with microwave background radiation we get

$$\begin{aligned} p + \gamma_{\text{CMB}} &\rightarrow \Delta^+ \rightarrow n + \pi^+ \\ &\rightarrow p + \pi^0 \\ &\rightarrow p + e^+ + e^-, \end{aligned} \tag{1.1}$$

where the energy loss by the photo-pions production is two orders of magnitude greater than that the loss associated with the pair production [24]. Through this mechanism, protons that travel relatively short intergalactic distances ( $\sim 100$  Mpc) can not have energies greater than  $5 \times 10^{19}$  eV. In Fig. 1.2, we show the average proton energy as a function of the distance traveled through the CMB. After 100 Mpc, the energy falls below  $10^{20}$  for initial energies between  $10^{20}$  eV and  $10^{22}$  eV.

Heavy nucleus energies are reduced on this scale by an analogous mechanism. In this case, considering a nucleus of  $A$  nucleons, the main processes are

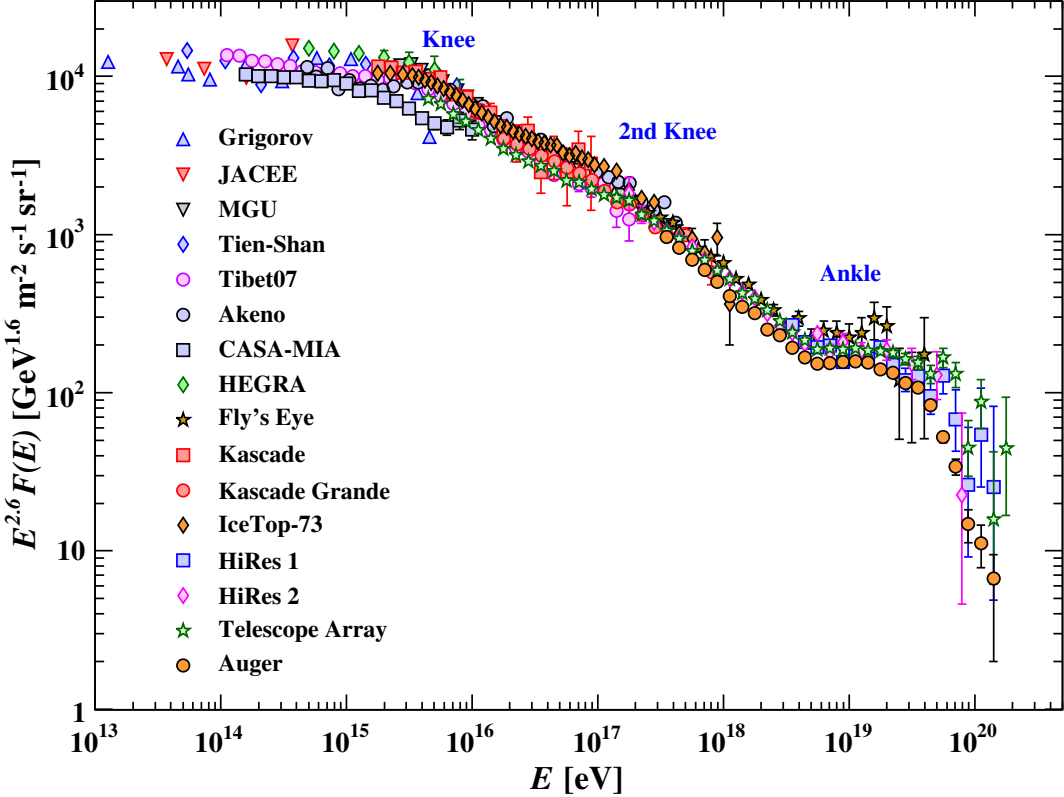
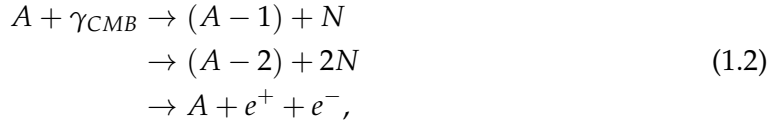


**Figure 1.1:** Energy spectrum of cosmic rays with the signaling of the “knee”, the “second knee”, the “ankle” and the “spectrum suppression” [23].



where  $N$  is a nucleon. The energy loss due to one-nucleon photodisintegration is an order of magnitude greater than the loss due to two-nucleon photodisintegration. The pair production channel conserves  $A$  and only leads to a decrease in the nucleus energy.

Finally, the main  $\gamma$ - $\gamma_{CMB}$  interaction would be a pair production



but in this case, the reaction occurs from energies in the order of  $10^{14}$  eV up to  $2 \times 10^{19}$  eV, which is less than  $E_{GZK}$ . For  $E > 2 \times 10^{19}$  eV the pair production dominates the energy loss of  $\gamma$ s.

The Pierre Auger Observatory located the energy where the cosmic ray spectrum is suppressed at  $E_{1/2} = (2.26 \pm 0.08 \text{ (stat.)} \pm 0.4 \text{ (syst.)}) 10^{19}$  eV [26], defined as the energy at which the integral spectrum drops by a factor of two below what would be expected with no cutoff [27]. This energy is at considerable odds with the prediction of  $E_{gzk} = 5.3 10^{19}$  eV. However, it is still not clear the nature of this cut, since the prediction for the spectrum suppression depends on the chemical composition of primary cosmic rays [28, 29]. Auger data favors mixed composition models for this energy region (see section 3.1). Furthermore, the energy and nature of the flux suppression has been a historical discrepancy between

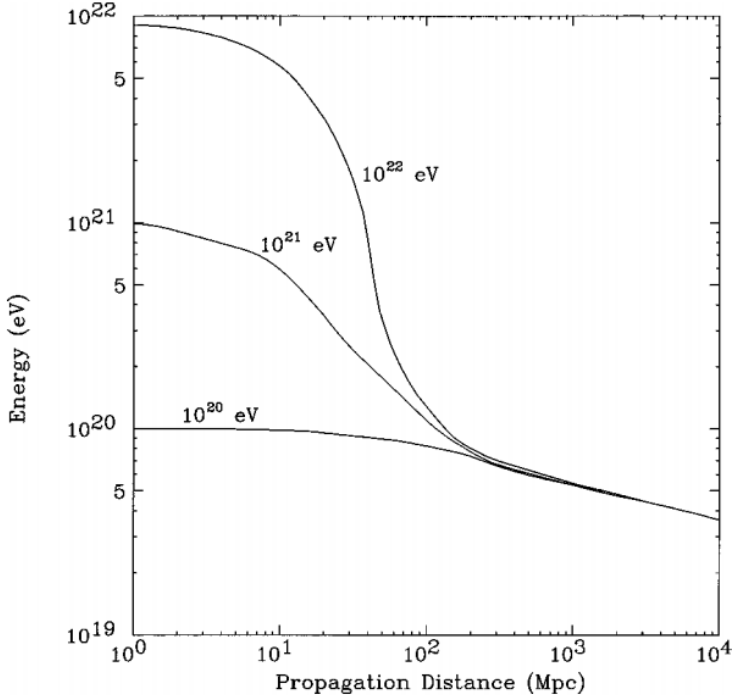


**Figure 1.2:** Average energy of protons as a function of the distance traveled through the CMB for different initial energy [25].

Auger and Telescope Array data [30]. Efforts and progress towards the understanding of this discrepancy are being made within both collaborations [31].

## 1.2 Chemical composition of primary cosmic rays

Currently, there are many open questions related to the chemical composition of UHECRs, as well as their origin. There is a consensus that index changes of the power law are due to changes in the chemical composition and sources of cosmic rays. To propose theoretical models that explain how UHECRs are generated, it is of utmost importance to study their energy spectrum according to the composition of the observed flux. Therefore, observables sensitive to the primary cosmic-ray energy and composition must be thoroughly analyzed. Some of these observables are, for example, the depth of the maximum development of the EAS ( $X_{\max}$ ), the fluctuation in the  $X_{\max}$  distribution, the air-shower muon content, among others [32].

Heavy nuclei are expected to interact and develop earlier in the atmosphere than protons [33], since the interaction probability increases with the number of nucleons. Therefore, showers produced by iron primaries reach their maximum development ( $X_{\max}$ ) higher in the atmosphere. Furthermore, and for the same reason, fluctuations in the first interaction depth are significantly smaller for iron primaries than for protons. Consequently, the  $X_{\max}$  distribution becomes narrower for iron primaries by a factor of three with respect to protons [19, 22]. Taking this into consideration,  $X_{\max}$  is a useful observable to study the mass composition of primary cosmic rays.

With the superposition principle it is established that nuclei with  $Z$  nucleons and energy  $E_0$  are equivalent to  $Z$  protons with energy  $E_0/Z$ . In equation 1.8, we illustrate the dependency of  $X_{\max}$  with  $Z$ . For nuclei, the maximum development of the shower occurs at

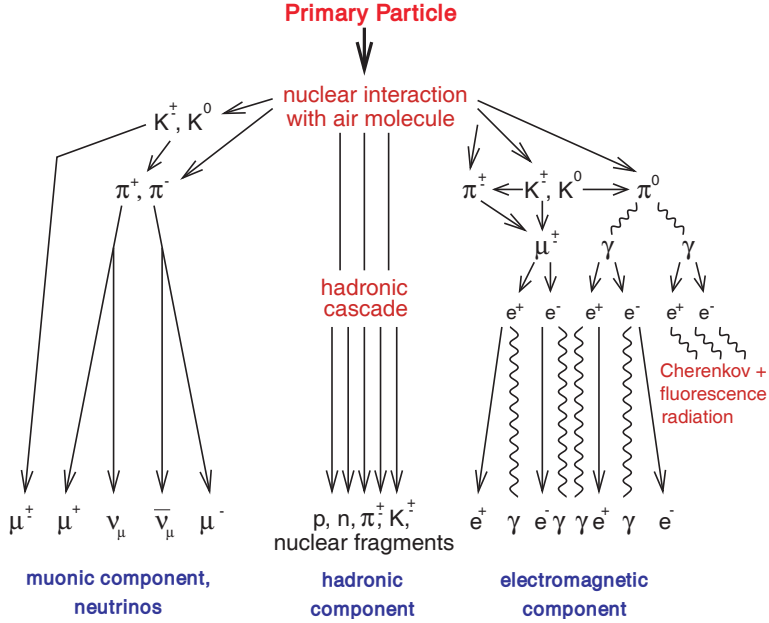


**Figure 1.3:** Production of secondary particles after a primary cosmic ray interacts with the Earth's atmosphere [34].

$X_{\max} \propto \ln E_0 / Z$ , and so for a single proton, this magnitude is  $X_{\max} \propto \ln E_0$ . It is thus apparent that  $X_{\max}$  depends not only on the primary cosmic-ray composition but also, on its energy.

As we mentioned before, there is consensus that different features in the cosmic-ray energy spectrum depict changes in the chemical composition of cosmic-rays or in their origin. Still, for UHECR ( $> 10^{18}$  eV) the Telescope Array and the Pierre Auger Projects have differed in their results and interpretations of the UHECR spectrum. A main issue is the lack of knowledge in the UHECR chemical composition which imposes severe limitations to the development of theoretical models that explain the origin of cosmic rays, and how experiments data should be interpreted.

### 1.3 Extensive Air Showers

When a primary cosmic ray with energy  $> 10^{14}$  eV reaches the Earth, it interacts with nuclei in the Earth's atmosphere producing successive particle decays that originates extensive air showers. These consist of secondary particles produced by successive interactions. In Fig. 1.3 we show a schematic of this process. Cosmic rays with energy above  $10^{14}$  eV can be studied through indirect detection by measuring EAS particles. These are mainly electromagnetic particles (electrons, positrons, and photons) and, to a lesser extent, muons and hadrons.

The Heitler model, developed in 1944, provides an analytical explanation of how secondary particles are produced from primary cosmic rays. Although the model was originally developed for photons, it is applicable to hadrons. The model consists of a branched development of showers, in which at each node a particle (and its energy) is split into 2. If  $\lambda$  is the average free path that a particle travels before being divided and  $X$  is the atmospheric depth along the shower axis, then after  $n$  ramifications of the primary particle, the amount of particles is

$$N(X) = 2^{X/\lambda} = 2^n. \quad (1.4)$$

Assuming that the energy is distributed evenly among  $2^n$  particles (which is this model hypothesis), the energy per particle results

$$E(X) = \frac{E_0}{N(X)}, \quad (1.5)$$

where  $E_0$  is the energy of the primary cosmic ray. Decays occur until the energy per particle is less than a critical energy  $E_c \sim 85$  MeV (in air), for which ionization processes predominate over the creation of new particles. Therefore,  $N_{\max}$ , the greatest amount of particles in the development of the shower verifies

$$N_{\max} = N(X_{\max}) = \frac{E_0}{E_c} = 2^{\frac{X_{\max}/\lambda}{\ln 2}}, \quad (1.6)$$

Simplifying  $X_{\max}$  we obtain the equation

$$X_{\max} = \lambda \frac{\ln \frac{E_0}{E_c}}{\ln 2}, \quad (1.7)$$

And from the equations 1.6 and 1.7 we obtain that

$$\begin{aligned} N_{\max} &\propto E_0 \\ X_{\max} &\propto \ln E_0, \end{aligned} \quad (1.8)$$

that is to say that the maximum amount of particles in the shower development is proportional to the energy of the primary cosmic ray, while the atmospheric depth in the direction of incidence of the primary particle is proportional to the logarithm of its energy. Heitler model successfully describes the main features of EASs, as expressed in equation 1.8.

The Heitler model has been generalized to hadronic showers by Matthews [35]. Although the “Heitler-Matthews model” constitutes a strong simplification of the complex hadronic multiparticle productions and particle decays, it accurately provides insights into the features of hadronic showers.

The primary hadron with energy  $E_0$  produces a number of  $n_{\text{tot}}$  new particles of which one third are neutral pions, that decay into two photons ( $\pi_0 \rightarrow 2\gamma$ ), and two thirds charged pions ( $n_{\text{ch}}$ ). As long as their energy is greater than the typical decay energy  $E_{\text{dec}}$ , the charged pions interact again with air nuclei after traveling the mean interaction length. If the energy falls below  $E_{\text{dec}}$ , the pions weakly decay ( $\pi^+ \rightarrow \mu^+ \nu_\mu$  or  $\pi^- \rightarrow \mu^- \bar{\nu}_\mu$ ) such that one muon is produced per hadron. The total number of muons obtained is

$$N_\mu = n_{\text{ch}}^n = \left( \frac{E_0}{E_{\text{dec}}} \right)^\alpha \quad (1.9)$$

where  $\alpha = \frac{\ln n_{\text{ch}}}{\ln n_{\text{tot}}} \approx 0.82 \dots 0.94$  [36] and  $E_{\text{dec}} = E_0 / n_{\text{tot}}^n$ . The Heitler-Matthews model yields the result that  $N_\mu$  has a power-law dependence on the energy of the primary cosmic ray. However, the exact parameters need to be determined through detailed simulations. Furthermore, a nucleus with atomic number  $A$  and total energy  $E_0$  is considered as  $A$  independent single nucleons with energy  $E_0/A$ . This superposition model leads to the predictions [37]

$$\begin{aligned} N_{\text{EM,max}}^A(E_0) &= A N_{\text{EM,max}}^P(E_0/A) \approx N_{\text{EM,max}}^P(E_0) \\ X_{\max}^A(E_0) &= X_{\max}^P(E_0/A), \quad \text{and} \\ N_\mu^A(E_0) &= A \left( \frac{E_0/A}{E_{\text{dec}}} \right)^\alpha = A^{1-\alpha} N_\mu^P(E_0) \end{aligned} \quad (1.10)$$

which denotes the sensitivity of  $X_{\max}$  and  $N_\mu$  to the composition of the primary cosmic ray. It is seen from the above last equation that, for a given energy, the number of muons increases with  $A$  as  $A^{1-\alpha}$ . Thus muons are an excellent tool towards cosmic-ray composition studies.



---

---

## CHAPTER 2

---

# The Pierre Auger Observatory

The Pierre Auger Observatory is located in the Departamento de Malargüe, Mendoza Province, Argentina. UHECRs are studied at the Pierre Auger Observatory, in particular, to achieve answers concerning their composition, spectrum, and origin. A hybrid detection technique is implemented to optimize the reconstruction of the energy and chemical composition of primary cosmic rays, reducing the systematic experimental uncertainties [38].

UHECRs are indirectly studied through the detection of EASs. At energies above  $\sim 10^{18}$  eV, EASs cover areas of several tens of  $\text{km}^2$  on the ground and their detection can be performed either at ground/underground level or at the atmosphere while they develop. Using different measurement techniques (explained in the following sections), the reconstruction of the arrival direction, chemical composition, and energy of primary cosmic rays is optimized in an unprecedented way. As mentioned in section 1.1, the original main motivation of the Pierre Auger Observatory was to study cosmic rays with energies above  $\sim 10^{19.5}$  eV [39] and the spectrum suppression, for which it is necessary to improve statistics at these energies, since one of the main challenges when studying these particles is their low flux ( $\sim 1$  particle per  $\text{km}^2$  per century).

### 2.1 Hybrid detection

To study EASs at ground level, a surface detector (SD) [40] is implemented. The SD consists of an array with a total area of  $3000 \text{ km}^2$  composed of 1660 water-Cherenkov detectors (WCDs) arranged in an equilateral triangular grid of 1500 m (SD-1500). The shower development in the atmosphere is observed with a fluorescence detector (FD), which consists of 24 fluorescence telescopes distributed in 4 buildings. In Fig. 2.1, we present how the SD and FD are arranged. Each SD station is represented with a black dot. On the edge of the array, the FD buildings (dots) and their field of view (lines) are displayed in blue. The map also depicts different enhancements described in section 2.2. Also, in red dots, the Central Laser Facility (CLF) [41] and eXtreme Laser Facility (XLF), used to test the FD and monitor the atmosphere are shown, along with the Balloon Launching Station (BLS) where weather balloons are launched.

EAS particles are measured with the SD at ground level. The fluorescence light, mainly produced by the interaction of the shower electromagnetic component with nitrogen molecules in the atmosphere (see section 1.2), is measured with the FD. The combination of these two

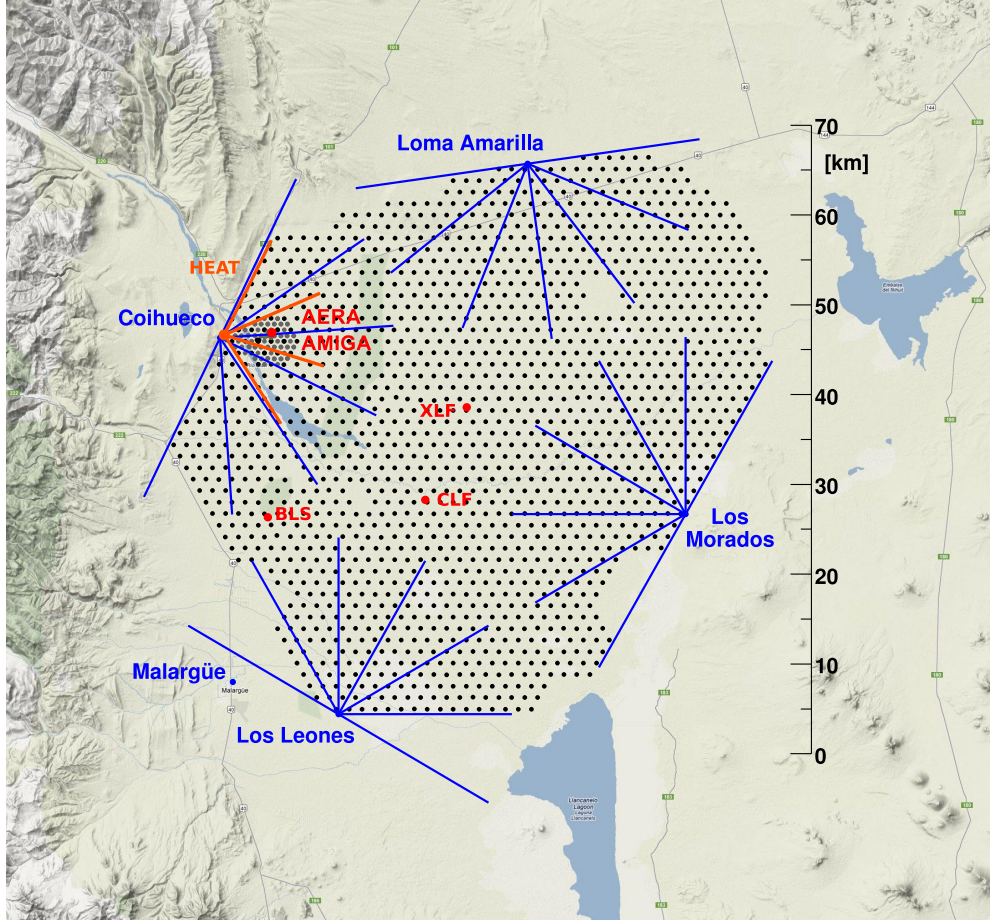


**Figure 2.1:** Map of the hybrid detector at the Pierre Auger Observatory. Each black dot corresponds to one of the 1660 surface detector stations (see section 2.1.1). The 24 fluorescence detector enclosures are shown, each with a 30° field of view distributed in four buildings (see section 2.1.2). The location of the low-energy enhancements are also displayed (see section 2.2)

detectors results in a hybrid detector [42] whose purpose is to determining the main features of UHECRs by reducing systematic uncertainties.

With the hybrid detector, the reconstruction of the primary cosmic-ray energy and arrival direction is performed. We show an example of such hybrid reconstruction in Fig. 2.2. In the following sections we present, in more detail, the detection principles of both SD and FD.

### 2.1.1 The Surface Detector

Each WCD (located at each SD station) consists of a cylindrical tank with 3.6 m diameter and 1.5 m height with a sealed liner with a reflective inner surface. The liner contains 12,000 liters of ultra-pure water. Three 9-in diameter Photonis XP1805/D1 photomultiplier tubes (PMTs) are symmetrically distributed on the surface of the liner at a distance of 1.20 m from the tank center looking downward into the water through windows of clear polyethylene. When a charged ultra-relativistic particle passes through the detector, since its speed is greater than the speed of light in water, Cherenkov radiation is produced; the Cherenkov photons are then detected with PMTs. In addition, each WCD has a GPS that provides the event time stamp, needed to build the hybrid events and to reconstruct the shower geometry (among other uses). PMTs and electronics (including the communication system and GPS) are power

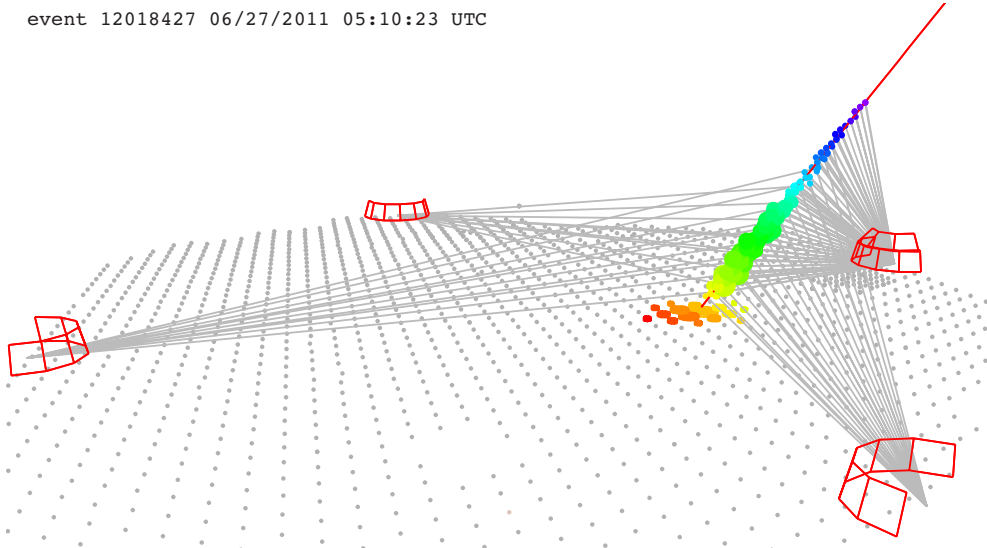


**Figure 2.2:** Example of an event simultaneously measured by both the SD and the FD at the Pierre Auger Observatory [43]. Colors denote different shower times at both shower axis and ground. The size of the markers correspond to the magnitude of measured signals at the ground and of the reconstructed energy at the shower axis. Red squares illustrate the field of view of the 27 fluorescence telescopes, the viewing directions of triggered pixels are shown as gray lines. The surface detector stations are displayed as gray dots. The obtained energy and  $X_{\max}$  from FD data was:  $E = (4.7 \pm 0.1) \times 10^{19}$  eV and  $X_{\max} = (730 \pm 3)$  g/cm<sup>2</sup>.

with two batteries charged with solar panels that provide an average power of 10 W. We show a picture of a WCD with its main components in Fig. 2.3.

The lateral density of the shower particles is measured with the SD, from which an estimator of the primary cosmic-ray energy is obtained. In addition, with the timing provided by the GPS, the arriving-time distribution of the shower front particles at ground level is obtained, from which the shower geometry can be reconstructed [45, 46]. The separation between the SD stations and their size are in accordance with the energy range to measure ( $\geq 10^{19}$  eV), since the shower footprint on the ground and its particle density are proportional to the primary cosmic-ray energy. The total size of the SD is conditioned by the need to obtain enough statistics for these low-rate events.

### The SD triggers

The main trigger is the shower trigger that results in the recording of the SD traces and has two levels of selection [47]. The first level, called T1, has 2 independent modes. The first one is a simple threshold trigger (TH) requiring the coincidence signal of all three PMTs to be above a certain threshold. This trigger is used to select large signals that are not necessarily spread in time. It is particularly effective for the detection of very inclined showers that have penetrated through a large atmospheric depth and are consequently dominantly muonic. The threshold has been adjusted to reduce the rate of atmospheric muon triggers from about 3 kHz to 100 Hz. The second T1 mode is a time-over-threshold trigger (ToT), which requires that two out of the three PMTs to be above a lower threshold for at least 13 time bins within a 3  $\mu$ s window (120 samples) in coincidence. The ToT trigger selects sequences of small signals spread in time, and is thus efficient for the detection of vertical events, and more specifically for stations near the core of low-energy showers, or stations far from the core of high-energy showers. The rate of the ToT trigger depends on the shape of the muon pulse in the tank

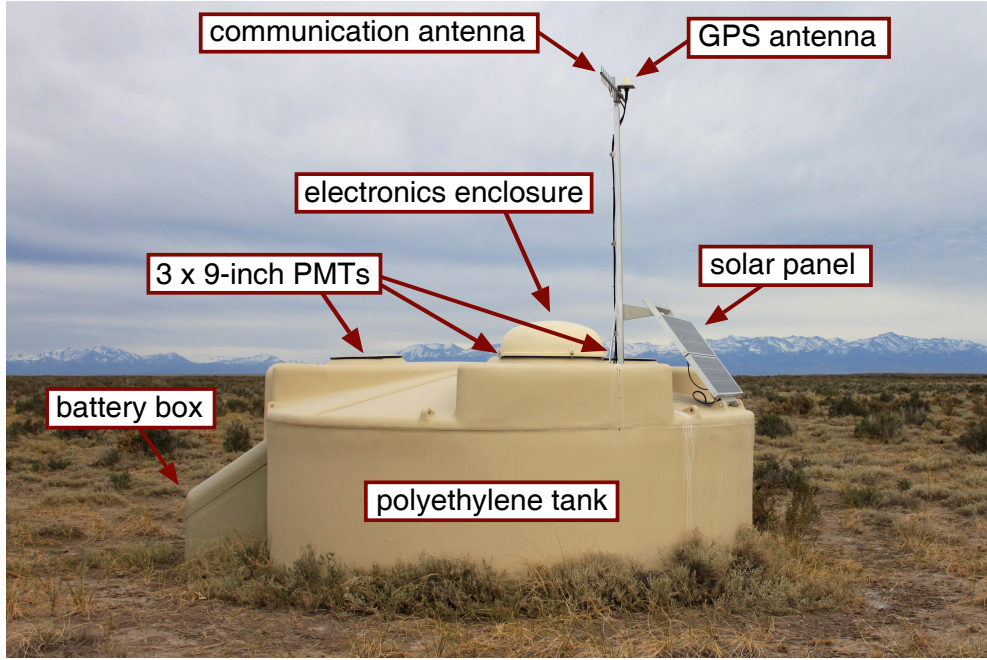


**Figure 2.3:** Water-Cherenkov detector at the Pierre Auger Observatory and its main components. Picture adapted from [44].

and averages to 1.2 Hz with a rather large spread (about 1 Hz rms). The second trigger level, called T2, is applied to decrease the global rate of the T1 trigger down to about 23 Hz. While all T1-ToT triggers are promoted to T2-ToT, only T1-TH triggers passing a single threshold in coincidence for the three PMTs will pass this second level and become T2-TH. All T2s send their time-stamp to the Central Data Acquisition System (CDAS) for the global trigger (T3) determination.

The global level trigger, T3, initiates the central data acquisition from the array. It is built at the CDAS, and it is based on the spatial and temporal combination of T2. Once a T3 is formed, all signals from WCDs passing the T2 are sent to the CDAS, as well as those from detectors passing the T1 but not the T2, provided that they are within 30 ms of the T3. The trigger of the array is performed in two modes. The first T3 mode requires the coincidence of at least three detectors that have passed the ToT condition and that meet the requirement of a minimum of compactness, namely, one of the detectors must have one of its closest neighbors and one of its second-closest neighbors triggered. It is called "ToT2C1&3C2", where Cn indicates the nth set of neighbors (see Fig. 2.4). Once the spatial coincidence is verified, timing criteria are imposed: each T2 must be within  $(6 + 5Cn)\mu\text{s}$  of the first one. An example of such T3 configuration is shown in Fig. 2.4, left panel. Since the ToT as a local trigger has a very low background, this trigger selects predominantly physics events. The second T3 mode is more permissive. It requires a four-fold coincidence of any T2 with moderate compactness. Namely, among the four fired detectors, within appropriate time windows, at least one must be in the first set of neighbors from a selected station (C1), another one must be in the second set (C2) and the last one can be as far as in the fourth set (C4). This trigger is called "2C1&3C2&4C4". Concerning timing criteria, we apply the same logic as for the "ToT2C1&3C2". An example of such T3 configuration is shown in Fig. 2.4, right panel. Such a trigger is efficient for the detection of horizontal showers that, being rich in muons

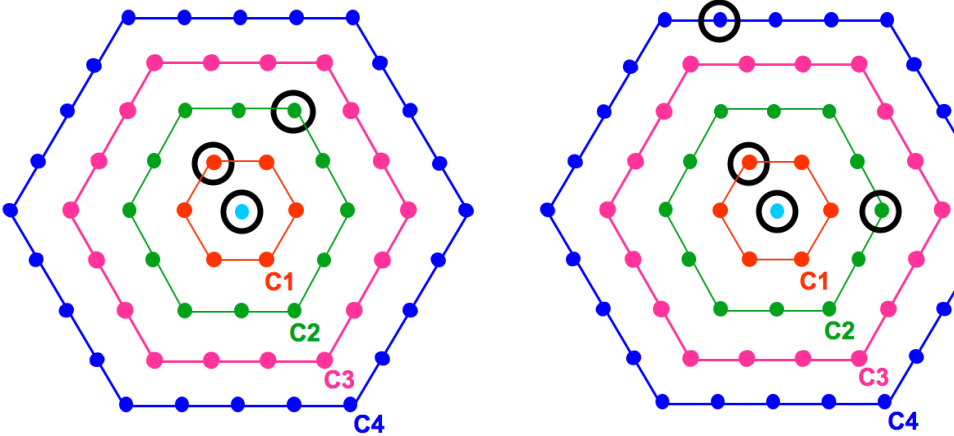


**Figure 2.4:** Example of T3 configurations: the 3-fold T3 mode ToT2C1&3C2 is shown on the left and the 4-fold mode 2C1&3C2&4C4 on the right (see text for the definitions). C1, C2, C3, C4 indicate the first, second, third and fourth sets of neighbors, respectively, at 1.5, 3, 4.5 and 6 km from a given detector

(i.e. the electromagnetic component being attenuated), generate in the detectors signals that have a narrow time spread, with triggered detectors having wide-spread patterns on the ground.

In June 2013, the Observatory installed across the entire array two additional SD T1 triggers. These triggers build upon the ToT trigger in two ways, applying more sophisticated analysis to the WCD traces. The time-over-threshold-deconvolved (ToTd) trigger deconvolves the exponential tail of the diffusely reflected Cherenkov light pulses before applying the ToT condition. This has the effect of reducing the influence of muons in the trigger, since the typical signal from a muon, with fast rise time and  $\sim 60$  ns decay constant, is compressed into one or two time bins. The multiplicity-of-positive-steps trigger (MoPS), on the other hand, counts the number of positive-going signal steps in two of three PMTs within a  $3\ \mu\text{s}$  sliding window. The steps are required to be above a small signal value ( $\approx 5 \times \text{RMS noise}$ ) and below a moderate value ( $\approx \frac{1}{2}$  vertical muon step). This reduces the influence of muons in the trigger. Both the ToTd and MoPS triggers also require the integrated signal to be above  $\approx 0.5$  VEM. Because these triggers minimize the influence of single muons, they reduce the energy threshold of the array, while keeping random triggers at an acceptable level. Thus they improve the energy reach of the SD, as well as improve the trigger efficiency for photon and neutrino showers.

### 2.1.2 The Fluorescence Detector

As mentioned before, the FD consists of 24 fluorescence telescopes that overlook the SD array from 4 sites. Within each site, 6 independent telescopes are located. Each telescope has a field of view of  $30^\circ \times 30^\circ$  in azimuth and elevation. As a result, each building provides a  $180^\circ$  coverage in azimuth of the SD array. A picture of the FD building located at *Los Leones* is shown in picture 2.5.

As EASs develop in the atmosphere, shower particles (mainly electromagnetic) interact with nitrogen molecules in the atmosphere. As a result of this interaction, the nitrogen molecules emit fluorescence light which is detected with the fluorescence telescope. The fluorescence detection system consists of a circular diaphragm with 1.1 m radius and a spherical mirror with 3.4 m radius of curvature. With the mirror, the light is focused into



**Figure 2.5:** FD building at Los Leones during the day. Behind the building, there is a communication tower. The picture was taken during daytime; shutters were opened because of maintenance [17].

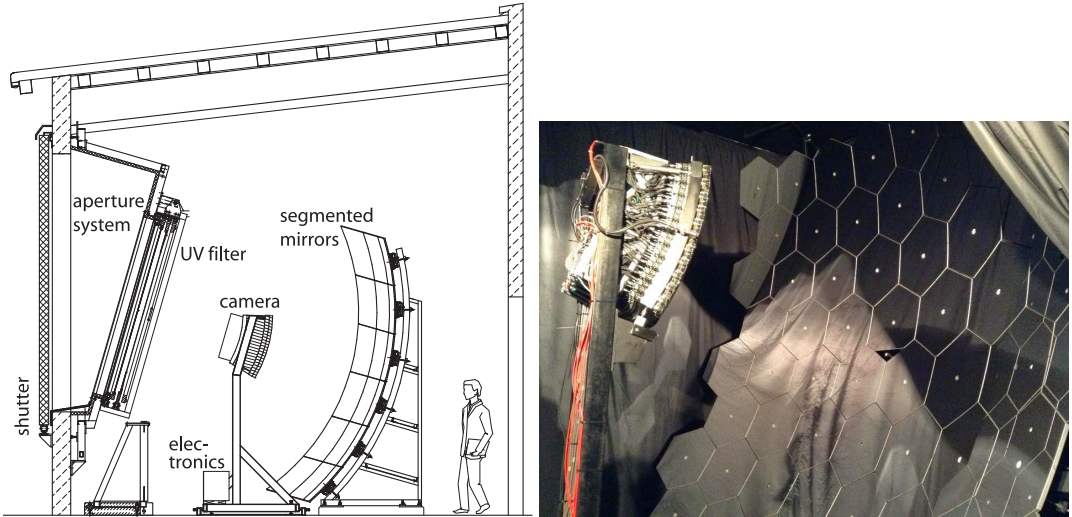


**Figure 2.6:** (Left) schematics of a fluorescence telescope at the Pierre Auger Observatory [48]. (Right) picture of the telescope mirror and camera.

a camera which consists of an array of  $20 \times 22$  PMT as shown in Fig. 2.6. A UV filter is used to reduce the background light and to improve the signal-to-noise ratio. The FD is only operated at night, with no moon near their field of view. For this reason, their duty cycle is limited up to  $\sim 19\%$  of the time, which is normally reduced to  $\sim 15\%$  due to weather conditions [17].

The intensity of the fluorescence light depends on the number of particles in the shower, which is related to the energy of the primary particle. Therefore, the signal intensity in the FD PMTs is an estimator of the calorimetric energy of the primary cosmic ray. Furthermore, by analyzing the arrival time of photons at the PMTs the arrival direction of the primary cosmic ray can be determined (as it is illustrated in Fig. 2.2). Finally, the  $X_{\max}$  can be estimated

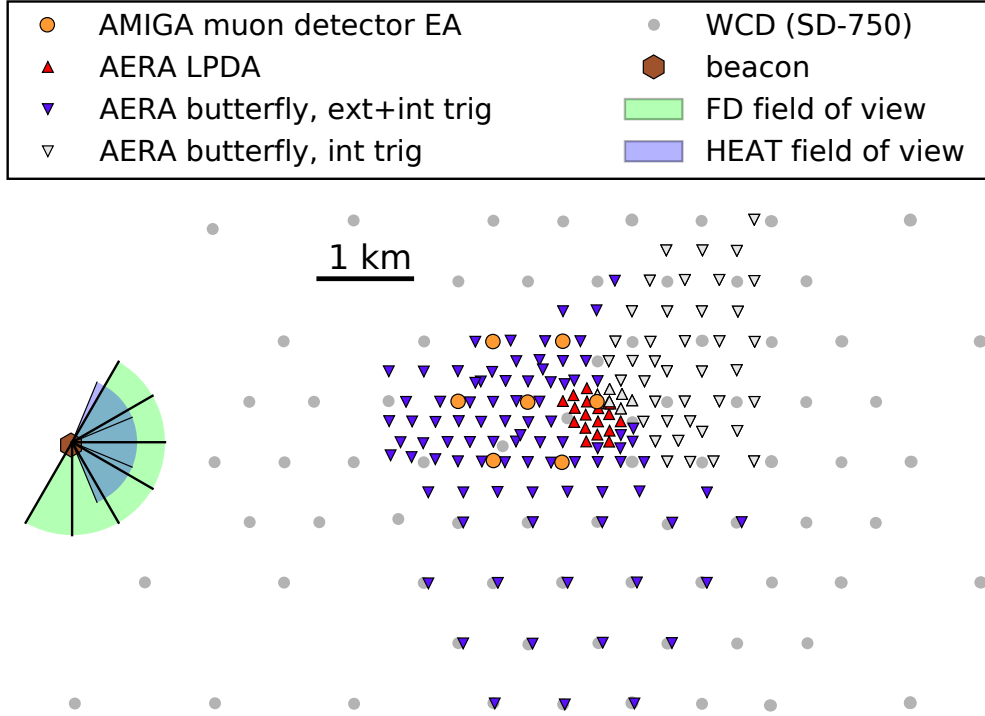


**Figure 2.7:** Map of the low-energy enhancements area adapted from [49]. It comprises AMIGA, HEAT, and AERA. The different AERA antennas, the SD-750 stations, the AMIGA muon detectors and HEAT field of view are shown.

by analyzing the intensity profile of the PMTs, and can be used for determining the mass composition of the primary cosmic ray (see section 1.3).

## 2.2 Enhancements of the Observatory

Several enhancements have been implemented at the Pierre Auger Observatory to extend its detection energy range and to improve its sensitivity to different observables. In this section, we describe three of the main enhancements: the *Auger Muon and Infill for the Ground Array* (AMIGA), the *High Elevation Auger Telescopes* (HEAT) and the *Auger Engineering Radio Array* (AERA). We show in Fig. 2.7 a map indicating where the low-energy enhancements are deployed.

### 2.2.1 Auger Muon and Infill For the Ground Array

To extend the energy detection range of the SD, a denser array with a 750 m spacing (SD-750) extending over 23.5 km<sup>2</sup> was deployed [50]. This smaller array is one of the two components of the AMIGA enhancement [51]. More recently, an even denser array with a 433 m spacing (SD-433) and an area of 1.9 km<sup>2</sup> is being deployed to extend the SD energy threshold down to 10<sup>16.5</sup> eV [52]. In Fig. 2.1 and 2.7, the location of the AMIGA infill is depicted.

AMIGA also allows direct measurements of the muonic component of EASs with muon detectors buried at 2.3 m associated with each SD-750/SD-433 station. A schematic and picture of the muon detector can be found in Fig. 2.8. The study of the muon content of EASs is of particular interest since the shower muon density is sensitive to the mass composition of primary cosmic rays [53]. Therefore, with the AMIGA muon detector, the cosmic-ray mass identification in the second knee - ankle region of the energy spectrum is improved.

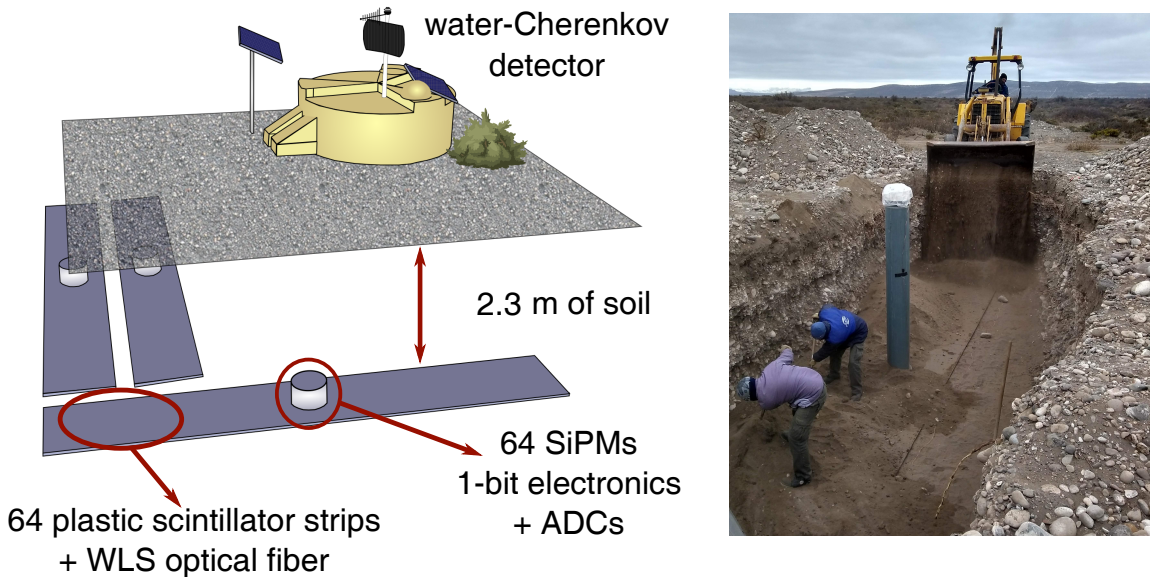


**Figure 2.8:** (Left) final-layout of the AMIGA production-phase design: each WCD of the SD-750/433 array is coupled to three  $10\text{ m}^2$  buried scintillator modules. (Right) a detector deployment in the field, where the tube to access the electronics and the optical sensor is seen.

Each muon detector consists of three  $10\text{ m}^2$  modules segmented into 64 plastic-scintillator strips with wavelength-shifting (WLS) optical fibers and photodetectors located at the center of the module [54]. During the prototype phase (finalized in November 2017), an engineering array was deployed for proof of concept, physics validation, and optimization of the detector design. In Fig. 2.9 the layout of the muon detector engineering array is shown. During this prototype phase,  $5\text{ m}^2$  and  $10\text{ m}^2$  modules were tested, as well as two different photodetectors: a 64-pixel multi-anode photomultiplier tube (PMT) and an array of 64 silicon photomultipliers (SiPMs). Upon completion of these tests,  $10\text{ m}^2$  modules equipped with SiPMs were chosen for the, currently ongoing, production phase of AMIGA.

The muon detectors are buried at  $(2.3 \pm 0.5)\text{ m}$  depth to shield them from the electromagnetic component of the air shower. Both electronics and optical sensor can be accessed through a tube of 3 m high and 30 m in diameter. The muon detector works in tandem with each WCD: once a T1 trigger condition is met, the SD station sends a trigger signal to the muon detector to keep its buffered data. Once a T3 condition is met, the muon detector sends the event information to the CDAS. Further details on the AMIGA muon detector performance and working principle are presented in section 3.6.

## 2.2.2 High Elevation Auger Telescopes

In addition to the standard FD telescopes, and as part of the energy range extension, three fluorescence telescopes covering the elevation range from  $30^\circ$  to  $58^\circ$  were built in front of the FD site at Coihueco (see Fig. 2.1). To accomplish this, three telescopes similar to the standard FD were deployed into individual inclined housings. The building housing for the HEAT telescopes is shown in Fig. 2.10. Unbiased detection of nearby low-energy showers, in combination with the SD-750 array, can be achieved with the HEAT enhancement, extending the energy range of high-quality hybrid measurements of air showers down to  $10^{17}\text{ eV}$  [55] since May 2010.

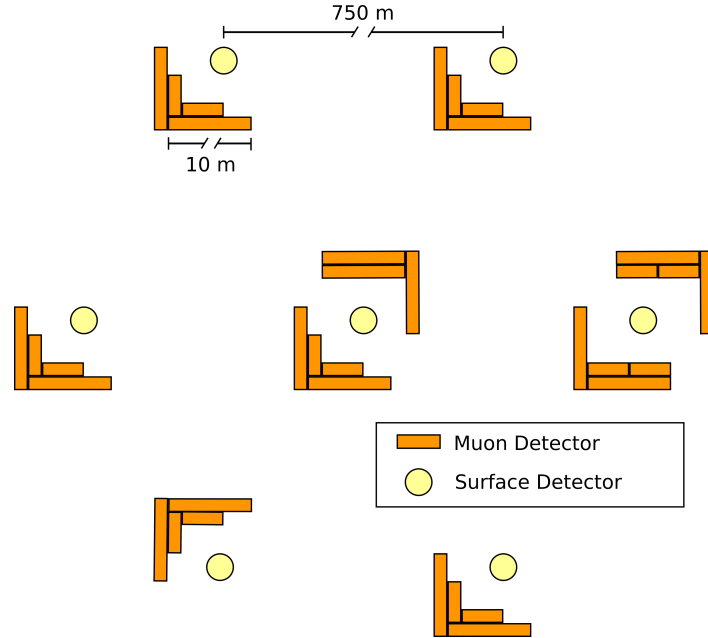


**Figure 2.9:** Layout of the engineering array of AMIGA muon detectors. In the prototype phase, each  $30\text{ m}^2$  muon detector was segmented in  $5\text{ m}^2$  and  $10\text{ m}^2$  modules. Also, two positions were equipped with extra *twin* modules to assess the detector uncertainties. Two optical sensors were tested, multipixel photomultiplier tubes and silicon photomultipliers.



**Figure 2.10:** Photograph of HEAT in tilted mode with closed shutters [55].

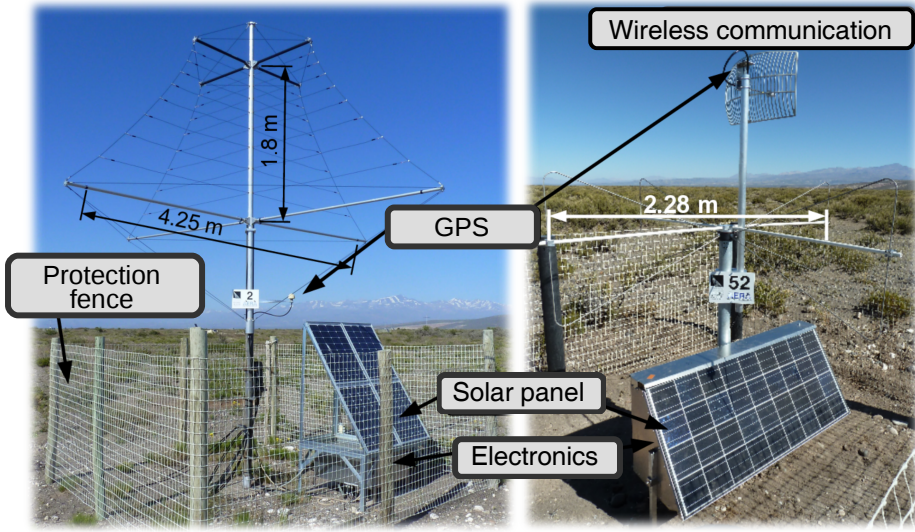


**Figure 2.11:** (Left) AERA station with LPDA antenna. (Right) AERA station with butterfly antenna.

### 2.2.3 Auger Engineering Radio Array

In an analogous way as the FD detects ultraviolet light produced while EASs develop in the atmosphere, radio antennas can measure the radio emission produced by this same development. This radio emission is mainly originated from the geomagnetic deflection of the air shower electrons and positrons [56], which is coherently amplified at wavelengths of a few meters, since this is the typical thickness of the shower front. Askaryan emission [56], i.e., radio emission due to the time-varying net-charge excess of the air shower also contributes but its contribution is almost an order of magnitude smaller.

AERA is built within the SD-750 array and covers an area of  $20 \text{ km}^2$ . 150 radio stations are arranged in grids with different spacing and enable the study of EAS radio emission in tandem with measurements from SD, FD, and MD in a multi-hybrid approach. AERA was built in three deployment phases and contains two different types of antennas: logarithmic periodic dipole (LPDA) and butterfly antennas. These are triggered externally from the SD and FD as well as self-triggered on the radio signal and internally triggered by build-in scintillators. A beacon at the site of the Coihueco fluorescence telescope building transmits continuous sine waves for the time calibration of antennas. The Central Radio Station (CRS) connects the LPDA and the internally triggered butterfly antenna stations to the central DAQ. In Fig. 2.11, we show two AERA stations with a different type of antennas and their main components.

Radio detectors are sensitive to the electromagnetic component of EASs. Therefore, they are not quite sensitive to the hadronic interaction models used to perform predictions on air shower particles, as is the muonic component. Different quantities related to the shower electromagnetic particles, and thus to the radio emission, are of use to study the energy and composition of primary cosmic rays.

## 2.3 Published results highlights

Auger has produced a number of results in the field of UHECR physics. It has unequivocally confirmed the suppression in the energy spectrum above  $5 \times 10^{19}$  eV [57]. It has also set leading photon [58] and neutrino [59] limits at the highest energies which rule out a significant effect of top-down processes in the production of cosmic rays in extragalactic sources. The observatory has also discovered a dipole in the arrival directions of cosmic rays with energies greater than  $8 \times 10^{18}$  eV with over  $5\sigma$  post-trial significance [8]. The lack of significant anisotropy at lower energies around the ankle also provides reasoning against a transition from galactic to extra galactic origins at the ankle, as a stronger anisotropy would be expected from cosmic rays produced within the galaxy at these energies, especially considering the measured dominance of a light component of the energy spectrum in this energy region (see section 3.1 for further discussion). Auger also measures a spectrum which grows increasingly heavier above the ankle [60]. Additionally, it has measured proton-air and proton-proton cross-sections at the highest energies [61], and demonstrated a muon deficit in EAS simulations using the latest LHC-tuned hadronic interaction models when comparing with measurements [62], demonstrating the observatory capability to perform studies related to particle physic. Some of these results are discussed in further detailed in section 3.1.



---

---

# CHAPTER 3

---

## AugerPrime

A number of questions related to UHECR remain open. The sources where these energetic particles are produced, and, thus, the processes involved in their production are still unknown. Also, the nature of the flux suppression, whether it is due to limits in the particle propagation such as photo-pion production and photo-disintegration of nuclei or if its produced by a limit in the sources, remains uncertain. Furthermore, statistical and systematic uncertainties impair the estimations of the chemical composition of primary cosmic rays, especially at the highest energies. A key point to resolve these questions is to understand the chemical composition of UHECRs at energies above the ankle and to improve statistics. To this aim, the Pierre Auger Observatory has started a major upgrade of its capabilities [63]. In this chapter, we present the main motivations and goals of this upgrade, along with its different components.

### 3.1 Motivation and goals

The disagreement between experimental data and simulations concerning the muon content of EASs motivates the search of observables sensitive to the electromagnetic component of air showers to perform analysis on the chemical composition of primary cosmic rays. In this sense,  $X_{\max}$  distributions at different energies have been studied to estimate the UHECR composition at Earth. To this aim, four mass groups were considered: proton (p), Helium (He), Nitrogen (N) and Iron (Fe). Simulations for each energy bin with different hadronic interaction models (EPOS-LHC [64, 65], QGSJET-II.04 [66] and SIBYLL-2.1 [67]) and different fractions of primaries were performed to create templates of the  $X_{\max}$  distribution with each configuration. The mass composition at each energy bin was inferred by selecting the template that minimizes the p-value when comparing it to the  $X_{\max}$  distribution from Auger experimental data. In Fig. 3.1, the results of this analysis using FD data is shown (from [68]). The systematic uncertainties that rise among different hadronic interaction models is apparent. Furthermore, the presence of a large fraction of protons in the energy range of the ankle ( $\sim 10^{18.5}$  eV) puts in contradiction the Auger data with the expectations for light particles flux to be produced in continuously distributed Galactic sources. According to Auger data, the anisotropy of the arrival directions of these protons cannot be larger than a few percents. However, considering how these protons propagate in the Galactic magnetic field, they [20, 69] are most likely of extra galactic origin, or one has to accept rather extreme assumptions about the Galactic magnetic field.

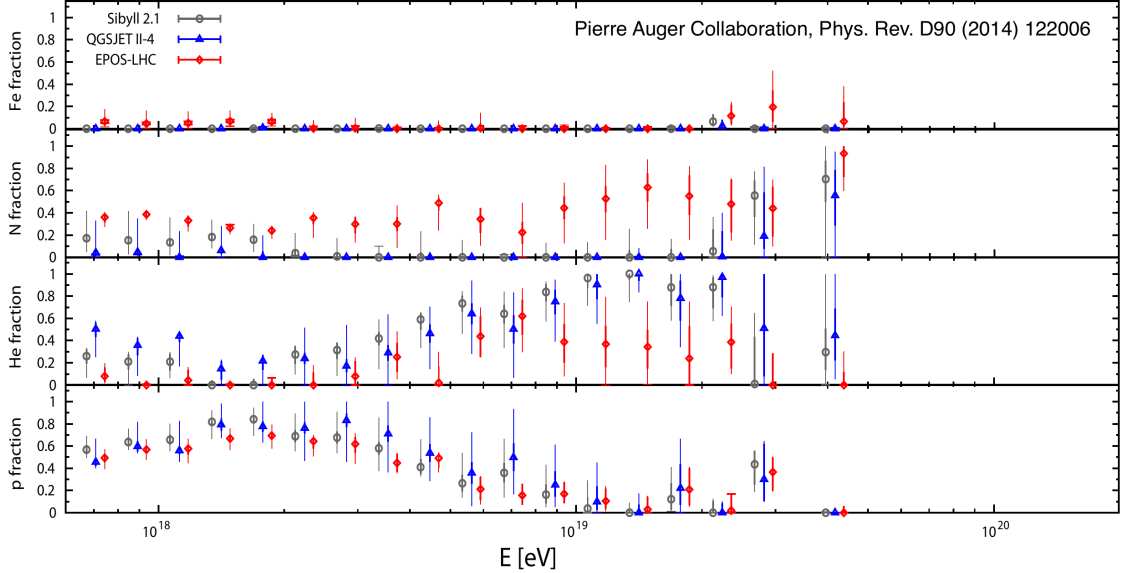


**Figure 3.1:** Estimation of the mass composition of primary cosmic-rays from the distribution of  $X_{max}$  measured with the FD at the Pierre Auger Observatory [68]. The data was fitted with a superposition of four mass groups accounting for detector resolution and acceptance effects. The error bars show the combined statistical and systematic uncertainties of the mass estimates, except those related to the choice of the hadronic interaction models. The results from the different models are slightly shifted in energy for better visualization (SIBYLL-2.1 to the left and EPOS-LHC to the right)

Another result observed in Fig. 3.1 is that two component transitions seem to take place. The first one occurs below  $10^{19}$  eV, where the proton flux decreases while the Helium spectrum increases. A second transition from Helium to Nitrogen seems to take place at energies close to the spectrum suppression. However, since the statistics at the higher energies are low, not only because of the low flux of UHECR but also, due to the limited duty cycle of the FD, this is only a hint. In addition, the discrepancy between hadronic interaction models at these energies introduces systematic uncertainties, which worsen these estimations. Finally, a fraction of proton seems to re-appear at energies above  $10^{19}$  eV. These are of particular interest since if they were there, they would point directly to their source, giving rise to anisotropies.

Motivated by these results, a major upgrade of the Pierre Auger Observatory has started, denominated AugerPrime. The general idea of the upgrade is to provide better statistics at the highest energies and to implement new detectors that will improve the mass discrimination for primary cosmic rays. The Pierre Auger Observatory is expected to operate until the end of 2024, which will triple the statistics of the data set presented in Fig. 3.1.

The main goals of AugerPrime is to determine the mass composition at the highest energies and to achieve a better understanding of the origin of the spectrum suppression (whether it is produced by a limit in the astrophysical sources, or if it is produced by energy losses during propagation). Understanding the origin of the flux suppression will provide fundamental constraints on the astrophysical sources and will allow much more reliable estimates of neutrino and gamma ray fluxes at ultra-high energy.

Secondly, determining whether there is a proton fraction of the spectrum at the highest energies is another important goal of the upgrade. The measurement of these protons is critical for estimating the physics potential of existing and future cosmic ray, neutrino, and gamma ray detectors; prospects for proton astronomy with future detectors will be clar-

fied. Moreover, the flux of secondary gamma rays and neutrinos due to proton energy loss processes can be estimated.

As we mentioned before, there are discrepancies between the predictions among different hadronic interaction models. Furthermore, inconsistencies between Auger experimental data and EAS simulation are obtained with observables strongly correlated to the hadronic interactions (such as the muon content of air showers). This has become a major shortcoming when performing analyses on the mass composition of cosmic rays with these observables. The third goal of the upgrade is to study the hadronic interactions by accomplishing a better estimation of the spectrum mass composition. This will include the exploration of fundamental particle physics at energies beyond those accessible at man-made accelerators, and the derivation of constraints on new physics phenomena.

Considering these motivations, with AugerPrime we attempt to significantly improve the composition sensitivity of the Pierre Auger Observatory, in particular, at the flux suppression region. To this aim, new and improved detectors will be implemented to obtain a better separability of the electromagnetic and muonic component of air showers, improve statistics, especially at the highest energies, and reduce systematic uncertainties.

## 3.2 Scintillator Surface Detector

The key element of AugerPrime is the deployment of plastic scintillator detectors above each WCD in the SD-1500 array. These scintillator surface detectors (SSD) will provide a complementary response to the WCD and improve the mass discrimination power of the surface detector. Due to its characteristics and energy threshold, the SSD will be more sensitive to the shower electromagnetics, whereas, the WCD is more sensitive to muons. By deconvoluting the sub-detectors signals, better separation of the shower electromagnetic and muonic components at ground level will be achieved. A picture of an SSD deployed on a WCD of the AugerPrime engineering array is shown in Fig. 3.2. The SSD is designed to have a dynamic range enabling measurement up to 200 m from the shower core even for the highest energy events [70].

Each SSD consists of two scintillator modules with a total area of  $3.8 \text{ m}^2$ . Each module is built with 12 extruded polystyrene scintillation strips. Each strip is 1.5 m long, 1 cm thick and 4 cm wide. The light produced in the scintillator segments of both modules is guided by WLS fibers to a single PMT. The fibers are positioned following the grooves of the routers at both ends, in a ‘U’ configuration that maximizes the light yield. A picture of an open SSD module is shown in Fig. 3.3.

## 3.3 Surface detector dynamic range

To improve the dynamic range of the surface detector, a “small” PMT (SPMT), Hamamatsu-R8619-22 [71], with a diameter of less than 30 mm will be deployed in each of the water-Cherenkov detectors. Furthermore, a major upgrade of the WCD electronics is being performed. The original front-end and unified board (UB) have 6 channels, a sampling frequency of 40 MHz, and a 10-bits analog-to-digital converter (ADC). All of the channels are being used for the high- and low-gain outputs of the 3 PMTs. The addition of a scintillator and SPMT requires additional channels. The upgraded unified board (UUB) is designed to accommodate this demand with 10 channels in addition to a faster sampling frequency of 120 MHz and 12-bit ADC [72].

With these upgrades, the WCD dynamic range will be extended to match the upper limits planned for the scintillator detectors such that both detector systems saturate at ap-

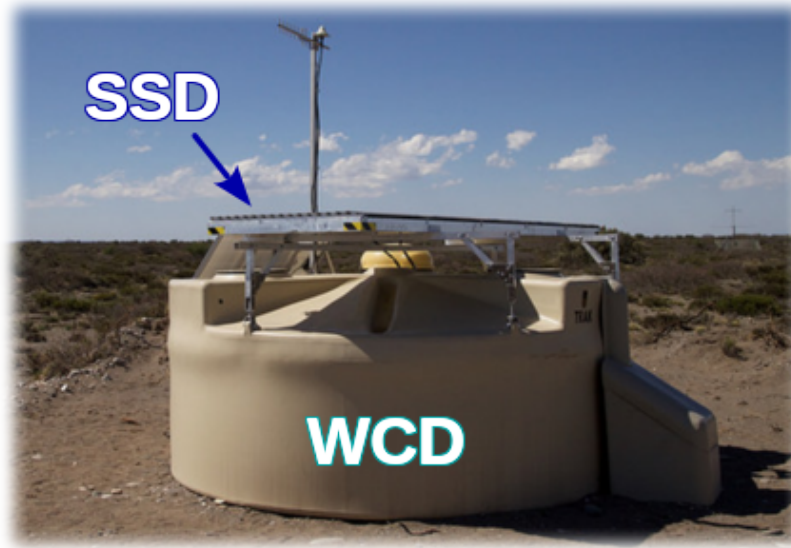


**Figure 3.2:** One station of the AugerPrime engineering array



**Figure 3.3:** Picture of one side of an open SSD.

proximately the same distance from the shower axis. For showers at energies of  $\sim 10^{20}$  eV, this distance is approximately 200 m. In addition, the faster acquisition of the UUB will generally improve the WCD performance by achieving a more finely digitizing of the detector analog signals.

### 3.4 Fluorescence detector duty cycle

To improve statistics, and thus, the mass discrimination at the highest energies, the FD will be equipped with an additional run mode to extends its duty cycle, which currently is 19%.

To this aim, PMT gains will be reduced to start the FD operation earlier in the evening till later in the morning, which will increment the FD duty cycle up to 29%. The procedure has been tested and shown to technically work while still collecting data of sufficient quality for FD reconstruction [73]. The effects of aging on the PMTs have also been examined and found to be acceptable for the expected lifetime of the Observatory.

## 3.5 Radio Upgrade

Through the AERA enhancement, it has been probed that radio detection is effective to study the features of primary cosmic rays, mainly, through inclined air showers (see section 2.2.3). Contrary to the FD, the radio antennas provide measurements of the electromagnetic component of EAS with a duty cycle of nearly 100%. Therefore, and in addition to its low costs, radio detection has become part of AugerPrime.

The radio upgrade of AugerPrime foresees to equip each SD-1500 station with a radio antenna. The reconstruction of shower parameters as the direction, energy, and, especially, the depth of shower maximum will increase the composition sensitivity for large zenith angles, for which the scintillator upgrade is not effective [74].

## 3.6 Underground Muon Detector

With AMIGA muon detectors it is possible to directly measure muons of a sub-sample of showers observed by the upgraded Auger SD-1500. On top of the rich physics studied with the AMIGA enhancement in the second knee-ankle region of the energy spectrum (see section 2.2.1), the muon detectors will serve as verification and fine-tuning of the methods used to extract the shower muonic content using SSDs and WCDs. As part of AugerPrime, the underground muon detector (UMD), which consists of AMIGA muon detectors, is being deployed in the SD-750 and SD-433 arrays.

In section 2.2.1, we have presented the layout of the UMD stations. Each muon detector consists of three modules with  $10\text{ m}^2$  plastic scintillator divided into 64 strips. To collect the light produced when a particle impinges on the scintillator strips, WLS optical fibers are used. These conduct the photons toward an array of 64 SiPMs. Modules are covered with a PVC container to protect them from the environment and buried 2.3 m depth to shield them from the electromagnetic component of air showers, thus, only muons can reach the UMD. A module under construction is shown in Fig. 3.4. Muon detectors are located in the vicinity of the WCD, so the same physical point of the shower development can be measured with all AugerPrime detectors (RD+SD+SSD+UMD) by sharing the temporary signals of GPS and telecommunications. This is of particular interest to perform multi-hybrid analysis and to perform cross-checks on the estimation of the muon content between the SSD+WCD and the muon detector. Since this thesis work is focused on the AMIGA muon detector, we describe in this section the main components of UMD modules in further detail.

### 3.6.1 Scintillators

Scintillators used in the UMD modules are extruded plastic scintillators produced and quality-controlled at Fermi National Accelerator Laboratory [75]. Each scintillator strip is 4 m long, 4 cm width and 1 cm height, built with polystyrene doped with fluor and co-extruded with titanium dioxide ( $\text{TiO}_2$ ) as an outer layer for reflectivity. These strips are built with a 2 mm groove in the center to glue the WLS optical fiber (see 3.6.2). The core of the scintillation strip consists of a compound of Dow Styron 663W polystyrene as the base material.

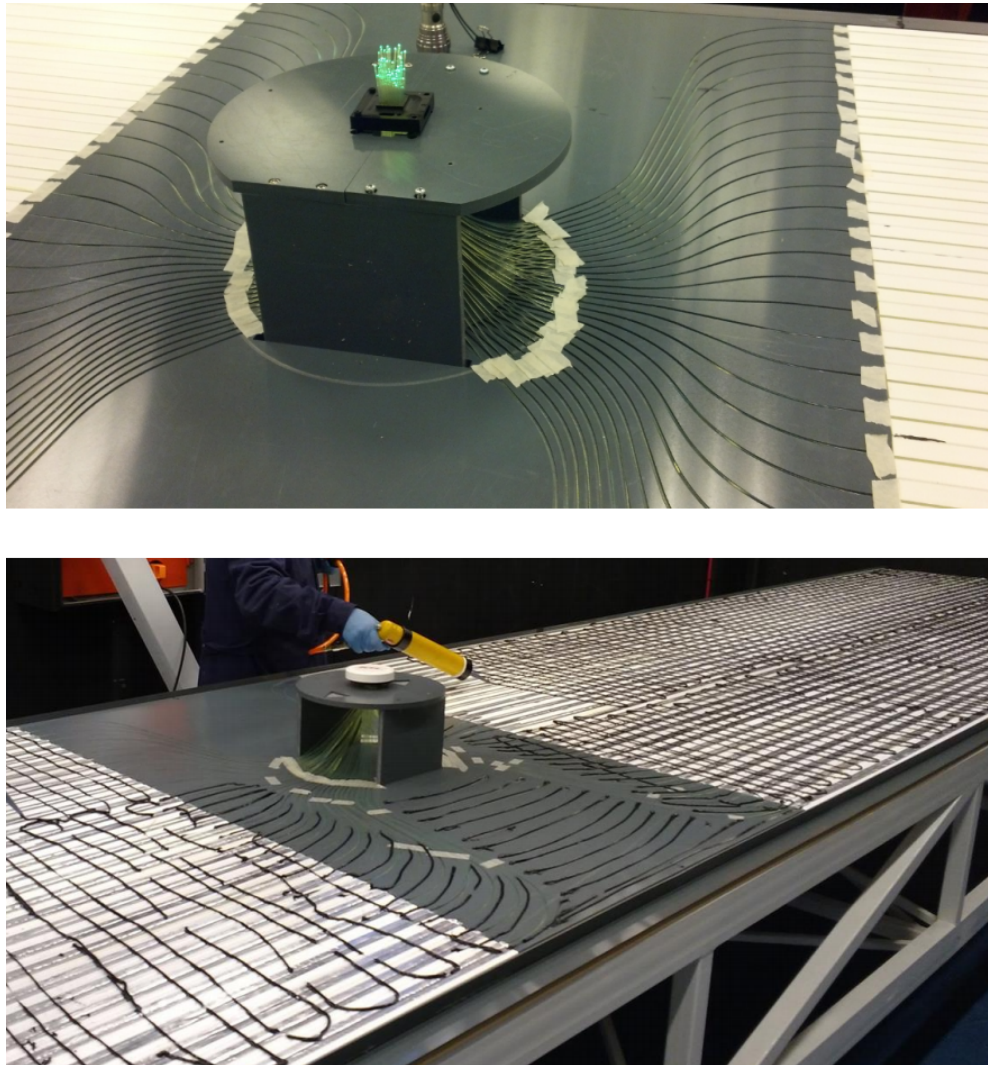


**Figure 3.4:** UMD module under construction. (Top) the optical connector with wavelength-shifting optical fibers, before polishing, is displayed. (Bottom) 64 plastic scintillator strips are shown, before closing the PVC casing.

The basic mechanism of scintillation in organic scintillators is fluorescence. In Fig. 3.5, we present a diagram of the characteristic energy levels of a plastic scintillator. The incident radiation transfers energy to the medium generating electronic transitions from the ground state  $S_0$  to different vibrational levels of the singlet  $S_1$ . The characteristic times of the vibrational states are of the order of  $10^{-12}$  s, smaller than those that characterize the radioactive transitions ( $\sim 10^{-8} - 10^{-9}$  s), so that molecules reach their thermal equilibrium before the backward transition from  $S_1$  to  $S_0$  occurs. During the transitions between the vibrational levels and the fundamental of the state  $S_1$ , the electrons lose part of the energy they absorbed when they were promoted from the ground state  $S_0$ . Consequently, the absorption and emission spectra do not match, which is a necessary feature to avoid the re-absorption of fluorescence photons. The shift between the peak of the emission and absorption spectrum is better known as *Stoke's Shift* [76].

The base material in UMD plastic scintillators is commercial quality polystyrene without additives (Styron 663 W) and is doped with PPO (at 1% by weight) and with POPOP (0.03% by weight). Also, it has a 0.25mm polystyrene reflective layer with 12% TiO<sub>2</sub> that

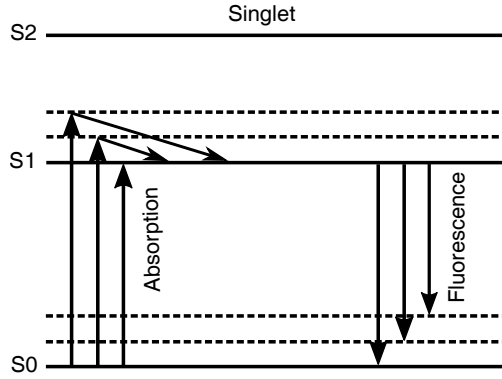


**Figure 3.5:** Schematics of the fluorescence mechanism in organic scintillators. The incident radiation transfers energy to electrons in the material, which are promoted from the ground state  $S_0$  to vibrational levels of the singlet  $S_1$ . Before the electrons return to the ground state  $S_0$ , they lose part of the energy absorbed and go from the vibrational levels to fundamental level of  $S_1$ . Then, by emitting fluorescence photons, the electron relaxes to the ground state. Diagram adapted from [77].

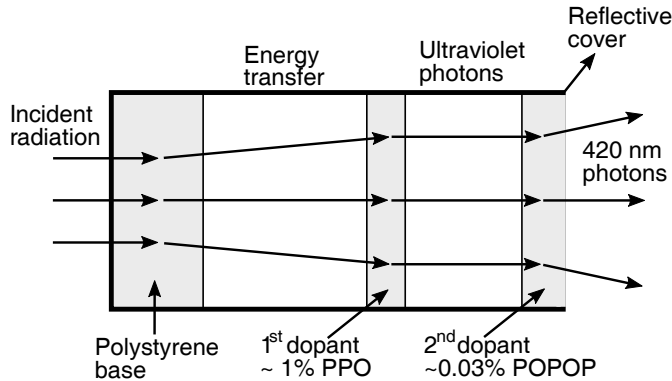


**Figure 3.6:** Diagram of mechanisms inside a plastic scintillator. Two dopants are mixed homogeneously in a plastic base. Picture adapted from [78].

decreases the probability of photons escaping from the strip. In Fig. 3.6 the composition of the scintillator used in the AMIGA muon detectors is outlined. The polystyrene base absorbs the incident radiation and emits photons in the ultraviolet spectrum; if there were no other materials in the polymer, this emission would be attenuated in millimeters. To improve this, the first dopant re-emits ultraviolet photons with a larger attenuation length. However, since the plastic is not transparent for these photons, a second WLS dopant is introduced, which absorbs the ultraviolet photons and re-emits 420 nm photons. In Fig. 3.7 we show a fragment of the plastic scintillator used in the UMD.

When the scintillator is excited by an impinging particle, it emits fluorescence photons with a probability that decays exponentially in time. Therefore, once the molecules of the material are excited, they emit a maximum of light at an instant  $t_0$  and then, as they relax, they continue to emit photons for longer times with a decreasing probability. This feature is important to understand the signals that are studied in this work and will be discussed in chapter 6.



**Figure 3.7:** Piece of scintillator strip used in the UMD modules.

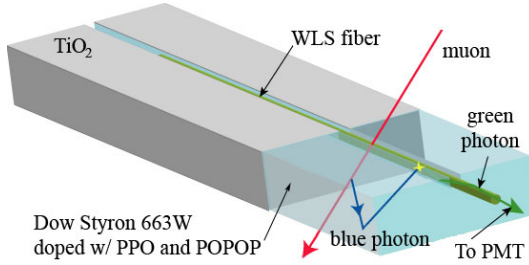


**Figure 3.8:** Schematic of the UMD scintillator with embedded optical fiber. Plastic scintillators emit blue photons in response to the passage of a particle. Then, the blue photons are absorbed with the WLS optical fiber and re-emitted into green photons that are propagated towards a photo-detector [79].

### 3.6.2 Optical fiber

Since the mean attenuation length of photons produced in the scintillator is between 5~25 cm, and the scintillator strip length is 4 m, an optical fiber is used to collect the scintillation light and conduct it to a photodetector. The optical fiber is meant to absorb as much fluorescence light possible and re-emit photons with longer wavelengths. To fulfill this requirement, WLS optical fibers are used. These optical fibers have a  $\sim 1.2$  mm radius and are coupled to the scintillator strip with optical cement. In Fig. 3.8 we show a schematics of the scintillator and optical-fiber system. Blue photons produced in the scintillator are reflected by the  $TiO_2$  layer and eventually reach the optical fiber. Then, these photons are absorbed and re-emitted as green photons with  $\lambda \sim 500$  nm in typical decay times between 3 - 10 ns. In this way, light can propagate several meters through the optical fiber until it is collected by a photodetector.

The Saint-Gobain BCF-99-29AMC multi-clad WLS fibers [80] of the AMIGA muon detector consist of a polystyrene core doped with a fluorophore, and cladded with a thin transparent film ( $2\text{-}5\ \mu\text{m}$ ) of PMMA with a refractive index lower than that of the nucleus. The total internal reflection at the interface between the core and the cladding makes it possible for photons to propagate several meters. The refractive index of the core and first cladding are 1.60 and 1.49 respectively, which implies an efficiency to capture photons of  $\sim 6\%$ . To increases, this efficiency, a second EMA cladding with a refractive index of 1.42 is used. With the second cladding the efficiency to capture photons is increased to  $\sim 10\%$ . A schematics of the WLS fiber is presented in Fig. 3.9.

Optical fibers have an attenuation, so that the light that arrives at the photodetector product of a particle impinging on the closest end of the scintillator strip significantly differs

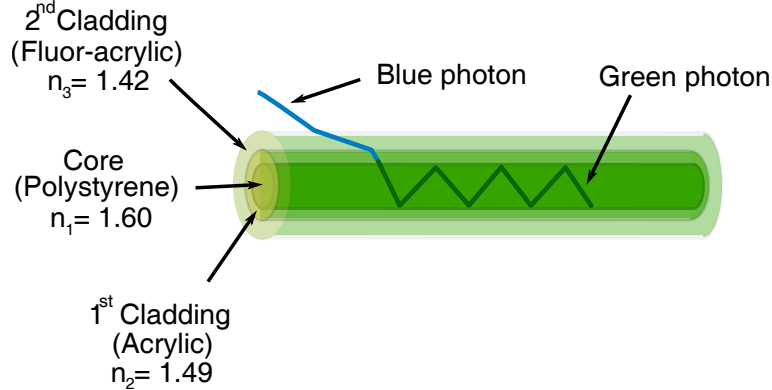


**Figure 3.9:** WLS optical fiber diagram. The core and the two claddings are illustrated.

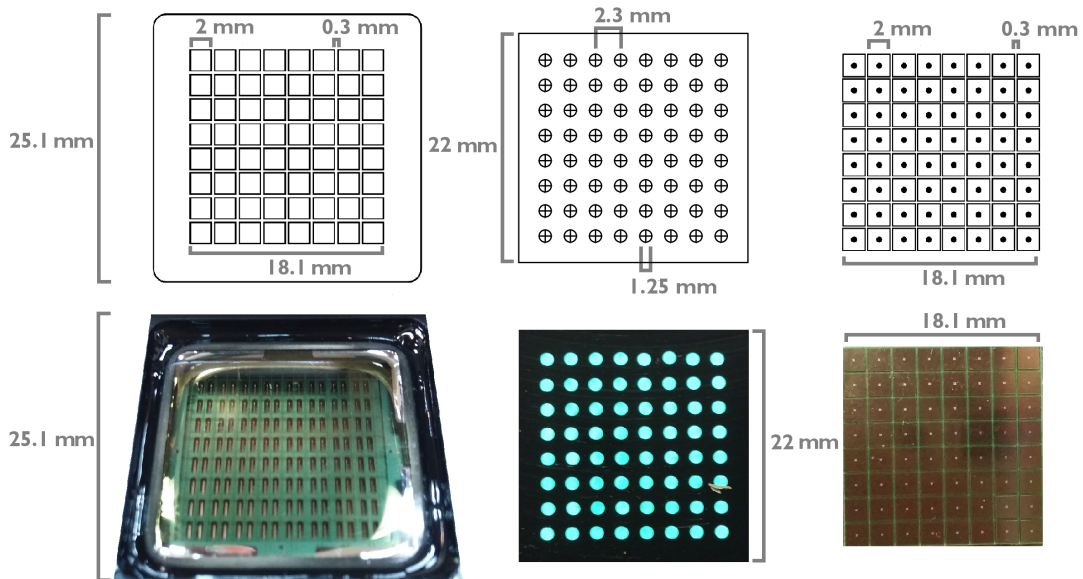


**Figure 3.10:** Schematics and pictures of muon counter photodetectors and optical connector. (Left) 8x8 multi-anode PMT. (Middle) connector for coupling the optical fibers with the photodetector. (Right) SiPM array.

from the amount of light that arrives from a particle impinging on the farthest end. In section 6.3.1, we present the attenuation curve of AMIGA optical fibers, and we discuss in chapters 4 and 5 how this attenuation impacts on the UMD performance.

### 3.6.3 From photomultiplier tubes to silicon photomultipliers

During the engineering phase, AMIGA muon detectors were operated with multi-anode PMTs Hamamatsu H8804-200MOD. More than a whole year of calibrated PMT data was obtained, from which the first AMIGA physic results were published [81, 82]. After several considerations, the PMTs were replaced by arrays of SiPMs, without performing major modifications in the module mechanical design. In Fig. 3.10, schematics with the dimensions of the 8x8 multi-anode PMT, optical connector and SiPM array, along with pictures of the devices are presented.

The strategic decision of replacing PMTs with SiPMs was primarily motivated by these considerations:

- Power consumption: SiPMs consume ten times less power than PMTs.
- Cost: 64-SiPM arrays are up to four times cheaper than PMTs.
- Efficiency: For the emission peak of the optical fiber ( $\sim 492$  nm), SiPM photodetection efficiency ( $\sim 40\%$ ) [83] is higher than PMT quantum efficiency ( $\sim 20\%$ ) [84].
- Crosstalk: the SiPM array, in contrast to the multi-anode PMT, has no crosstalk between pixels.

However, there are also shortcomings to consider. Firstly, SiPMs have a high thermal noise; this has been thoroughly analyzed and can be filtered with the read-out electronics and the data analysis (see chapter 4). Secondly, the SiPM gain strongly depends on the SiPM temperature. Considering that the temperature in which the SiPMs operate in the field can only be monitored but not controlled, it is crucial to count on a mechanism of self-calibration and temperature compensation. We discuss how SiPMs perform in the field under temperature variation in chapter 4.

To test the SiPM performance in the field and to prove the feasibility of replacing PMTs with SiPMs, a SiPM prototype module was built [85]. This prototype consists of a module with four Hamamatsu S12572-100C SiPMs ( $3 \times 3 \text{ mm}^2$ ) attached to customized electronics (fast-shapers and pre-amplifiers) and the standard AMIGA PMT back-end [85]. This prototype has been deployed in a module associated with the station with Id 688. In addition, a temperature sensor is located next to the SiPM, on the analog front-end board. Temperature information was recorded periodically in the module log.

The SiPM module prototype was also built and deployed to perform the first tests to compare SiPMs and PMTs responses. To this aim, we compared traces measured by one channel of the prototype SiPM module to traces acquired by a channel of a standard PMT module. The addition of the binary traces, stored after each T3-request and acquired during one month (May 2015), are shown in Fig. 3.11 (along with the peak fits). Both peaks are well-above the noise/background level and therefore clearly distinguishable. The modules are paired with the same counter; thus, they measure the same showers. As the signal widths are dominated by the shower timing, the peak widths on Fig. 3.11 are expected to be comparable. The standard deviation obtained for the PMT peak is  $\sigma_{\text{PMT}} = (9.07 \pm 0.36)$  ns, and for the SiPM peak  $\sigma_{\text{SiPM}} = (9.37 \pm 0.32)$  ns. The mean values are not relevant as delays on the signals are mainly due to differences in the cable lengths. Also, the peak height and background noise are expected to be different as both photodetectors have very different features.

After several tests in the field and laboratory, the replacement of PMTs with SiPMs was performed. The muon detector associated with the station with Id 1764 was the first to be fitted with SiPMs, in December 2016. In January 2018, the deployment of SiPMs in the whole AMIGA engineering array was completed.

### 3.6.4 Silicon photomultipliers

SiPMs are arrays of avalanche photodiodes (APDs) operated in Geiger mode (G-APDs), each of which is commonly named micro-cell or cell. APDs are designed in different architectures, based on the working principle of p-n junctions. A schematic of a typical APD design is shown in the top panel of Fig. 3.12. The detector is made of a lightly doped p-type material ( $\pi$ ) between a heavy doped p-type ( $p^+$ ) side and a heavy doped n-type side ( $n^+$ ). Another

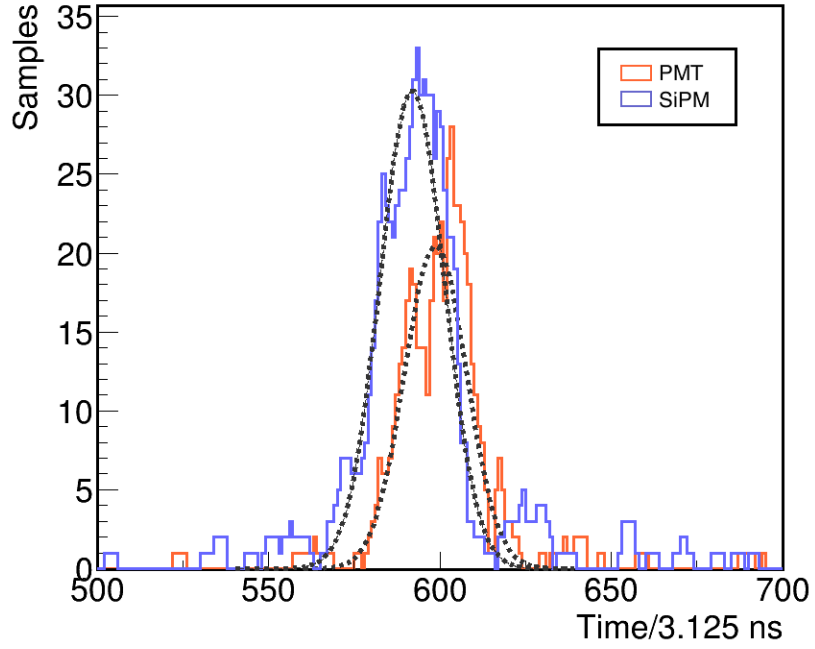


**Figure 3.11:** Trace comparison between PMT (orange) and SiPM (blue) with their respective fits. The data were extracted from a prototype module (Id: 102) and a standard module (Id: 1) paired with the same station (Id: 688). Each peak displays events acquired during three months. The standard deviation for the PMT peak is  $\sigma_{\text{PMT}} = (9.07 \pm 0.36)$  ns, and for the SiPM peak  $\sigma_{\text{SiPM}} = (9.37 \pm 0.32)$  ns.

p-type region is also introduced between the  $\pi$  and n<sup>+</sup> side. The n-type dopant is rich in free charge carriers (e<sup>-</sup>) and the p-type dopant is rich in holes. At the p-n junction, free electrons in the n-type and holes in the p-type attract and cancel each other. As a result, in the n-type, a region near the junction becomes positively charged, while in the p-type, a region near the junction becomes negatively charged. The significant accumulation of charge around the p-n interface produces a strong electric field. Furthermore, the regions near the p-n junction lose their neutrality and most of their mobile carriers, forming a depletion layer. If a reverse bias voltage is applied at the side of the junctions, meaning the p region is connected to a negative terminal, and the n region to a positive terminal, then the voltage at the cathode is comparatively higher than at the anode. Therefore, very little current flows until the diode breaks down. Once the electric field intensity increases beyond a critical level (which corresponds to the breakdown voltage), the p-n junction depletion zone breaks down and current begins to flow, usually by an avalanche breakdown process. An illustration of the electric field in an APD after applying a reverse bias is presented in the bottom panel of Fig. 3.12. Based on this electric field profile two regions can be identified: an absorption region R<sub>abs</sub> and a multiplication region R<sub>mult</sub>. Radiation reaching R<sub>abs</sub> produces electron-hole pairs, which are accelerated by the electric field (produced by the reverse voltage) in different directions. When electrons arrive to the intensive electric field region (or avalanche region) a multiplication process begins. The electrons produced by the incident radiation generate more and more electron-hole pairs. As a result, a macroscopic current is obtained.

Depending on the applied reverse bias ( $V_{\text{bias}}$ ), APDs can be operated in different modes [86], which we illustrate in Fig. 3.13. When  $V_{\text{bias}} < V_{\text{APD}}$  the device behaves as a photodiode, whose gain equals to 1, thus for every electron-hole pair created, a single electron is collected. This working mode can be used, for example, to measure high-levels of light.

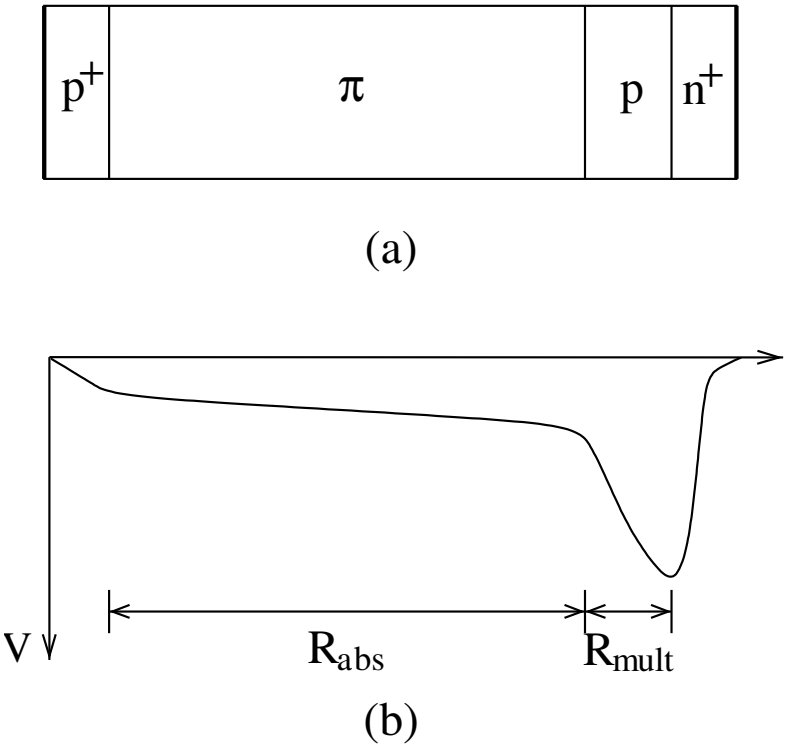


**Figure 3.12:** (Top) schematics of APD design.  $\pi$  represents either a lightly doped p-material or intrinsic material while the superscript (+) refers to heavy doping. P-type region is rich in holes while n-type region is which in electrons. (Bottom) electric field profile of the structure shown in the top panel after applying a reverse bias voltage between n<sup>+</sup> and p<sup>+</sup> [78].

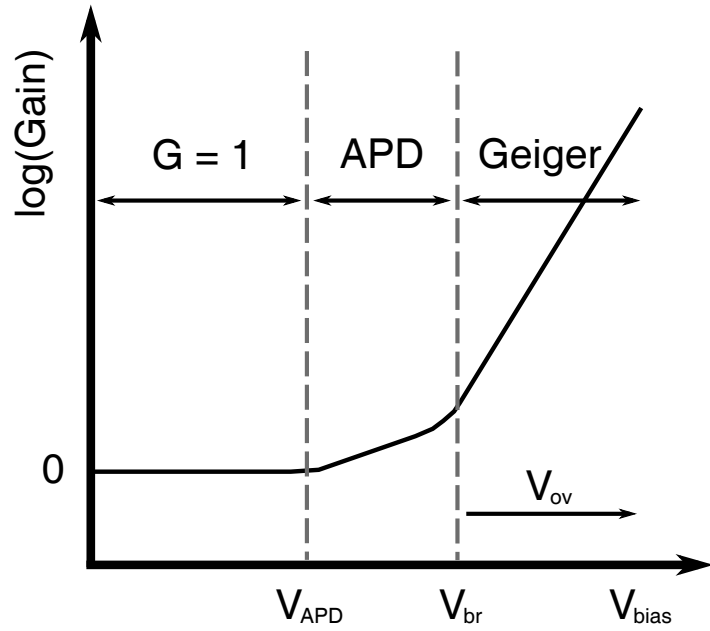


**Figure 3.13:** Illustration of APD operation modes.

If  $V_{\text{bias}} > V_{\text{APD}}$  but smaller than the diode breakdown voltage ( $V_{\text{br}}$ ), the detector runs in a linear mode (commonly referred as APD mode). In this case, avalanches develop only in

one direction (from the p-type towards the n-type) and stop multiplying when the charge carriers reach the low field area of the n region. Very rarely are secondary avalanches started by holes or secondary photons in the p-type region. In this case, for every electron-hole pair produced in the depletion region, a finite multiplication is generated, and the total charge collected is  $\langle M \rangle$ , where  $M$  is the device gain. A higher  $V_{\text{bias}}$ , results in a higher gain. This working mode is useful for detecting low level of light, however, it is not ideal for photon counting, since the output gain fluctuates significantly.

When  $V_{\text{bias}} > V_{\text{br}}$ , the APD is operated in *Geiger-mode*. In this mode, a charge carrier generated in the depletion region can trigger a diverging avalanche multiplication (infinite gain) of carriers. Both positive and negative carriers (and also photons generated in the avalanche multiplication) are involved with a positive feedback effect, which makes the carrier multiplication self-sustaining. In G-APDs, the essential new process is the additional initiation of secondary avalanches, triggered by holes and secondary photons in the p-type region. Therefore, an G-APD avalanche does not stop by itself and, as a consequence, the avalanche process must be quenched by the voltage drop across a high-ohmic serial resistor or by an active quenching circuit. G-APDs provide a uniform output, which mainly depends on the applied  $V_{\text{bias}}$  and the equivalent quenching resistor.

As we mentioned before, SiPMs are arrays of G-APDs. Each G-APD or cell can be triggered once within its recovery time. Therefore, the SiPM output depends on the number of triggered cells and not on the number of electron-hole pairs produced by the incident radiation. We commonly refer to the number of triggered cells as photon-equivalents (PEs). SiPMs used in the AMIGA muon detectors is HAMAMATSU S13361-2050NE-08, which have a total of 1584 cells [83]. Therefore, each SiPM can detect a maximum of 1584 simultaneous photons. However, the probability of photons hitting more than once the same cell increases with the number of incident photons. SiPM saturation is produced by photons that pile up in the same cell.

## SiPM features

We describe in this section some SiPM characteristics relevant to this thesis work:

- **Breakdown voltage ( $V_{\text{br}}$ ):** as we mentioned before, the  $V_{\text{br}}$  is the minimum voltage required for an APD to run in Geiger-mode and it is an intrinsic property, which only depends on the SiPM temperature.
- **Reverse bias voltage ( $V_{\text{bias}}$ ):** voltage set between the SiPM anode and cathode, analog to the PMT high-voltage.
- **Over voltage ( $V_{\text{ov}}$ ):** difference between  $V_{\text{bias}}$  and  $V_{\text{br}}$ . The SiPM operating point is determined by the  $V_{\text{ov}}$ , which is adjusted by setting  $V_{\text{bias}}$ .
- **Gain:** the amplitude and transported charge of the SiPM output current depend on the  $V_{\text{ov}}$ . The device gain, and thus, the output current, increases with  $V_{\text{ov}}$ .
- **Quantum efficiency (QE):** the probability for an impinging photon to transfer energy to the silicon and produce an electron-hole pair. QE is a function of the incident light wavelength ( $\lambda$ ) and the angular direction of incident photons.
- **Fill factor ( $\epsilon_{\text{geom}}$ ):** corresponds to the total active area of the SiPM. It accounts for the fact that each cell in the SiPM has necessarily some dead area on its periphery to accommodate isolating structures and metal lines for signal routing.

- **Avalanche trigger probability ( $\epsilon_{\text{trigger}}$ ):** it is the probability of initiating a self-sustaining avalanche process and thus an output current pulse, once an electron-hole pair is produced.  $\epsilon_{\text{trigger}}$  depends on  $V_{\text{ov}}$ , and it increases with it. Also,  $\epsilon_{\text{trigger}}$  is wavelength-dependent since the avalanche initiation probability depends on the position inside the G-APD where the electron-hole pair was created. Since different wavelength has different penetration depths in silicon, this dependence is apparent.
- **Photodetection efficiency (PDE):** the probability for a SiPM to detect an incident photon is  $\text{PDE} = \text{QE} \epsilon_{\text{geom}} \epsilon_{\text{trigger}}$  and depends on  $\lambda$ ,  $V_{\text{ov}}$  and the direction of the incident light.
- **Optical crosstalk:** SiPM crosstalk between cells may occur when electrons are recombine during the avalanche emitting photons. These may escape from the triggered cell and hit a neighbor cell producing a simultaneous avalanche. As a result, an output of two PEs may be obtained, despite having only one cell triggered by incident radiation.
- **Afterpulsing:** electrons in an avalanche may get trapped into silicon impurities and get release after the avalanche was quenched. In this scenario, a second avalanche may be triggered by the release of this electron generating a new output signal equivalent to one PE.
- **Dark count rate (or dark rate):** noise in SiPMs is represented by spurious output current pulses produced in absence of light. In silicon, there is a finite probability for carriers to be generated by thermal agitation. If an electron-hole pair originates inside the active region of a cell, an avalanche may be initiated. We refer to this as a dark count, and to the number of dark counts per unit of time as dark rate. In SiPMs, the thermal generation of carriers doubles approximately every  $10^{\circ}\text{C}$ , and so does the dark rate. Moreover, the it is an increasing function of the  $V_{\text{ov}}$ . A dark count can also originate an afterpulsing event or crosstalk, resulting in thermal noise with an amplitude of more than a PE.
- **Recovery time:** after a cell breaks down, it recharges exponentially before it finally recovers its full sensitivity. The time that takes for the detection efficiency and gain of the cell to recover is known as recovery time.

### 3.6.5 Read-out electronics

To attain a broad dynamic range, the readout electronics of the UMD modules implements both *counter* and *integrator* modes. Schematics of the electronics can be found in Fig. 3.14. The *counter* mode independently handles the 64 SiPM signals through a pre-amplifier, fast-shaper, and a discriminator, built within each channel of two 32-channel Application-Specific Integrated Circuits (ASICs), in this case CITIROCs [87] furnished by WEEROC. The discriminator signal is sampled at 320 MHz (3.125 ns sample time) with a Field-Programmable Gate Array (FPGA) into 64 2048-bit traces, giving a trace length of  $6.4\mu\text{s}$ . In each trace, a “1”-bit is output if the signal is above the discriminator threshold, set at 2.5 PE to reject most of the SiPM dark rate [88], and a “0”-bit otherwise. In this working mode, muons can be identified as sequences of “1”s in the binary traces. A simulated single-muon trace is shown in the left panel of Fig. 3.15.

On the other hand, with the *integrator* mode the 64 SiPM signals are summed analogically and the result is amplified with low- and high-gain amplifiers. The signals are then sampled at 160 MHz (6.25 ns sample time) with two ADCs resulting in two waveforms of 1024 samples. In the right panel of Fig. 3.15, a simulated trace of a single-muon signal in the

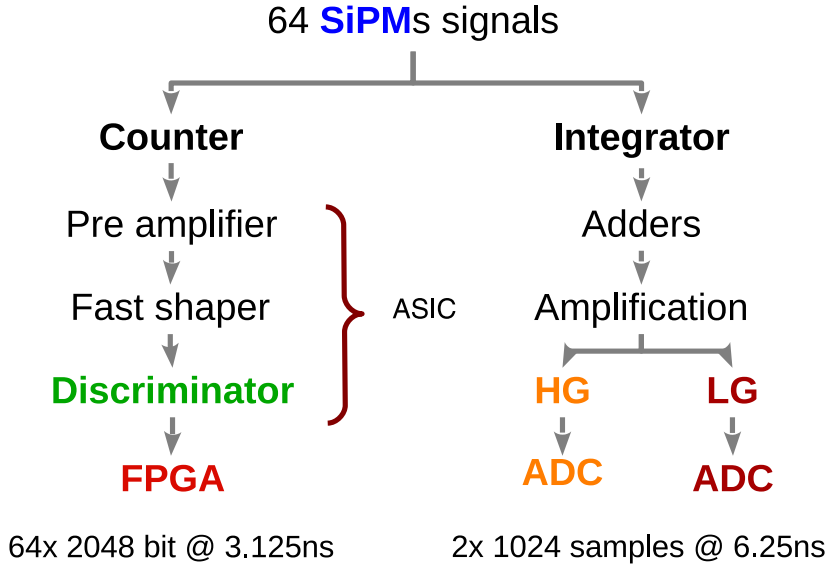


**Figure 3.14:** Schematics of the AMIGA muon detector electronics. The modules implement a *counter* and an *integrator* mode. In the *counter* mode, the output consists of 64 binary traces in which muons can be identified as sequences of "1". The *integrator* mode outputs two waveforms from which the muon number can be estimated dividing the signal charge by the mean charge of a single muon.

*integrator* mode is displayed. The number of muons can then be estimated by dividing the signal charge by the mean charge of a single muon.

Both modes work in a complementary way. The *counter* mode is limited by the detector segmentation; two muons arriving at the same strip simultaneously will be counted as a single particle. This effect limits the number of muons that can be detected at the same time. The *integrator* mode improves this limit and extends the detector dynamic range to measure higher muon densities, thus reaching distances closer to the shower core. The *integrator* mode has larger uncertainties with smaller muon number since there will be statistical fluctuations in the output signal. Furthermore, each working mode has different biases, resolutions, and systematics. Still, they both measure simultaneously the same particles and as such a combined analysis is foreseen [89] and could be useful to understand these features and to reduce their impact in the detection uncertainties.

The main goal of the UMD is to measure the muons of extensive air showers, including their arrival time. As described before, particle counting is performed individually muon-by-muon with the *counter* mode and proportionally to the signal charge with the *integrator* mode. The read-out electronics of the *counter* mode produces binary signals relying on the signal amplitude while for the *integrator* mode the output signal is based on the total-signal charge.

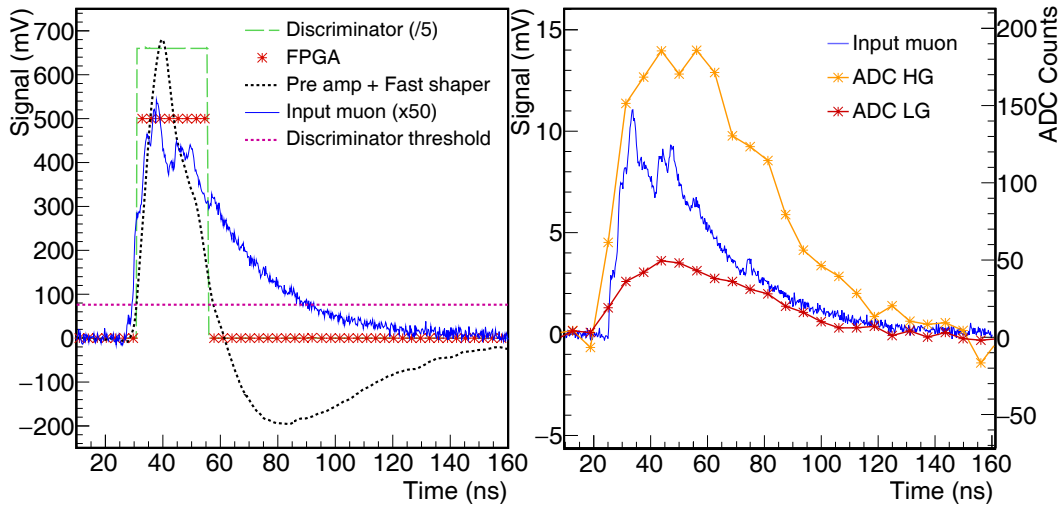


**Figure 3.15:** (Left) A simulated single-muon trace in the *counter* mode. The signal from the SiPM and the discriminator pulse are re-scaled for illustration. The FPGA outputs a “1”-bit in the binary trace when the fast-shaper output is above the discriminator threshold. (Right) A simulated single-muon trace in the *integrator* mode. The two ADC outputs (low- and high-gains) are shown.

---

---

## CHAPTER 4

---

# The Underground Muon Detector - Binary channel

As mentioned in section 3.6, the underground muon detector of AugerPrime has two operation modes: *counter* and *integrator*. Since the first mode outputs 64 binary traces, we commonly refer to the output of this mode as the *binary channel*. In this chapter, we introduce the different characteristics of the UMD binary output to propose a counting strategy and determine its noise level and efficiency.

In section 4.1, we describe the calibration procedure of the binary channel, which consists of determining each SiPM  $V_{\text{bias}}$  and discriminator threshold to obtain an equalized response in the whole SiPM array [88]. To this aim, by measuring the photo-equivalent peak ( $\text{PE}_{\text{peak}}$ ) at different  $V_{\text{bias}}$ , the  $V_{\text{br}}$  of each SiPM is obtained. As detailed in [88], the final  $V_{\text{bias}}$  is set to accomplish a  $V_{\text{ov}} = 3.5 \text{ V}$  and the discriminator threshold is set to 2.5 PE. During operation, the  $V_{\text{bias}}$  is re-adjust to compensate for the temperature fluctuations as explained in section 4.2, which is fundamental in achieving a uniform response.

In section 4.3 we describe two acknowledged sources of noise: the SiPM dark rate, which can reach the 2.5 PE threshold due to the crosstalk between the SiPM cells, and the noise from the optical fiber. In this section, data from the field are also analyzed to study the background fluctuation under temperature variation for two discrimination thresholds: 2.5 and 3.5 PE. We also determine the noise level from laboratory measurements in section 4.4. With these measurements, we describe the main characteristics of the single-muon signals, from which we propose different counting strategies. For each of these strategies, we estimated the background noise level and efficiency, which we present in subsections 4.4.1 and 4.4.2.

### 4.1 Calibration

Contrary to PMTs, SiPMs have a well-defined PE spectrum. Therefore, it is possible to calibrate them using dark-rate pulses. The PE amplitude spectrum can be obtained by measuring the dark rate as a function of an amplitude threshold. The well-defined SiPM pulses turn into well-defined plateaus as shown in Fig. 4.1. Each plateau corresponds to the transition between PE peaks. When the threshold level moves near one of the peaks (green), the number of events changes rapidly and therefore a transition between plateaus is observed (blue). On the other hand, when the trigger moves through the valleys between two peaks, the number of events varies slowly and, when integrated, plateaus are obtained. The transi-

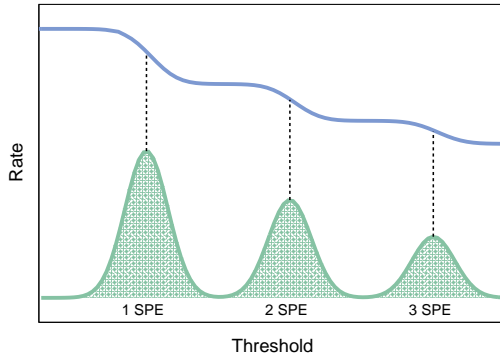


**Figure 4.1:** Schematic of the dark-rate curve as a function of an amplitude threshold (blue); its derivative (green) shows the PE amplitude spectrum.

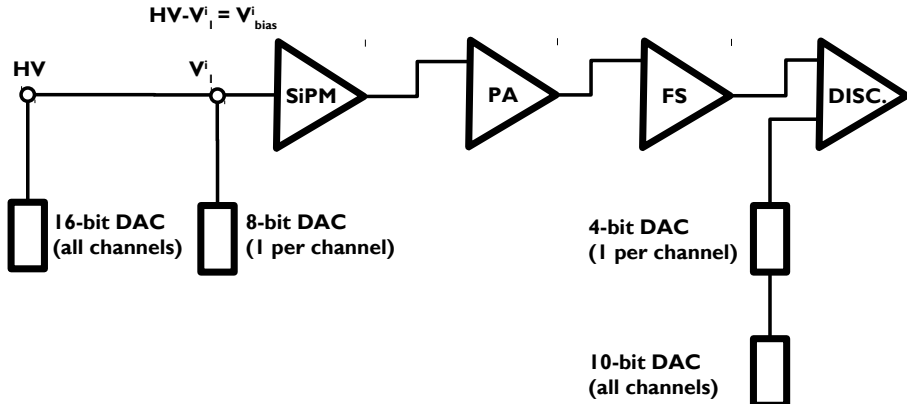


**Figure 4.2:** Simplified schematic of the binary channel electronics relevant to the SiPM calibration. The CITIROC preamplifier, fast shaper, and discriminator are represented (section 3.6). The high-voltage (HV) is set with a Hamamatsu high-voltage source in the whole SiPM array with a 16-bit DAC. The  $V_1^i$  bias for the i-SiPM can be tuned with the CITIROC through an 8-bit DAC ( $V_1^i$ ). Analogously, the discriminator threshold can be first set with a 10-bit DAC in the whole SiPM array and the smoothly adjusted at each channel with a 4-bit DAC.

tion from one plateau to the following denotes the corresponding PE amplitude that can be readily identified via the curve derivative and its position is relative to the SiPM gain.

To set the  $V_{\text{bias}}$  (see section 3.6), it is necessary to first determine the  $V_{\text{br}}$  of each SiPM. To this aim, dark-rate curves are measured at different  $V_{\text{bias}}$  using the ASIC (CITIROC) discriminator [88] of the AMIGA front-end electronics. In Fig. 4.2, a simplified schematic of the *counter* mode electronics relevant to the calibration procedure is shown. We apply an equal bias to the whole SiPM array with a Hamamatsu high-voltage (HV) source C11204-01 [90] controlled by a 16-bit digital-to-analog converter (DAC). The  $V_1^i$  voltage is controlled by an 8-bit DAC and enables fine tuning of the  $V_{\text{bias}}$  at each individual SiPM. The resulting

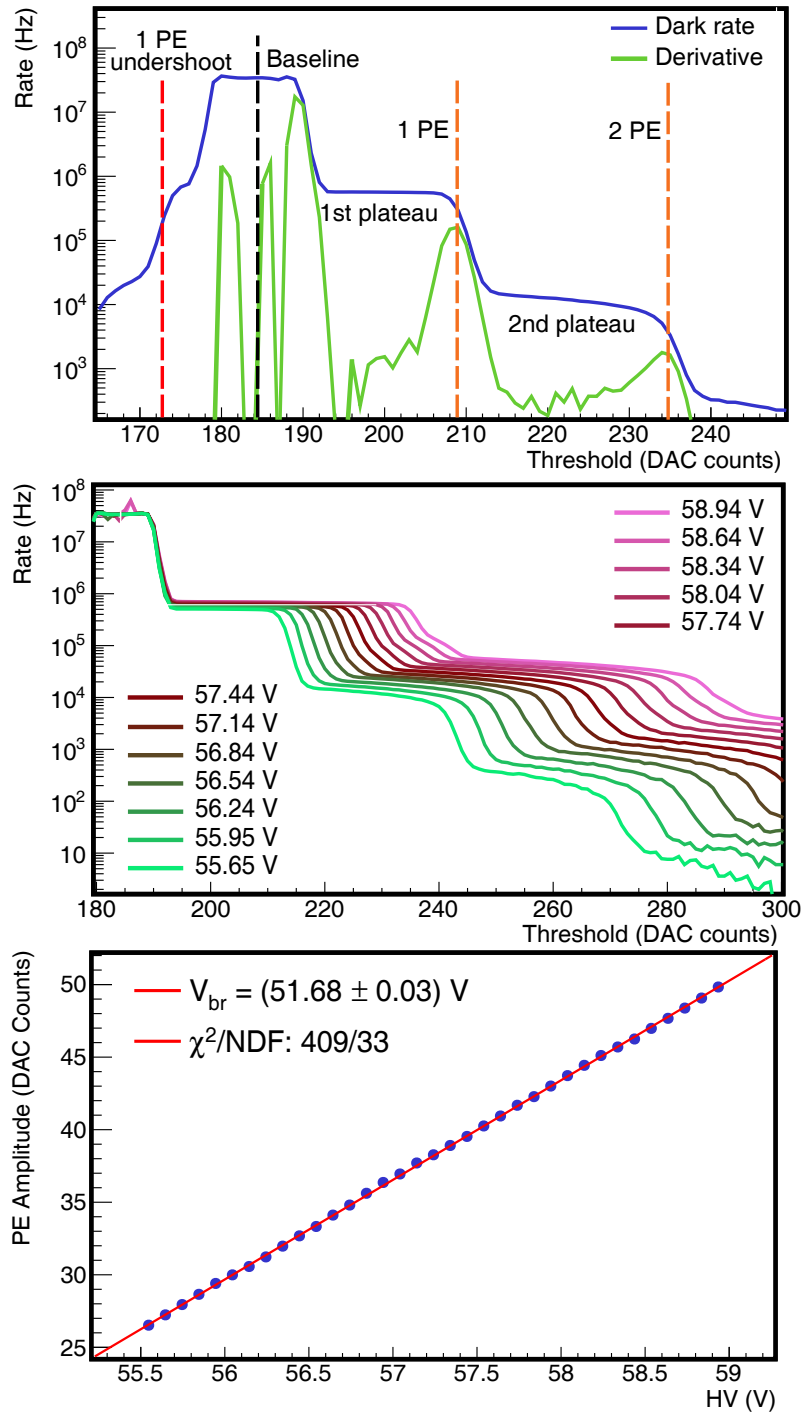


**Figure 4.3:** (Top) Dark-rate curve as a function of the discriminator threshold (blue). The first plateau (below 190 ADC counts) corresponds to the baseline while the following indicate an increasing number of PEs. The derivative of this rate curve (green) readily identifies the PE amplitude spectrum (statistical fluctuations of plateaus might produce lesser peaks). (Middle) dark-rate curves at different  $V_{br}$ . It is seen how the dark rates and PE amplitudes shift towards higher values with increasing high-voltage; and (bottom) breakdown voltage,  $V_{br}$ , determination for an individual SiPM. The linear extrapolation to 0 amplitude indicates the  $V_{br}$  value.

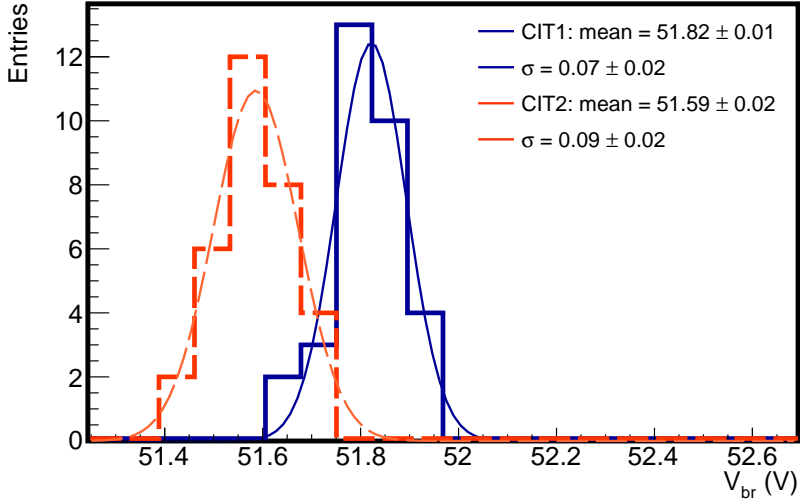


**Figure 4.4:**  $V_{br}^i$  histograms of CITIROC 1 (blue) and CITIROC 2 (orange). Due to the differences between the  $V_{br}^i$ 's it is necessary to individually set the  $V_{bias}$  in each SiPM to achieve a uniform response in the whole array. Units for the fit results are volts in all cases.

$V_{bias}^i$  for the i-SiPM is  $V_{bias}^i = HV - V_1^i$ . In the same way, the discriminator threshold can be set with a 10-bit DAC for all channels and smoothly tuned for each individual SiPM with a 4-bit DAC. For calibration purposes, the individual adjustment of both the  $V_{bias}^i$  and the discriminator threshold are turned off and the same  $V_{bias}$  and threshold are set in the whole array. By varying the discriminator 10-bit DAC we obtain the dark-rate curves at a certain high-voltage.

In the top panel of Fig. 4.3 the measured dark-rate curve (blue) and its derivative (green) with a high-voltage of 55.54 V is shown. The rate is estimated as the number of pulses that cross over the threshold in one second. For low thresholds, the rate obtained is produced by the fast-shaper undershooting as denoted with the red vertical line. The rate increases abruptly when the threshold is close to the baseline (marked with a black vertical line), and decreases drastically when the threshold is well above the baseline. The plateaus symmetry before and after the baseline is produced by the fast-shaper undershooting which mimics the SiPM signal, but with a lower amplitude. The orange lines indicate the position of 1 and 2 PE peaks; from the dark-rate curve derivative (green), the PE peak is fitted with a Gaussian function. This procedure is repeated with different high-voltages as shown in the Fig. 4.3 middle panel. The PE amplitude, dark rate and crosstalk (ratio between two plateaus) increase when the high-voltage is increased. From these curves, the single PE amplitude as a function of the high-voltage is obtained, as shown in the bottom panel of Fig. 4.3. The extrapolation of this curve to 0 (in amplitude) indicates the voltage corresponding to  $V_{br}^i$ .

In Fig. 4.4 the  $V_{br}^i$  of all SiPMs in one array is shown. The difference in  $V_{br}^i$  leads to a significant difference in the gain [83]. For this reason, it is necessary to individually set each  $V_{bias}^i$  to achieve a uniform response.

Once the 64  $V_{br}$  are known for the 64 SiPMs, the  $V_{bias}$  is roughly adjusted with the Hamamatsu high-voltage source, which sets the same preliminary  $V_{bias}^{prel}$  to all SiPMs. The value of this preliminary bias is determined by the maximum breakdown voltage found and the desired over-voltage of 3.5 V [88],  $V_{bias}^{prel} = \max\{V_{br}\} + V_{ov}$ . To compensate for the  $V_{br}$  difference of each SiPM channel, a smooth adjustment per channel is performed with the CITIROC, which allows setting an individual voltage per channel to ensure the same  $V_{ov}$  for all SiPMs. As an example of the impact of the above described procedure, dark-rate curves

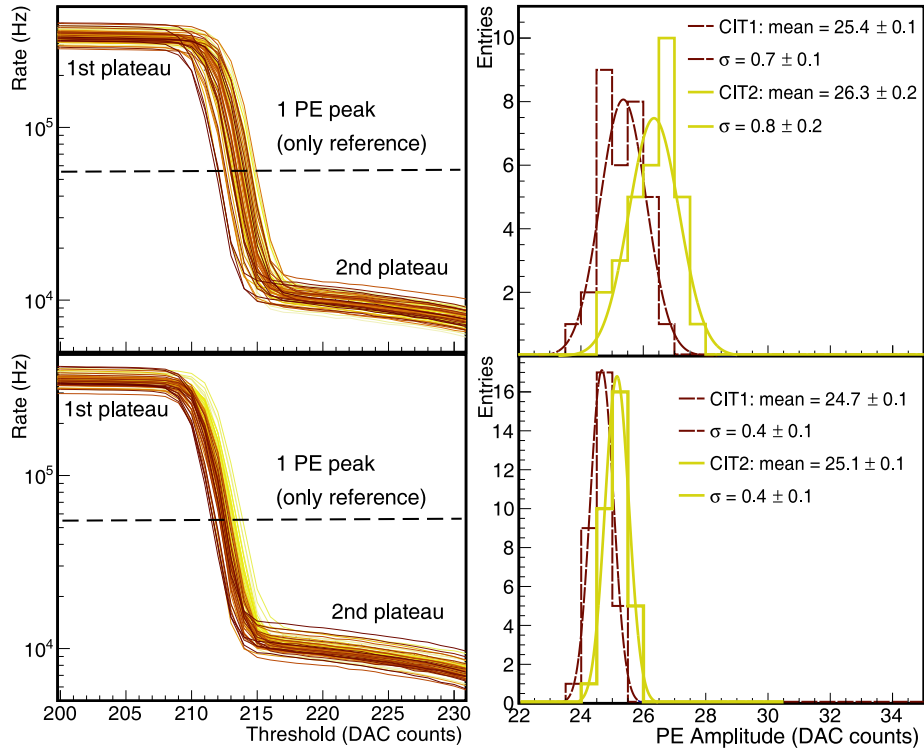


**Figure 4.5:** Calibration: after breakdown voltages have been found, all SiPMs are set to the same over-voltage to assure a uniform gain. We show the dark-rate curves and 1 PE amplitude histograms before (top) and after (bottom) the calibration. Units of fit results are DAC,counts in all cases.

and the corresponding 1 PE amplitude histograms are shown in Fig. 4.5, before (top) and after (bottom) the calibration run for  $V_{ov} = 3.5$  V. After calibration, the curves show fewer fluctuations. In particular the standard deviation in the 1 PE amplitude is reduced by a factor of  $\sim 2$ , which translates to a more uniform detector response.

The operating point of each UMD module is set by choosing a  $V_{ov}$  and a discriminator threshold for all 64 of its SiPMs. In Fig. 4.6, the gain, dark rate, and crosstalk are shown as a function of  $V_{ov}$ . Note that raising  $V_{ov}$  increases both noise and efficiency. However, a higher discrimination threshold reduces noise but may also reduce the detector efficiency. During the engineering array phase, these two parameters were optimized to enhance the detector performance. Laboratory measurements [88] have shown that both low background noise and high efficiency are achieved with  $V_{ov} = 3.5$  V and a discriminator threshold set to 2.5 PE. A signal equal or above this threshold will produce a positive sample in the binary trace, from which muons can be identified.

To verify the consistency of the calibration method, we performed two calibration runs (August 2016 and December 2017) in the station with Id 1764.  $V_{br}$  histograms of all SiPMs in the eight modules of this station are shown in the left panel of Fig. 4.7. In the right panel, the difference in  $V_{br}$ , calculated as  $V_{brRun2} - V_{brRun1}$ , is displayed. Note the difference between the two runs is  $(-0.08 \pm 0.01)$  V, which denotes that the calibration method is quite robust.

As a final remark, in Fig. 4.8 we analyze the uniformity of the SiPM  $V_{brs}$  deployed in the UMD engineering array.  $V_{brs}$  are distributed in two populations. On the right, the result corresponding to the first batch of the electronics production is observed and on the left, the second batch can be found. This shift might be produced by differences in

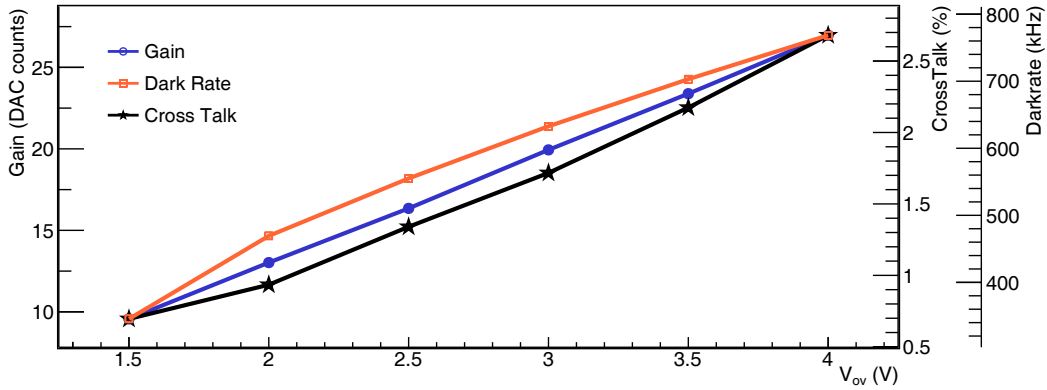


Figure 4.6: Gain, dark rate, and crosstalk as a function of the over-voltage.

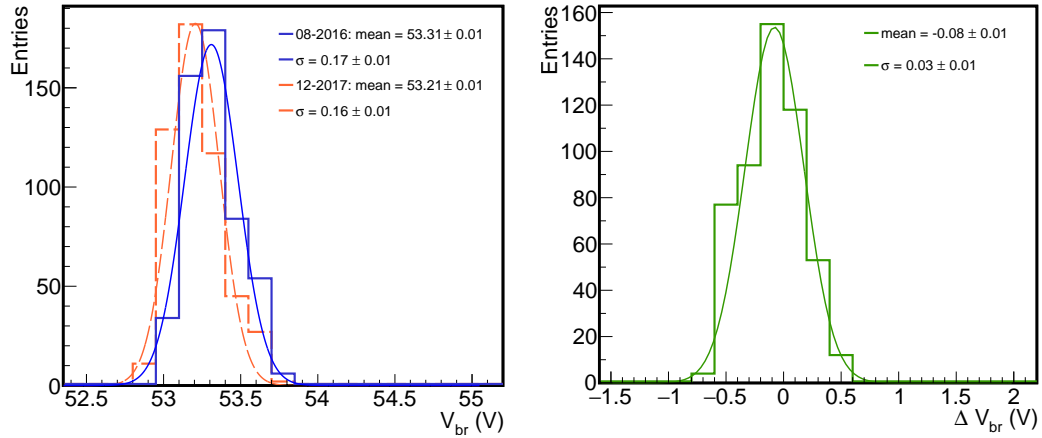


Figure 4.7: (left)  $V_{br}$  obtained from two calibration runs (August 2016 and December 2017) and (right) histogram of the differences in the obtained  $V_{br}$ s. Fit results units are volts in all cases.

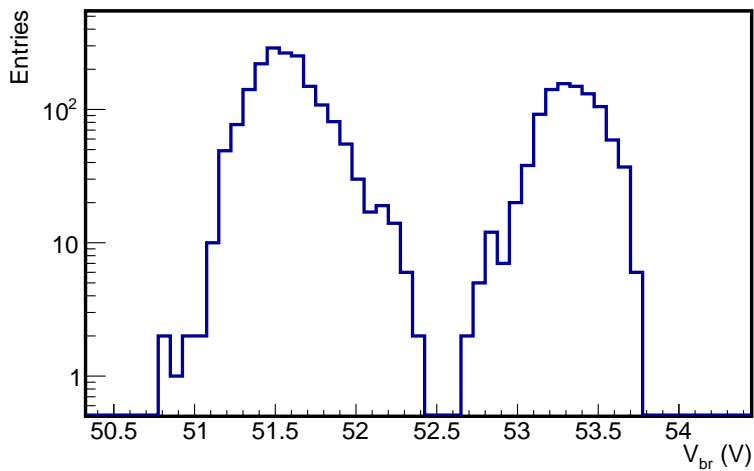
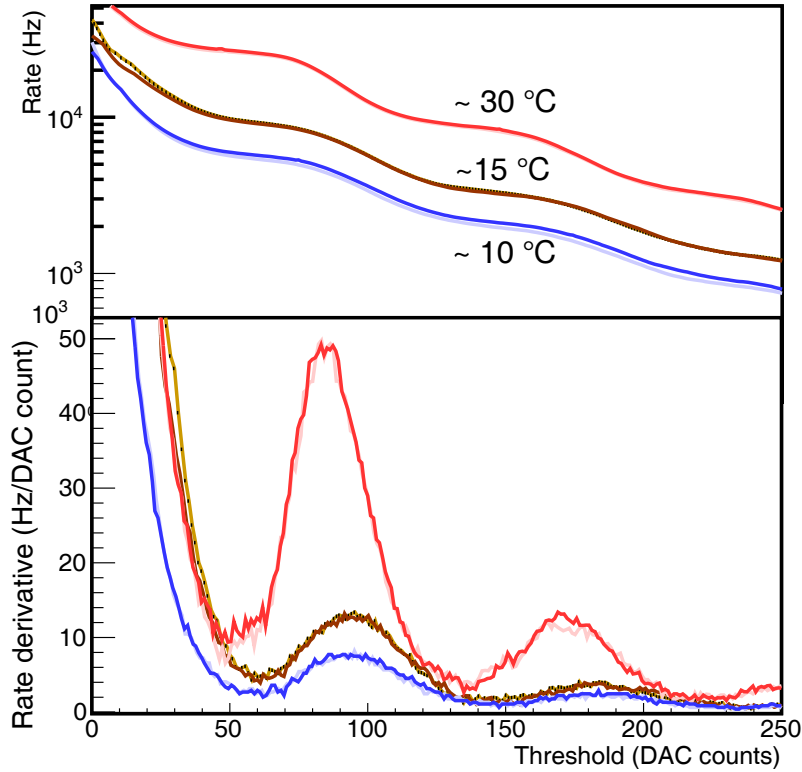


Figure 4.8:  $V_{br}$  of all SiPMs deployed in the UMD engineering array. The right population corresponds to the first production batch while the left population corresponds to the second batch.



**Figure 4.9:** Results for six different calibration runs at different temperatures. The shift in the 1 PE spectrum can be observed. As a consequence of the temperature increase, the breakdown voltage increases accordingly and, therefore, the gain decreases.

construction during the production process and emphasizes the importance of an individual configuration for each module and SiPM.

## 4.2 Temperature compensation

The  $V_{br}$  depends on the temperature, and therefore, also does the gain if the  $V_{bias}$  is not re-adjust to maintain the  $V_{ov}$  stable. To study the impact of this effect on the PE amplitude, a prototype module has been built [85]. The prototype consists of a module with four Hamamatsu S12572-100C SiPM ( $3 \times 3 \text{ mm}^2$ ) attached to customized electronics (fast shapers and pre-amplifiers) and the former UMD back-end [85] developed for PMTs (see section 3.6.3). This prototype has been deployed in the station with Id 688. In addition, a temperature sensor is located next to the SiPM, on the analog front-end board. Temperature information is recorded periodically with the module logger. Dark-rate curves at different temperatures have been measured with this prototype and are shown in Fig. 4.9. It is noticeable the shift on the 1 PE amplitude due to temperature variations since, when temperature increases, the  $V_{br}$  increases accordingly and therefore  $V_{ov}$  (along with the SiPM gain) decreases.

The environmental conditions under which modules operate in the field cannot be controlled and, therefore, it is necessary to have an automatic adjustment of the  $V_{ov}$ , so the SiPM gain remains stable under temperature fluctuations. As proof of design, a temperature compensation mechanism was integrated into the prototype module. Through the high-voltage source, the  $V_{bias}$  on the cathode is set. For the anode, the tension is set through a DAC. When the temperature changes, it is possible to perform a rough adjustment on the tension of the cathode followed by a smooth adjustment on the tension of the anode to keep  $V_{ov}$  stable. To

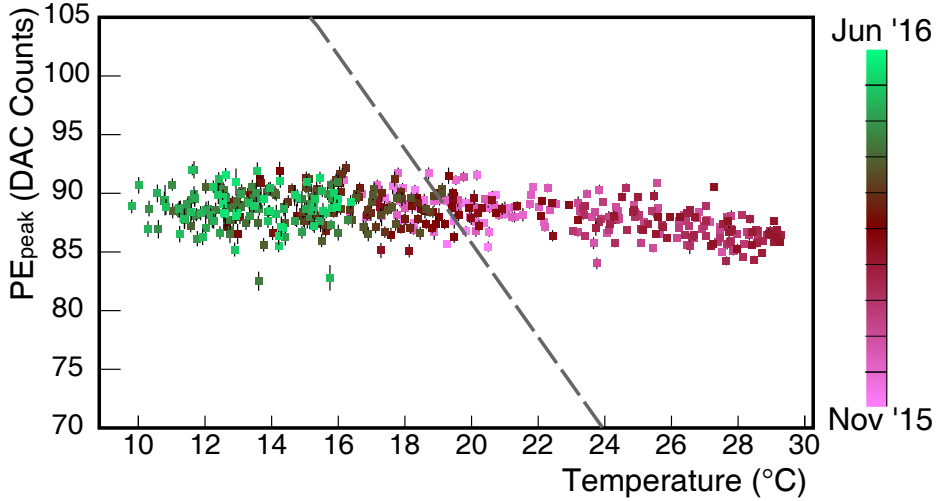


**Figure 4.10:** 1 PE amplitude as a function of the SiPM temperature over an eight-month period with a temperature range of  $\sim 10 - 30^{\circ}\text{C}$ . The colors indicate the months: greenish for the coldest season and reddish to the warmest. The dotted-gray line shows 1 PE amplitude temperature dependence had there not been any temperature compensation in the front-end electronics. The almost constant 1 PE amplitude shows that the gain stabilization works at the level of 0.2%/ $^{\circ}\text{C}$ .

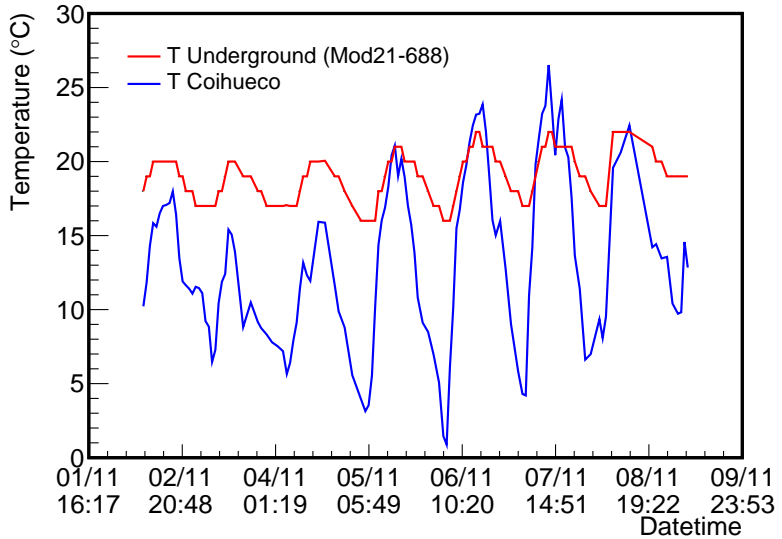


**Figure 4.11:** Temperature as a function of date time in the SiPM prototype module buried 2.3 underground (red) and at the closest weather station (blue) between November, 1st and November, 9th. The maximum variation is  $\sim 26^{\circ}\text{C}$  at the weather station and  $\sim 6^{\circ}\text{C}$  at the underground module.

study the performance of this compensation mechanism, the  $\text{PE}_{\text{peak}}$  position was estimated repeatedly for more than eight months. Over periods lasting for approximately one to two weeks, both SiPM gain and temperature were measured every two hours. The resulting dependence of gain on temperature is displayed in Fig. 4.10 where a temperature correspondence with seasonal changes can be observed. The data points acquired during the coldest months (May and June in the Southern hemisphere) cluster on the left-hand side while on the right-hand side, are those corresponding to the warmest months (January and February). The average gain over the entire period was  $(88.7 \pm 1.6)$  in DAC-counts units. The corresponding gain variation was approximately 0.2% / $^{\circ}\text{C}$ . Without the compensation, the

variation would have been  $4.3\% / ^\circ\text{C}$  [91]. Thus, the compensation mechanism is reducing the gain variations by a factor of 20.

Since the UMD are buried 2.3 m deep, the overall temperature variation, as shown in Fig. 4.10, is only  $\sim 20 / ^\circ\text{C}$ . If the modules were deployed on the surface, this variation would be significantly higher as we see in Fig. 4.11. We obtained the surface temperature from the closest weather station (Coihueco) [92]. In the period analyzed, from November, 1st to November, 9th, the daily temperature modulation is observed with a maximum amplitude variation of  $\sim 26 / ^\circ\text{C}$  on the surface and  $\sim 6 / ^\circ\text{C}$  underground.

In the final design of the UMD, the temperature compensation mechanism is integrated into the Hamamatsu high-voltage source [90]. This mechanism adjusts the high-voltage according to the temperature variation thus compensating for any fluctuations in  $V_{\text{br}}$  and, therefore, stabilizing  $V_{\text{ov}}$ . The compensation mechanism is set with a reference value of  $25 / ^\circ\text{C}$ , and compensates  $54 \text{ mV} / ^\circ\text{C}$ , which is the expected  $V_{\text{br}}$  temperature dependence as specified in [83]. In Fig. 4.12, monitoring data from the module with Id 108 of the station with Id 1764 is shown. We display in the top (middle) panel, the high-voltage set and temperature of the Hamamatsu source as a function of the date time in one-month (year) period. The daily and yearly temperature modulations and, in response, the oscillation of the high-voltage set is seen. Note that the maximum variation in one year is  $\sim 20 / ^\circ\text{C}$  in temperature and  $\sim 1 \text{ V}$  for the high-voltage. In the bottom panel of Fig. 4.12, the high-voltage set as a function of the Hamamatsu source temperature is shown. From the linear fit, the slope obtain is  $(54.0 \pm 0.1) \text{ mV} / ^\circ\text{C}$ , which indicates the compensation mechanism is performing as expected.

### 4.3 Noise sources

We have identified two main sources of noise from calibration data (see section 4.1). Firstly, the SiPM dark rate, which can reach the 2.5 PE threshold due to the crosstalk between inner-cells [93], was identified. In the top panel of Fig. 4.13, the dark rate at 0.5 PE (left) and crosstalk (right) in each pixel are shown. In the bottom panel, we present the corresponding histograms of dark rate (left) and crosstalk (right). The dark rate varies between (460-630) kHz and the crosstalk between (1.5-2.2) %, which implies that for a threshold of 2.5 PE, a noise level between (103~305) Hz per SiPM is expected. However, as the dark rate is strongly correlated to the temperature [94], this estimation might vary during the module operation.

The second source of noise that we have identified is only observed when SiPMs are coupled to optical fibers. In Fig. 4.14, dark-rate curves of two SiPMs with and without optical fiber can be seen. At low thresholds, the rate is dominated by the SiPM dark rate, as the PE plateaus are distinguishable. Above  $\sim 3 \text{ PE}$  (250 DAC counts) the rate at the SiPM without fiber begins to fall to 0, while the SiPM with optical fiber remains above 100 Hz. This level of background is not consistent with the expected background from atmospheric muons we expect in one scintillator strip ( $\sim 1 \text{ muon cm}^2 / \text{minute}$  [95] = 27 muons  $\text{strip}^{-1} \text{s}^{-1}$ ) and could be produced by spontaneous light emission of optical fibers [96].

#### Background with monitoring data from the field

To study the noise level of a buried module in the field, we analyzed monitoring data of the module with Id 108 of the station with Id 1764. In Fig. 4.15, we present the temperature of the CITIROCs between March 2017 and May 2018 and the mean rate (over the 64 SiPMs) of background signals above the discriminator threshold. The temperature and rate modulation through the day and the year is shown. As we explained in section 3.6, the dark rate depends on the SiPM temperature independently of the  $V_{\text{ov}}$ , and therefore, a temperature

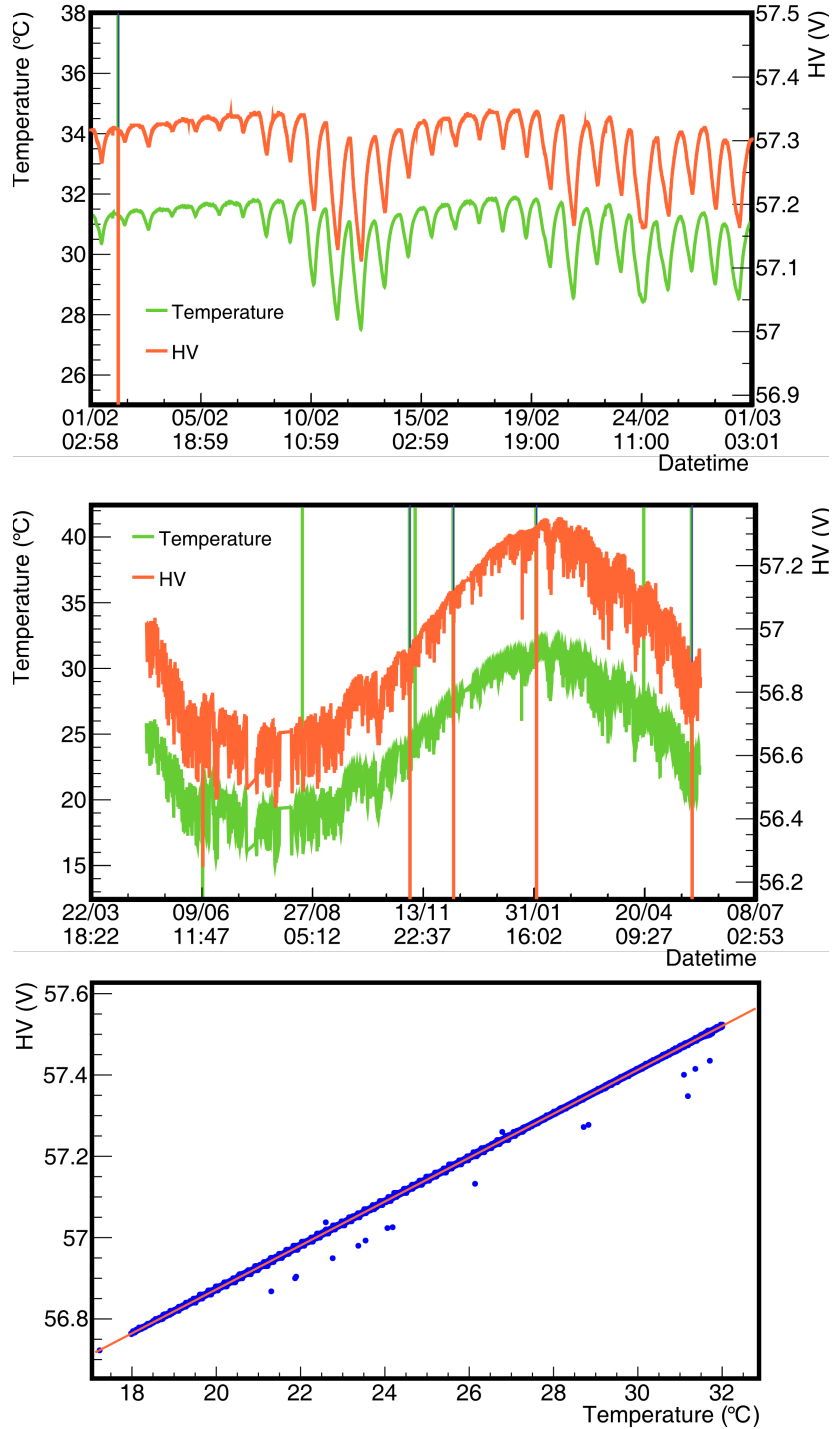


**Figure 4.12:** Monitoring of the Hamamatsu high-voltage source at module with Id 108 of the station with Id 1764. In the top (middle) panel, the temperature and high-voltage set are shown for a one-month (year) period. The temperature modulations can be seen. The bottom panel displays the high-voltage set as a function of the temperature. The slope obtained from the linear fit is  $(54.0 \pm 0.1) \text{ mV} / ^{\circ}\text{C}$ .

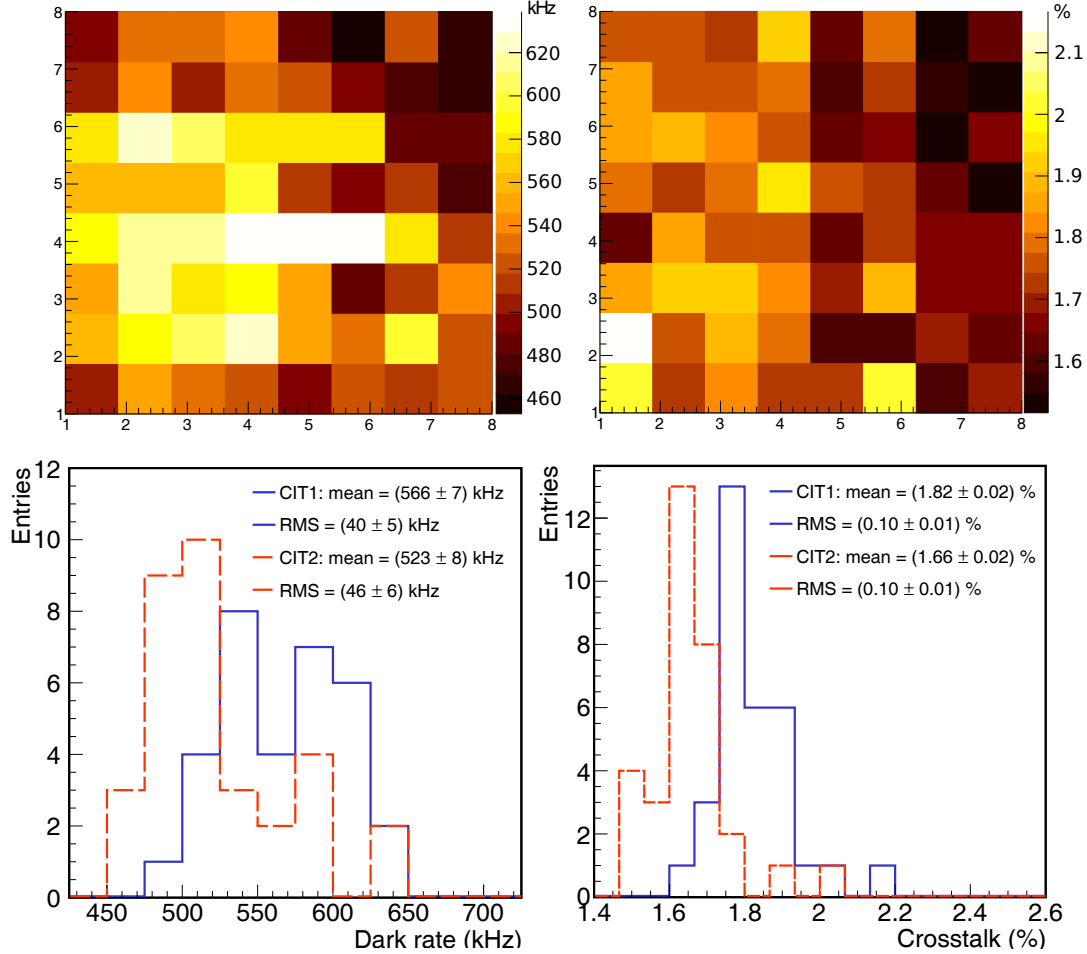


**Figure 4.13:** (Top) dark rate at 0.5 PE (left) and crosstalk (right) of a SiPM array, obtained from calibration. (Bottom) dark rate and crosstalk histograms. The rate of dark counts at 2.5 PE is estimated to be between (103~305) Hz in each SiPM.

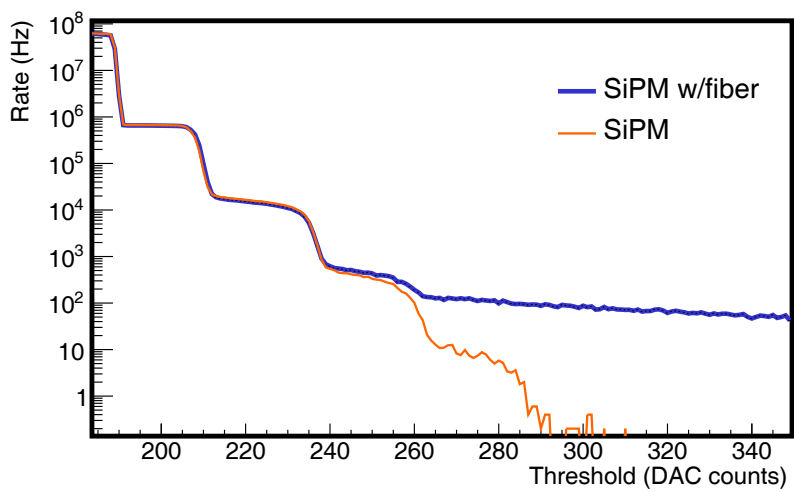


**Figure 4.14:** Signal rate as function of the discriminator threshold for a SiPM with and without optical fiber coupled, represented by the blue and orange curve respectively. Note the rate of the SiPM without fiber falls rapidly after  $\sim 3$  PE, while the rate of the SiPM with optical fiber remains close to 100 Hz.

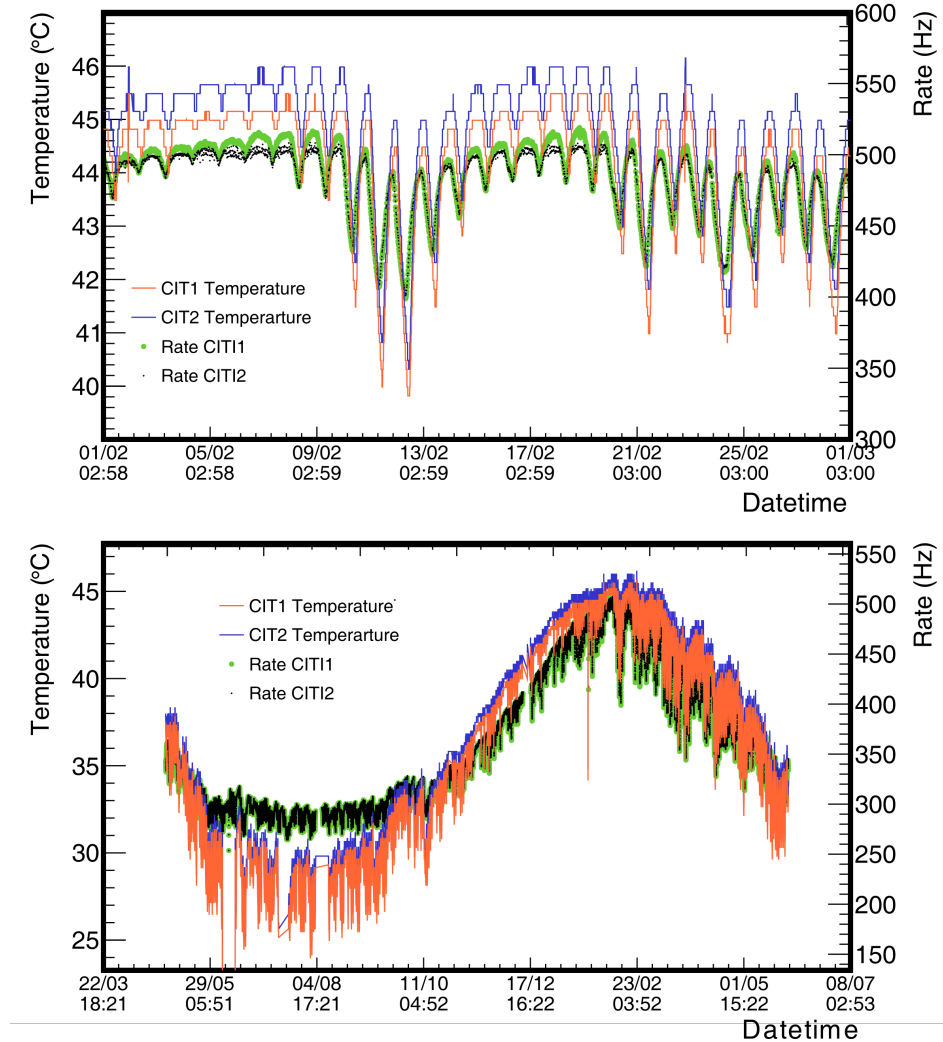


**Figure 4.15:** CITIROC temperature and mean rate per SiPM of the module with Id 108 of the station with Id 1764 extracted from monitoring data between March, 2017 and May, 2018. In the top panel, a zoom-in of a month is shown, in which the daily modulation of the temperature and, thus, also the rate is observed. In the bottom panel, the whole data range is displayed, in which the year modulation can be seen.

modulation is obtained despite the stability of the  $V_{ov}$ . A factor of 2 in the noise level between the warmest and the coolest months of the year is obtained, as the mean rate per SiPM varies between 250 and 500 Hz. These rates translate into a probability between 10% and 20% of over-counting one muon for each  $10\text{ m}^2$  module in an event if we consider the whole SiPM array and a trace length of  $6.4\ \mu\text{s}$  (see section 3.6.5). These results are consistent with measurements in the laboratory that we present in Fig. 4.13.

During a period of three months (December 2016 to March 2017) this module was operated with a discriminator threshold of 3.5 PE, to perform studies related to the module efficiency, calibration and background. Data from these months were compared with data at 2.5 PE between 12-2017 and 03-2018 and it is shown in the top panel of Fig. 4.16. At 3.5 PE the noise rate is reduced to  $(144.2 \pm 0.1)$  Hz and  $(143.9 \pm 0.1)$  Hz (CITIROC 1 and 2 respectively). The probability of over-counting a muon is  $\sim 144\ \text{s}^{-1} \cdot 64 \cdot 6.4 \cdot 10^{-6}\ \text{s} = 0.059 = 5.9\%$  in  $6.4\ \mu\text{s}$ , which is also consistent with the results in the laboratory that we present in section 4.4.

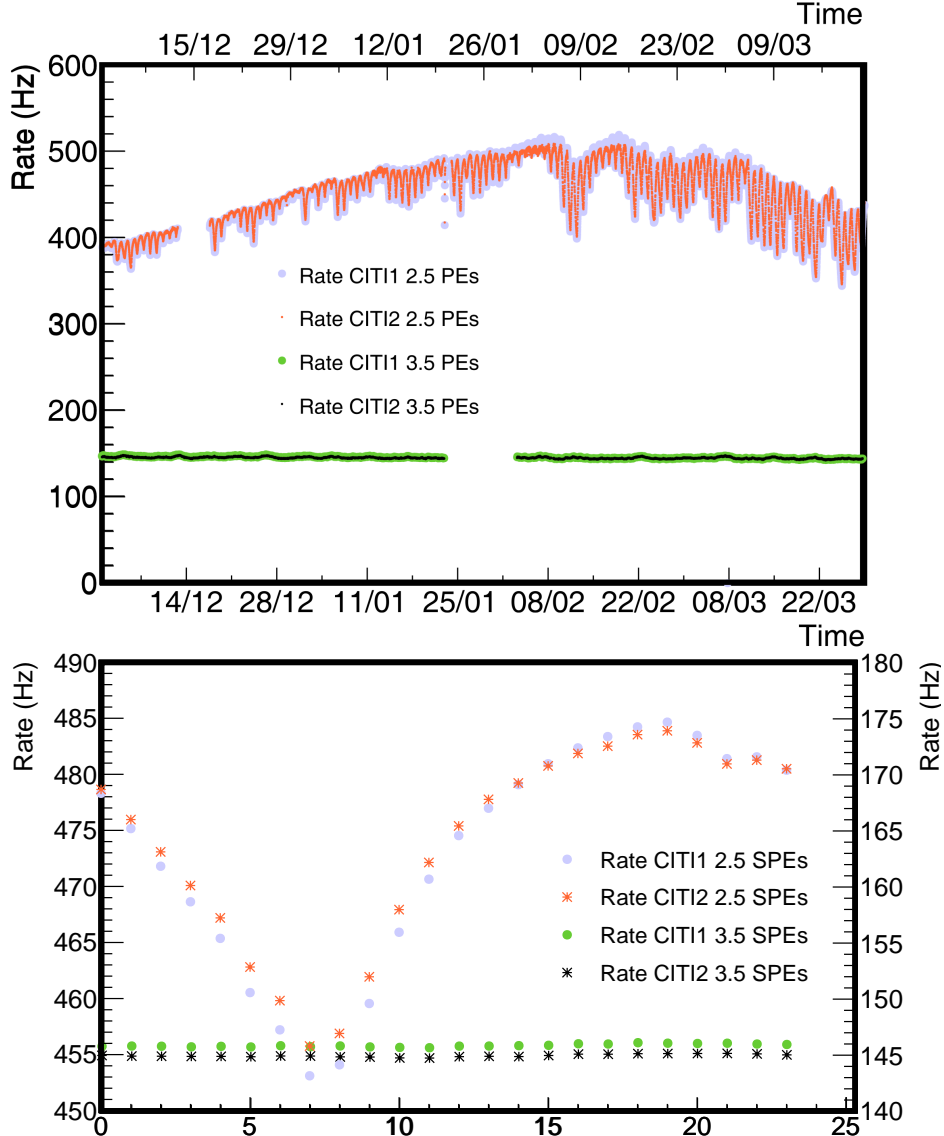


**Figure 4.16:** Mean rate per channel as a function of time for 2.5 and 3.5 PE thresholds. (Top) monitoring data between December 2016 and March 2017 (December 2017 and March 2018) at 3.5 (2.5) PE. (Bottom) average rate per hour during a two-week window. The right (left) axis corresponds to the 2.5 (3.5) PE data.

In the bottom panel of Fig. 4.16, the average rate per hour during a two-week window can be found. A temperature dependence with the 3.5 PE threshold cannot be seen. However, the day modulation is distinguishable for the data taken at 2.5 PE.

From Fig. 4.16 it is implied that at 2.5 PE the background rate in this range has a temperature dependent component (probably dominated by the SiPMs dark rate), and a temperature independent component (probably from the optical-fiber noise). The background rate can be modeled as,

$$R_{\text{BGD}} = R(T) + R_0 = A (T + 273 \text{ K})^{\frac{3}{2}} \exp \left( -\frac{E_g(T)}{2k(x + 273 \text{ K})} \right) + R_0, \quad (4.1)$$

where the first term of the equation corresponds to the dark rate [97] with  $A$  a model constant,  $E_g(T)$  the silicon band gap and  $k$  the Boltzmann constant. The second term of the equation

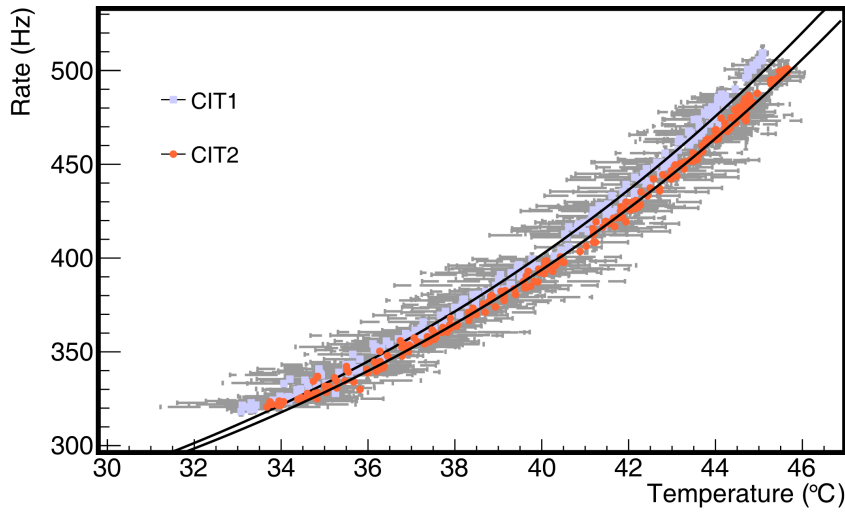


**Figure 4.17:** Mean background rate per SiPM as function of the temperature of the two CITIROCs for data between December 2017 and March 2018.

Rate	CITIROC1 (Hz)	CITIROC2 (Hz)
estimated	$127.0 \pm 2.0$	$129.0 \pm 1.0$
measured	$144.2 \pm 0.1$	$143.9 \pm 0.1$

**Table 4.1:** Background rate results at 3.5 PE with model correction.

corresponds to the temperature independent background which is expected to be, from Fig. 4.16,  $\sim 144$  Hz.

The silicon band gap depends on temperature as [98],

$$E_g(T) = 1.18 \text{ eV} - 9.03 \cdot 10^5 \frac{\text{eV}}{\text{K}} (T + 273 \text{ K}) - 3.05 \cdot 10^{-7} \frac{\text{eV}}{\text{K}^2} T^2. \quad (4.2)$$

As the average temperature between December 2017 and March 2018 is  $\sim 43$  °C (see Fig. 4.15) and  $E_g(T)$  depends weekly on  $T$ , we assume in equation 4.1 a constant  $E_g = 1.1205$  eV.

In Fig. 4.17, the mean rate per channel as a function of the temperature is shown. The results of the fit with the model from equation 4.1 are also shown. It was obtained for the CITIROC 1 ( $R_0 = 175 \pm 2$ ) Hz and for the CITIROC 2 ( $R_0 = 177 \pm 1$ ) Hz.

To estimate the rate at 3.5 PE using the corrected rate at 2.5 PE ( $R_0$ ), the curves for the 64 channels of the module were fit as it is shown in Fig. 4.18. A linear fit was used in the range between 4 and 7.5 PE and extrapolated to 2.5 and 3.5 PE. The rate at 3.5 PE is estimated as  $R_{\text{estimated}}^{3.5 \text{ PE}} = R_0 - \Delta R$ . In Table 4.1 the results are summarized. The difference between the measurements and the estimation is  $\sim 16$  Hz. At 3.5 PE, the background rate is dominated by the optical-fiber noise, but the SiPM dark rate also has a small contribution. However, in this range, the temperature modulation cannot be seen. In Fig. 4.19, the average per hour of the channels mean rate at 3.5 PE and 2.5 PE corrected are shown. The results from the field are consistent with the model in equation 4.1 and Table 4.1. However, the correction is better between 10 and 13 hours and could be improved for all the range by estimating  $\Delta R$  at different temperatures.

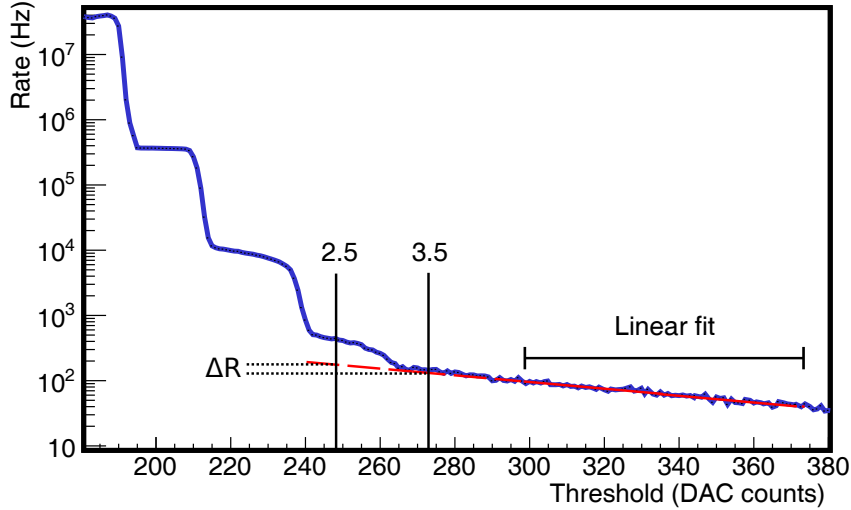


**Figure 4.18:** Example of the rate as a function of the DAC level for one strip of the module with Id 108 of the station with Id 1764. The correction of the rate at 2.5 PE ( $\Delta R$ ) is estimated from the extrapolation of the rate between 4 and 7.5 PE.

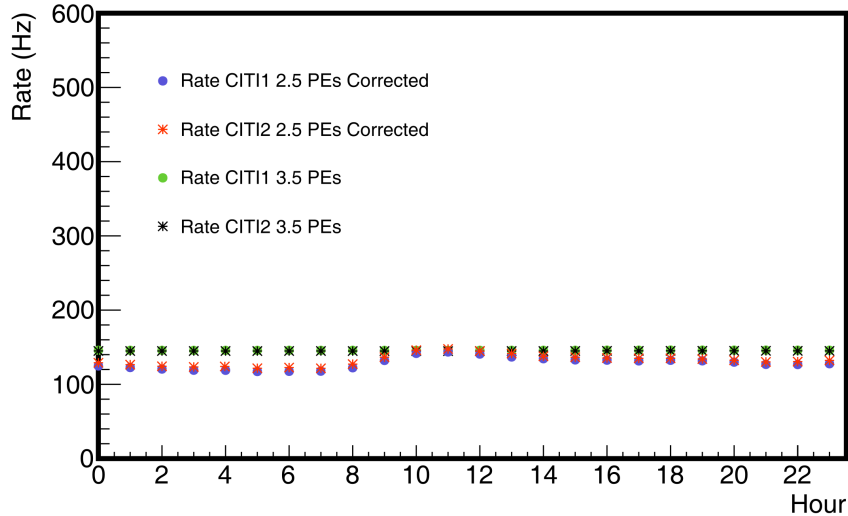


**Figure 4.19:** Background rate at 2.5 and 3.5 PE after corrections in equation 4.1 and Table 4.1. After the corrections the two rates become similar.

## 4.4 Signal characterization

As we mentioned in section 3.6.3, the UMD engineering array has been operating with SiPMs since the end of January 2018. To analyze this newly acquired data, it is necessary to find proper counting strategies as in [99] to maximize the signal-to-noise ratio. In this section, we present different approaches employing laboratory measurements performed with the setup sketched in Fig. 4.20.

The setup consists of four scintillator strips of 4 m long with optical fibers placed one upon another. The strips are identical as those in the UMD modules [54] and they were built with the same materials that will be used in the production phase [100]. The optical fibers were coupled through an optical connector to a standard UMD SiPM array (Hamamatsu

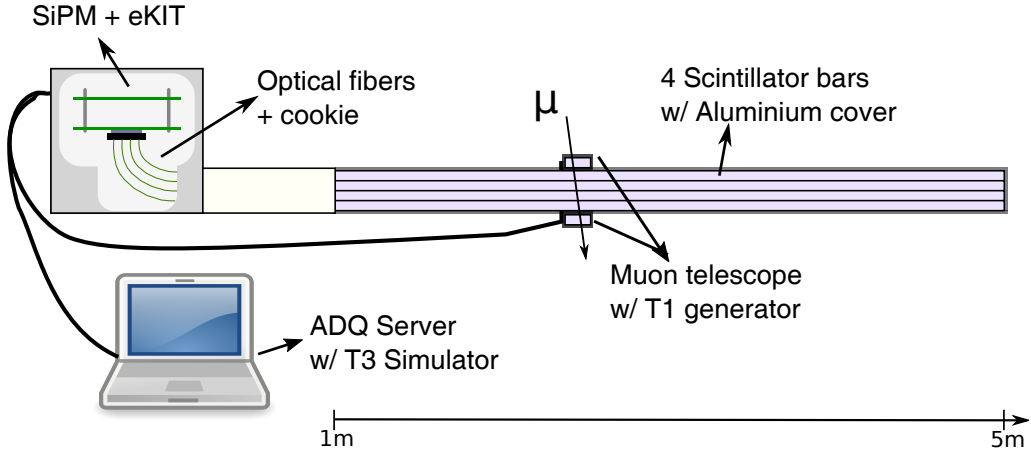


**Figure 4.20:** Schematics of the laboratory setup. The four scintillator strips with optical fiber are shown. The optical fibers are coupled through an optical connector to a standard SiPM array. The signals are processed with an eKIT. Events are triggered with a muon telescope, while a T3 request is simulated with an external computer to store the events.

S13361-2050NE-08 [83]), which we connected to an electronics kit (eKIT) [88]. In this scenario, we refer to a SiPM with its corresponding readout electronics as a *channel*. Four channels, in the described setup, are coupled to optical fibers, whereas 56 channels are passive and can only contribute with dark rate. The remaining four channels were off, as they were coupled to four scintillator strips built with old materials (designed for studies not related to this work). The strips are covered with an aluminum container to shield them from the environment light. For the same purpose, SiPMs and eKIT are contained in a PVC box.

To trigger the signal, we used a muon telescope built with two scintillator segments of 4 cm x 4 cm x 1 cm and customized electronics. These electronics inject a T1 into the eKIT when a coincidence (muon signal in both segments) in the telescope is found. To extract the event, a T3 request is simulated with a computer which runs an acquisition server, storing the data in the same way as the UMD modules. The telescope allows triggering with muons crossing a specific position of the strip (with a 4 cm resolution).

In Fig. 4.21, an event output example is shown. Once the T1 is received, the muon signal is outputted as a sequence of positive samples in channels where SiPMs are coupled to optical fibers. In some events, we obtain sequences of positive samples in passive channels produced by dark-rate pulses of more than 2.5 PE (see section 4.3). Also, positive samples in channels with strips, but away from the trigger bin are observed. These are produced both by SiPM dark rate and optical fiber noise. Both these effects are considered to be the background noise in this experiment.

As we presented in section 4.3, the lower the discriminator threshold, the higher the noise rate. However, increasing the threshold might produce signal loss. In this analysis, we have studied two discrimination levels tested in the UMD engineering array: a low level of 2.5 PE and a high level of 3.5 PE. Binary traces of 6.4  $\mu$ s long were measured all along the scintillator strip in eight different positions. At each position, we obtained 24000 and 20000 events with the 2.5 and 3.5 PE thresholds, respectively.

In Fig. 4.22 the raw events are shown. We display in the top panels the sum of all binary traces per channel in time, with a discriminator threshold of 2.5 (left) and 3.5 PE (right). The channels with strips attached are distinguishable as they accumulate events at the trigger bin ( $\sim 1400 \times 3.125$  ns). The positive samples at these channels outside the trigger scope are due to both SiPM and optical-fiber noise. The rest of the entries correspond to the passive

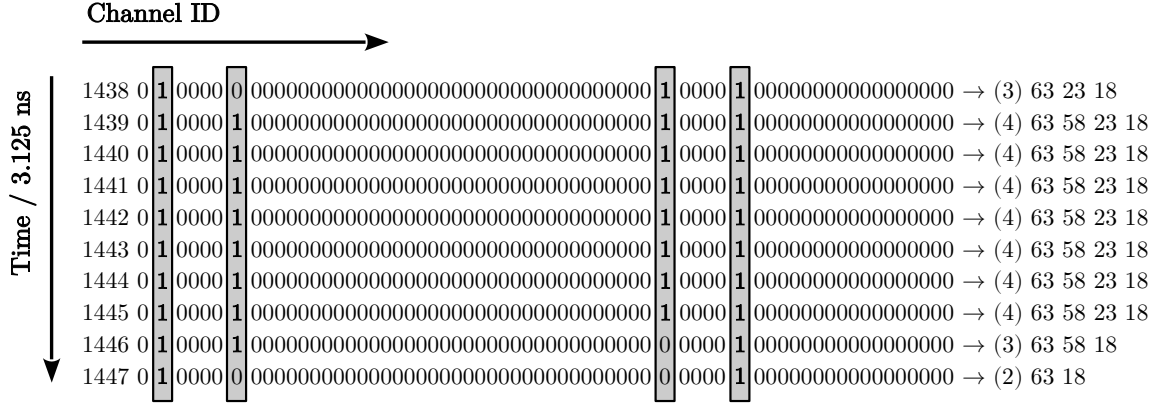


**Figure 4.21:** An example of a typical event, composed by binary traces from the 60 available channels. The muon signal is visible as sequences of positive samples in the four active channels.

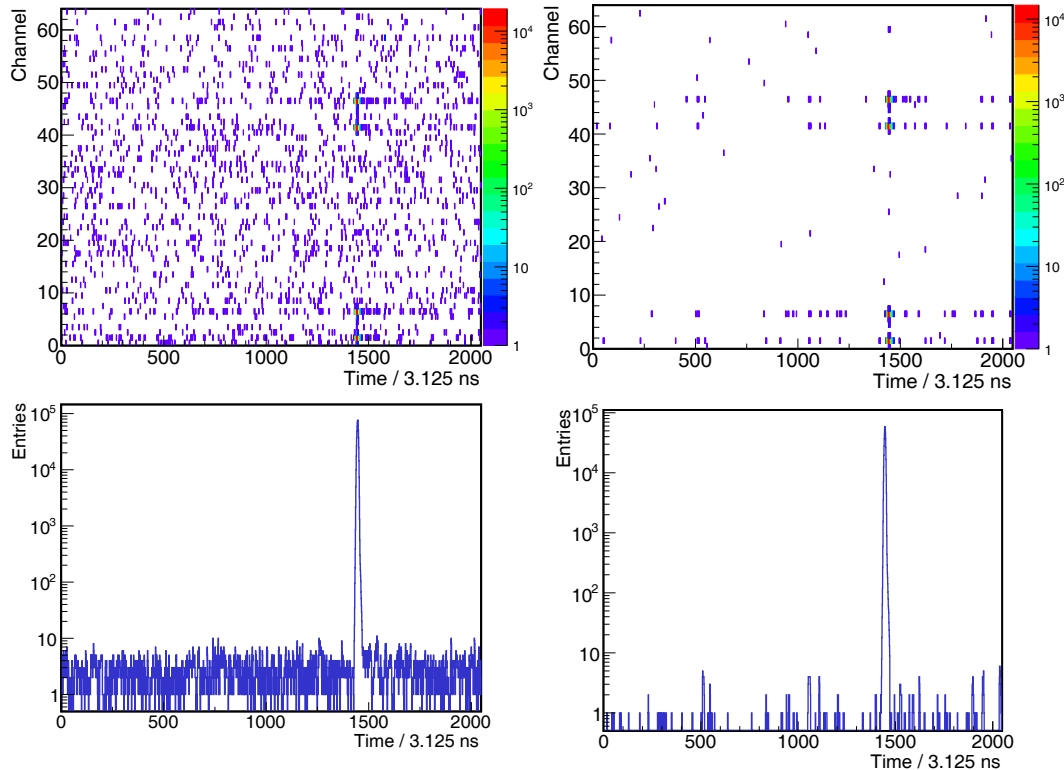


**Figure 4.22:** (Top) Number of events per channel and time bin for a discriminator threshold of 2.5 (left) and 3.5 PE (right). Channels 2, 7, 42 and 47 are coupled to optical fibers; positive samples are accumulated around the trigger bin. Channels 4, 25, 44 and 59 have no positive samples as they were off. (Bottom) time projection of positive samples in all channels per time bin. The peak at the trigger bin can be seen, along with the background noise, which is more noticeable in the 2.5 PE threshold setup.

channels in which dark rate generates positive samples. Channels 4, 25, 44 and 59 have no entries as they were off. In Fig. 4.22 bottom panel, the time projection is shown. The muon peak at the trigger bin is above the noise level. By raising the discriminator threshold most of the background is reduced: from 9% at 2.5 PE to 1% at 3.5 PE in a  $6.4 \mu\text{s}$  trace. For a UMD module, these values are underestimated since in this setup, only the noise from four strips is considered.

SiPM muon signals are expected to have no structure [88] and be compact, meaning they have no 0s in between its positive samples. For this reason, if we define the muon width as the distance (in samples) between the first and last positive sample, muon widths are typically the number of ones in the trace. In Fig. 4.23, the number of positive samples in the binary traces as a function of the signal width are shown, along with the signal width histograms. In the left (right), the events for the 2.5 (3.5) PE threshold are displayed. In black, the signal from the strips is shown. In red, the signal from the passive channels corresponding to SiPM noise is displayed. In blue, the signal from the strips outside the trigger scope is shown. These signals are identified as noise both from optical-fibers and from SiPMs.

In Fig. 4.23, most of the strip signals are distributed along an identity function. However, data points away from the identity are also found. These points correspond to muons signals in the strip channels with noise at the beginning or end of the trace. When raising the threshold to 3.5 PE, most of the noise composed of dark rate above 2.5 PE is eliminated. Along the identity function, the signals from the passive channels, which are significantly shorter than the signal from the muons, and the noise from the strip are also found.

The signal mean widths ( $\mu$ ) and standard deviations ( $\sigma$ ) are also shown in Fig 4.23. The muons signal widths is  $\mu = 7.8$  samples (24.4 ns) and  $\sigma = 1.5$  samples (4.7 ns) for 2.5 PE and  $\mu = 7.1$  samples (22.2 ns) and  $\sigma = 1.7$  samples (5.3 ns) for 3.5 PE. An inhibition window of 12 samples contains more than 99% of signals. At the passive channels, the signal width is  $\mu = 3.0$  samples (9.4 ns) and  $\sigma = 0.7$  samples (2 ns) for 2.5 PE and  $\mu = 2.8$  samples (8.8 ns) and  $\sigma = 0.7$  sample (2.2 ns) for 3.5 PE. From Fig. 4.23, we deduce that in the case of the 2.5 PE level, identifying a muon as a signal with more than three positive samples will reject more than 95% of the SiPM noise. On the other hand, two positive samples will reject 65% at 3.5 PE. Both cases with less than 1% of signal loss.

In the histograms (bottom panels of Fig. 4.23) the different contributions to the noise are shown. From events with a threshold of 2.5 PE (left), the width distributions of noise in channels with strip (blue dotted) and passive channels (red dashed) are strongly overlapped. This denotes that the main contribution to noise in the channels with strip, at this level of threshold, is the SiPM dark rate. When rising the threshold to 3.5 PE, the SiPM noise is considerably reduced and the remaining noise corresponds probably to the spontaneous light emission from optical fibers. We can use these histograms to estimate the probability of having a positive sample from noise in field data (64 strips always attached). The noise (probability of having a positive sample in a  $6.4 \mu\text{s}$  trace) from each strip contributes with  $\frac{222}{96000} = 0.2\%$  at 2.5 PE and  $\frac{71}{80000} = 0.09\%$  at 3.5 PE. This extrapolates to  $0.23\% \cdot 64 = 14.8\%$  and  $0.09\% \cdot 64 = 5.7\%$  respectively, if we considered 64 scintillator strips and  $10 \text{ m}^2$  modules.

In Fig. 4.24 the signal mean widths (top) and width  $\sigma$  (bottom) are shown as function of the muon telescope position. Due to the optical fiber attenuation, the muons mean width decreases when moving the muon telescope towards the end of the strips. The signal width changes in the order of  $\sim$  half a sample when rising the threshold from 2.5 to 3.5 PE, which is an effect of the shaping of the CITIROCs [87]. Also, signals shorter than four positive samples can only be found at the back of the strip. At 1 m and 1.5 m, signals close to  $3\sigma$ s can be wider than 12 positive samples. It is worth to note that these wide muon signals could produce over-counting if they match the counting pattern more than once.

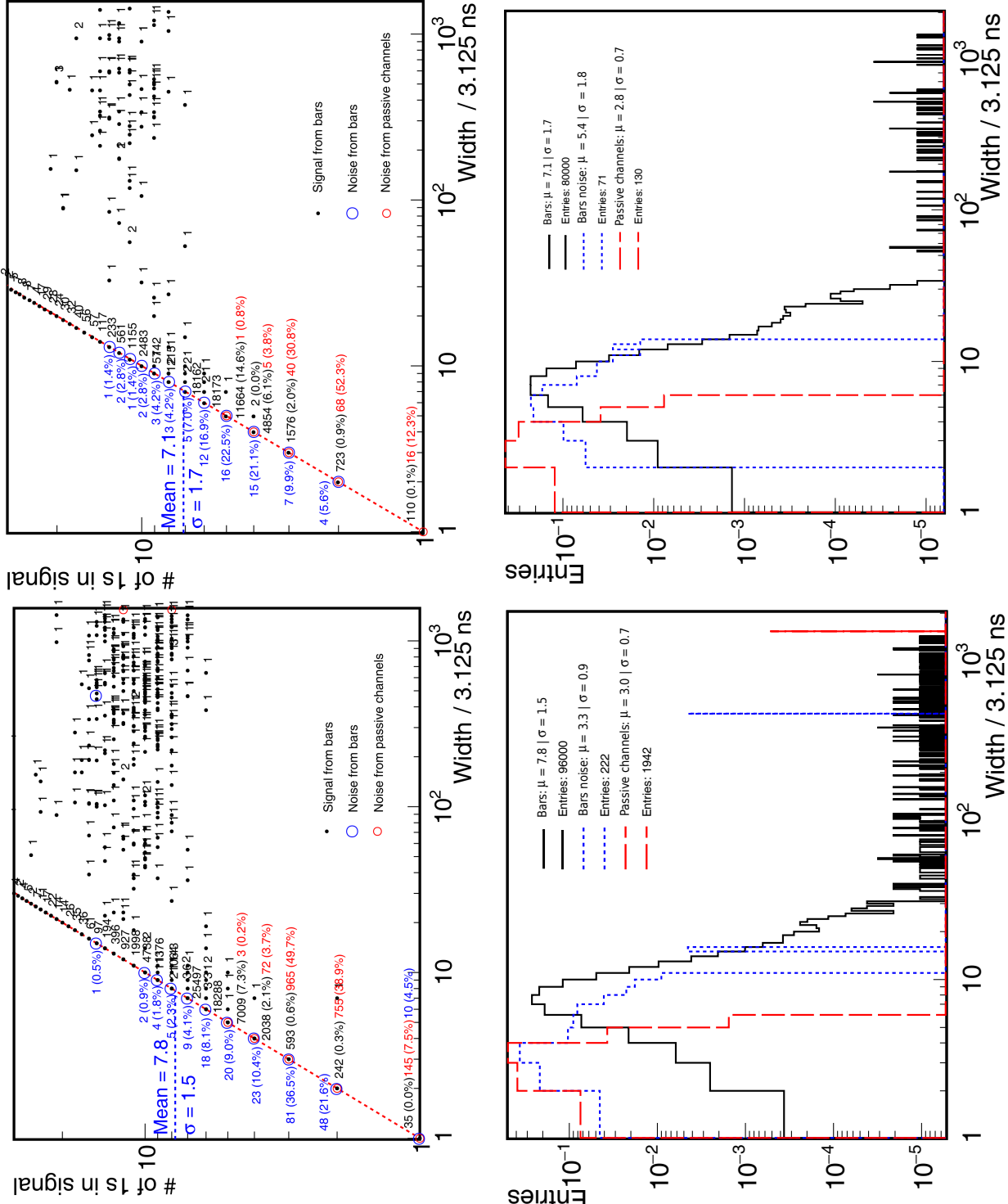


**Figure 4.23:** (Top) number of positive samples (“1’s”) as a function of the signal width, defined as the distance between the first and last “1” in the  $6.4\ \mu\text{s}$  trace, for 2.5 (left) and 3.5 (right) PE. (Bottom) signal width histograms. In black, the total signal of the channels with strips is shown. In red, the signal from the passive channels, corresponding to SiPM noise. In blue, the signal from the strips outside the trigger scope can be seen. Most of the signals are located along an identity function, indicated with the red dashed line. The events away from the identity are acknowledged to be muon signals with noise away from the trigger scope.

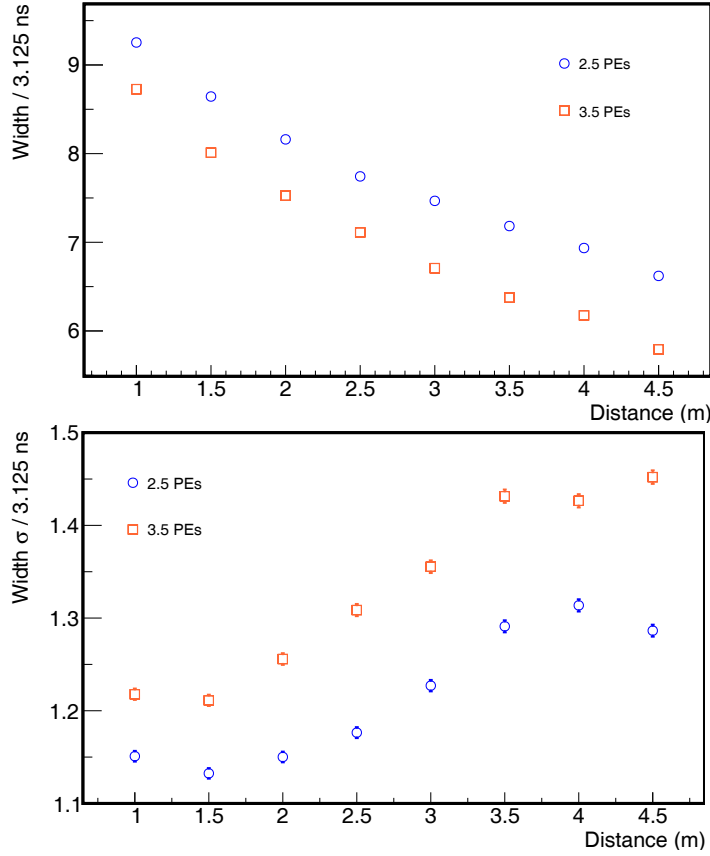


**Figure 4.24:** The mean width (top) and standard deviation (bottom) of the muon signal in binary traces as a function of the trigger position for the 2.5 and 3.5 PE thresholds is displayed. The mean width of the signals decreases when moving the muon telescope towards the end of the strip, which is an effect of the optical fiber attenuation.

#### 4.4.1 Counting strategy

After characterizing the muon signal in the laboratory, we can propose a preliminary counting strategy as a compromise between the under-counting due to the strip efficiency (see next section 4.4.2) and over-counting due to both the detector noise (4.3) and wide muon signals (4.4). Concerning the inhibition window, we have shown that approximately 99% of the muon signals can be completely contained in 12 samples. We have also shown that a matching pattern  $1111x$  for the 2.5 PE threshold would reject significantly the SiPM noise, with a signal loss of less than 1%. Analogously, a similar result can be achieved for the 3.5 PE threshold if we select a  $111x$  matching pattern. Furthermore, with these counting patterns, wide signal such as those produced at the beginning of the strips do not introduce over-counting as they need 16 positive samples to be counted twice.

In Fig. 4.25 the muon counting for 2.5 (left) and 3.5 (right) PE threshold with two different counting strategies is shown. Each entry corresponds to the first positive sample in the inhibition windows matching the counting pattern. The first pattern (top) for both cases is  $1x$ . The second patterns (bottom) are  $1111x$  and  $111x$  for 2.5 and 3.5 PE, respectively. As we mentioned before, most of the background is eliminated for the 2.5 PE threshold. In the second case, as the SiPM noise is already low, the counting strategy does not have such a significant impact.

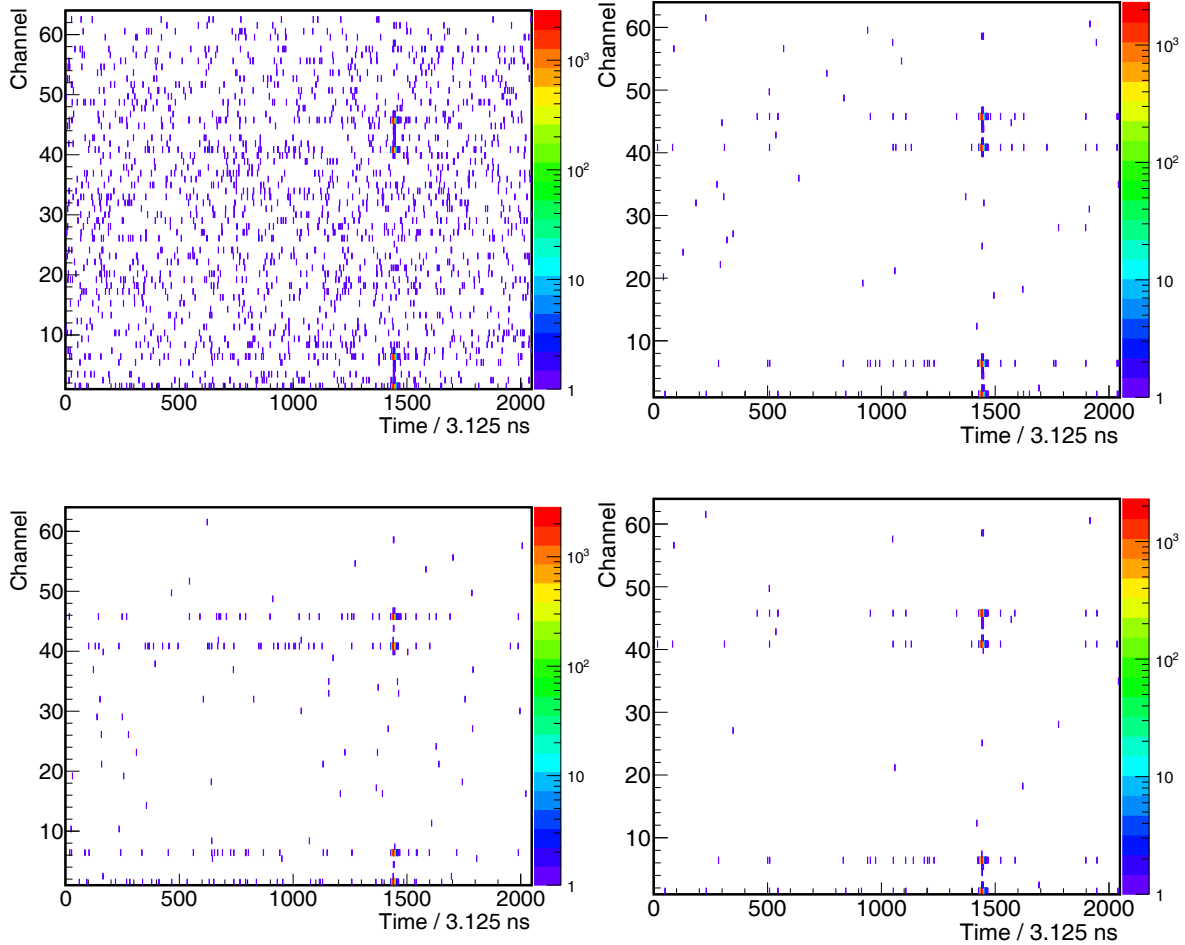


**Figure 4.25:** (Top) muon counting for 2.5 PE (left) and 3.5 PE (right) for a 1x strategy. (Bottom) muon counting for 2.5 PE (left) and 3.5 PE (right) for a 1111x and 111x (respectively) pattern. In all cases, we used an inhibition window of 12 samples. In particular, for the 2.5 PE threshold, the background is significantly reduced when using the 1111x matching pattern.

#### 4.4.2 Counting efficiency

As we mentioned in the previous section, choosing a counting strategy comes from a compromise between the over-counting probability produced mostly by background noise and under-counting probability produced by signal loss. To estimate this signal loss, we have analyzed the muon counting efficiency with the different strategies and discriminator thresholds.

In Fig. 4.26 the mean efficiency, estimated as the average of the four strips in setup 4.20, is shown as a function of the telescope position. Signal loss is observed at the end of the strip, and increased when selecting a 1111x or 111x matching patterns. This may imply that the signal loss is mainly produced by either short muon signals at the end of the strip as we explained in section 4.4, or it may be an effect of the noise rejection. Rising the discriminator threshold from 2.5 to 3.5 PE also decreases efficiency, as more PEs per muon are needed to generate positive samples. At 1 m and 1.5 m, the 1x strategy efficiency is above 100% due to muon over-counting, caused by noise and by muon signals wider than the inhibition windows. In this work, we have minimized these effects by selecting a matching pattern different from 1x. Firstly, because the noise is rejected and, secondly, because the signals that

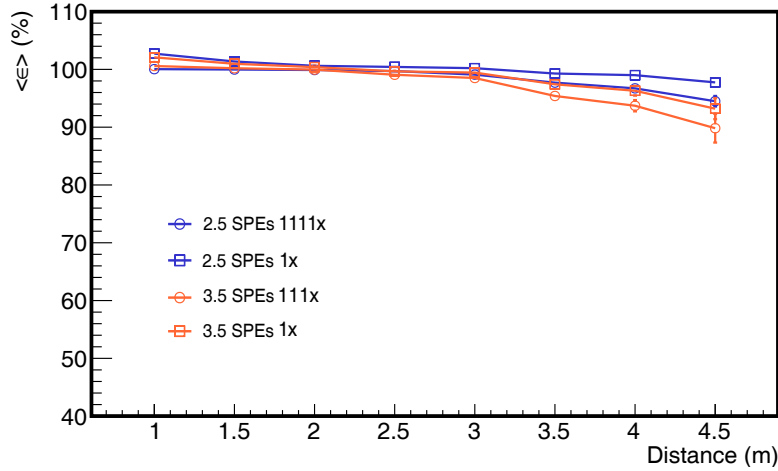


**Figure 4.26:** Efficiency as a function of the trigger position for the 2.5 and 3.5 PE thresholds and different matching patterns. Signal loss is produced mostly at the end of the strip when increasing the discriminator threshold or requesting a higher number of positive sample to count a muon. At the beginning of the strip, muon over-counting is observed resulting in an efficiency higher than 100%. We summarize the results for all these scenarios in Table 4.2

exceed the inhibition windows are not wide enough to match the pattern for a second time. In this sense, part of what it seems efficiency loss is in fact reduction of over-counting.

In Table 4.2, the results are summarized for the 2.5 and 3.5 PE thresholds. Although the final design of the UMD consists of three modules of  $10\text{ m}^2$  per station and a discriminator threshold of 2.5 PE, modules of 5 and  $10\text{ m}^2$  were tested as a proof of concept during the engineering phase. For this reason, we have estimated the integrated efficiency for both  $10\text{ m}^2$  and  $5\text{ m}^2$  modules by averaging the four strips. With the 1x matching pattern the modules tend to slightly over-count, thus, the efficiency is higher than 100%. In section 4.3, we have calculated the detector noise as the probability of counting one muon in  $6.4\text{ }\mu\text{s}$  (one event) in one module due to background. The noise in the laboratory is the noise directly measured with setup 4.20. The noise in a module is first an estimation from extrapolating the laboratory results, presented in section 4.4, to 64 strips, and then, the results of measurements in the field, which we presented in section 4.3. For the 2.5 PE threshold, the noise can be rejected using a 1111x strategy, but, for the 3.5 PE threshold there is no significant change when applying a counting strategy different than 1x. The 2.5 PE threshold with the 1111x counting strategy and the 3.5 PE threshold, with the 1x counting strategy result in similar efficiency and background levels.

#### 4.4.3 Discussion

In this section, we analyzed four counting strategies at two discrimination threshold levels with laboratory data of mostly vertical muons, proving that the detector background can be significantly reduced by choosing a proper matching pattern. However, effects such as materials aging, signal undershooting, pile-up and clipping corner muons in showers may produce biases that cannot be observed in the laboratory with single muon events. We address most of these biases in chapter 8 using simulations of extensive air shower measured with the muon detector. Nevertheless, we cannot address potential or unknown bias sources such as material aging with this method and therefore, a low discriminator threshold with a counting strategy that reduces the noise is the most conservative option to minimize the impact of these potential issues. Further counting strategies could be studied to cope with

<b>Parameter</b>	<b>2.5 PE</b>		<b>3.5 PE</b>	
	<b>1x</b>	<b>1111x</b>	<b>1x</b>	<b>111x</b>
Efficiency 10 m <sup>2</sup> (%)	100.2 ± 0.3	98.5 ± 0.3	98.7 ± 0.5	97.2 ± 0.7
Efficiency 5 m <sup>2</sup> (%)	101.1 ± 0.2	99.7 ± 0.1	100.5 ± 0.2	99.7 ± 0.2
Noise in laboratory (%/6.4μs)	9.0	0.7	1.0	0.6
Noise in module (%/6.4μs)	Estimated Measured	14.8 10.0 ~ 20.0	5.5 -	5.7 5.9
Signal mean width (ns)	24.4		22.2	
Signal width $\sigma$ (ns)	4.7		5.6	
Suggested inhibition window (samples)	12.0		12.0	

**Table 4.2:** Comparison of the 2.5 and 3.5 PE threshold with different counting strategies applied to traces of 6.4μs. It is possible to achieve similar levels of background noise and efficiency for both threshold by choosing a 1111x (1x) matching pattern at 2.5 (3.5) PE. The levels of noise observed in the laboratory are compatible with the results obtained in the field.

<b>Parameter</b>	<b>2.5 PE</b>		<b>3.5 PE</b>	
	<b>1x</b>	<b>1111x</b>	<b>1x</b>	<b>111x</b>
Noise in laboratory (%/1μs)	1.4	0.1	0.2	0.1
Noise in module (%/1μs)	Estimated Measured	2.3 1.6 ~ 3.1	0.9 -	0.9 -

**Table 4.3:** Comparison of the 2.5 and 3.5 PE threshold with different counting strategies for a 1 μs trace.

eventual signal loss. We performed estimations in this analysis using the whole event trace (6.4 μs), but as seen in previous work [101], the muon shower signal is significantly shorter. For this reason, a counting strategy that reduces the trace length within the shower scope could also be considered. It is expected that most of the showers are contained in 1 μs. In Table 4.3 the noise level that might be obtained by extrapolating the results in section 4.4.1 to 1 μs is shown. In this scenario, a matching pattern 1x would be enough to preserve the noise level.

## 4.5 Conclusions of this chapter

In this chapter several counting strategies were studied in full detail (number of PEs, number of time bins, inhibition window, muon-signal event duration) to optimize the counter efficiency and reduce over-counting due to noise level. Such optimization was performed both with laboratory and field data, which shows the versatility and flexibility of the muon counter in as much that all studied strategies perform rather well. The 2.5 PE threshold, 1111x

pattern, and 12 time-bin inhibition windows appear to be the most conservative and safe strategy to follow and following this thesis work it has officially been adopted by AMIGA.

We have also corroborated the robustness of the SiPM calibration both in the laboratory and in the field. Furthermore, we have evaluated the performance of the temperature compensation mechanism of SiPMs in a prototype module and shown, that the dependence of the gain with the temperature is reduced by a factor of 20 with this mechanism.

---

---

# CHAPTER 5

---

## The Underground Muon Detector - ADC channel

In chapter 4 we have presented the main characteristics of the UMD *counter* mode, alongside with its calibration, reconstruction and noise sources. In this section, we present the main features of the *integrator* mode. Since the output of this mode consists of two ADC traces we commonly refer to the *integrator* mode output as the ADC channel.

In section 5.1, we describe the signal timing using a laboratory setup, from which we extracted single muon and four muon events. From this data, we also characterized the signal charge, which is of utmost importance to understand the resolution of this channel.

The data acquisition with both *integrator* and *counter* modes started when the SiPMs were deployed in the engineering array. However, as the ADC channels were not calibrated, these data have not yet been interpreted. Since in the ADC channel the number of muons is obtained from dividing the signal charge by the mean charge of a single muon, the ADC calibration consists of finding this value of charge. To this aim, we propose two procedures. The first one is presented in section 5.2. This calibration is based on shower events and can be performed offline, which is of use since when the data acquisition started there was not an online calibration available. The second one, presented in section 5.3, runs online and uses data from T1s background events that can be extracted in parallel while modules operate in acquisition.

### 5.1 Signal characterization

As we mentioned in section 3.6, the UMD engineering array has been operating with SiPMs since the end of January 2018. To include the new ADC channel into the standard UMD reconstruction, it is first necessary to understand its traces. To this aim, we use the setup described previously in Fig. 4.20 to obtain single-muon signals with the ADC channel. This setup consists of four scintillator strips with a 4 m length one upon the other. The strips are identical as those in the UMD modules [54] and they were built with the same materials that will be used in the production phase [100]. Optical fibers were glued to each strip and coupled through an optical connector to a standard SiPM array. The SiPM array consists of 64 SiPMs connected to the front-end of the electronics kit (eKIT) [88]. Four channels, corresponding to the described setup, are coupled to optical fibers, whereas 56 channels are passive and can only contribute with SiPM noise. The remaining four channels were

off, as they were coupled to four scintillator strips built with different materials (designed for measurements not related to this work). The SiPM array was calibrated as explained in section 4.1. The photo-equivalent amplitude obtained for SiPMs 1, 2, 3 and 4 is  $(31.98 \pm 0.26)$  mV,  $(31.59 \pm 0.26)$  mV,  $(30.16 \pm 0.03)$  mV and  $(29.85 \pm 0.04)$  mV respectively.

The strips are placed inside an aluminum container to shield them from the environmental light. For the same purpose, the eKIT and SiPMs are sealed into a PVC box. To trigger the acquisitions, a muon telescope built with two scintillator segments of  $4\text{ cm} \times 4\text{ cm} \times 1\text{ cm}$  with customized electronics was used. The telescope electronics inject a T1 signal into the eKIT when a coincidence (muon signal in both segments) is found. To extract the event, a computer simulates a T3 request, storing the data in the same format as in the UMD modules in the field. Events are triggered with the telescope when a muon crosses a specific position of the strips (within a 4 cm resolution). As each SiPM can be switch on or off, we can measure from one to four muons in the same event. Due to the light attenuation in optical-fibers, the detector response depends on the position where the muon impinges the scintillator. To study this effect, events produced at different positions on the strip were measured.

The average of 2500 ADC and binary traces measured at different positions on the strip is displayed in the top panels of Fig. 5.1 when one (left) or four (right) muons are detected. The signal start time is shifted, due to the delay introduced by the photon propagation in the optical fiber. The signal amplitude decreases due to light attenuation. In the bottom plots, the traces average for all distances for one (left) and four (right) muons are shown. The signal average at all distances could be seen with field data, while the signal as a function of the distance to the SiPM is only attainable in the laboratory since a muon telescope is needed. The one-muon charge fluctuation is not expected to directly extrapolate to four muons as the fluctuation sources are not exactly the same. In the first case, only the first SiPM was used; when measuring four muons, the four SiPMs are averaged.

### 5.1.1 Timing

As the *counter* and the *integrator* electronics are built in different architectures, the signal delays in each channel (binary/ADC) are different. The signal starts later in the ADC than in the binary as shown in Fig. 5.1. Another noticeable effect, already mentioned, is the shift in start times according to the position in the strip where the muon is injected, as above-mentioned, this is caused by the delay of photons as they propagate through the fiber (see Fig. 5.2 top panel). The start time of the binary channel is considered to be the first positive sample in the trace while the ADC start time is located when the signal separates  $5\sigma$  from the baseline. From linear fits, it was obtained that the signal is shifted  $(5.67 \pm 0.05)\frac{\text{ns}}{\text{m}}$  in the *counter* mode and  $(7.17 \pm 0.05)\frac{\text{ns}}{\text{m}}$  or  $(6.80 \pm 0.04)\frac{\text{ns}}{\text{m}}$  in the *integrator* mode (for one muon and four muons signals). These results are consistent with previous analysis for a PMT prototype [102], in which the shift measured was  $6.25\frac{\text{ns}}{\text{m}}$ . In the current case, it was obtained that photons in the optical fiber propagate at  $0.18\frac{\text{m}}{\text{ns}} \sim 0.60\text{ c}$ , where  $c$  is the speed of light. Considering that the *counter* (*integrator*) mode sample time is  $3.125$  ( $6.25$ ) ns, these results are consistent with the expected propagation speed of  $0.63\text{ c}$  for the Saint-Gobain BCF-99-29AMC fibers (refraction index of 1.6 [80]) employed in the UMD modules. As the delay between the binary and the ADC channel is mainly produced by differences in the electronics timing, the difference in start times ( $\Delta t$ ) is constant independently of the trigger position (see Fig. 5.2 bottom panel).

When estimating the signal charge, it is necessary to limit the integration window to the signal scope to avoid integrating over the SiPM dark rate. The single-muon width depends on where the muon is injected in the strip due to the optical fiber attenuation, as displayed in Fig. 5.3. In the case of the binary trace, the signal width is considered as the spanned time

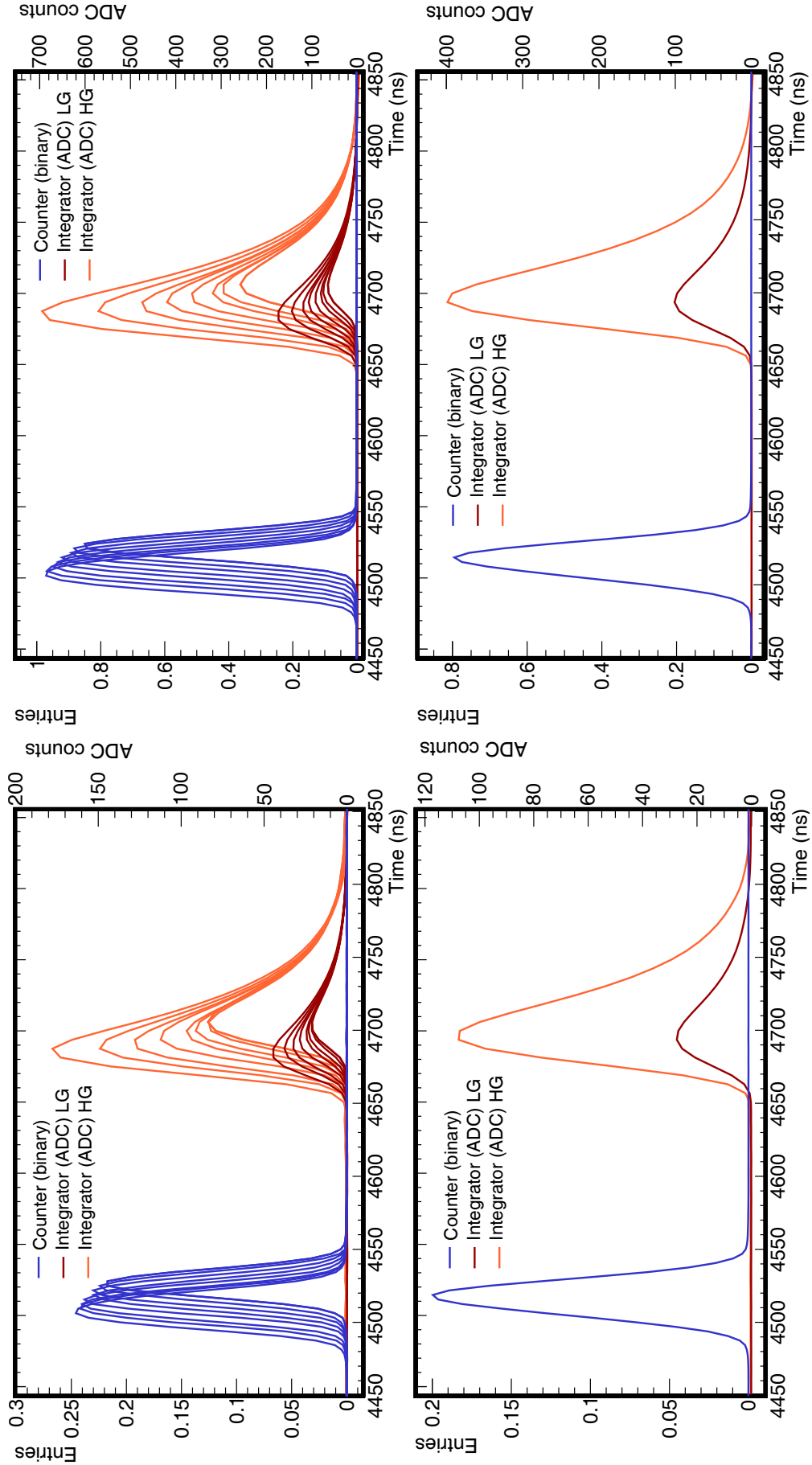


**Figure 5.1:** (Top) average trace as a function of the trigger position for one (left) and four (right) muons. The signal is shifted and attenuated when the trigger is moved towards the end of the strip. (Bottom) average trace of all positions for one (left) and four (right) muons.

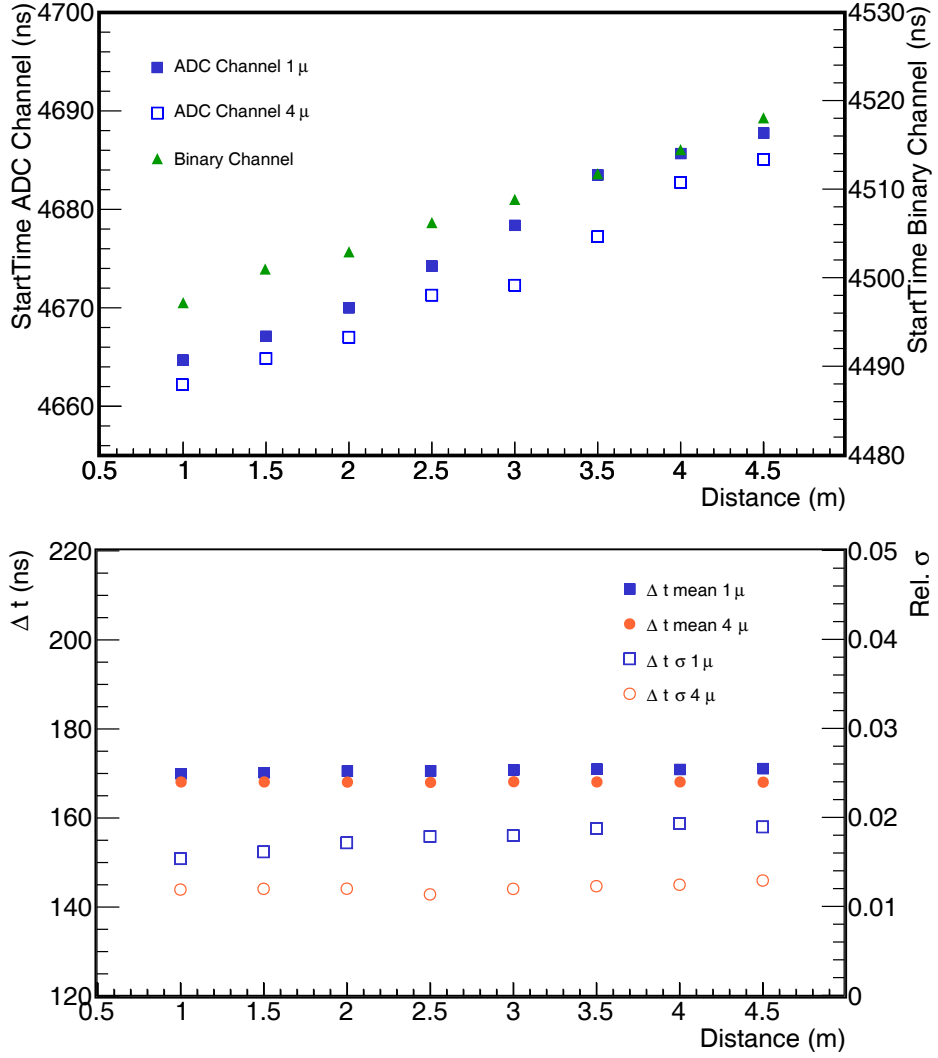


**Figure 5.2:** (Top) Signal start time as a function of the trigger position on the strip. The start time of the binary and ADC channels (one and four muons) signal is shown. The start time is shifted when moving the muon telescope to the end of the strip due to the delay introduced by the photon propagation. (Bottom) difference between the channel start times ( $\Delta t$ ) as a function of the position on the strip.

between the first and the last positive sample of the trace. On the other hand, for the ADC signal, the chosen criteria is considering the time over the  $5\sigma$  from the baseline level. Due to light attenuation in the fiber, the mean number of PEs in the signal depends on the position of the telescope and, therefore, the signal narrows, and the relative fluctuations grow, as the trigger moves towards the end of the scintillator strip. The width of the four-muon signal is only shown for reference, as in the field the signal is convoluted with the time profile of the muon shower.

### 5.1.2 Charge

As mentioned, with the ADC channel estimate the number of muons in the detector dividing the signal charge by the mean charge of a single muon. In this sense, the main contributions to the resolution are the charge fluctuations due to attenuation of light in the optical fiber, energy deposit in the scintillator, and photon production.

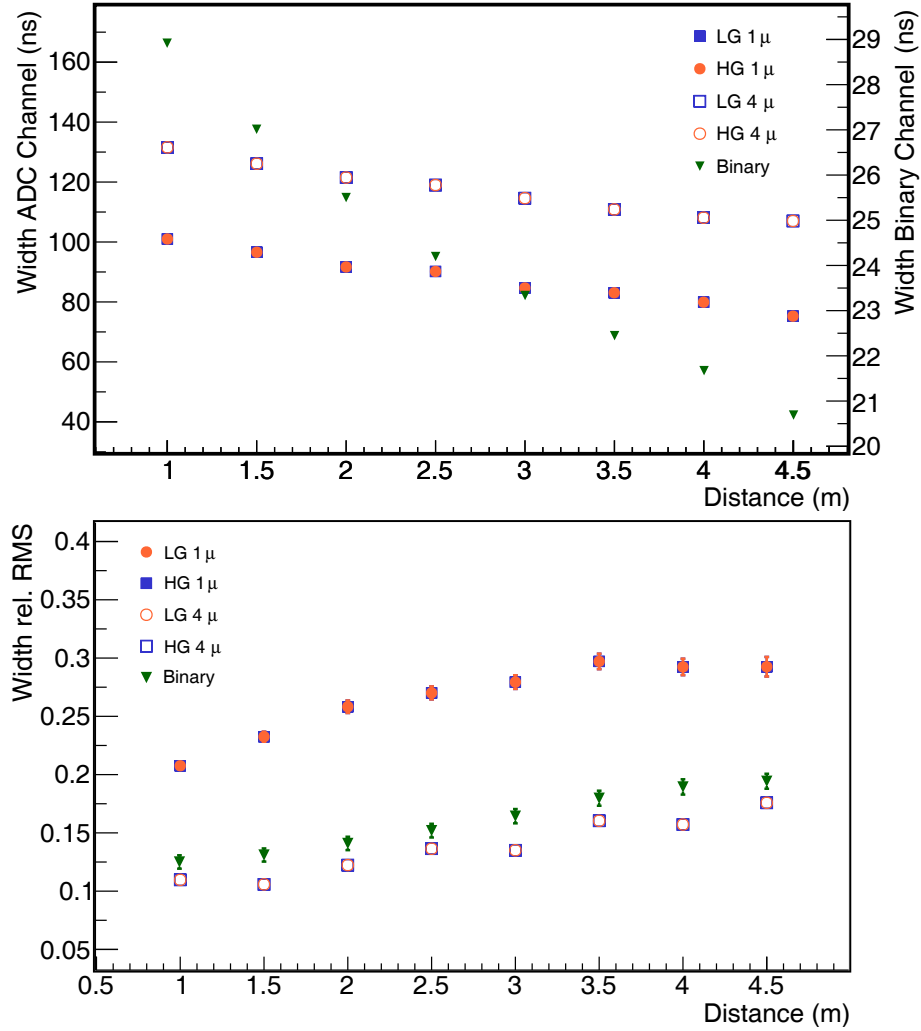


**Figure 5.3:** (Top) signal mean width as a function of the trigger position. Due to light attenuation in the fiber, the signal becomes narrower when the trigger is moved towards the end of the scintillator strip. (Bottom) width relative fluctuations as a function of the trigger position.

In Fig. 5.4 we show how the optical fiber attenuation impacts in the signal charge as the relative fluctuation increases and the charge decreases when moving the muon telescope towards the end of the strip. A relative 62% of spread in the single muon charge (see Fig. 5.5) was obtained. To fit the attenuation, a double exponential decay law was used [103]:

$$f(x) = a \exp\left(\frac{-\lambda_1}{x}\right) + (1 - a) \exp\left(\frac{-\lambda_2}{x}\right), \quad (5.1)$$

where  $\lambda_1, \lambda_2$  are the attenuation lengths and  $a$  is a proportionality constant.

Concerning the attenuation curve, not only are the normalization of one and four-muons curves differ but also there is a 15% difference in the attenuation lengths as it can be observed in Table 5.1. This is expected since measurements of one muon come from channel 1, whereas four-muon acquisitions are due from channels 1-4, and therefore the charge fluctuations produced by both processes may differ. This same feature is found in the charge histograms (Fig. 5.5).

As it was mentioned before, to estimate the number of muons with the ADC channel, the mean charge per muon is needed. Therefore, the ADC channel calibration consists of estimating the *minimum ionizing particle* (MIP) as in the WCD [104]. In this case, the main

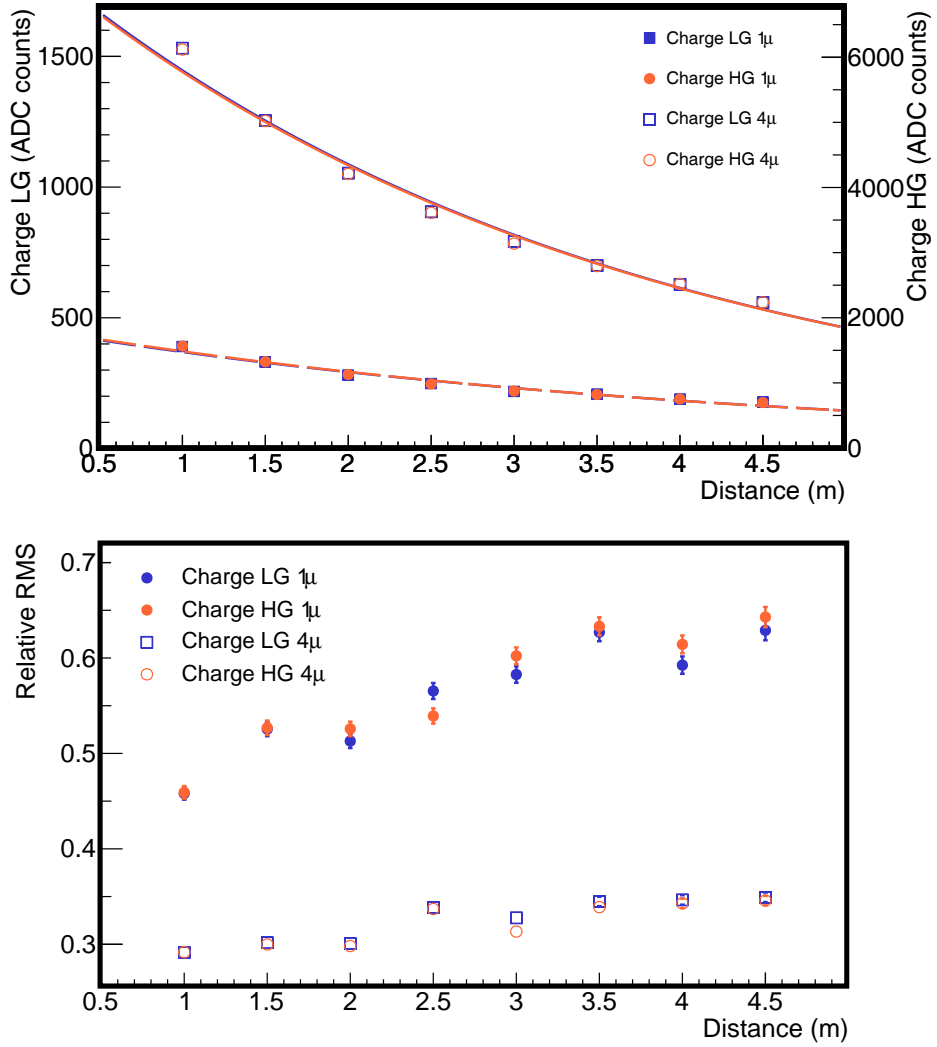


**Figure 5.4:** Mean charge and relative RMS as a function of the position on the strip for one and four muon signals. The signal is attenuated (and the relative fluctuation increases) when moving the trigger towards the end of the strip. The fits results can be found in Table 5.1.

difficulty lays in the baseline fluctuations due to the SiPMs dark rate. In 64 active channels, a dark rate of  $\sim 32$  MHz is expected (as explained in section 4.3). A typical number of photo-equivalents in a muon pulse is  $\sim 20$  PEs (see Fig. 6.11 in chapter 6), therefore the amount of charge distributed in the baseline due to dark rate in a WCD event of  $6.4\ \mu\text{s}$  is equivalent to  $\sim 10$  muons. In Fig. 5.6 the baseline histograms for different integration windows along with the signal width of muons can be found. For example, for a typical muon width of 100 ns, the baseline spans from -400 to 400 ADC (HG), this region slightly overlaps with the MIP charge distribution, as seen from Fig. 5.5: mean charge 1038 ADC with an RMS of 642 ADC. The second difficulty lays in the muon detector dependence on the WCD T1 triggers [47], as it cannot be self-triggered. The ratio of background particles from T1 events is low (see section 5.3) and becomes lower when narrowing the integration window to control the baseline noise. We discuss two calibration methods for the ADC channel in sections 5.2 and 5.3.

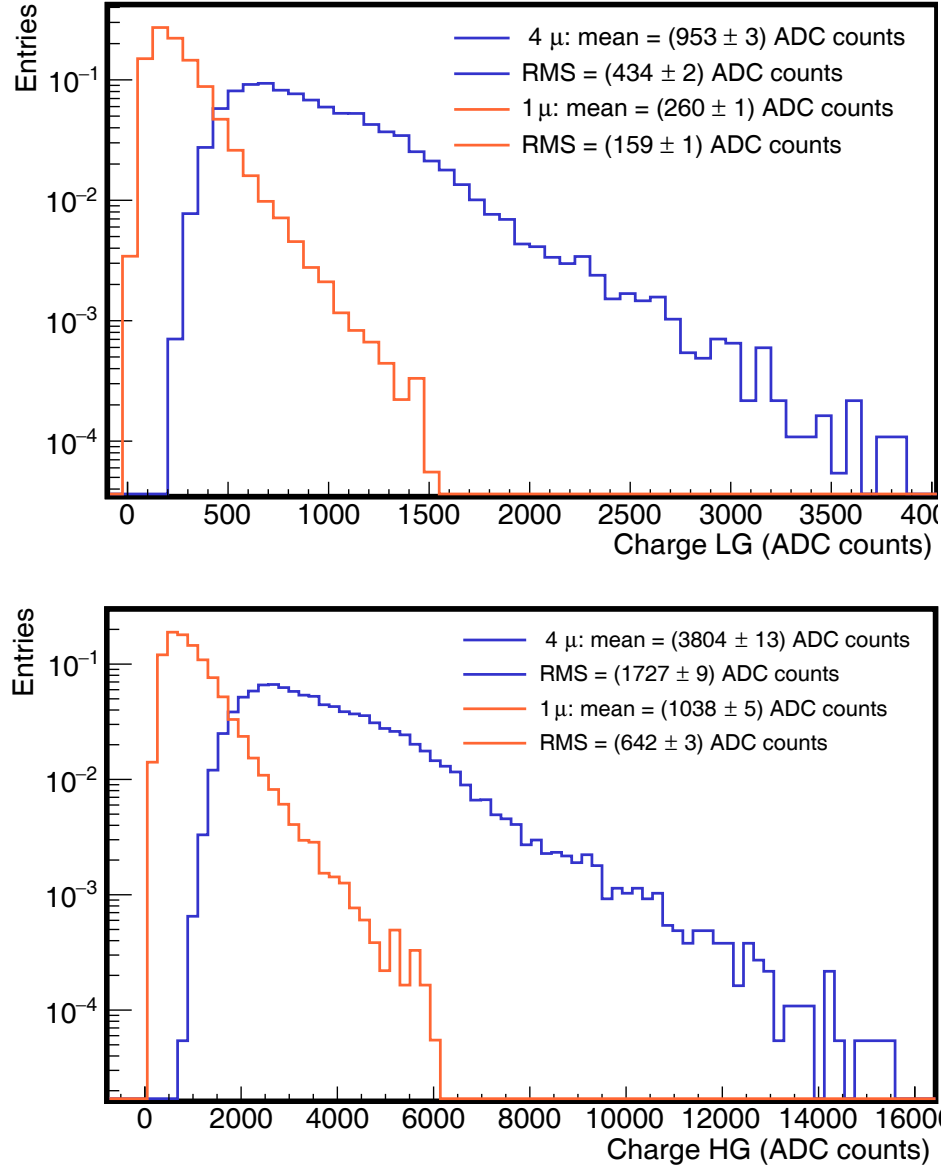


**Figure 5.5:** Top (bottom) charge histograms for one and four-muon signals low (high) gain channel.

### 5.1.3 ADC signal model and field data

To compare laboratory measurements with field data, events from the module with Id 108 of the station with Id 1764 were analyzed using the binary channel to select one and four-muon events. The signal charge, width, and start time difference between the binary and the ADC traces were estimated. In addition, the signals were fitted using a log-normal like function:

$$f(t; \mu, \sigma) = A \frac{1}{(t - t_0)\sigma\sqrt{2\pi}} \exp \left( \frac{(-\ln(t - t_0) - \mu)^2}{2\sigma^2} \right), \quad (5.2)$$

where  $A$  is a normalization factor, and  $t_0$  is the signal start time. An example of the fit for an average signal is shown in Fig. 5.7 (only as a reference as the fits were performed over individual signals). The fit describes accurately the signal shape. The mean value and standard deviation for each parameter are summarized in tables 5.1 and 5.2 respectively, along with the fit results from Fig. 5.4 obtained at the laboratory. The signal shape (determined

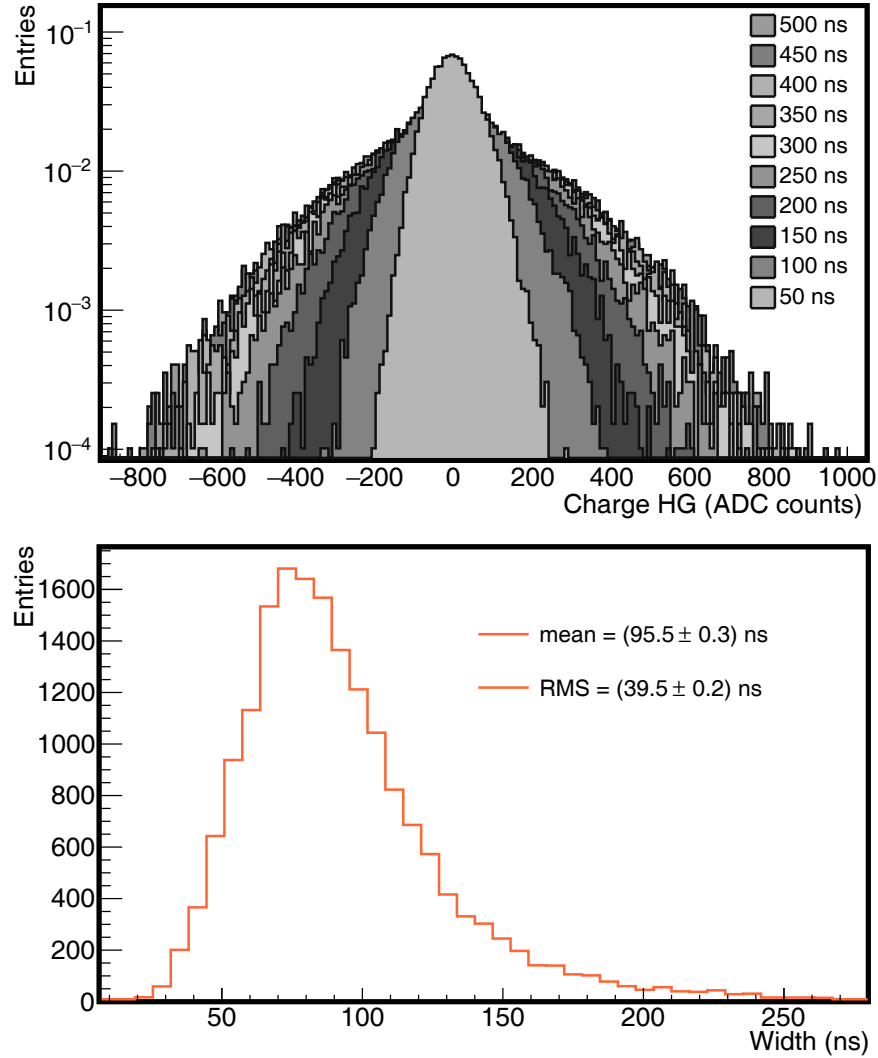


**Figure 5.6:** (Top) baseline histograms for different integration windows. (Bottom) single-muon width histogram. For a mean muon width of 100 ns, the baseline spans from -400 to 400 ADC, which overlaps with MIP charge distribution.

by parameters  $\mu$  and  $\sigma$  in equation 5.2) for all laboratory cases are similar, except for the normalization factor which is  $\sim 3.4$  times larger for four muons. In field data, four-muon signals cannot be fitted with equation 5.2 as their signal timing is convoluted with the time profile of the arriving muons.

As a final remark, we present in Fig. 5.8 the fit parameters of equation 5.2 as function of the position of the muon telescope. We show results of fitting the average trace at each position on the setup and of fitting individual traces from which parameter means are obtained. Both methods to extract the signal features are consistent. In the top panels of Fig. 5.8, we show that the signal shape, determine by parameters  $\mu$  (left) and  $\sigma$  (right), remains constant along the strip. The normalization factor (bottom left panel), relative to the signal amplitude, is attenuated as the muon telescope moves towards the end of the strip due to the light attenuation. Finally, the signal start time is shifted, as explained in section 5.1.1, due to the delay in the photon propagation. The results of the fitted start times and the start times in Fig. 5.2 are consistent, as they differ approximately in one-sample time (6.25 ns).

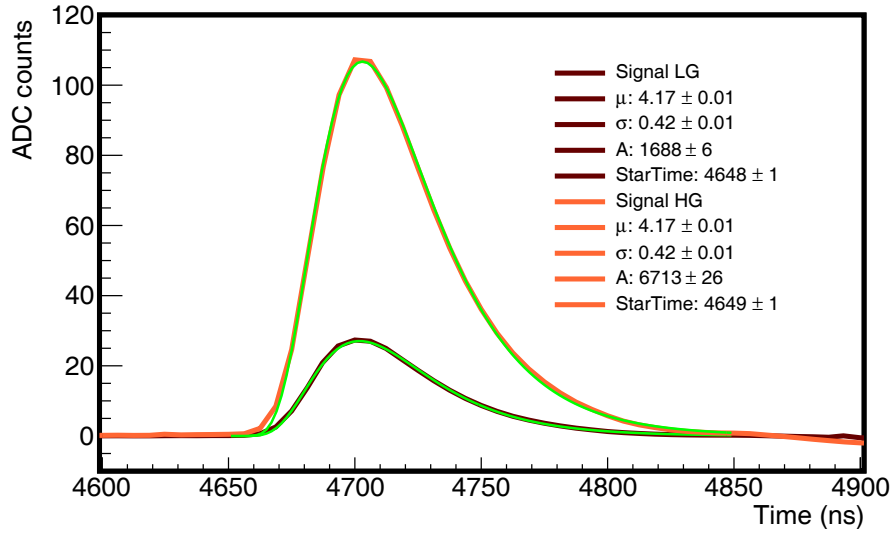


**Figure 5.7:** Equation 5.2 fit for the average ADC trace of single muons. The average was obtained using 20000 laboratory events.

Parameter	1 $\mu$		4 $\mu$		
	LG	HG	LG	HG	
$\mu$	Lab	$3.986 \pm 0.004$	$4.039 \pm 0.004$	$0.573 \pm 0.001$	$0.548 \pm 0.001$
	Field	$3.970 \pm 0.020$	$4.050 \pm 0.020$	-	-
$\sigma$	Lab	$0.578 \pm 0.002$	$0.547 \pm 0.002$	$0.694 \pm 0.001$	$0.663 \pm 0.001$
	Field	$0.590 \pm 0.010$	$0.550 \pm 0.010$	-	-
Norm	Lab	$1748 \pm 12$	$6820 \pm 41$	$6011 \pm 27$	$23433 \pm 100$
	Field	$1535 \pm 30$	$5959 \pm 119$	-	-
Charge (ADC counts)	Lab	$260 \pm 1$	$1038 \pm 5$	$953 \pm 3$	$3804 \pm 14$
	Field	$222 \pm 5$	$874 \pm 18$	$824 \pm 12$	$3278 \pm 70$
$\Delta t$ (ns)	Lab	$170.72 \pm 0.03$		$168.08 \pm 0.02$	
	Field	$163.00 \pm 0.10$		$162.70 \pm 0.40$	
Signal Width (ns)	Lab	$84.5 \pm 0.4$		$119.8 \pm 0.2$	
	Field	$91.0 \pm 1.0$		$192.0 \pm 5.0$	
Attenuation Length 1 (m)		$3.90 \pm 0.10$	$4.10 \pm 0.10$	$3.50 \pm 0.04$	$3.51 \pm 0.04$
Attenuation Length 2 (m)		$0.017 \pm 0.001$	$0.022 \pm 0.001$	$0.021 \pm 0.001$	$0.019 \pm 0.001$
Proportionality constant		$504 \pm 8$	$2000 \pm 30$	$1971 \pm 16$	$7882 \pm 64$

**Table 5.1:** Mean values obtained from parameter histograms of one and four muons. 20000 laboratory events were used. Concerning the field data, 681 single-muon signals and 121 four-muon signals were used.

<b>Parameter</b>	<b>1 <math>\mu</math></b>		<b>4 <math>\mu</math></b>		
	<b>LG</b>	<b>HG</b>	<b>LG</b>	<b>HG</b>	
$\mu$	Lab	$0.506 \pm 0.003$	$0.563 \pm 0.003$	$0.214 \pm 0.001$	$0.199 \pm 0.001$
	Field	$0.510 \pm 0.010$	$0.620 \pm 0.010$	-	-
$\sigma$	Lab	$0.234 \pm 0.001$	$0.228 \pm 0.001$	$0.097 \pm 0.001$	$0.096 \pm 0.001$
	Field	$0.230 \pm 0.010$	$0.240 \pm 0.010$	-	-
Norm	Lab	$1423 \pm 8$	$4982 \pm 29$	$3253 \pm 19$	$12154 \pm 71$
	Field	$870 \pm 21$	$3495 \pm 84$	-	-
Charge (ADC counts)	Lab	$159 \pm 1$	$642 \pm 3$	$434 \pm 2$	$1727 \pm 10$
	Field	$133 \pm 3$	$521 \pm 13$	$254 \pm 12$	$1013 \pm 49$
$\Delta t$ (ns)	Lab	$3.10 \pm 0.02$		$2.03 \pm 0.01$	
	Field	$2.87 \pm 0.01$		$2.24 \pm 0.03$	
Signal Width (ns)	Lab	$33.5 \pm 0.5$		$19.3 \pm 0.1$	
	Field	$35.0 \pm 1.0$		$72.0 \pm 3.0$	

**Table 5.2:** RMS obtained from the parameter histograms of one and four muons. 20000 laboratory events were used. Concerning the field data, 681 single-muon signals and 121 four-muon signals were used.

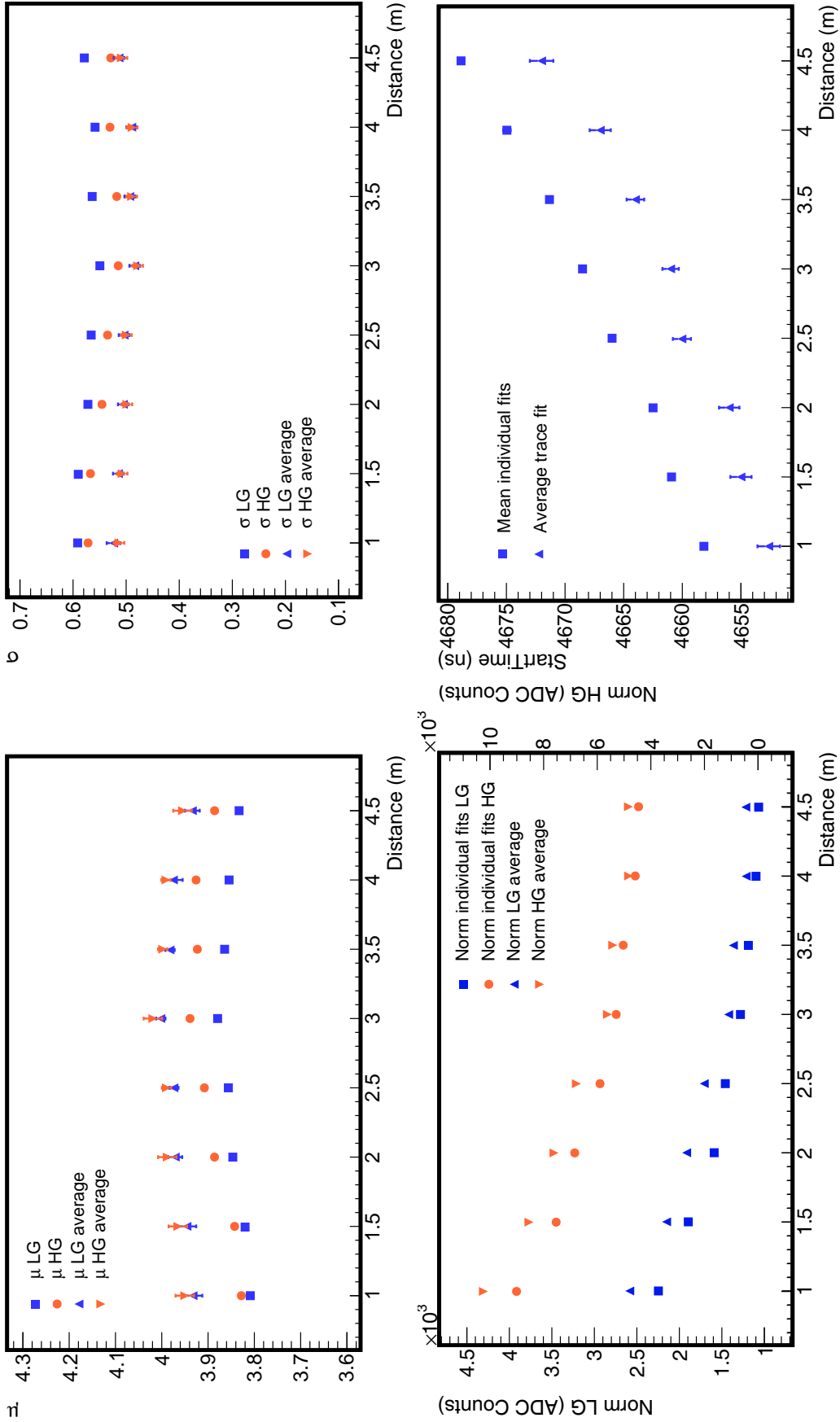


**Figure 5.8:** Results of equation 5.2 parameters as a function of the muon telescope position. At each position, fits were performed over 20000 individual events and over the average trace. The consistency between the two analysis is apparent. The signal shape is determined by parameters  $\mu$  (top left) and  $\sigma$  (top right) and remain rather constant in the whole strip. The normalization factor (bottom left) decreases as the telescopes are moved towards the end of the strip due to the light attenuation in the optical fiber. The signal start time is shifted due to the photons propagation delay as explained in section 5.1.1. The result obtained from the fits is consistent with the result in Fig. 5.2 within the sampling time of the ADC channel (6.25 ns).

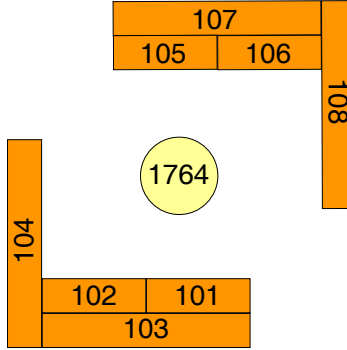


**Figure 5.9:** Muon detector associated to the station with Id 1764. In this case, the muon detector is comprised of two twins (north and south). Each twin consists of two  $5\text{ m}^2$  modules with Ids 101, 102, 105 and 106, and two  $10\text{ m}^2$  modules with Ids modules 103, 104, 107 and 108.

## 5.2 Offline calibration with shower events

The calibration of the ADC channel consists of obtaining the mean charge of a single-muon. We present an offline calibration using shower events, and to this aim, we analyzed events from the station with Id 1764, as it was the first station to be fully equipped with SiPMs (since December 2017). A schematics of station Id. 1764 with its modules Ids is displayed in Fig. 5.9. This muon detector is arranged in two  $30\text{ m}^2$  twins (north and south); each consisting in two  $5\text{ m}^2$  and two  $10\text{ m}^2$  modules. We analyzed data from shower events detected between May, 16<sup>th</sup> 2017 and June, 30<sup>th</sup> 2017.

### 5.2.1 Integration window

In section 4.3, we described two sources of noise: the SiPM dark rate and the optical-fiber noise probably caused by spontaneous light emission from the fibers [96]. The SiPM dark rate produces fluctuations in the ADC baseline and, furthermore, it may produce “1”s in the binary traces due to crosstalk among SiPM inner cells [93]. This noise can be mostly rejected by choosing a proper counting strategy as explained in 4.4.1. The optical-fiber noise is slightly smaller than the muon signal but not distinguishable. To reject this noise in the calibration we restrict the analyses of traces to the shower scope. To this aim, it is necessary to synchronize the traces [101], as different trigger types produce shifts in the signal start times [47]. In Fig. 5.10 top panel, we show the signal start times for binary and ADC traces. In the first case, the start time is identified as the first “1” in the trace. In the second case, the start time is taken when the signal separates  $> 5\sigma$  from the baseline. We discriminated the events according to the trigger type: the first two peaks correspond to the T2-ToT trigger and the second peaks to the T2-TH trigger. Since the T2-TH trigger is built faster than the T2-ToT, it appears first in the electronics circular buffer. The results from the fits are summarized in Table 5.3. Further to this, we used the WCD timing information [101] to synchronize the traces according to the trigger type and to narrow the analysis to the shower scope. We show in the middle panel of Fig. 5.10 the signal start times after synchronizing the traces. From the Gaussian fit (summarized in Table 5.3) we can locate the signal start time in a window limited by the mean start time ( $4337\text{ ns}$ )  $\pm 3\sigma$  ( $240\text{ ns}$ ). Furthermore, we have also estimated the delay between the binary and the ADC channels in Fig. 5.10 bottom panel, from which we obtained  $\Delta\text{T2 - ToT} = (162.4 \pm 0.1)\text{ ns}$  and  $\Delta\text{T2 - TH} = (162.2 \pm 0.1)\text{ ns}$ . These results are compatible with the delay obtained in the laboratory setup,  $(170.62 \pm 0.03)\text{ ns}$ , presented in section 5.1, Fig. 5.2 bottom panel.

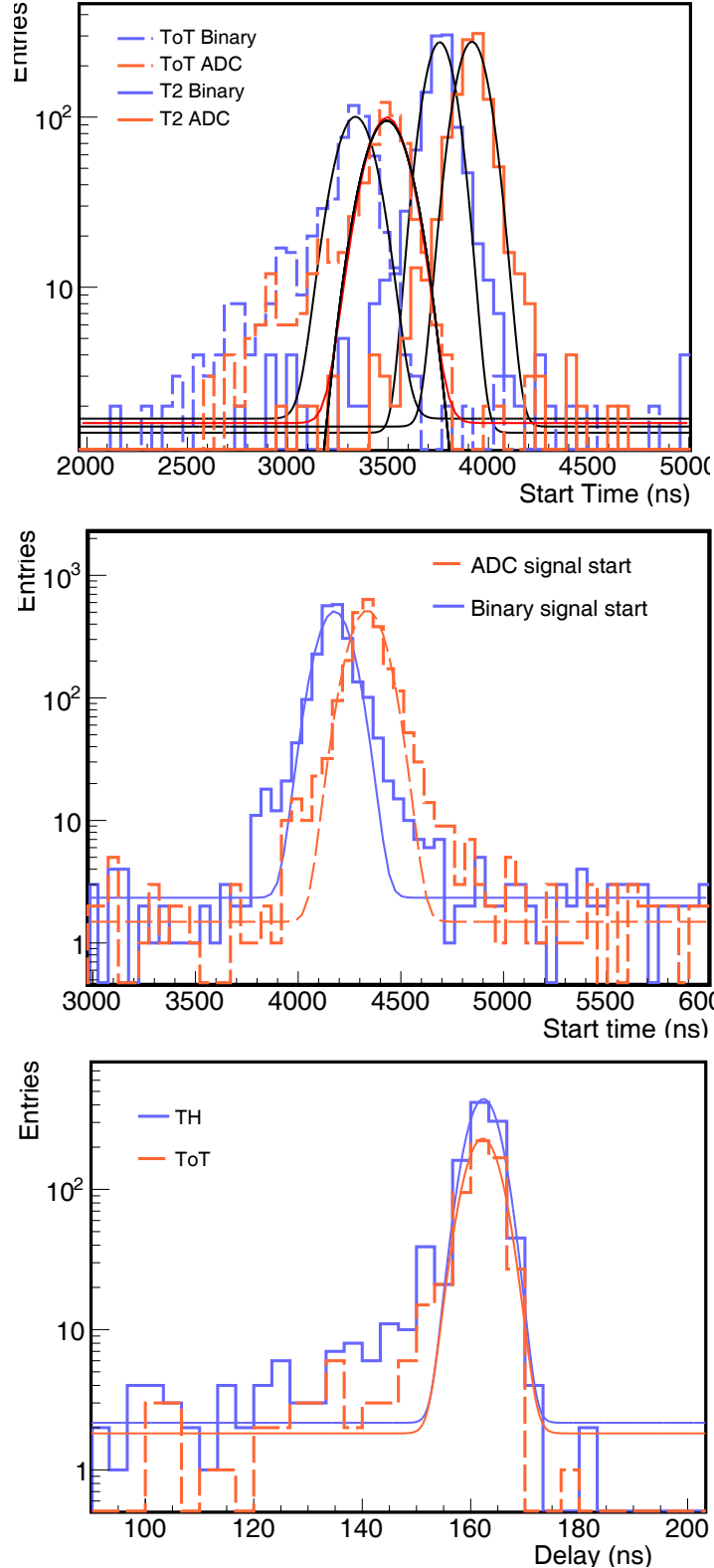


**Figure 5.10:** (Top) signal start time by trigger type. In each channel (binary/ADC) two peaks are identified, corresponding to the T2-TH and T2-ToT triggers. (Middle) signal start time after synchronizing the traces according to the WCD timing type. (Bottom) delay between the ADC and the binary channels for the T2-TH and T2-ToT triggers. The results from the fits are summarize in Table 5.3.

Parameter	$\mu$ (ns)	$\sigma$ (ns)
T2-ToT Binary	$3337 \pm 5$	$91 \pm 6$
T2-ToT ADC	$3495 \pm 5$	$98 \pm 6$
T2-TH Binary	$3757 \pm 2$	$70 \pm 3$
T2-TH ADC	$3918 \pm 2$	$74 \pm 2$
Start time binary (sync)	$4177 \pm 2$	$77 \pm 2$
Start time ADC (sync)	$4337 \pm 2$	$80 \pm 2$
$\Delta T_2 - \text{ToT}$	$162.2 \pm 0.1$	$3.0 \pm 0.1$
$\Delta T_2 - \text{TH}$	$162.4 \pm 0.1$	$2.9 \pm 0.1$

**Table 5.3:** Fit results for the start time histograms in Fig. 5.10.

To estimate the signal charge in the ADC channel and minimize fluctuations, we need to restrict the integration window to the signal scope. To this aim, the integration algorithm locates the first muon in the binary trace within the expected signal start time (between 4097 ns and 4577 ns), determined from the results in Fig. 5.10. Once the first muon is located, the algorithm locates the ADC start time after the leading muon, when the signal amplitude separates  $5\sigma$ s from the baseline. Then, the end time is located when the signal amplitude decreases to the baseline level. The signal charge is calculated between these start and end times. If the impinging muon does not produce enough light to be detected with the ADC channel, it might not be possible to locate the signal start and end times with these criteria. In that case, the signal charge is calculated within a 100 ns (typical muon width as presented in section 5.1.2) window starting at the leading muon time plus 162 ns (which is the typical delay between the ADC and binary channels).

An example event is presented in Fig. 5.11. We show the counting histogram extracted from the binary traces (top) and the ADC traces (bottom). The green (red) arrows indicate the signal start (end) times. The signal at  $\sim 500$  ns is outside the typical shower scope and, therefore, we assume it to be background (see section 4.3). This is an example of how the integration algorithm removes the noise that matches the counting strategy and might be mistaken as muons.

### 5.2.2 The uncertainty model

In the ADC channel, the main contribution to the detector resolution is the charge fluctuation, produced by fluctuations of the energy deposit in the scintillators, the optical-fiber attenuation, and the photon production. Furthermore, fluctuations in the baseline (mainly produced by the SiPMs dark rate), also adds to this uncertainty. Therefore, high relative fluctuations are expected for a low number of muons.

For a signal of  $N$  muons, the charge distribution will be the convolution of  $N$  times the distribution of  $N = 1$  if we assume a normally distributed charge. As each variable is uncorrelated, the variance follows the Bienaymé formula [105], and therefore for  $N$  muons:

$$\sigma_N^2 = N\sigma_1^2 \quad \text{and} \quad \frac{\sigma_N}{N} = \frac{\sigma_1}{\sqrt{N}},$$

where

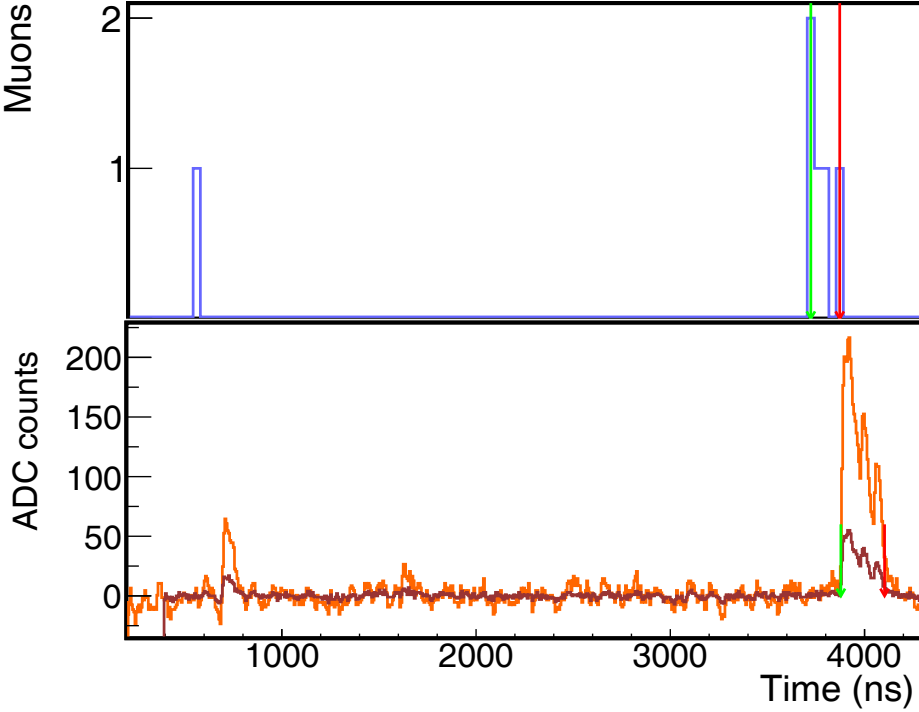


**Figure 5.11:** Example event in module with Id 104 of the station with Id 1764. We show the muon histogram from the binary channel (top) and the ADC traces (bottom). The green (red) arrows indicate the signal start (end) times. The “muon” at 500 ns, is outside the typical shower scope and therefore, we assume it is produced by noise.

$$\sigma_N = \sqrt{\frac{\sum_{i=1}^n (x_i - \bar{N})^2}{n-1}}, \quad \text{and } n \text{ is the number of events} \quad (5.3)$$

In this uncertainty model, the relative fluctuation is maximum at  $N = 1$  and the only parameter to be determined is  $\sigma_1$ , which is the detector resolution for a single muon. Using the binary channel to identify the number of muons injected in the detector ( $N$ ), we created histograms of the signal charge in the ADC channel for each  $N$ . From these histograms we extracted the  $\sigma_N$  using equation 5.3. In Fig. 5.12, we present this  $\sigma_N$ s as a function of  $N$ . In the top (bottom) panel, the results for the 5 (10)  $m^2$  modules can be found. The  $\sigma$  error bars used for the fits were approximated as Gaussian. In Table 5.4 the results from the fits are summarized. The  $\sigma_1$ s obtained from the statistical formula (equation 5.3) applied to the  $N = 1$  histogram are also shown for comparison. Both estimations of  $\sigma_1$  are compatible within an average difference of 6%.

### 5.2.3 Calibration curves of the ADC channel

The calibration of the ADC channel consists of obtaining the mean charge of the single-muon signal. One method to obtain this value is to compare the ADC channels to the output of the binary channel using shower events. In Fig. 5.13, we plot the signal charge of the ADC channel as a function of the number of muons ( $N$ ) estimated with the binary channel for the module with Id 104 ( $10 m^2$ ). The mean charge per  $N$  is shown along with the individual events, from which the signal dispersion is shown. Since in this analysis we are comparing the number of injected particles in the muon detector as seen by both the ADC and the binary channel, the error bars in both axis correspond to the channel resolution. In the case

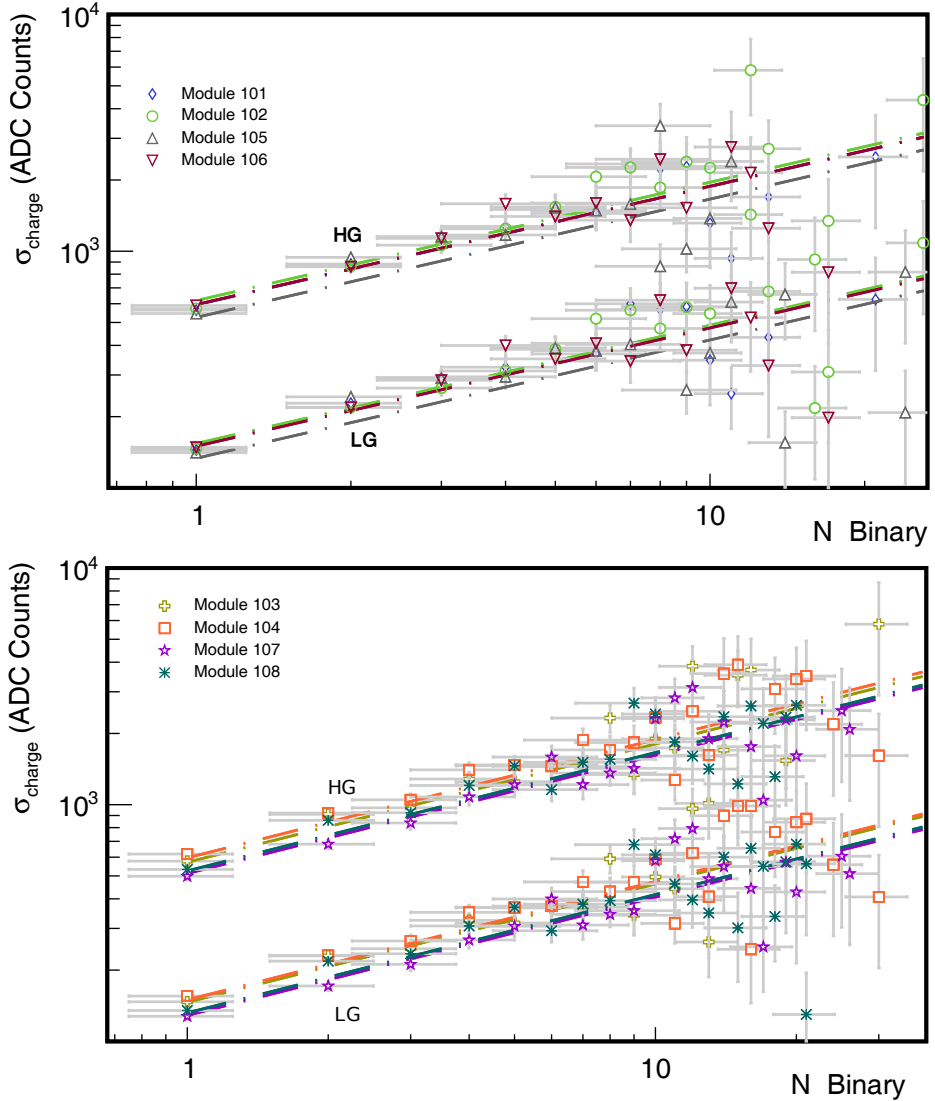


**Figure 5.12:**  $\sigma_{\text{Ns}}$  in the ADC channel as a function of the number of muons ( $N$ ) estimated with the binary channel. In the top panel, the results for  $5\text{ m}^2$  modules is shown, for both low- and high-gain channels. In the bottom panel, the results for  $10\text{ m}^2$  are shown. We have fitted each module data set with a  $\sigma_1 \sqrt{N}$  function. We summarized the results of the fits in Table 5.4.

of the ADC, we presented how to estimate this resolution for each  $N$  in section 5.2.2, using equation 5.3 and the results in Table 5.4. For the binary channel, we used the resolution estimated using shower simulations, as explained in chapter 8.

As the difference in charge between  $N$  muons and  $N+1$  muons should be the charge of one muon, the ADC calibration is achieved by fitting the data with a linear fit, where the slope corresponds to the single-muon mean charge. In this range, the ADC charge in its mean values behaves linear with the number of muons reconstructed with the binary traces. Though the integrator fluctuations will be larger for a small number of muons, the overall uncertainty will be significantly reduced with a large number of events. We performed the fits using the individual events, and the charge mean and its uncertainty are shown in Fig. 5.13.

Module Id	LG (ADC counts)		HG (ADC counts)	
	$\sigma_1$ fit	$\sigma_1$	$\sigma_1$ fit	$\sigma_1$
101	$153 \pm 8$	$145 \pm 5$	$594 \pm 31$	$564 \pm 19$
102	$154 \pm 8$	$146 \pm 5$	$619 \pm 34$	$572 \pm 19$
103	$146 \pm 7$	$147 \pm 5$	$571 \pm 25$	$577 \pm 19$
104	$150 \pm 6$	$155 \pm 5$	$596 \pm 24$	$619 \pm 21$
105	$133 \pm 6$	$141 \pm 5$	$525 \pm 25$	$546 \pm 20$
106	$150 \pm 8$	$148 \pm 5$	$595 \pm 31$	$590 \pm 21$
107	$129 \pm 6$	$128 \pm 4$	$512 \pm 24$	$498 \pm 17$
108	$132 \pm 5$	$135 \pm 5$	$525 \pm 22$	$533 \pm 18$

**Table 5.4:** Fit results for Fig. 5.12. We show the  $\sigma_1$ s obtained from fitting the data with a  $\sigma_1\sqrt{N}$  function, and also, we show for comparison the  $\sigma_1$  extracted from the  $N_1$  histogram calculated as in equation 5.3. As expected, both methods are consistent. Errors are smaller when using the fits, which indicates that the fits lead to a better estimation of the model parameter ( $\sigma_1$ ) by improving statistics.

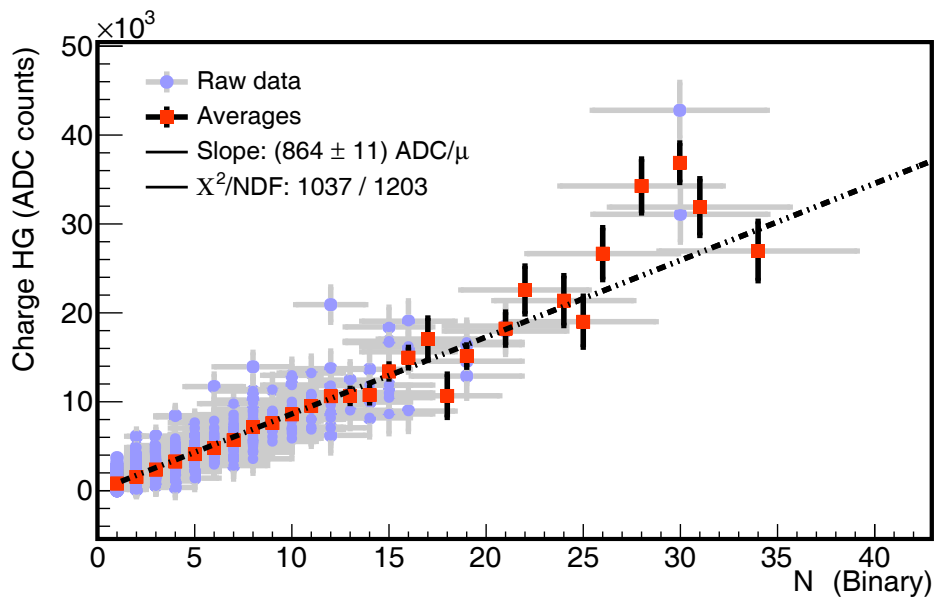


**Figure 5.13:** Signal charge in the ADC channel as a function of  $N$  estimated with the binary traces for the module with Id 104. For each  $N$ , we plot the charge of each individual event (blue) and mean (red). From the individual events, the charge dispersion is observed. The slope of the linear fit equals to the mean charge of a single muon.

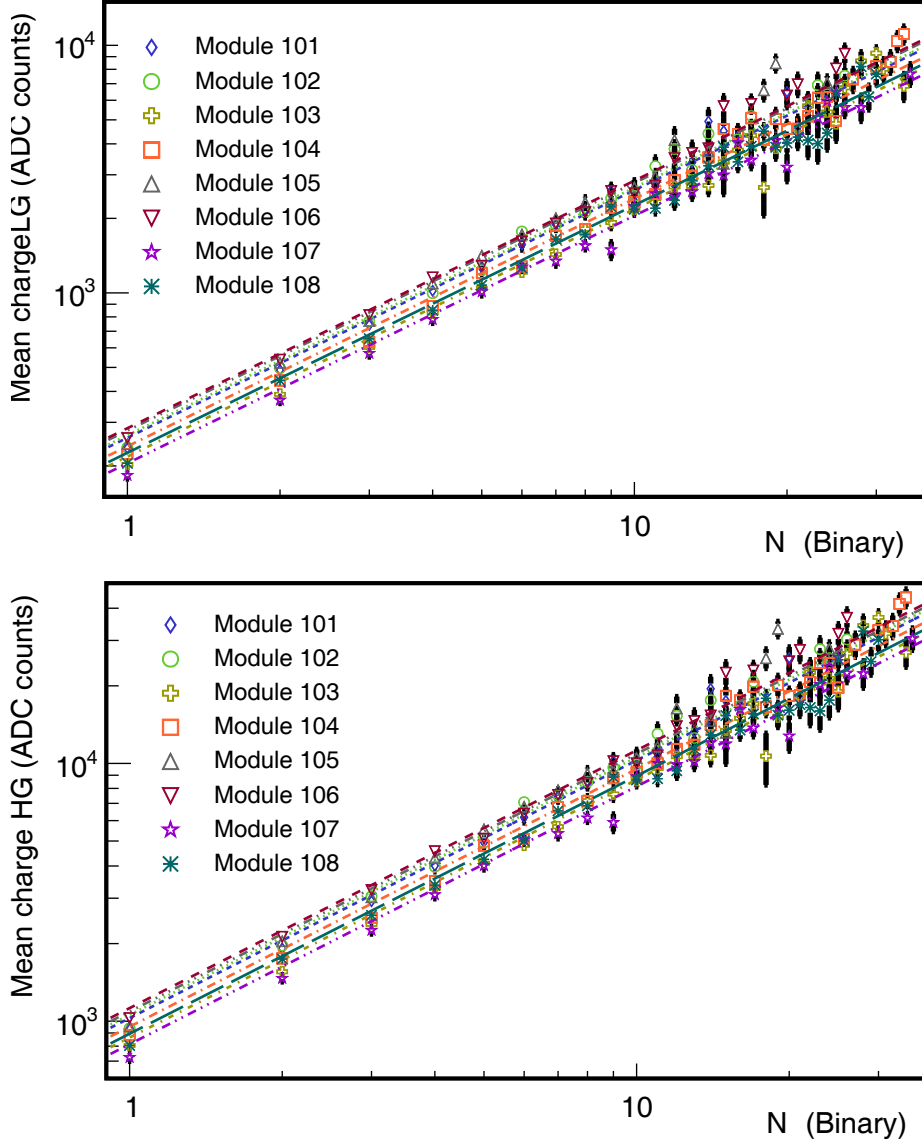


**Figure 5.14:** Mean charge in the ADC channel as a function of  $N$  estimated with the binary traces for all modules of the station with Id 1764. On the top (bottom) panel, the results of the low-gain (high-gain) channel is displayed. We show the mean values as a reference since the fits were performed using individual events. The fits results are summarized in Table 5.5.

In Fig. 5.14, we present the calibration curves for all modules in the station with Id 1764. Although the fits are performed over the individual events, we only show, for clarity, the mean charges and the linear fits. In Table 5.5 we summarized the fit results. It is apparent that the slopes of the  $5\text{ m}^2$  modules are steeper than the slopes of the  $10\text{ m}^2$  modules, as we expected, since the longer the optical fiber, the higher the attenuation, and therefore, the lower the mean light-output.

## Summary

In Table 5.6, we present the calibration summary of sections 5.2.2 and 5.2.3. For each module, we show the mean charge per muon ( $\bar{Q}_1$ ), the resolution for one muon ( $\sigma_1$ ), the relative fluctuation per muon ( $\frac{\sigma_1}{\bar{Q}_1}$ ), and the ratio between the low- and high-gain channels ( $\frac{HG}{LG}$ ). The light-output for  $5\text{ m}^2$  modules (101, 102, 105, 106) is in average 22% higher than for  $10\text{ m}^2$

Module Id	LG		HG	
	Slope ( $\frac{\bar{Q}}{\mu}$ )	$\chi^2/\text{NDF}$	Slope ( $\frac{\bar{Q}}{\mu}$ )	$\chi^2/\text{NDF}$
101	$260 \pm 4$	707/920	$1025 \pm 16$	708/920
102	$266 \pm 4$	706/920	$1057 \pm 16$	688/920
103	$218 \pm 3$	1026/1203	$864 \pm 11$	1037/1203
104	$240 \pm 3$	1006/1177	$952 \pm 12$	1012/1177
105	$278 \pm 4$	781/842	$1090 \pm 16$	765/842
106	$284 \pm 4$	664/860	$1124 \pm 17$	664/860
107	$205 \pm 3$	868/1118	$814 \pm 11$	859/1118
108	$226 \pm 3$	1029/1200	$894 \pm 11$	1017/1200

**Table 5.5:** Fit results of the ADC channel calibration (Fig. 5.14) for all modules in the station with Id 1764. The light-output in  $5\text{ m}^2$  modules (101, 102, 105, 106) is higher than in  $10\text{ m}^2$  modules (103, 104, 107, 108), which is expected due to the optical-fiber attenuation. Units of the mean charge per muon ( $\frac{\bar{Q}}{\mu}$ ) are  $\frac{\text{ADC counts}}{\mu}$ .

Module Id	LG			HG			$\frac{\text{HG}}{\text{LG}}$
	$\frac{\bar{Q}}{\mu}$	$\sigma_1$	$\frac{\sigma_1}{\bar{Q}_1}$	$\frac{\bar{Q}}{\mu}$	$\sigma_1$	$\frac{\sigma_1}{\bar{Q}_1}$	
101	$260 \pm 4$	$153 \pm 8$	0.59	$1028 \pm 16$	$594 \pm 31$	0.58	3.95
102	$266 \pm 4$	$154 \pm 8$	0.58	$1057 \pm 16$	$619 \pm 34$	0.59	3.98
103	$218 \pm 3$	$146 \pm 7$	0.67	$864 \pm 11$	$571 \pm 25$	0.66	3.97
104	$240 \pm 3$	$150 \pm 6$	0.63	$952 \pm 12$	$596 \pm 24$	0.63	3.97
105	$278 \pm 4$	$133 \pm 6$	0.48	$1090 \pm 16$	$525 \pm 25$	0.48	3.92
106	$284 \pm 4$	$150 \pm 8$	0.53	$1124 \pm 17$	$595 \pm 31$	0.53	3.96
107	$205 \pm 3$	$129 \pm 6$	0.63	$814 \pm 11$	$512 \pm 24$	0.63	3.96
108	$226 \pm 3$	$132 \pm 5$	0.58	$894 \pm 11$	$525 \pm 22$	0.59	3.96

**Table 5.6:** Calibration summary of the station with Id 1764. We show the mean charge per muon ( $\bar{Q}_1$ ), the resolution for one muon ( $\sigma_1$ ), the relative fluctuation per muon ( $\frac{\sigma_1}{\bar{Q}_1}$ ), and the ratio between the low- and high-gain channels ( $\frac{\text{HG}}{\text{LG}}$ ) for both  $5\text{ m}^2$  (101, 102, 105, 106) and  $10\text{ m}^2$  modules (103, 104, 107, 108). This results are extracted from Fig. 5.12 (Table 5.4) and 5.14 (Table 5.5). Units of the mean charge per muon ( $\frac{\bar{Q}}{\mu}$ ) are  $\frac{\text{ADC counts}}{\mu}$  and for the resolution ( $\sigma_1$ ), ADC counts.

Module Id	LG (ADC counts)		HG (ADC counts)	
	$\mu$	$\sigma$	$\mu$	$\sigma$
101	$0 \pm 1$	$29 \pm 1$	$1 \pm 3$	$106 \pm 3$
102	$-1 \pm 1$	$28 \pm 1$	$-2 \pm 3$	$104 \pm 2$
103	$-0 \pm 1$	$31 \pm 1$	$0 \pm 4$	$117 \pm 3$
104	$-0 \pm 1$	$31 \pm 1$	$-1 \pm 4$	$111 \pm 3$
105	$-0 \pm 1$	$30 \pm 1$	$1 \pm 3$	$105 \pm 2$
106	$-1 \pm 1$	$29 \pm 1$	$-5 \pm 3$	$105 \pm 2$
107	$1 \pm 1$	$25 \pm 1$	$4 \pm 4$	$90 \pm 2$
108	$1 \pm 1$	$27 \pm 1$	$-4 \pm 3$	$95 \pm 3$

**Table 5.7:** Results of the baseline histogram fit from Fig. 5.15 for all modules in the station with Id 1764.

modules (103, 104, 107, 108), which was expected since the light attenuation is higher in  $10\text{ m}^2$  modules. This difference is 30% for the North twin and 15% for the South twin. When  $N = 1$ , the average relative fluctuations is 0.54 for  $5\text{ m}^2$  and 0.63 for the  $10\text{ m}^2$ , thus relative fluctuation for  $5\text{ m}^2$  modules is lower than for  $10\text{ m}^2$  modules, also expected, as  $10\text{ m}^2$  have more charge dispersion due to fiber attenuation and less light-output. Finally, the average ratio between the high- and low-gain channels is 3.96 (with less than 1% fluctuation), which denotes that the difference in amplification between the low- and high-gain is stable.

As a remark, we have mentioned before that the baseline fluctuations (mainly produced by the SiPM dark rate), leads to significant fluctuations on the ADC signal, which has an impact on the estimation of the signal charge. In Fig. 5.15, we present the baseline histograms (after removing the offsets) of all modules in the station with Id 1764 for the low- (top panel) and high-gain (bottom panel) channels. The baselines were calculated using only events where the number of muons estimated by the binary channel was 0. We summarized the results of the Gaussian fits in Table 5.7. The baseline charge is integrated within a 100 ns windows (the mean width of a single muon in the ADC, as shown in section 5.1.2). From Table 5.6, the single muon charge distribution overlaps with the baseline histograms, which denotes the importance of using the binary channel to identify when a particle is injected in the detector, mainly when the number of particles is low. These results are compatible with the laboratory data presented in section 5.1.2.

#### 5.2.4 Test and discussion

To test and verify this calibration method, we analyzed a new data set from 01-July-2017 to 31-July-2017, from which we obtained the number of muons measured with the ADC channel by normalizing the signal charge with the mean charge of a single muon, obtained from the calibration accomplished in section 5.2.3. To validate this analysis, we compared the number of muons estimated both with the binary and the ADC channels. If the calibration is consistent, the mean values of both estimations should agree. To illustrate this, we present in Fig. 5.16 the number of muons obtained with the ADC channel as a function of the number of muons obtained with the binary channel. We plotted in the top (bottom) panels the results for the low-gain (high-gain) channel and in the left (right) panels the results for

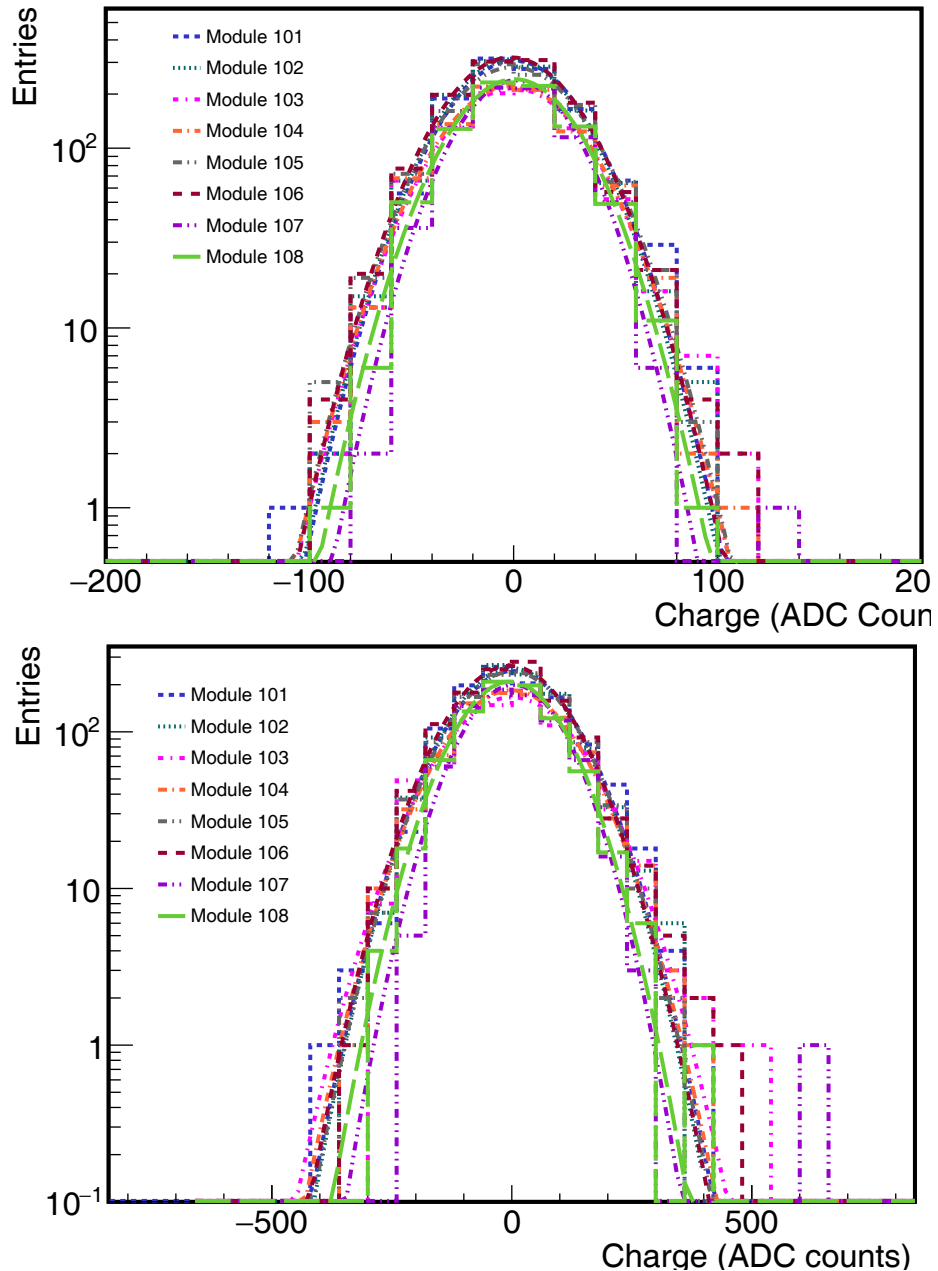


**Figure 5.15:** Baseline histograms for all modules in the station with Id 1764. We show in the top (bottom) panel the histograms of the low-gain (high-gain) channel. The results of the Gaussian fits are summarized in Table 5.7.

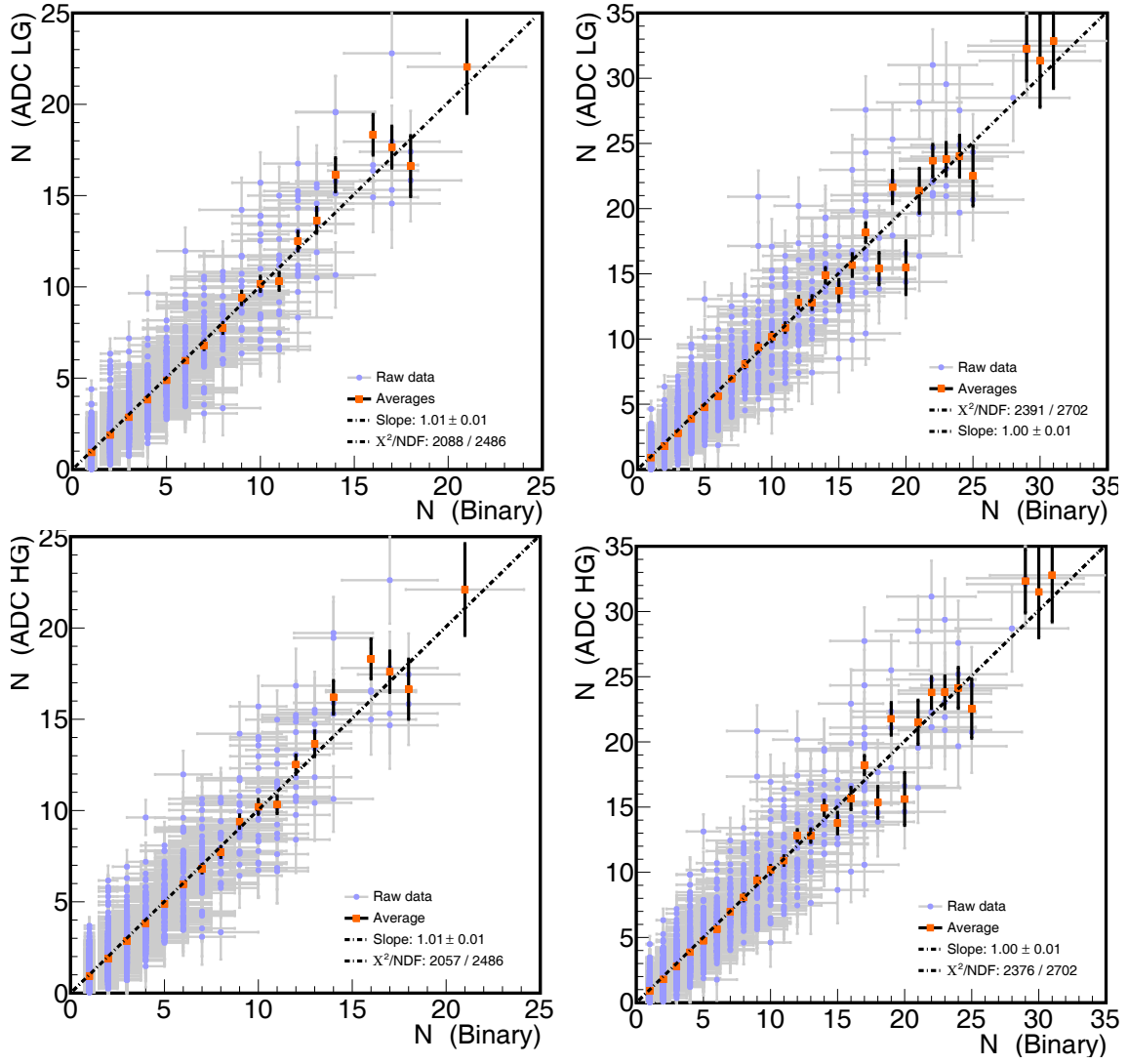


**Figure 5.16:** Comparison between the number of muons estimated with the binary and the ADC channels. In the top (bottom) panels we display the results obtained with the low-gain (high-gain) channels, and in the left (right) panels, we show the results for the  $5$  ( $10 \text{ m}^2$ ) modules. In all cases the fits approximate an identity function. The results of the fits per module are summarized in Table 5.8.

the  $5$  ( $10 \text{ m}^2$ ) modules. We fitted the individual events using a linear function and the fit results are summarized in Table 5.8. In all cases, the fits approximate to an identity function, which means that the estimations with both binary and ADC channels, and therefore the calibration, are consistent.

We have also analyzed the relative fluctuations as in section 5.2.2, but with the normalized signals. In the same way, we created histograms of the signal charge in the ADC channel for each  $N$  estimated with the binary trace. We then plotted  $\sigma_N$  calculated with equation 5.3 as a function of the  $N$  in Fig. 5.17. We extracted the  $\sigma_1$  parameter of the error model by fitting the data in with a  $\sigma_1 \sqrt{N}$  function. The  $\sigma_1$ s obtained in this test are consistent with the results inferred from Table 5.6 ( $\frac{\sigma_1}{Q_1}$ )

With this calibration method, we have estimated the mean charge per muon in the ADC channel and its resolution using shower events. However, to achieve this calibration we have used the binary channel without implementing corrections such as clipping corners or signal

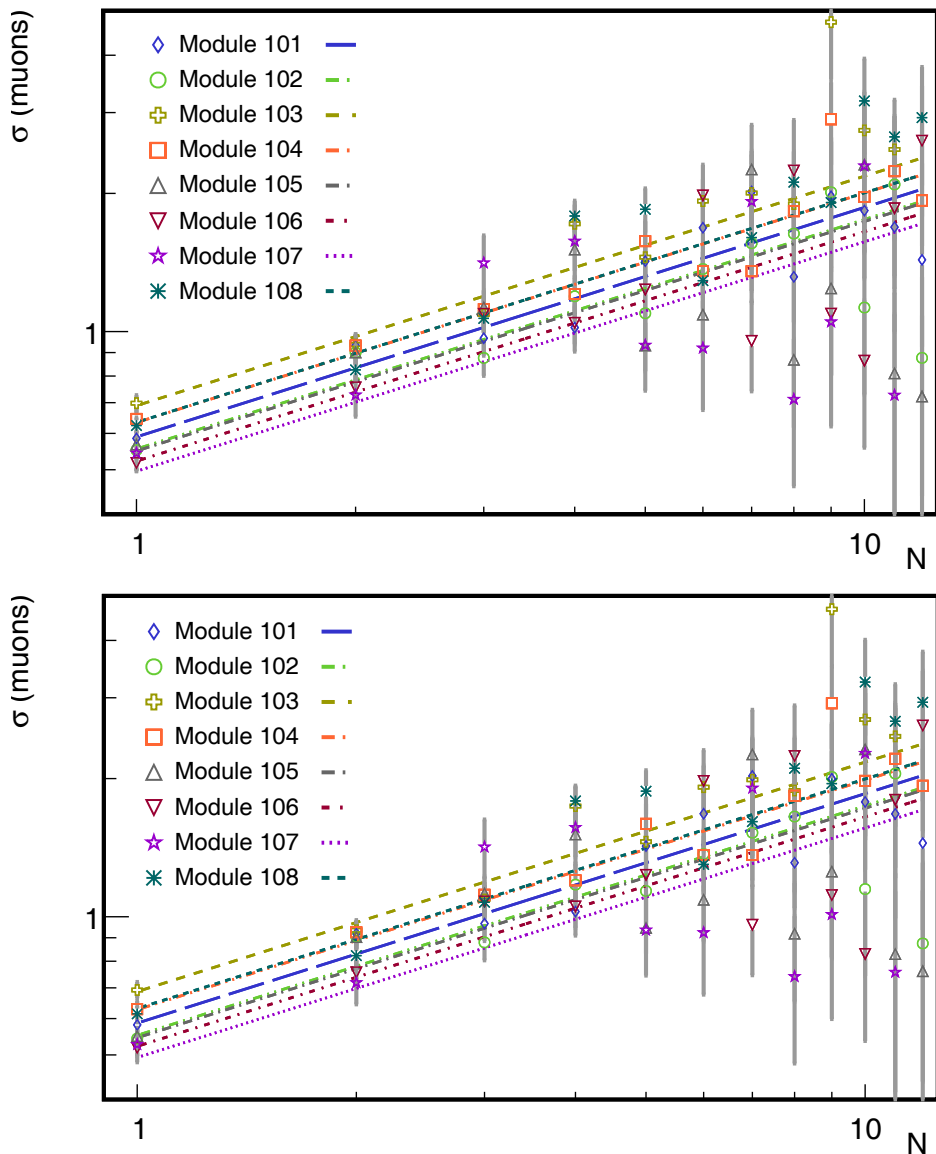


**Figure 5.17:**  $\sigma$ s of the normalized low- (top panel) and high-gain (bottom panel) ADC signals as a function of the  $N$  estimated with the binary channel. We have fit the  $\sigma_1$  parameter of the error model (section 5.2.2) with a  $\sigma_1\sqrt{N}$  function. The results of the fits are summarized in Table 5.8.

Module Id	LG		HG	
	$\sigma_1$	Slope	$\sigma_1$	Slope
101	$0.59 \pm 0.02$	$1.03 \pm 0.02$	$0.59 \pm 0.02$	$1.02 \pm 0.02$
102	$0.55 \pm 0.02$	$0.99 \pm 0.02$	$0.55 \pm 0.02$	$0.99 \pm 0.02$
103	$0.69 \pm 0.02$	$1.02 \pm 0.02$	$0.69 \pm 0.02$	$1.02 \pm 0.02$
104	$0.63 \pm 0.02$	$0.97 \pm 0.02$	$0.63 \pm 0.02$	$0.97 \pm 0.02$
105	$0.54 \pm 0.02$	$1.02 \pm 0.02$	$0.54 \pm 0.02$	$1.01 \pm 0.02$
106	$0.52 \pm 0.01$	$0.99 \pm 0.02$	$0.52 \pm 0.01$	$0.99 \pm 0.02$
107	$0.50 \pm 0.03$	$0.95 \pm 0.03$	$0.49 \pm 0.03$	$0.95 \pm 0.03$
108	$0.63 \pm 0.02$	$1.03 \pm 0.02$	$0.63 \pm 0.02$	$1.03 \pm 0.02$

**Table 5.8:** Fit results of the tests performed to validate the consistency of the offline calibration. We show the  $\sigma_1$  from the error model fitted in Fig. 5.17 and the slopes fitted in Fig. 5.16.

pile-up (see chapter 8). Nevertheless, these corrections would only improve the number of muons estimated with the binary traces, and are not expected to have a qualitative impact in the ADC calibration.

### 5.2.5 Resolution

When estimating the muon density ( $\rho_\mu$ ) of air showers, the uncertainties are dominated by the Poissonian fluctuation in the muon content and, to a lesser extent, the detector resolution to the number of injected particles [106]. We can then consider the standard deviation of a Poissonian distribution with parameter N to be  $\sqrt{N}$  and the detector resolution (as described in section 5.2.2) to be  $\sqrt{N}\sigma_1$ . To estimate the uncertainties when measuring the muon densities with the ADC channel we can add these two contributions in quadrature:  $\sqrt{N + N\sigma_1^2} = \sqrt{N(1 + \sigma_1^2)}$ , then  $\sigma_N = \sqrt{N(1 + \sigma_1^2)}$ , and therefore  $\frac{\sigma_N}{N} = \frac{\sqrt{N(1 + \sigma_1^2)}}{N} = \sqrt{\frac{(1 + \sigma_1^2)}{N}}$ . As  $\sigma_1 \sim 0.59$ , it is apparent how the uncertainty is dominated by the Poissonian contribution. Furthermore, if  $N = 1$ , then  $\sigma_{N_1} = \sqrt{\frac{1+0.35}{1}} \simeq 1.16$ , which means that the integrator resolution adds  $\sim 20\%$  to the total resolution of an ideal Poissonian detector. To illustrate this, we show in Fig. 5.18, the relative uncertainties for the low- and high-gain channels as a function of N.

### 5.2.6 Example of a calibrated event

As illustration, in Fig. 5.19, the muon densities measured with the binary and calibrated ADC channel for an example event with a reconstructed energy of  $(9.5 \pm 0.4 \pm 0.2) \times 10^{17}$  eV and zenith angle of  $(21.8 \pm 0.4)^\circ$  is displayed as a function of the muon detector distance to the shower core. The geometry and energy were obtained from the SD-750 reconstruction [107]. The muon lateral distribution function (MLDF) [108] was fitted using only the *counter* mode. Note that the reconstruction of data with the two modes is not expected to entirely agree at this point, as the final corrections for different sources of bias (from clipping corners, noise, etc. [109]) are not yet implemented. Still, it is apparent that both muon-density estimations are quite consistent for this example event.

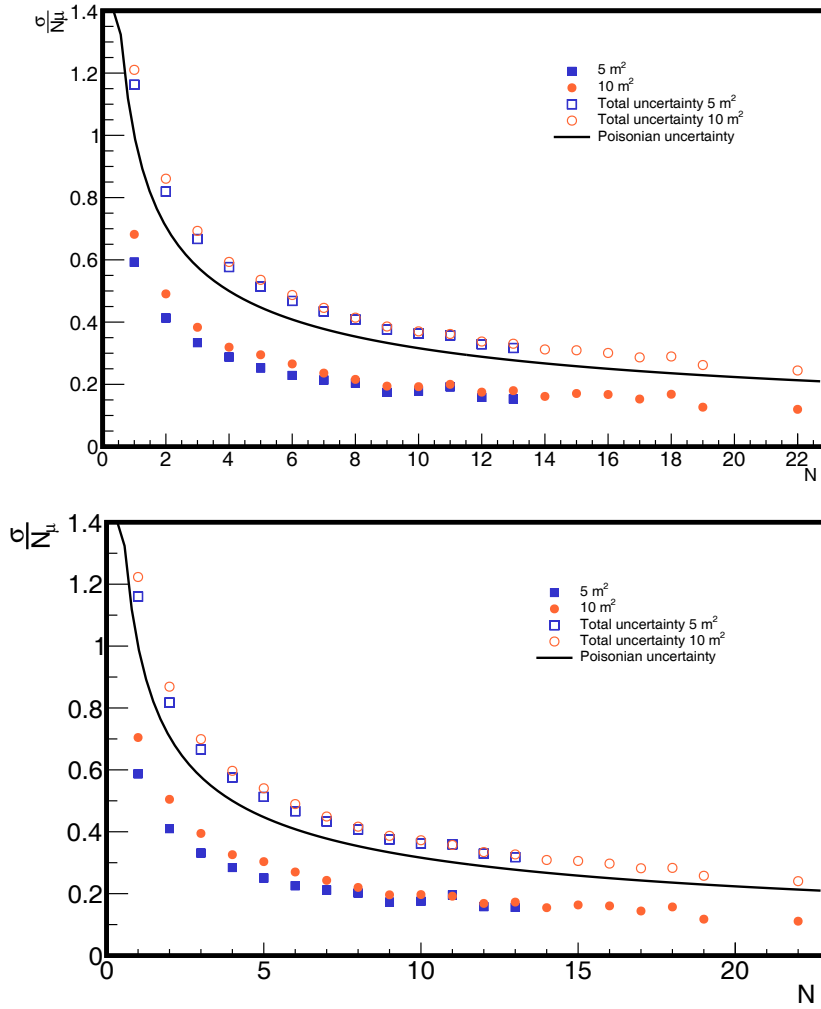


**Figure 5.18:** Relative uncertainties for the low- (top) and the high-gain (bottom) channels. We display the Poissonian uncertainty along with the integrator resolution and the addition in quadrature of both uncertainties. The Poissonian uncertainty dominates in the whole range.

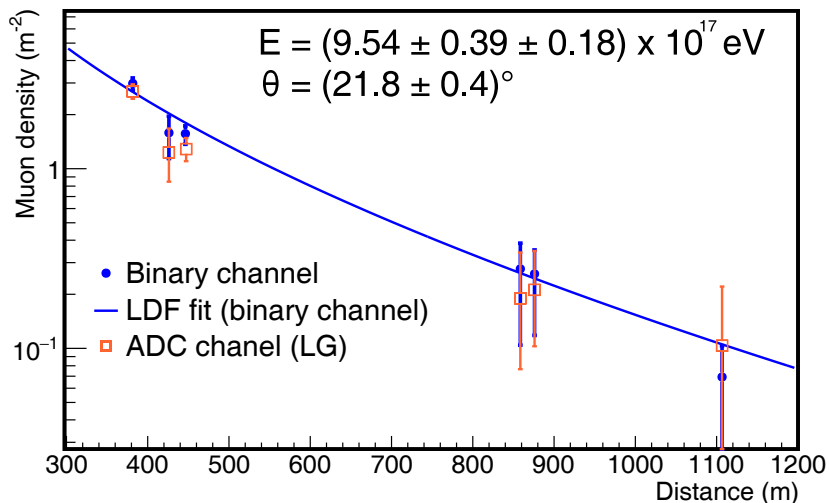


**Figure 5.19:** Muon lateral distribution function reconstructed with the binary channel for an example event. The muon densities estimated with the ADC channel are also shown.

## 5.3 Online calibration with background events

In the previous section, we showed how to achieve the ADC channel calibration using the binary traces of shower events. In this section, we discuss the possibility of accomplishing an online end-to-end calibration using background data. One of the main challenges is that the UMD modules cannot be self-triggered, and therefore, it depends on the WCD T1 triggers. Each event is stored only after the T3 condition is met [47], meaning that all the first level triggers (T1), mostly background, are discarded if they are not promoted to T3.

### 5.3.1 Data set selection

For the purpose of testing, we used the module with Id 101 of the station with Id 93, which has been removed from its normal operation in August 2018. The module was set to automatically promote T1s into T3s, so background events are stored. The expected rate of these T1 is  $\sim 100$  Hz [47]. To avoid bandwidth issued, we stored 1 event per second (1 Hz) during 100 hours to gather the equivalent of one hour of all T1s (360000). We extract this data set to analyze if a MIP histogram can be built out of this background data. In Fig. 5.20 top panel, the 360000 binary traces are displayed. Positive samples produced by background (see section 4.3) are randomly distributed all along the trace, and still, an accumulation of signal is located around the trigger scope. We denote the sample time where the maximum accumulation is located as the *latch bin*. In the bottom panels of Fig. 5.20 the ADC low-(middle) and high-gain (bottom) raw traces are displayed. As expected, most of the events consist only of the baseline, since in most of T1 events, the signal in the WCD is uncorrelated to the signal in the UMD. However, as in the binary channel, we observed accumulation of signal around the trigger scope, along with randomly distributed noise peaks. A few shower signals were also detected, which produced undershoot.

To determine when a muon impinges on the detector, we need to analyze the signal timing. The top panel of Fig. 5.21 displays the binary channel start time, which is defined as the first positive sample in the binary traces. In the middle panel, we show the time of the maximum signal amplitude in the ADC channel. The exponential decay at the beginning of the histogram is a consequence of the ADC amplitude resolution. In events with only baseline, the maximum amplitude value is recurrent several times along the trace. As we select the first sample that reaches the signal maximum to entry the histogram, there are more entries at the beginning of it than at the end. In the bottom panel of Fig. 5.21 the delay between the binary-channel start time (top panel) and the maximum amplitude time in the ADC channel (middle panel) is shown. The mean delay ( $\mu$ ) and standard deviation ( $\sigma$ ) in the low-gain channel is  $\mu = (183.84 \pm 0.05)$  ns and  $\sigma = (7.50 \pm 0.05)$  ns and  $\mu = (185.07 \pm 0.04)$  ns and  $\sigma = (6.97 \pm 0.04)$  ns in the high-gain channel. The difference between low- and high-gain is within the ADC sample time (6.25 ns). The mean delay between the binary channel and ADC channel is stable and can be used to narrow the integration window in the ADC to the muon signal once the binary channel start time is located. This result is expected, as the delay between channels is due to the different time response of the electronics components.

### 5.3.2 Integration windows

Since the rate of background particles underground in the T1 events is low, it is necessary to remove the background noise to avoid biases in the calibration. As explained in section 4.3, it is not possible to entirely reject the background noise with a counting strategy. Furthermore, the noise signals, probably produced by spontaneous light emission from the optical fibers [96], are almost indistinguishable from muons. If we look into a time window around

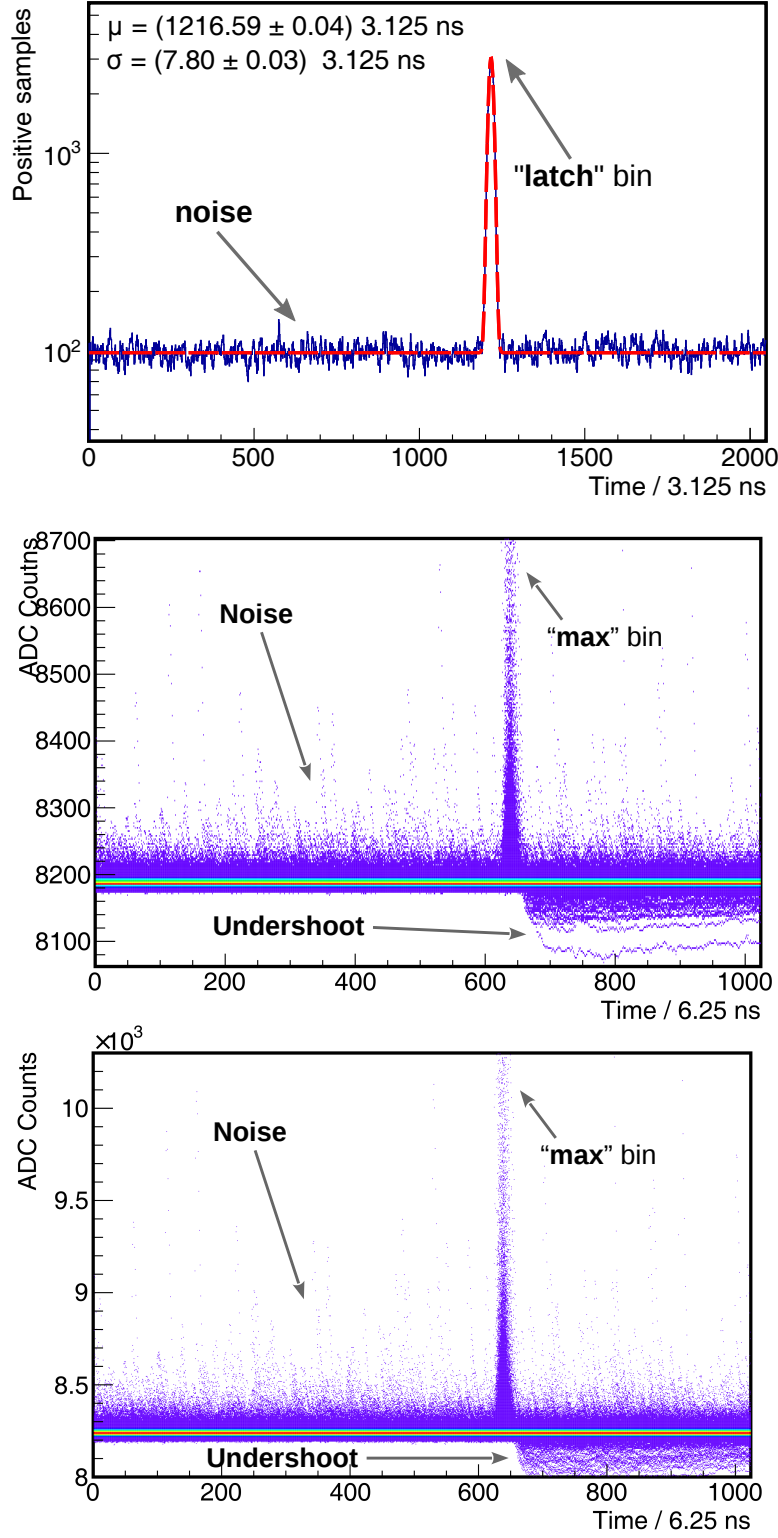


**Figure 5.20:** (Top) binary channel raw traces. Signal accumulation around the trigger scope is observed. Randomly distributed entries produced by background noise are also observed. (Middle) raw traces of the ADC low- and (bottom) high-gain channels. Analogously to the binary channel, accumulation of signal can be found within the shower scope, along with randomly distributed noise. A few pulses with undershoot produced by shower events were identified

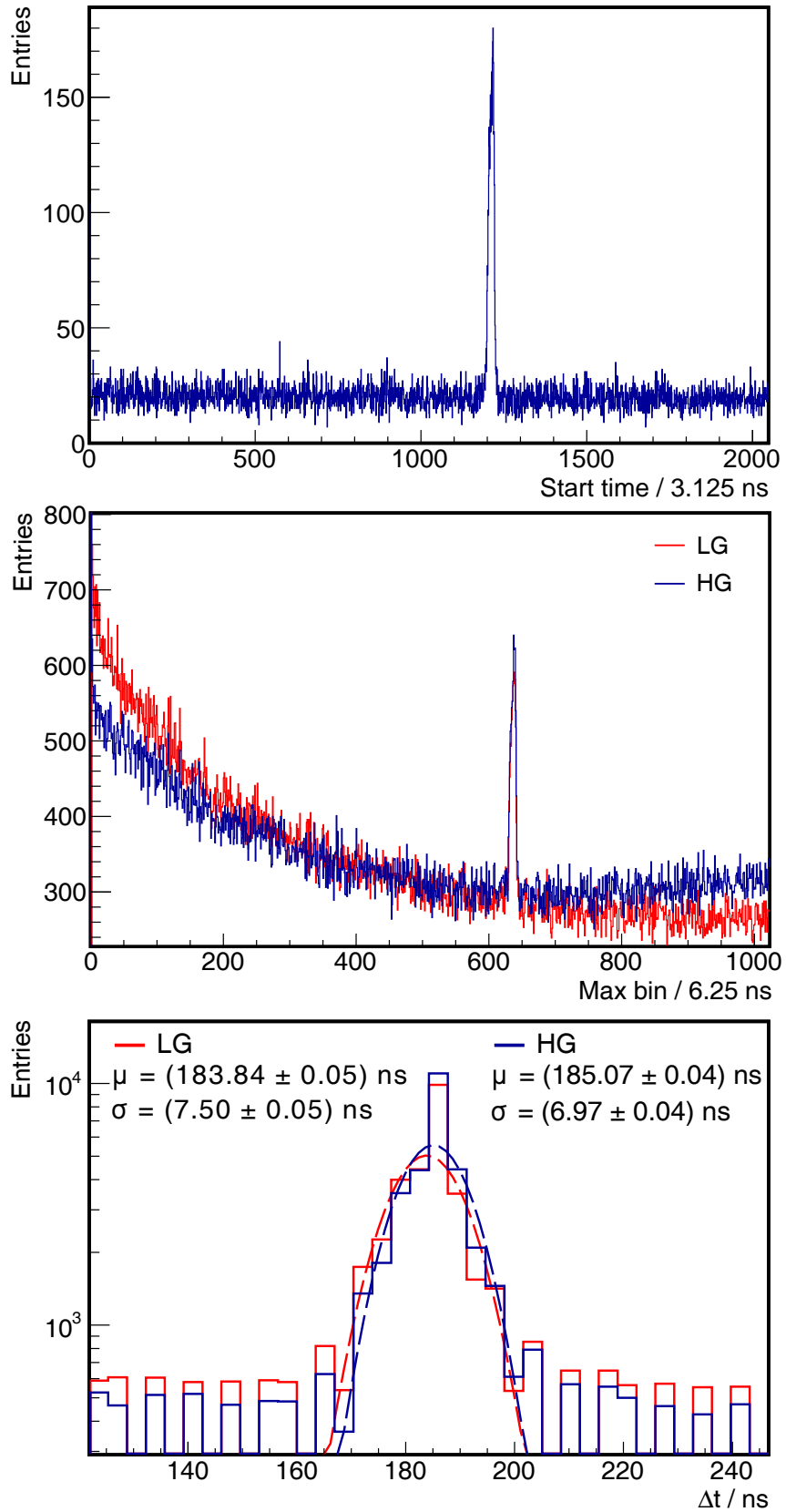


**Figure 5.21:** (Top) signal start time of the binary channel, defined as the first "1" in the trace. (Middle) time of the maximum signal amplitude in the ADC channel. (Bottom) difference between the binary channel start time and the maximum signal amplitude in the ADC. From the fits, it was obtained that this difference is stable with  $\sim 7.24$  ns fluctuation, which correspond to  $\sim 1$  sample of the ADC (6.25 ns).

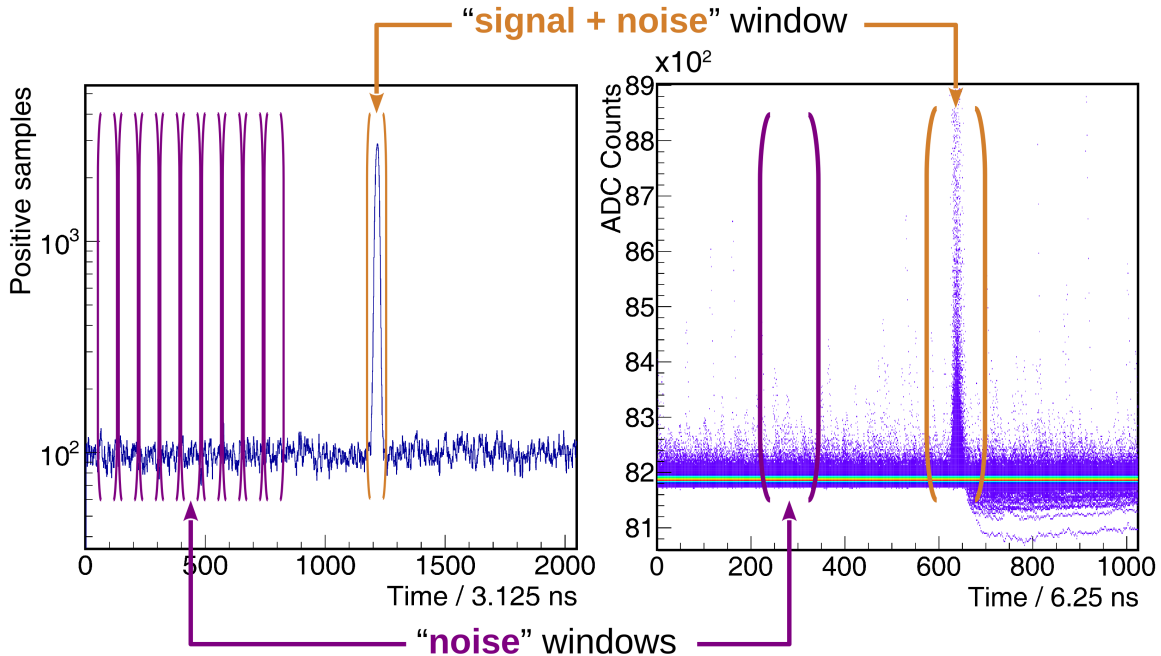


**Figure 5.22:** Schematics of the procedure to extract the signal charge from the T1 traces. First, the muon condition is searched around the *latch* bin of the binary channel. Once the condition is met, the signal in the ADC channel is integrated within a 200 ns window around the signal maximum amplitude. Since these signals also includes noise, we repeat the same analysis away from the trigger scope to obtain the charge of the noise signals. The noise is average within ten windows to improve statistics.

the trigger scope, we would be including both muon and noise events. To subtract this noise, we consider windows away from the trigger scope, as it is shown in Fig. 5.22, which will only contain noise. Understanding this noise is the key to obtain an unbiased calibration, and therefore, in this analysis, we have averaged ten ‘noise’ windows (instead of one) to improve the statistics.

To obtain the signal charge in the ADC, we first search for muons in a window around the *latch* bin of the binary traces (see Fig. 5.20 top). The criteria to determine when a particle is injected is explained in 4.4.1, and consists of finding a sequence of positive samples in the binary channel with more than four “1”s and less than twelve. Once the muon condition is satisfied, we integrate the ADC signal around the time of the maximum signal amplitude. This time is located knowing the muon start time plus the mean delay from Fig. 5.21 bottom. To extract the signal charge, we use an integration window of 200 ns corresponding to the  $3\sigma$  deviation from the mean width of a single muon (see 5.6). We repeat the same procedure in the “noise” windows, to obtain the charge of the noise signals.

The next step towards an unbiased ADC calibration is to choose an optimal window size. Narrowing the windows shown in Fig. 5.22 will reduce the number of noise events, however, this will also reduce the number of signal events. To illustrate this effect, we show in Fig. 5.23 top panel, the number of events, of both “noise” and “signal + noise”, as a function of the

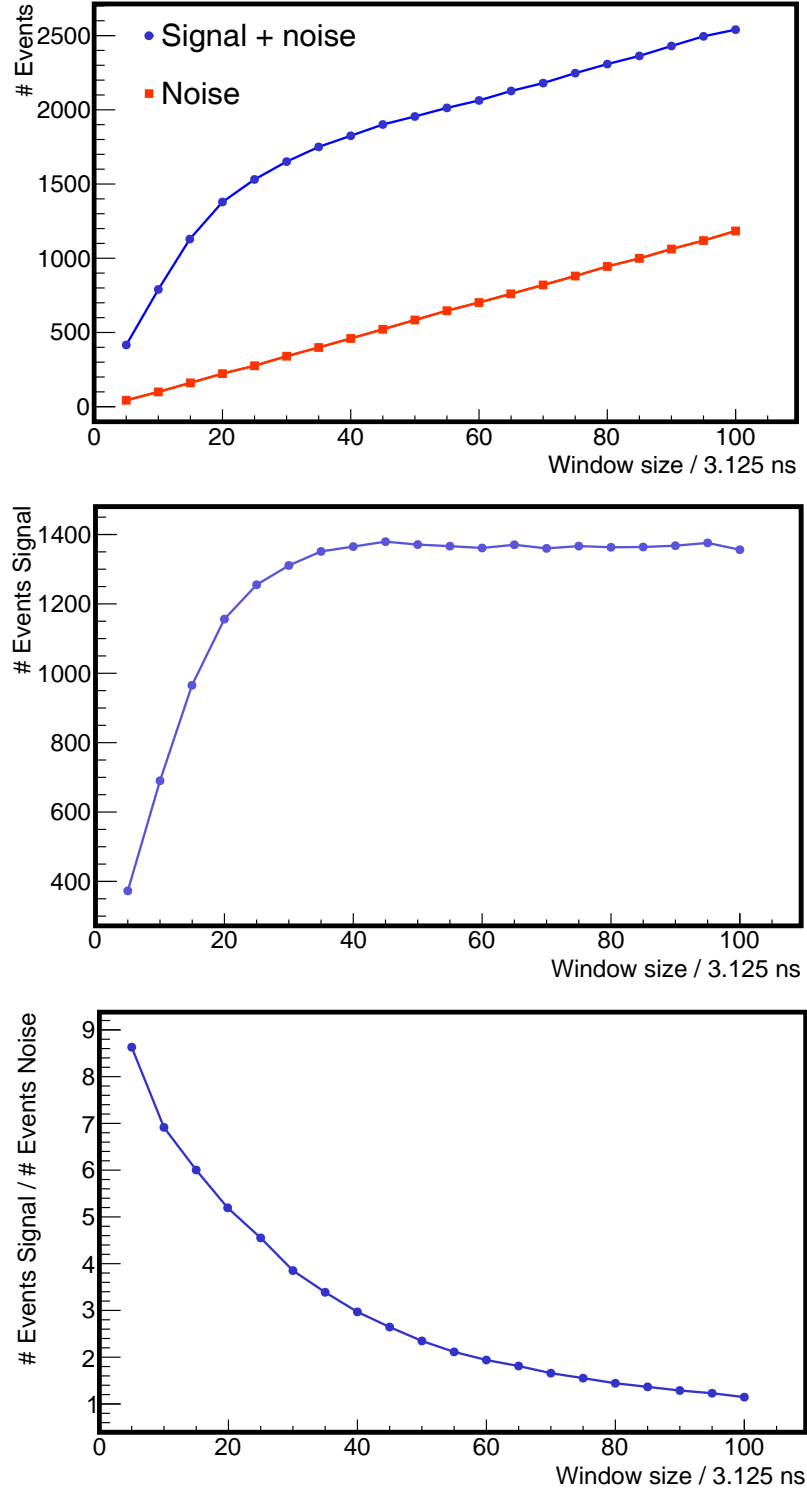


**Figure 5.23:** (Top) number of events in both “noise” and “signal + noise” windows as illustrated in Fig. 5.22. The two curves become parallel when the signal events are completely contained in the “signal + noise” window. (Middle) difference between the number of “noise” and “signal + noise” events. The difference becomes constant once all signal events are contained in the window. (Bottom) ratio between the number of signal events and noise events. The signal-to-noise ratio decreases when enlarging the window size, although the number of signal events increases.

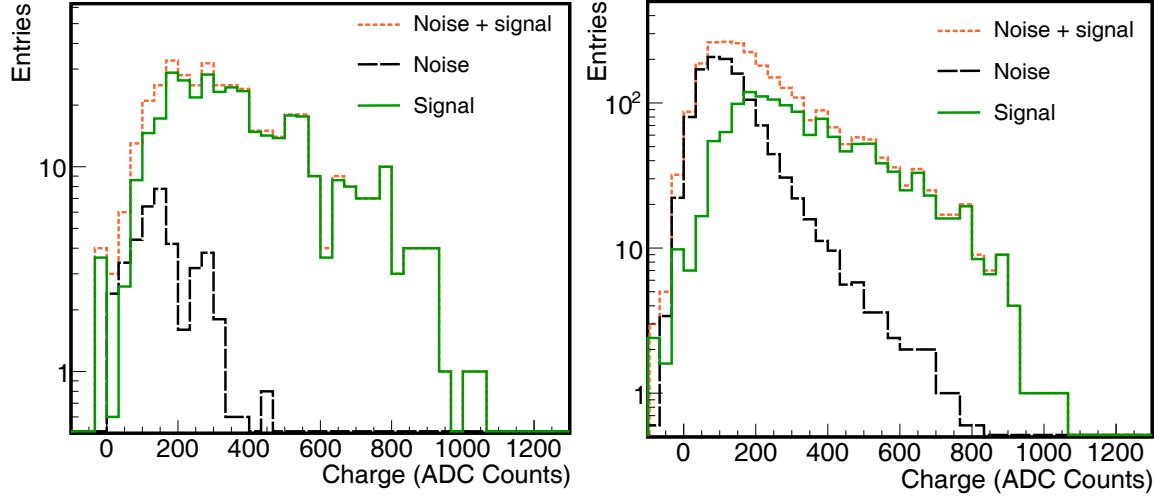


**Figure 5.24:** Charge histograms with a window size of 5 (left) and 100 (right) samples. We show the results of both “noise” and “signal + noise” windows. The “signal” histogram is built by subtracting the “noise” to the “signal + noise”. It is apparent how the number of events increments with the window size.

window size. As there are no muon signals in the noise window, the number of events grow linear with the window size, contrary to the “signal + noise” window. In this case, when the window size is rather small the number of events can grow both with muon and noise signals. When the window size is bigger than  $\sim 35$  samples, all the muon signal is contained in this window and the number of events can only grow with noise. At this point, the “noise” and “noise + signal” curves become parallel and the difference between them becomes constant. In Fig. 5.23 middle panel, we show the difference in the number of events between the “noise” and “noise + signal” windows, which results in the number of “signal” events. For windows smaller than 35 samples, the number of signal events increases with the window size; when all the signals are contained in the window, the curve becomes constant. In the bottom panel in Fig. 5.23, we present the ratio between the number of signal events and noise events. Enlarging the window size increments the number of signal events, but also decreases the signal-to-noise ratio, which asymptotically tends to 1 with the window size. Choosing a window size results from maximizing this ratio, but conserving enough statistics to have a suitable calibration histogram.

To demonstrate the effects of the window choice on the statistics, we present in Fig. 5.24 the charge histograms for a window size of 5 (right panel) and 100 (left panel) samples for both “noise” and “signal + noise” windows. By subtracting the “noise” to the “signal + noise” histogram, we built the “signal” histogram, from which the mean charge of a muon can be extracted. When we enlarge the window size, the number of signal events increases, but the number of noise events increases significantly more, and therefore, the signal-to-noise ratio is reduced. With a 5 sample window, the “signal” histogram is very similar to the “signal + noise” histogram, meaning that few noise events are being included in the “signal + noise” window. Negative entries are produced mainly by noise in the part of the trace used to calculate the baseline offset. If a noise signal occurs within this region, the whole signal is shifted to negative values.

<b>Module Id</b>	<b>LG</b>		<b>HG</b>	
	<b>Noise</b>	<b>Signal</b>	<b>Noise</b>	<b>Signal</b>
$\mu$	$4.82 \pm 0.07$	$5.69 \pm 0.02$	$6.12 \pm 0.06$	$7.05 \pm 0.02$
$\sigma$	$0.69 \pm 0.09$	$0.62 \pm 0.02$	$0.71 \pm 0.05$	$0.65 \pm 0.02$
$E[X]$ (ADC counts)	$157 \pm 9$	$358 \pm 17$	$586 \pm 14$	$1420 \pm 30$
$SD[X]$ (ADC counts)	$123 \pm 6$	$245 \pm 12$	$477 \pm 10$	$1027 \pm 21$

**Table 5.9:** Results for the charge histograms of the low- and high-gain channels presented in Fig. 5.25 with a window size of 20 samples. We show the results of both noise and signal.

### 5.3.3 Mean charge and standard deviation

To obtain the mean and standard deviation we fitted the charge histograms with a log-normal function as in equation 5.2. From the log-normal function, we can extract the arithmetic mean and standard deviation from the  $\mu$  and  $\sigma$  parameters as

$$E[X] = \exp(\mu + \frac{1}{2}\sigma^2), \quad (5.4)$$

$$SD[X] = \exp(\mu + \frac{1}{2}\sigma^2) \sqrt{\exp(\sigma^2) - 1} \quad (5.5)$$

As we mentioned before, to improve statistics we average ten “noise” windows. To corroborate the consistency of the analysis, we obtained the signal charge using the averaged noise and using each of the ten individual noise histograms. In Fig. 5.25, we show the histograms for a 20-sample window in the low- (top panel) and high-gain (middle panel) channels and the corresponding fits. In green, we display the fit of the signal histogram obtained using the averaged noise. In pink, we present the fits of the signal histograms obtained using each of the individual noise histograms (not plotted). It is worth to notice that the fits using the individual noise histograms (pink) do not deviate significantly from the fit using the averaged noise histogram (green). To illustrate this effect, we plotted in Fig. 5.25 bottom panel the bias as a function of the window size. We defined the bias as

$$\frac{\sum_{i=1}^{10} E[X_i] - E[X]_{\text{average}}}{E[X]_{\text{average}}} \text{ for the mean and}$$

$$\frac{\sum_{i=1}^{10} SD[X_i] - SD[X]_{\text{average}}}{SD[X]_{\text{average}}} \text{ for the standard deviation,}$$

where  $\frac{\sum_{i=1}^{10} E[X_i]}{10}$  is the averaged mean charge obtained using each of the individual noise histograms and  $E[X]_{\text{average}}$  is the mean charge obtained using the averaged noise (the same applies to the standard deviation). Both  $E[X]$  and  $SD[X]$  are estimated as in equation 5.5. The bias is in all cases below 2% which demonstrates that the noise estimation we are using is robust. In table 5.9 we summarized the results of the fits for both noise and signal of the histograms displayed in Fig. 5.25. The mean ( $E[x]$ ) and standard deviation ( $SD[X]$ ) are also shown.

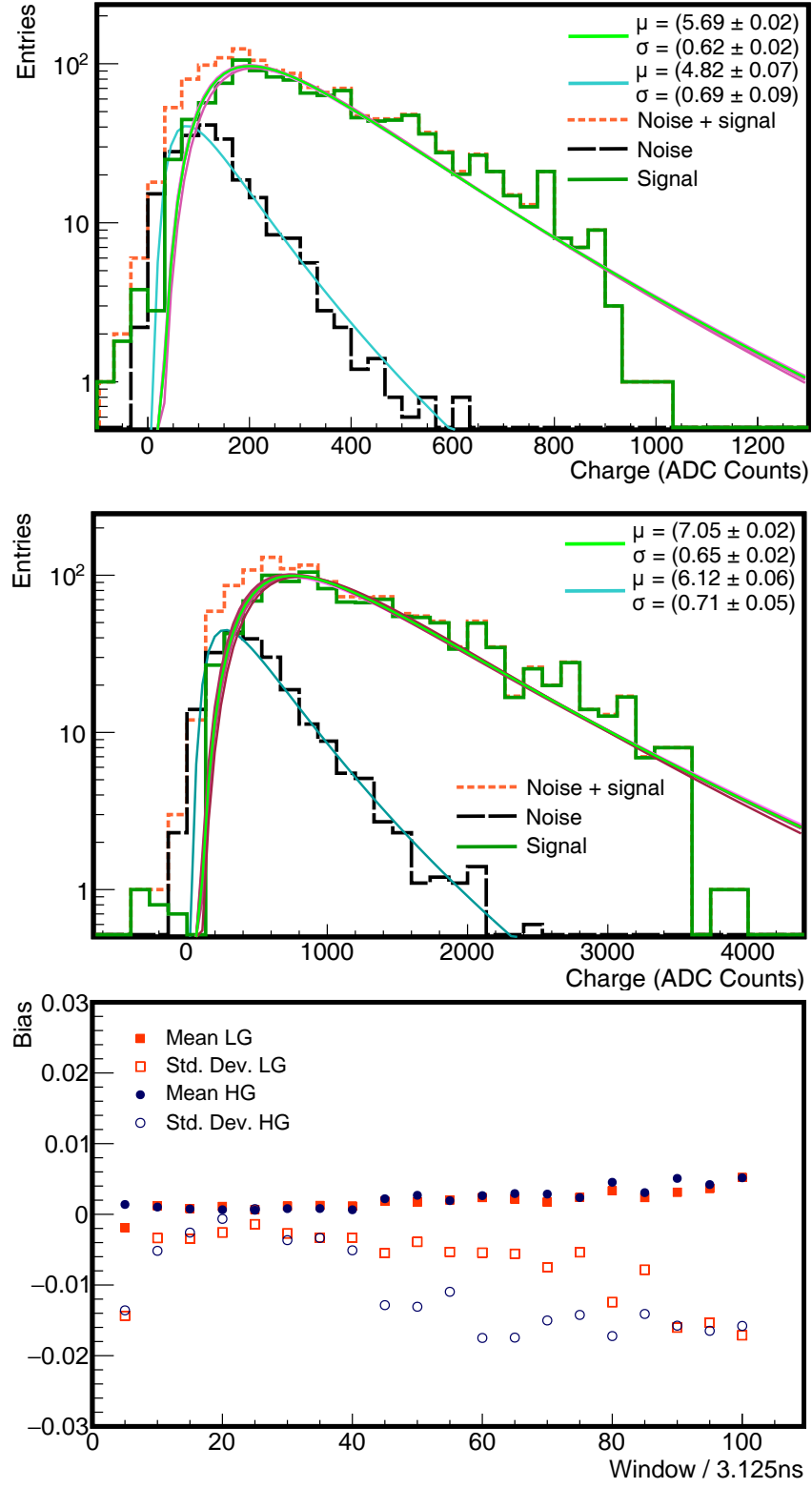


**Figure 5.25:** Low- (top) and high-gain (middle) charge histograms for a window size of 20 samples. We show the log-normal fits of the signal and noise histograms using the averaged noise. In pink, we also display the fits using each of the individual noise windows instead of the averaged noise. We summarized the fits results in Table 5.9. (Bottom) bias of the signal mean charge and standard deviation using the averaged noise and each of the individual noise histograms.

To assess the impact of the window choice on the estimation of the signal charge, we show in the top panels of Fig. 5.26 the signal mean charge and standard deviation obtained for different windows in the low- (left) and high-gain (right) channels. It is apparent how for windows smaller than  $\sim 20$  samples, the mean and standard deviation decreases with the window size. When the window is too small (i.e. 5 samples), it is likely that some of the “1”s of the binary trace are not contained in the window. Short signals, such as those with only four ones, need to fall in the middle of the window to meet the 1111x request from the counting strategy, meaning that low-charge events tend to be rejected. For the same reason, small windows tend not to reject large signals, as it is unlikely to have all its “1” contained in the window, and will unlikely surpass the twelve “1”s limit from the counting strategy. These two effects bias the estimations of the mean charge to higher values. For a window of 20 samples, the value of the mean charge and standard deviation starts to stabilize, while the signal-to-noise ratio (seen in Fig. 5.23) is still above 20%. For this reason, we have chosen a window size of 20 samples to perform this online calibration. In Fig. 5.26 bottom panels, we show the ratio between the mean charge and the mean charge estimated with the 20 sample window ( $\text{Mean}_{20}$ ). There is  $\sim 4\%$  shift in the mean charge to respect with  $\text{Mean}_{20}$  when using windows bigger than 20 samples.

### 5.3.4 Calibration stability

To verify the stability in time of the proposed online calibration, we have repeated the analysis previously described with  $\sim 2$  months of T1 data. We have created subsets of 360000 events, each of which is equivalent to one hour of all T1 events, or 100 hours of T1s in the current configuration. The results are shown in Fig. 5.27, in which we show the mean charge for the low- and high-gain channels in a time line. The first data point corresponds to the data we have used in the previous analysis. There is a gap between the end of September and the end of December produced by an acquisition issue. The mean charge obtained for the whole period is  $(373 \pm 4)$  ADC counts and  $(1502 \pm 21)$  ADC counts for the low- and high-gain channels respectively with an RMS of  $(14 \pm 3)$  ADC counts and  $(75 \pm 15)$  ADC counts. This implies a mean fluctuation of less than 4% in the whole analyzed period, which denotes a stable calibration. Still, it is necessary to verify this stability among seasonal fluctuations. We expect to continue this analysis to search for modulations during the year.

To calibrate the ADC, we depended on the binary channel, and therefore, on its counting strategy. Until this point, we have used in this analysis the strategy explained in section 4.4.1. However, to verify the robustness of this method, we need to check the calibration stability under changes in this strategy. To this aim, we have plotted in Fig. 5.28 the number of signal events as a function of the window size for different matching patterns (111x, 1111x, 11111x). It is apparent how the number of signal events increases when relaxing the condition to count muons since more signals match the counting pattern. In each case, the mean charge obtained is  $(353 \pm 7)$  ADC counts,  $(358 \pm 7)$  ADC counts, and  $(363 \pm 7)$  ADC counts for each of the patterns respectively. These results show that the calibration is consistent for the different strategies. This approach could be used in the future for long time performance studies. The signal loss when changing the matching pattern should remain stable, unless some effect, such as material aging, produces more signal loss than expected.

### 5.3.5 Module-to-module optimization

As this calibration depends on the signal timing, we need to analyze how to optimize it for all the UMD modules. The difference in the timing is mainly due to the time that takes to

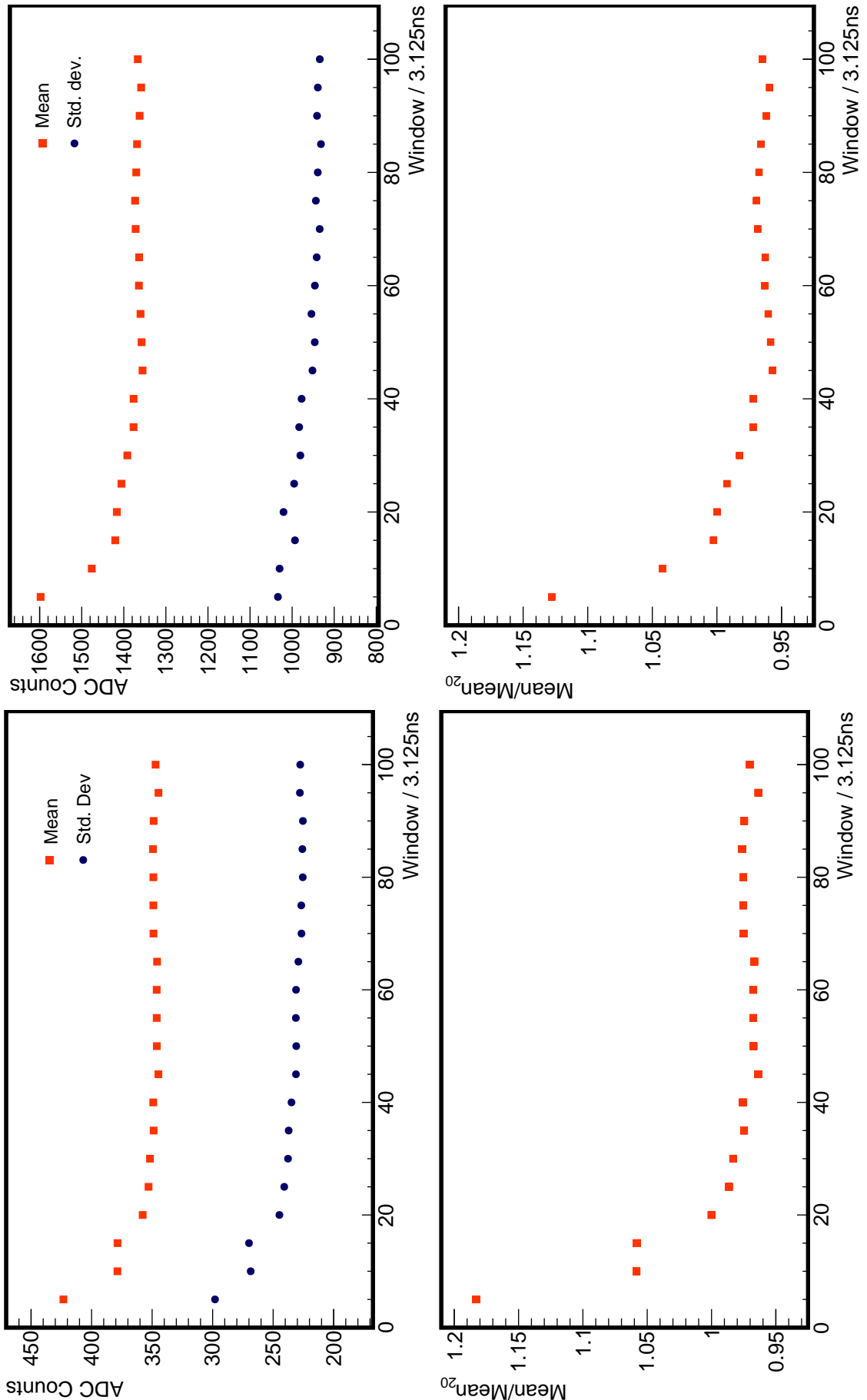


**Figure 5.26:** Charge mean and standard deviation as a function of the window size for the low- (left) and high-gain (right) channels. The mean and standard deviation start to become stable at  $\sim 20$  samples. In the bottom panels, we show the ratio between the mean charge and the mean charge with a window of 20 samples ( $\text{Mean}_{20}$ ). The mean charge estimated with windows bigger than 20 samples is shifted  $\sim 4\%$  from  $\text{Mean}_{20}$ .

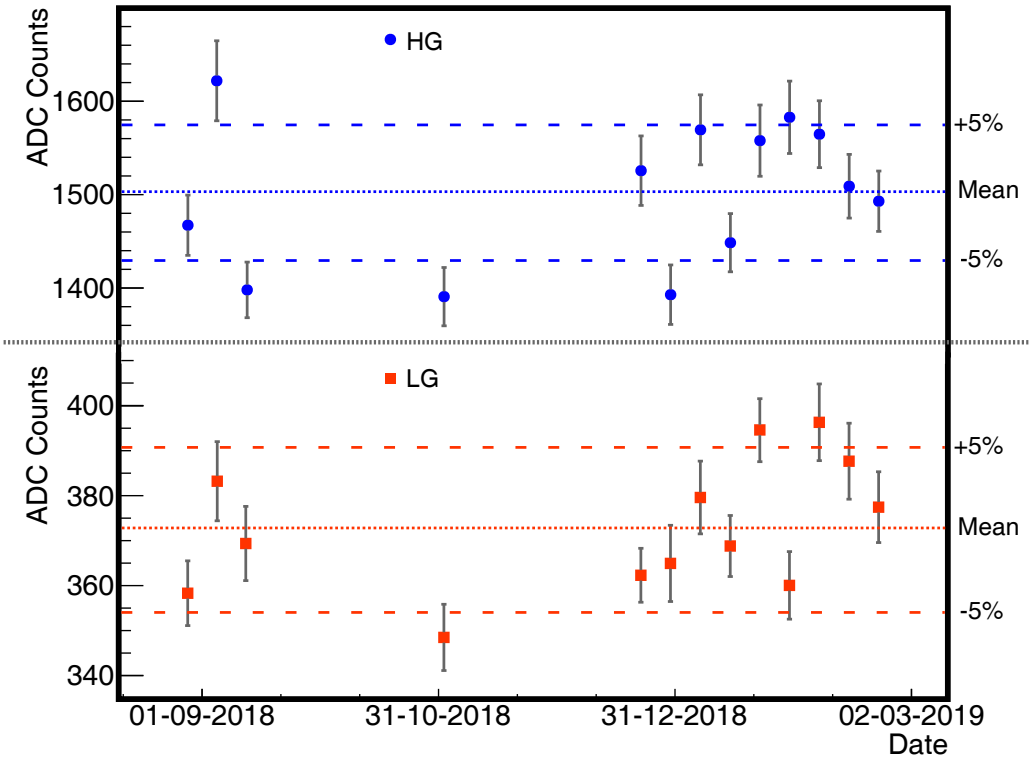


**Figure 5.27:** Mean charge in the high-gain (top) and low-gain (bottom) channels between the end of August an beginning of March. Each data point is extracted from a subset of 360000 T1 events. In dashed lines, we show the mean charge for the period and the 5% deviation limit. We obtained a mean charge of  $(373 \pm 4)$  ADC counts and  $(1502 \pm 21)$  ADC counts for the low- and high-gain channels respectively with an RMS of  $(14 \pm 3)$  ADC counts and  $(75 \pm 15)$  ADC counts. This implies a mean fluctuation of less than 4% in the online calibration during this time period.

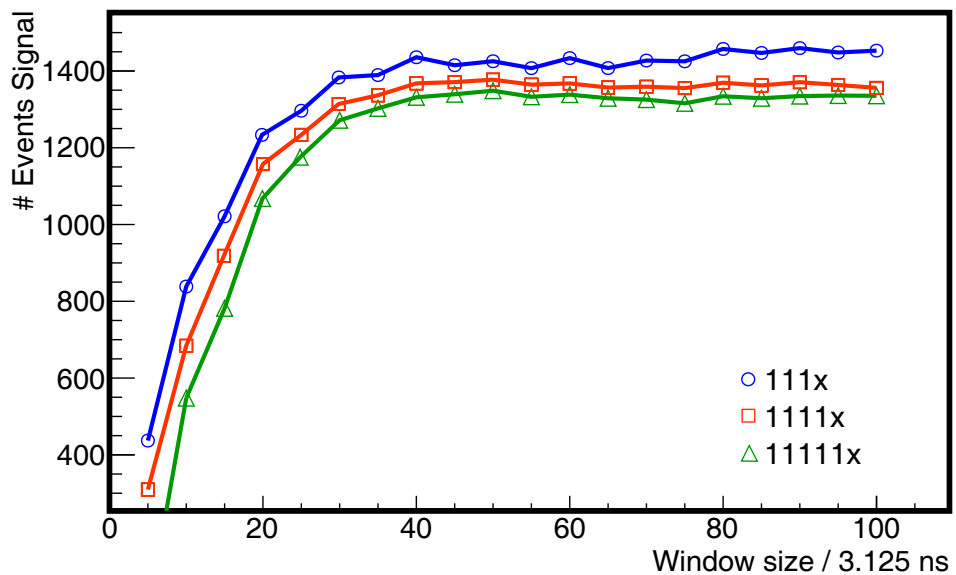


**Figure 5.28:** Number of signal events as a function of the window size for different matching patterns. The mean charge value in each case is  $(353 \pm 7)$  ADC counts,  $(358 \pm 7)$  ADC counts, and  $(363 \pm 7)$  ADC counts for the 111x, 1111x and 11111x patterns respectively.

build the trigger in the electronics, and to a lesser extent, the delay due to the different cable lengths. In Fig. 5.29 top left panel, we show the mean difference of all the engineering array modules between the binary channel start time and the maximum of signal in the ADC channel (analog to Fig. 5.21 top panel). The delay between the binary and ADC channels is stable (within a mean fluctuation of  $\sim 2.5\%$ ) and independent of the module, since it is produced by the delay in the electronics components themselves. In the left top panel, we show the standard deviation of these delays to demonstrate that the fluctuations event-to-event are relatively small, and therefore, there is no need to optimize this value in each individual module.

Concerning the signals start times, needed to locate the muons in the T1s events, in the bottom panels of Fig. 5.29, that there are differences between the modules. Since this data was extracted from T3 events, we observe two trigger types [47]: T2-ToT and T2-TH. In the case of the T1s, since the rate of TH1-TH triggers (100 Hz) is much higher than the rate of TH1-ToTs (1.2 Hz) we only see the first one. However, all TH1-ToTs are automatically promoted to TH2, while less than a fourth of TH1-TH are promoted to T2. For this reason, the two trigger types are clearly distinguishable in T3 events. Since in the T1 calibration we only consider the TH triggers, it is only necessary to compensate for the cables length. Still, we need to optimize the calibration algorithm for each module in the engineering array. This might not be necessary for the whole array, since this issue has been addressed for the production phase, and cables length are expected to be standardized in all modules positions.

### 5.3.6 Comparison to offline calibration

An offline calibration using T3 shower events was presented in section 5.2. To verify the consistency of both calibrations, we show in Fig. 5.30 the results of the offline calibration for the module with Id 101 of the station with Id 93, the same module used to extract the T1 events analyzed in this work. In the offline calibration, the limited statistics does not allow us to estimate and extract the noise from the muon histograms in the same way as we do in the online calibration. However, this is not necessary, since in the offline calibration we consider the charge difference between N and N+1 muons, and therefore, the noise is automatically subtracted. Still, noise signals bias the individual  $N_\mu$  histograms to lower charge values. For the 1 muon histogram, if the signal charge was normally distributed, the mean charge would be  $\sim \text{Charge}_{\text{muon}} - \text{Charge}_{\text{noise}}$ . If we subtract to the 1 muon histogram the slope from the linear fit, the result should be close to minus the noise mean charge, which is where the linear fit intercepts the y-axis. We obtained for the low-gain channel a mean charge per muon of  $(366 \pm 4)$  ADC counts and  $(1450 \pm 16)$  ADC counts for the high-gain. If we compare these with the results of the online calibration in Table 5.9, we can see that both calibrations are consistent within a difference of less than 3%.

### 5.3.7 Implementation in the UMD electronics

To achieve an online calibration in the field, it is necessary to implement a charge calculation algorithm in the UMD electronics, which runs in parallel to the normal module operation. To this aim, we have modified the electronics software to replicate the buffer data after a T1 trigger is received and to automatically download this data to the microprocessor, where the calibration algorithm was implemented. The algorithm is similar as explained in section 5.3.6. A “noise” and a “signal + noise” window was defined. When the muon condition in the binary channel is met in either window, the electronics output the charge of both low- and high-gain channels in a plain-text file stored in the acquisition server.

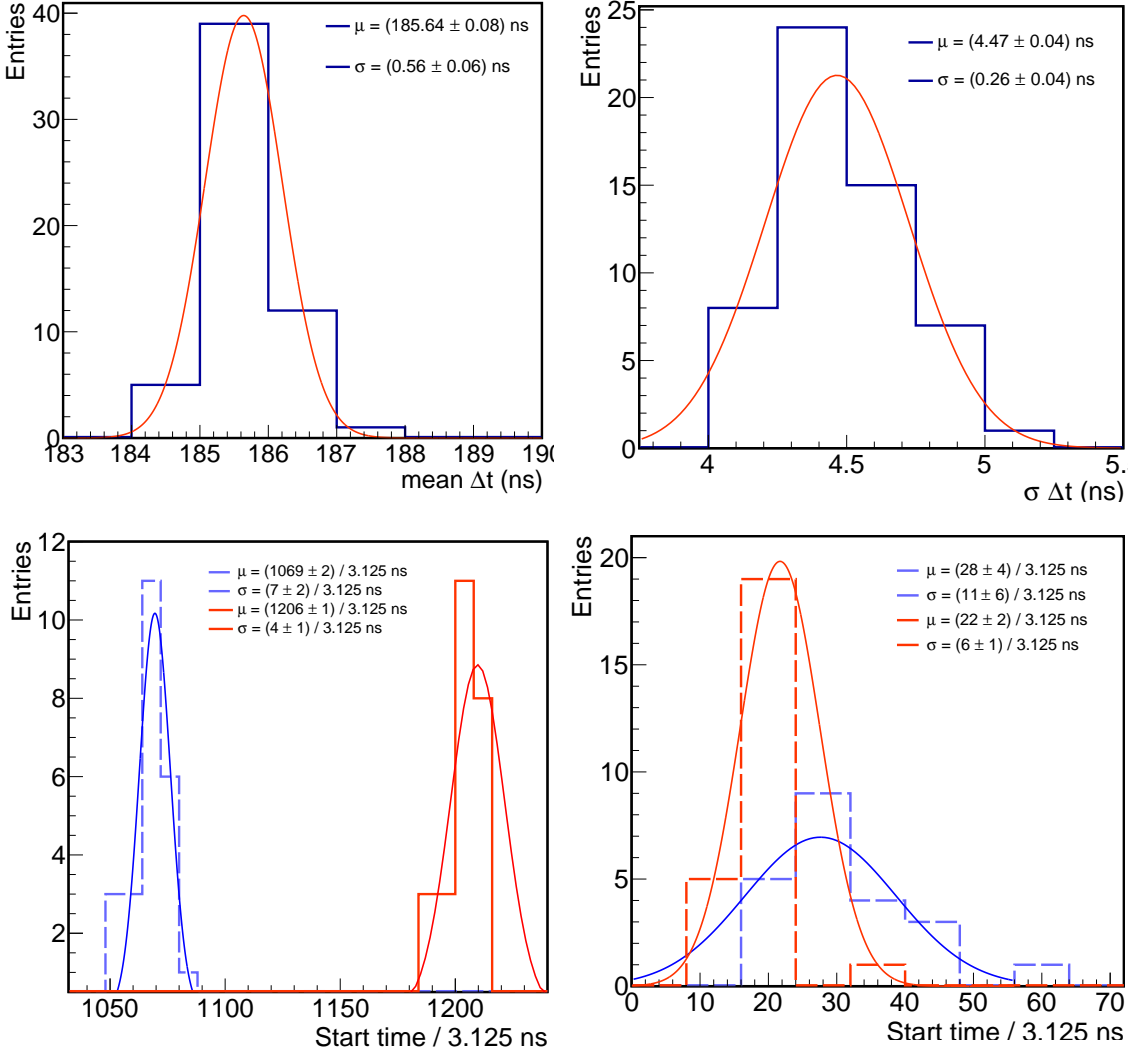


**Figure 5.29:** (Top) delay between the binary channel start time and maximum signal amplitude time in the ADC channel. We show the means (left) and standard deviations (right) of the delays for all the UMD engineering array modules. The maximum difference between the modules is  $\sim 4$  ns which is less than the sample time of the ADC channel. It is also apparent that this delay is stable since the mean fluctuation is  $\sim 2.5\%$ . (Bottom) means (left) and standard deviations (right) of the binary trace start time. The T2-ToT and T2-TH triggers are distinguishable. In this case, the maximum difference in the start time of two modules is  $\sim 40$  ns ( $\sim 13$  sample times of the binary channel). Therefore, we need to optimize the calibration for each module in the UMD engineering array to compensate for these differences.

Before proceeding to the implementation of the new software in the test module, we deployed the software in the laboratory setup described in section 5.1 (Fig. 4.20). We repeated the measurement described in 5.1, in which we extracted single-muon signals using a scintillator strip and a muon telescope at 2.5 m while the calibration algorithm was running in the electronics. In Fig. 5.31 top panel we show the low-gain charge histogram of single muons by analyzing the events extracted with the T3 simulator (as in section 5.1.2) and in the bottom panel the charge histograms obtained with the calibration algorithm in the electronics. In the top panel, low-charge events are produced when noise in the baseline shifts the charge calculation to negative values. The differences between both histograms in the baseline width

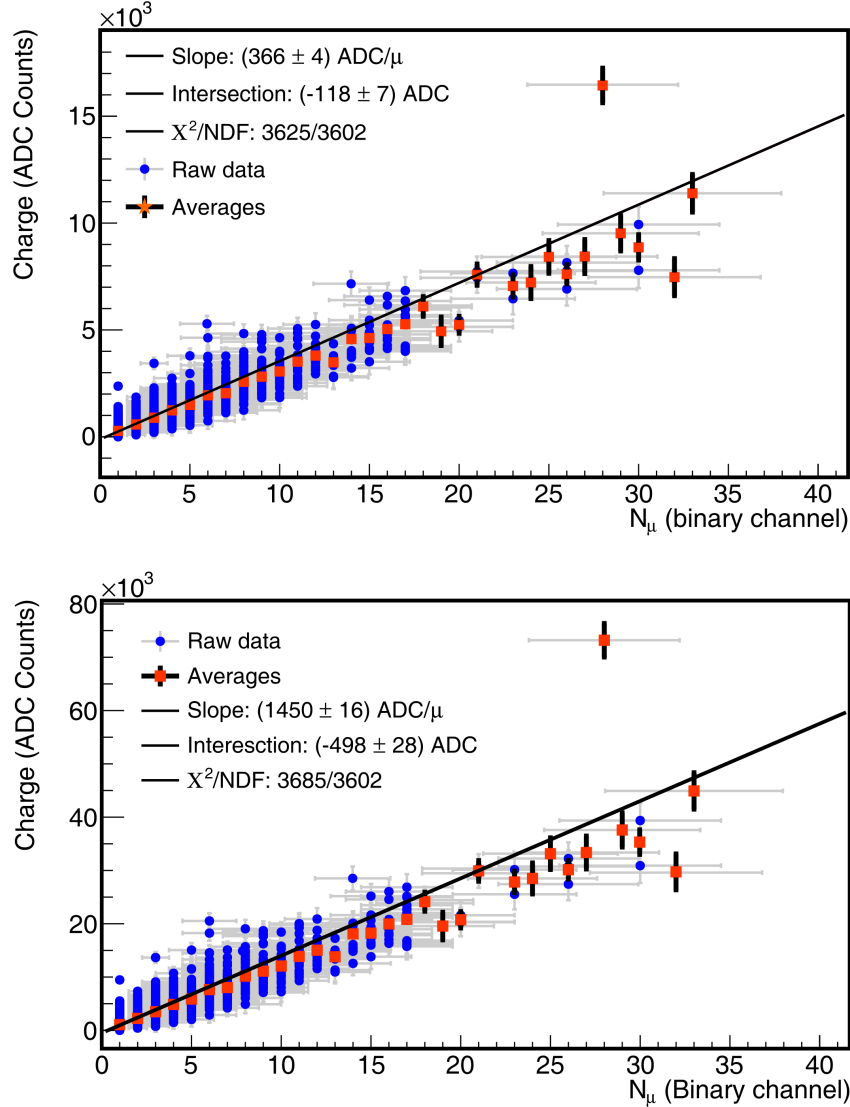


**Figure 5.30:** Offline calibration using shower events for the module with Id 101 of the station with Id 93. We present the results for the low- (top) and high-gain channels. The fit results are consistent with the results obtained using the online calibration summarized in Table 5.9

are mainly produced by the choice of the integration window. When analyzing the T3 data, as we have access to the whole event, we limit the integration window to the shower scope. When calculating the charge in the electronics, this windows is fixed to 200 ns, which is  $3\sigma$ s from the mean width of single muons (as shown in Fig. 5.15). Still, both analyses are compatible. Since in the laboratory the T1 trigger is injected when a muon impinges on the muon telescope, it is unlikely to find a noise signal in the trace.

After validating the new electronics software in the laboratory, we deployed the software upgrade in the module with Id 101 of the station with Id 93 (the same module used in section 5.3). We built a data set with approximately five hours of calibration data. The result is shown in Fig. 5.32. In this case, we present the same analysis as in section 5.3.3, in which the calibration histogram is built out of the charge histograms from both “noise” and “signal + noise” windows. The mean charge in this case is consistent with the obtained in the previous analysis (see section 5.3.4). These results are encouraging and show that after fine-tuning the algorithm will be ready to be deployed in all UMD modules.

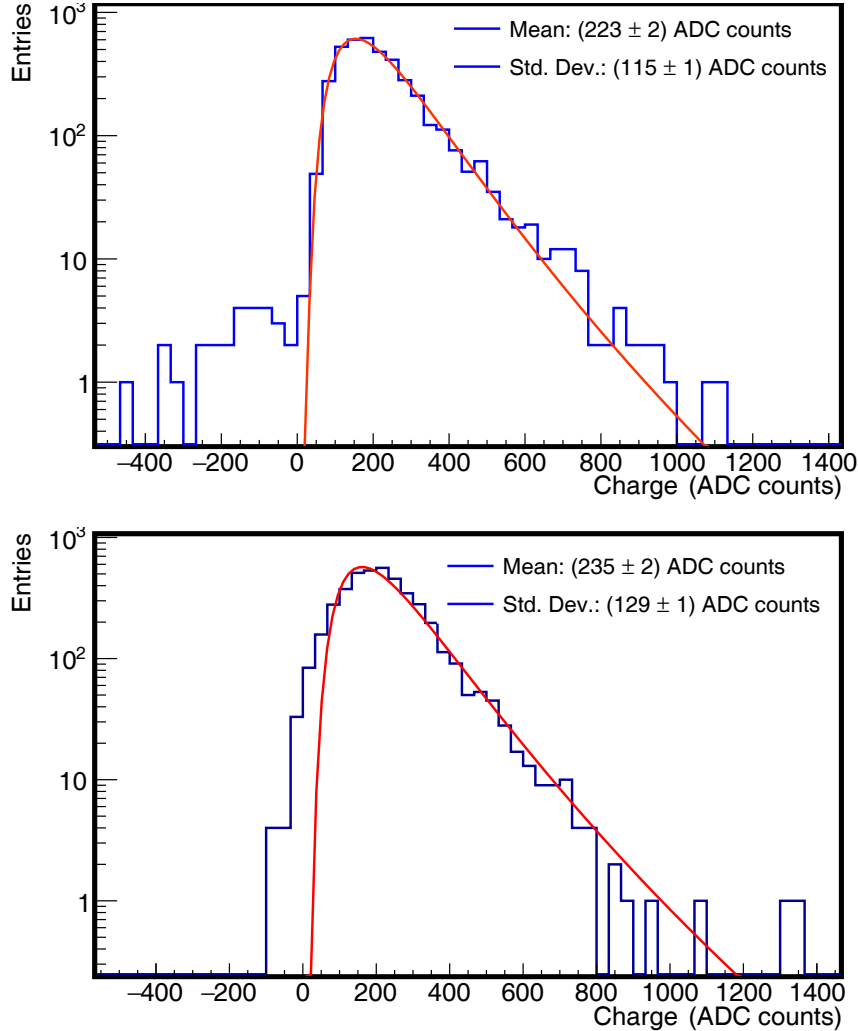


**Figure 5.31:** Charge histograms of the low-gain channel obtained in the laboratory analyzing T3 events (top) and the charge extracted with the calibration algorithm implemented in the electronics (bottom).

## 5.4 Conclusions of this chapter

In this chapter, laboratory and field data was used to assess the main features of the AMIGA ADC channel. With this data we have fully characterized the signal charge, timing and shape.

We have also presented an offline calibration for the ADC channel and an uncertainty model with one free parameter. By comparing the ADC charge with the number of muons ( $N$ ) estimated with the binary channel, the mean charge per muon was obtained. Furthermore, we calculated a resolution of  $\sim 60\%$  for detecting one muon with the ADC channel. Still, the uncertainties expected when estimating the shower muon density are dominated by the Poissonian fluctuation in the whole range. For  $N = 1$ , the ADC channel resolution is  $\sim 20\%$  higher than an ideal Poissonian detector. The signal charge in the ADC channel (in mean values) varies linearly with the number of muons. The ADC and binary channel working range overlapped in a wide scope. This constitute the basis for a combined analyses that can unprecedentedly reduce systematic uncertainties in the estimation the muon content of air showers.

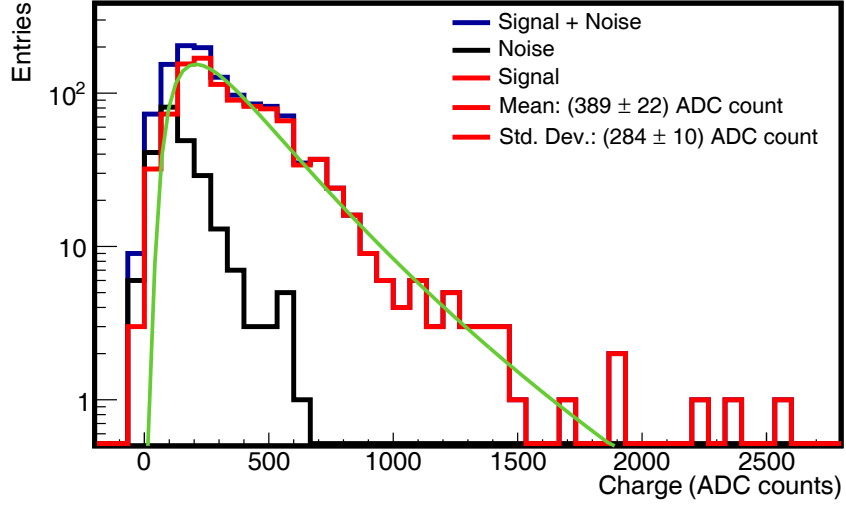


**Figure 5.32:** Charge histograms obtained using the calibration algorithm implemented in the UMD electronics and deployed in the module with Id 101 in the station with Id 93.

Finally, an end-to-end online calibration for the ADC channel of the AMIGA muon detector has also been assessed using a test module in the field. We have achieved a calibration in real-time of the AMIGA *integrator* mode to run in parallel with the acquisition. The tests performed both in laboratory and field denote that the electronics update is nearly ready to be deployed as part of the standard electronics software of AMIGA modules.



---

---

# CHAPTER 6

---

## SiPM and muon simulations

The UMD simulation in the Auger analysis and simulation framework ([Offline](#) [110]) has been recently updated to match the final design of the AMIGA muon detector by including the simulation of the SiPMs with the *counter* and *integrator* mode electronics. In this chapter, we present the first part of the UMD simulations, which consists of the analog signal at the SiPM output after a muon impinges on the detector, which is, in turn, the electronics input. We present how this simulation was developed and validated using laboratory data, for which a dedicated setup was built (presented in section 6.1). Firstly, in section 6.2, a generator of single-PE SiPM pulses is described. We have used dark-rate events to obtain a phenomenological characterization of the PE signal. The results of this analysis are used to simulate the single-PE signals. Secondly, in section 6.3, we describe how the scintillator and optical-fiber are simulated. We use a parametrization of the light-output attenuation to describe the number of PE produced after a muon impinges on the detector. We have, then, simulated the time profile of the arriving photons by convoluting the decay times of the scintillator and optical fiber.

### 6.1 Experimental setup and calibration

The first step towards the development and implementation of SiPM simulations in [Offline](#) is to simulate the muon analog signals input before the electronics. In this section, we describe a PE pulse generator, that we created and tested using the laboratory setup illustrated in Fig. 6.1. In general, the setup consisted of one scintillator strip of 4 m long with optical fibers, both identical as those in the AMIGA modules [54] and built with the same materials that will be used in the production phase [100]. The optical fiber was coupled through an optical connector to a standard AMIGA SiPM. The scintillator strip was covered with an aluminum container to shield it from the environment light.

As the detector response depends on the position on the strip where the muons are injected due to the optical-fiber attenuation, events produced at different positions were measured. To trigger the signal, a muon telescope built with two scintillator segments of 4 cm x 4 cm x 1 cm and customized electronics was used. The telescope electronics generate a trigger signal when a coincidence in the telescope (muon signal in both segments) is found and it is used to trigger events with muons crossing a specific position on the strip (within a 4 cm resolution).

To extract the SiPM signals, we implemented a customized inverter amplifier (Gali 84+) to obtain analog waveforms with an oscilloscope (LeCroy WaveSurfer 104MX-B) and a

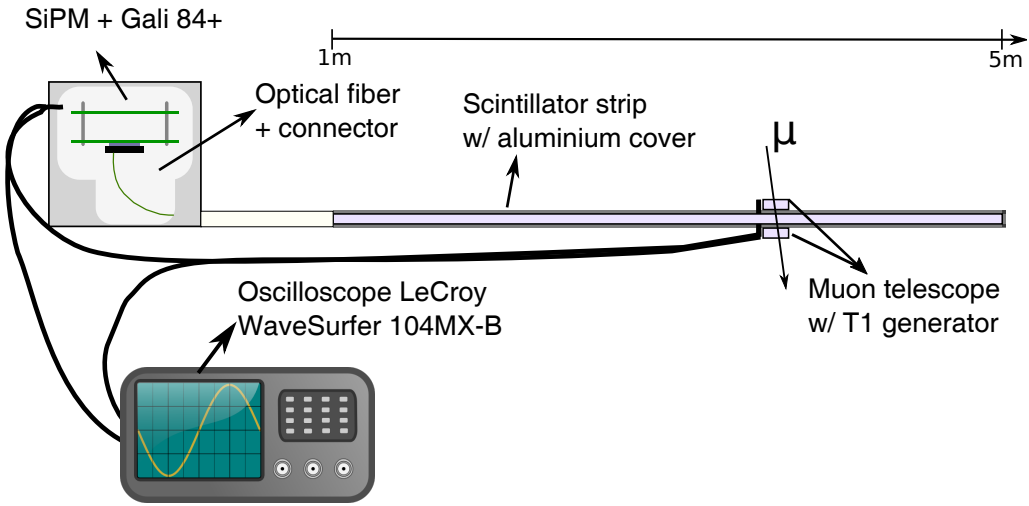


**Figure 6.1:** Schematics of the laboratory setups. A scintillator strip with optical fiber is shown. The optical fiber is coupled via an optical connector to a standard AMIGA SiPM. The signals are processed with an inverter amplifier (Gali 84+). A muon telescope is used to trigger the events, which are acquired with an oscilloscope.

sampling time of 0.2 ns. To shield the SiPMs from the environmental light, both SiPMs and read-out electronics were deployed in a PVC box. With this setup, both analog signals of dark-rate and muons can be obtained.

Before proceeding with the acquisition, it is necessary to calibrate the SiPMs ([88]) in order to obtain data compatible with those in the field. The SiPM  $V_{bias}$  was set following the procedure explained in section 4.1, in exactly the same way as performed for the detectors deployed in the Observatory. In Fig. 6.2, we show the calibration curve (top panel) and dark-rate curve (bottom panel) with  $V_{ov} = 3.5$  V, which is the configuration selected for acquiring data. From the dark-rate curve, we obtained a dark rate at  $\sim 199$  DAC counts (0.5 PE) of 650 kHz and a crosstalk probability of 2.2% which is estimated as the ratio of the dark rate at 1.5 PEs and 0.5 PEs (see chapter 4).

## 6.2 Single-PE simulation

Once calibrated, we have obtained PE analog waveforms by measuring dark-rate pulses with an inverse amplifier and an oscilloscope (see Fig. 6.2). However, the dark rate is not entirely composed of single-PEs pulses, as the crosstalk between the SiPM inner cells may produce thermal noise with higher amplitude [93]. Furthermore, the single-PE waveform can also be altered with afterpulses. In the top panel of Fig. 6.3, we present a set of measured dark-rate waveforms, where the effect of the crosstalk and after-pulses is seen. The single-PE, two-PEs and three-PEs signals are distinguishable, as well as the afterpulses following the first peak.

To filter the events that not exclusively contain single-PEs, we show in the bottom panel of Fig. 6.3 the signal charge as a function of its amplitude. The three distinct populations correspond to the single-PE, two-PEs and three-PEs signals. The fact that these populations are completely separated denotes how well defined is the PE spectrum of SiPMs, both in charge and in amplitude. To select the single-PE signals, we dismissed all events outside the first population.

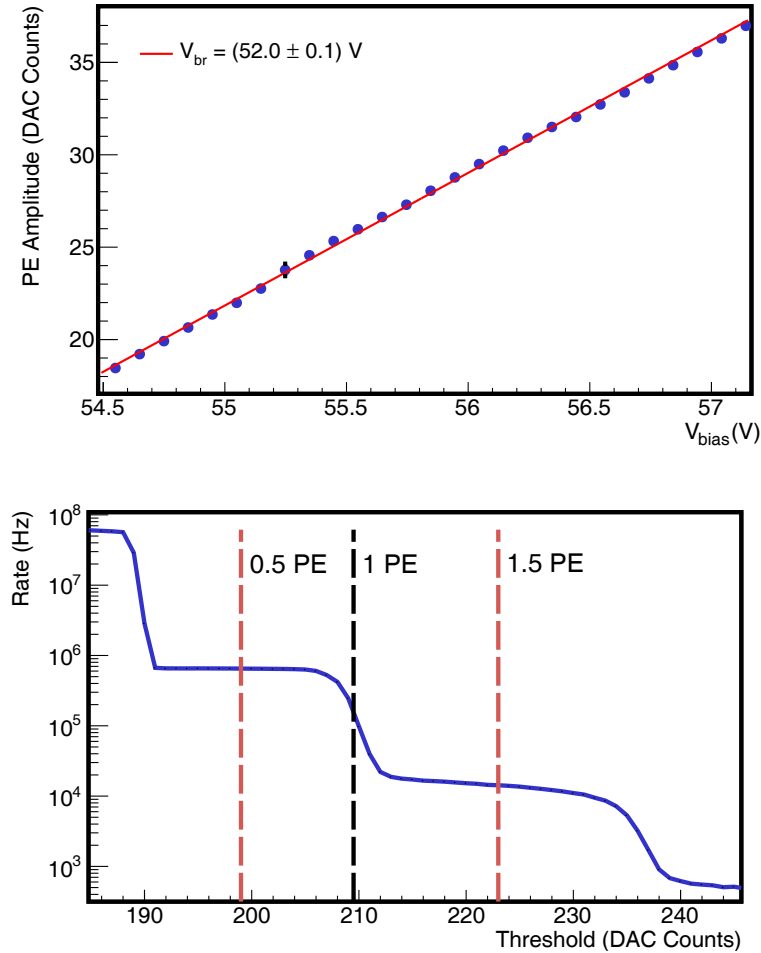


**Figure 6.2:** (Top) PE as a function of the  $V_{\text{bias}}$ . By extrapolating the curve to 0, the  $V_{\text{br}}$  is obtained. (Bottom) dark-rate curve as a function of the discriminator threshold acquired with  $V_{\text{ov}} = 3.5$  V. The dark rate obtained at 0.5 PE level is 650 kHz and the crosstalk probability is 2.2%.

### 6.2.1 Deconvolution algorithm

Since we are using an amplifier to extract PE pulses from laboratory data that is not accessible in the actual electronics chain, we need to implement a deconvolution algorithm to reverse any possible distortion of the input signal and to recover an accurate PE waveform to model it accordingly. If we consider an input  $V_{\text{in}}$ , and an output  $V_{\text{out}}$ , not constant in time ( $t$ )

$$V_{\text{in}} = f_{\text{in}}(t), \quad V_{\text{out}} = f_{\text{out}}(t), \quad (6.1)$$

and we convolute the input with a given response, we may describe the output through a transfer function ( $H(t)$  in time-space) as

$$f_{\text{out}}(t) = f_{\text{in}}(t) * H(t). \quad (6.2)$$

Applying a Fourier transform, and using the convolution theorem [111], we can write

$$\mathcal{F}(f_{\text{out}}(t)) = \mathcal{F}(f_{\text{in}}(t)) \mathcal{F}(H(t)), \quad (6.3)$$

which in Fourier space can be written as

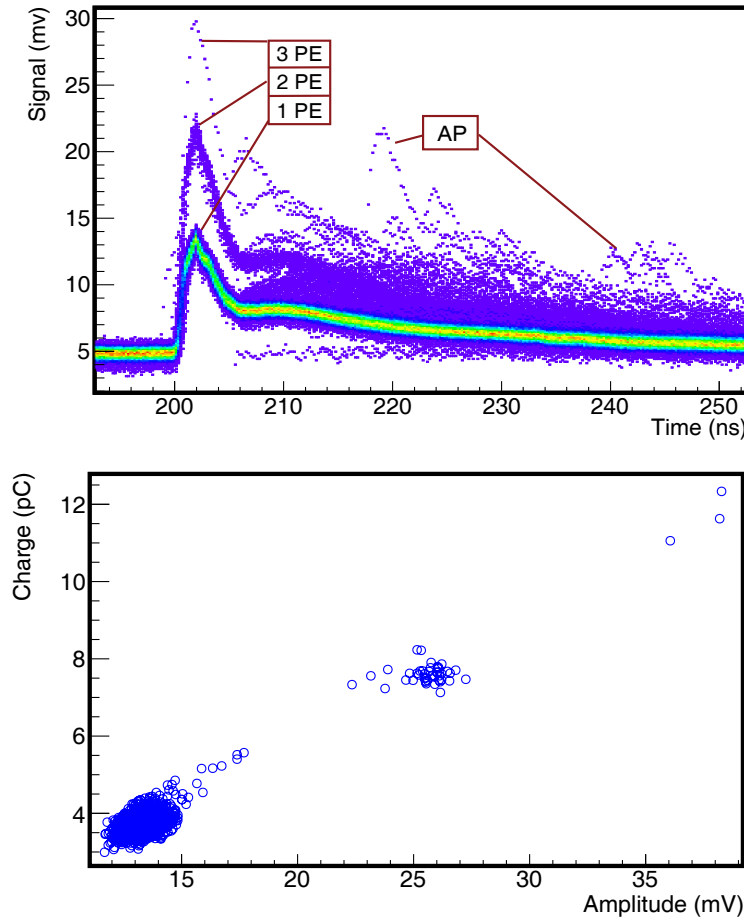


**Figure 6.3:** (Top) dark-rate pulses measured with an oscilloscope. We can clearly identify the afterpulses, along with the different PE peaks produced by crosstalk within the SiPM inner-cells. (Bottom) signal charge as a function of its amplitude. The three populations correspond to one, two and three PEs signals.

$$\begin{aligned} f_{\text{out}}(\omega) &= f_{\text{in}}(\omega)H(\omega), \\ f_{\text{out}}(t) &= \mathcal{F}^{-1}(f_{\text{in}}(\omega)H(\omega)), \end{aligned} \quad (6.4)$$

where  $\omega$  is the signal frequency since the Fourier-domain is equivalent to the frequency-domain. In the laboratory, we are measuring the output ( $f_{\text{out}}$ ) with an oscilloscope and we intend to recover the input ( $f_{\text{in}}$ ). Therefore, we need to transform the measured signals into the frequency-domain, apply the inverse transfer function of the used amplifier, and transform the result back to the time-domain

$$\begin{aligned} f_{\text{in}}(\omega) &= f_{\text{out}}(\omega)H^{-1}(\omega) \\ \implies f_{\text{in}}(t) &= \mathcal{F}^{-1}\left(f_{\text{out}}(\omega)H^{-1}(\omega)\right). \end{aligned} \quad (6.5)$$

In this deconvolution algorithm we separate the functions in the frequency-domain into their real (Re) and imaginary (Im) parts to improve the algorithm performance:

$$\begin{aligned}\operatorname{Re}[f_{\text{in}}(\omega)] &= \operatorname{Re}[f_{\text{out}}(\omega)]\operatorname{Re}[H^{-1}(\omega)] - \operatorname{Im}[f_{\text{out}}(\omega)]\operatorname{Im}[H^{-1}(\omega)] \\ \operatorname{Im}[f_{\text{in}}(\omega)] &= \operatorname{Re}[f_{\text{out}}(\omega)]\operatorname{Im}[H^{-1}(\omega)] + \operatorname{Im}[f_{\text{out}}(\omega)]\operatorname{Re}[H^{-1}(\omega)].\end{aligned}\quad (6.6)$$

We could also write the algorithm using the polar form:

$$\begin{aligned}H^{-1}(\omega) &= |z|e^{i\phi} = M[H^{-1}(\omega)] \exp i\Phi[H^{-1}(\omega)], \text{ with} \\ M[H^{-1}(\omega)] &= \sqrt{\operatorname{Re}[H^{-1}(\omega)]^2 + \operatorname{Im}[H^{-1}(\omega)]^2}, \text{ and} \\ \Phi[H^{-1}] &= \operatorname{atan2}(\operatorname{Im}[H^{-1}(\omega)], \operatorname{Re}[H^{-1}(\omega)])\end{aligned}\quad (6.7)$$

where  $M$  is the complex-function magnitude and  $\Phi$  its phase. Applying the inverse transfer to the input in the polar form we infer:

$$\begin{aligned}M[f_{\text{in}}(\omega)] &= M[f_{\text{out}}(\omega)]M[H^{-1}(\omega)] \\ \Phi[f_{\text{in}}(\omega)] &= \Phi[f_{\text{out}}(\omega)] + \Phi[H^{-1}(\omega)]\end{aligned}\quad (6.8)$$

### 6.2.2 Amplifier transfer function

To apply the deconvolution algorithm explained above to the single-PEs signals measured in the laboratory in Fig. 6.3, we characterize first the transfer function of the used amplifier ( $H(\omega)$ ) as

$$H(s) = \frac{2 \cdot 10^{60} \text{ Hz}^7}{(s + 4 \cdot 10^9 \text{ Hz})(s^2 + s \cdot 1.53 \cdot 10^9 \text{ Hz} + 4.096 \cdot 10^{19} \text{ Hz}^2)(s + 9 \cdot 10^9 \text{ Hz})^3}, \quad (6.9)$$

where  $s = i\omega$ .

In the top panel of Fig. 6.4, we show the magnitude of  $H(s)$ . The amplifier is rather flat in a broad bandwidth (up to  $\sim 1$  Ghz). As we shall see in section 6.2.3, the characteristic rise times of the single-PE signal is of the order of nanoseconds and therefore an amplifier with a flat response up to  $\sim 200$  MHz is sufficient to measure the single-PEs signal.

In the middle panel of Fig. 6.4, we show an example of a measured single-PE signal (i.e. deconvoluted with the amplifier response). In the bottom panel of Fig. 6.4 we present the waveform after applying the deconvolution algorithm. It is apparent, that both waveforms are similar except for the signal amplitude, meaning the amplifier has rather a flat response within the signal bandwidth, with an amplification factor of  $\sim \times 15$ .

### 6.2.3 Single-PE model

To emulate the single-PE pulses, we used a phenomenological approach in which we implement a model for the PE pulses. The parameters of the model function are estimated by fitting the measured dark-rate pulses. The mean and RMS values of the model parameters are input in a random generator to finally simulate single-PE pulses. To fit the PE signals, we used a function with one rise time and three decay times [112]:

$$f(t) = A_1 \left( 1 - \exp \frac{-t}{\tau_r} \right) \left( A_2 \exp \frac{-t}{\tau_{f1}} + A_3 \exp \frac{-t}{\tau_{f2}} + \exp \frac{-t}{\tau_{f3}} \right), \quad (6.10)$$

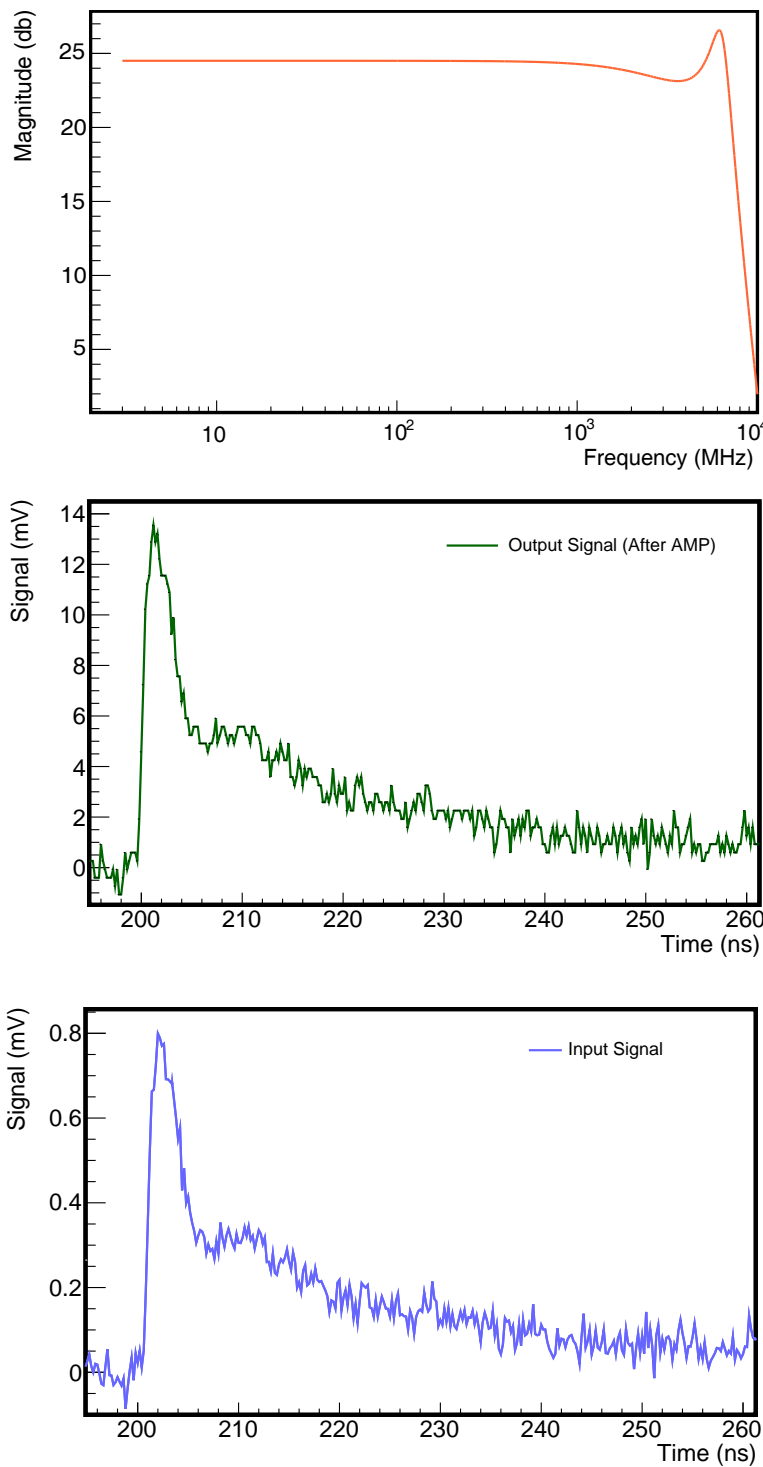


**Figure 6.4:** (Top) Transfer function of the amplifier Gali 84+. (Middle) single-PE signal measured with the oscilloscope (after amplification). (Bottom) single-PE signal from SiPM (after applying the deconvolution algorithm). Similar waveforms are obtained due to the flat response of the amplifier.

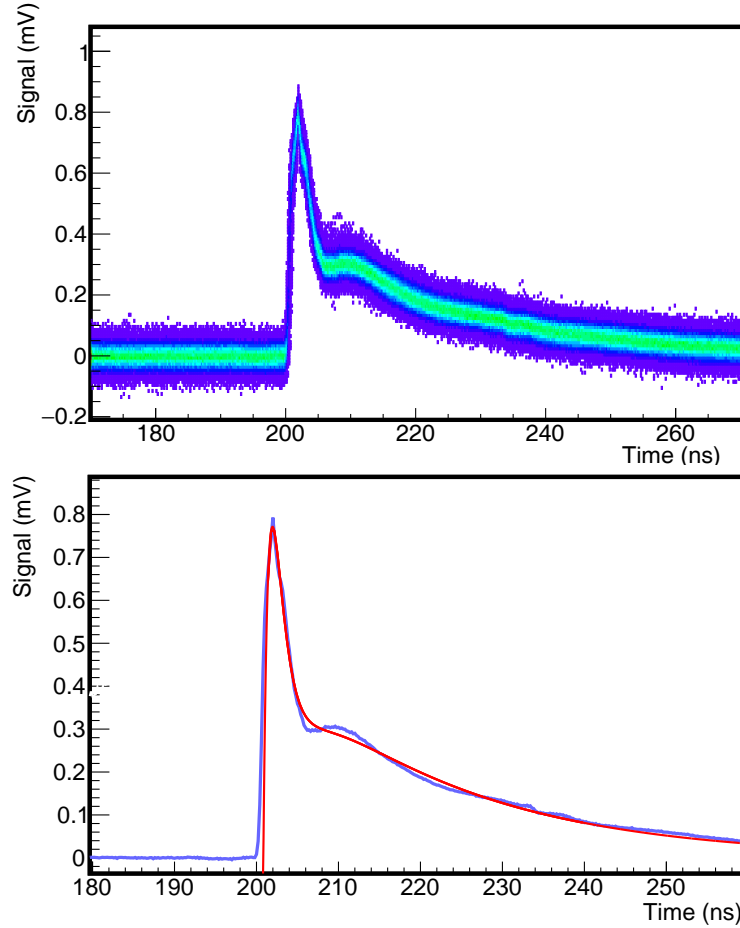


**Figure 6.5:** (Top) data set of 2000 single-PE pulses extracted from dark-rate measurements after removing crosstalk and afterpulses. (Bottom) average single-PE signal (blue), obtained by averaging the data in the top panel. The model (equation 6.10) fit (red) is also shown. We summarized the fit results in Table 6.1.

where  $A_1, A_2, A_3$  determine the signal amplitude,  $\tau_r$  is the rise time,  $\tau_{f1}, \tau_{f2}, \tau_{f3}$  are three fall times. The first fall time is a fast decay which is produced by the coupling of parasitic capacitors to the entrance impedance of the oscilloscope. The second fall time corresponds to the quenching and the third and slow decay corresponds to the recovery time of the SiPM [93, 112].

In the top panel of Fig. 6.5, we show the data set used to find the parameters of the model, from which we removed signals with crosstalk and/or after pulse as these are not properly described by the electric model in equation 6.10. To include in the simulations the parameters fluctuations, we fitted each of the individual single-PE pulse and we created histograms of the parameters from which the mean value ( $\mu$ ) and standard deviation ( $\sigma$ ) were extracted.

As in illustration, in the bottom panel of Fig. 6.5, we show the average single-PE signal, along with its corresponding fit. The model provides quite a good description of the signal. To corroborate the consistency of the previous analysis, we compare the results of the fits, including the results of fitting each of the individual pulses. In Table 6.1, we present the parameters results of fitting the average signal plus the mean values and standard deviation obtained from the fits of a set of individual signals. Both analyses are compatible.

Parameter	Average	$\mu$	$\sigma$
$A_1$ (mV)	$0.30 \pm 0.01$	$0.29 \pm 0.01$	$(1.37 \pm 0.03) 10^{-2}$
$A_2$	$23.80 \pm 0.20$	$23.22 \pm 0.07$	$2.94 \pm 0.06$
$A_3$	$1.59 \pm 0.01$	$(16.09 \pm 0.01) 10^{-1}$	$(0.54 \pm 0.01) 10^{-1}$
$\tau_r$ (ns)	$3.90 \pm 0.20$	$3.82 \pm 0.01$	$0.62 \pm 0.01$
$\tau_{f1}$ (ns)	$1.13 \pm 0.02$	$(11.87 \pm 0.02) 10^{-1}$	$(0.70 \pm 0.01) 10^{-1}$
$\tau_{f2}$ (ns)	$22.20 \pm 0.40$	$23.44 \pm 0.04$	$1.95 \pm 0.04$
$\tau_{f3}$ (ns)	$(2.51 \pm 0.03) 10^{-1}$	$(2.21 \pm 0.01) 10^{-1}$	$(3.24 \pm 0.04) 10^{-2}$

**Table 6.1:** Fit results of the model in equation 6.10. In the average column, we show the results of fitting the average single-PE signal shown in Fig. 6.5 bottom panel. In the columns  $\mu$  and  $\sigma$  we show the mean value and standard deviation of the histograms built by fitting the individual single-PE signals shown in the top panel of Fig. 6.5. The mean obtained by fitting the individual pulses is compatible with the results of fitting the average single-PE signal.

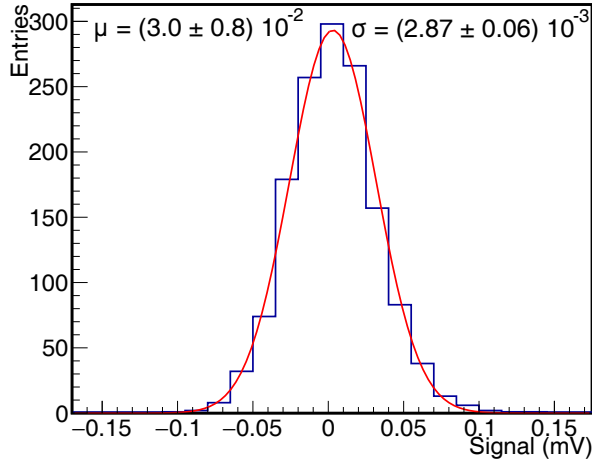


**Figure 6.6:** Baseline histogram of SiPM single-PE signals. Units of the fit results are mV.

Finally, we have also included in the pulse simulation the baseline fluctuations obtained for the dark rate measurements. In Fig. 6.6, the baseline histogram is shown. We simulate the baseline via a Gaussian random generator, which we set up with the fit results in Fig. 6.6.

### Parameter correlations and principal components analysis

In the previous section, we have obtained the means and standard deviation of the parameters used in the model of the single-PE. However, this parameter characterization may not necessarily be enough to fully describe the PE signals. Another feature to be considered is the parameter correlations, as they are not completely independent. Not taking these correlations into consideration may lead to an inaccurate description of the SiPM pulses. Therefore, to include these correlations we used principal component analysis (PCA) [113]. For each dark-rate pulse, we obtain the model parameters by fitting the signal:

$$\mathbf{x}_i = \begin{bmatrix} A_1^i & A_2^i & A_3^i & \tau_r^i & \tau_{f1}^i & \tau_{f2}^i & \tau_{f3}^i \end{bmatrix}^T$$

where  $\mathbf{x}_i$  corresponds to the fit result of each single-PE pulse. After fitting all the signals, we compute the co-variance matrix as:

$$\mathbf{C} = \langle \mathbf{y}\mathbf{y}^T \rangle \quad \text{where} \quad \mathbf{y} = \mathbf{x} - \langle \mathbf{x} \rangle, \quad \text{with} \quad \mathbf{C}\mathbf{v}_n = \lambda_n \mathbf{v}_n,$$

the eigenvalues ( $\lambda_n$ ) and eigenvectors ( $\mathbf{v}_n$ ) of the co-variance matrix. To convert the variables from their original space to a decorrelated space, also called the principal components space, we can write the transformation matrix by ordering the eigenvectors  $\mathbf{v}_i$ , with  $i \in \{1, \dots, 7\}$ , in columns:

$$\mathbf{T} = \begin{bmatrix} \mathbf{v}_1 & \mathbf{v}_2 & \vdots & \mathbf{v}_7 \end{bmatrix} = \begin{bmatrix} \mathbf{v}_{11} & \mathbf{v}_{21} & \cdots & \mathbf{v}_{71} \\ \mathbf{v}_{12} & \mathbf{v}_{22} & \cdots & \mathbf{v}_{72} \\ \vdots & \vdots & \ddots & \vdots \\ \mathbf{v}_{17} & \mathbf{v}_{27} & \cdots & \mathbf{v}_{77} \end{bmatrix},$$

which is an orthogonal transformation. We can use the description of the parameters in the decorrelated space to input the simulation. By generating the parameters in the principal components space we can then anti-transform to the variables original space and obtain the correlated parameters. In the top panel of Fig. 6.7 we show an example of two parameters correlation for laboratory data and the simulation without using PCA. It is apparent how in this simulation there is no correlation between the variables. In the bottom panel, we display the result of including the correlations, where the agreement between the laboratory data and simulation can be seen.

Despite the parameters correlations in the simulations improve the output of the simulated signals, including them in the whole shower simulations may lead to performance issues, since the space transformation needs to be performed for every single-PE. In the following sections, we will show that there is no need to include the parameter correlations to accomplish an accurate description of the features relevant to the UMD performance (see also sections 7.1 and 7.2).

#### 6.2.4 Single-PE pulse generator

After characterizing the parameters of the single-PE model, we have created random generators with the mean value and RMS summarized in Table 6.1. We used the pulse generator to create a data set of 2000 single-PEs, which is shown in the top panel of Fig. 6.8. To study the behavior of the pulse generator, we repeated the same analysis performed over the laboratory data in section 6.2.3. In Fig. 6.8 bottom, we compared the results of the fits using the simulated data with the results using the laboratory data by computing  $\Delta = \frac{\mu_{\text{sim}} - \mu_{\text{data}}}{\mu_{\text{data}}}$  and  $\Delta = \frac{\sigma_{\text{sim}} - \sigma_{\text{data}}}{\sigma_{\text{data}}}$ , which illustrates the difference of the parameter mean and standard deviation respectively. The difference for the signal charge ( $Q$ ) and maximum amplitude ( $V_{\text{peak}}$ ), which are the two main features of the PE signal, are also shown. The difference between data and simulation of most of the parameters are within less of 5% deviation and the maximum deviation is less than 9%, which means that the single-PE pulse generator accomplished provides a good description of the SiPM behavior.

### 6.3 Muon pulse simulation

After achieving a generator which accurately simulates the single-PEs signals, we can simulate the muon signal. When a muon impinges on the scintillator, photons are produced with a characteristic decay time of 3.7 ns [114]. The photons are absorbed and re-emitted by

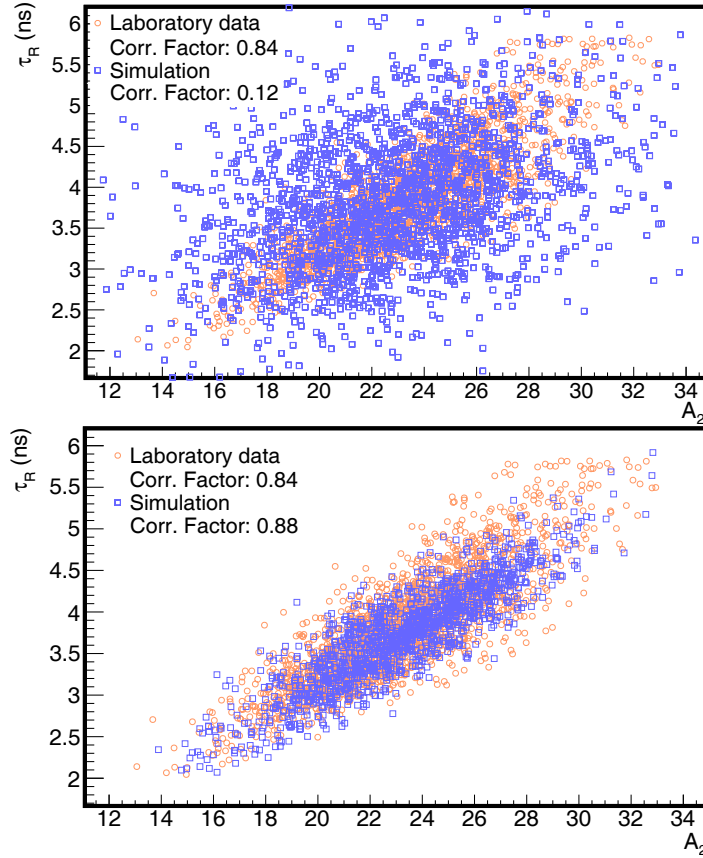


**Figure 6.7:** (Top) example of parameter correlation when simulating uncorrelated parameters. In this case, the simulation does not match the laboratory data. (Bottom) example of correlation parameters when using PCA to include correlations between parameters in the simulation. The agreement between data and simulation can be seen.

the optical fiber, which has a characteristic decay time of 3.5 ns [80]. Some of these photons propagate through the optical fiber to the SiPM, which detects  $\sim 40\%$  of the arriving photons due to its photo-detection efficiency [83]. Each detected photon produces a single-PE signal. The final muon output is the result of adding all these PE signals. Due to the decay times of scintillator and optical fiber, the arriving photons spread in time and do not pile-up. For this reason, the total amplitude differ to the total charge, since not all photons add to the total signal amplitude but they do to the total charge.

To measure analog muon signals, we used the same amplifier and deconvolution algorithm described in section 6.2.1. In this case, we coupled the SiPM to an optical fiber and scintillator strip and we use a muon telescope to trigger signals at different positions on the scintillator strip as explained in setup 6.1. An example of a muon signal measured at 2 m on the scintillator strip can be seen in the top panel of Fig. 6.9. It is apparent how photons do not pile-up due to their time profile. In the bottom panel of Fig. 6.9, we show the correlation between the charge and amplitude of the muon signals measured at 2 m on the scintillator strip. The linearity between these two features denotes that the muon pulses are rather uniform.

### 6.3.1 Attenuation curve

To simulate muon signals, we implement a parametrization of the optical-fiber attenuation curve. This parametrization provides the number of PEs at each position of the scintillator

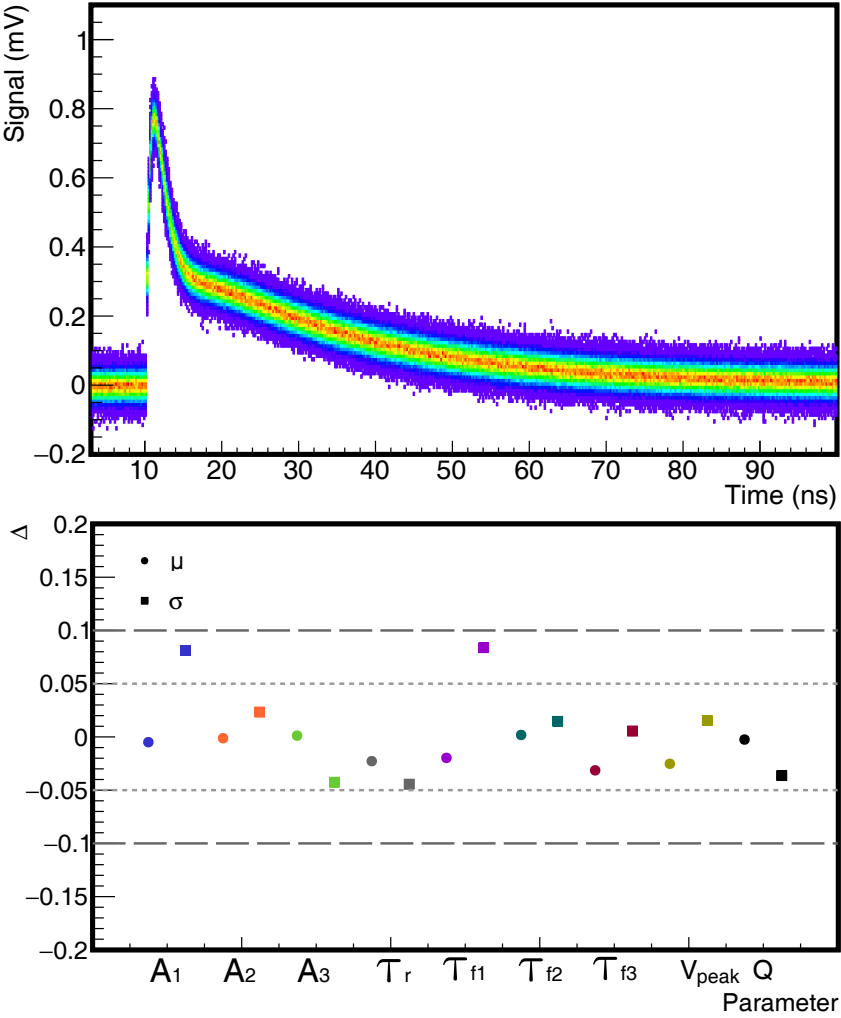


**Figure 6.8:** (Top) Data set of 2000 simulated single-PE pulses obtained with the pulse generator. (Bottom) comparison between the model parameters fitted using laboratory data and simulated data. Data and simulations differ typically less than 5%.

strip without requiring a detailed simulation of the photo-production in the scintillator or the photon propagation in the optical-fiber. Furthermore, the parametrization of the number of PEs already includes the SiPM photo-detection efficiency and crosstalk [93], which also improves the simulation time performance. To obtain the parametrization, we measured the number of PEs at different positions on the scintillator strip and fitted the data with a double-exponential function [103]:

$$f(x) = a \exp\left(\frac{-\lambda_1}{x}\right) + (1-a) \exp\left(\frac{-\lambda_2}{x}\right), \quad (6.11)$$

where  $\lambda_1$ ,  $\lambda_2$  are the attenuation lengths and  $a$  is a proportionality constant.

To estimate the number of PEs, we measured 2000 muon events at each position on the strip. Since we depend on the background muon flux to obtain this data, each acquisition runs for several days. For this reason, the SiPM is affected by the daily temperature modulation, which may have an impact on the SiPM performance (see section 4.2). To verify that this temperature variation is properly compensated, we monitor the SiPM gain during the acquisition. Before and after starting each acquisition at a position of the strip, we obtained a set of 2000 dark rate events, from which the mean charge was computed. In Fig. 6.10

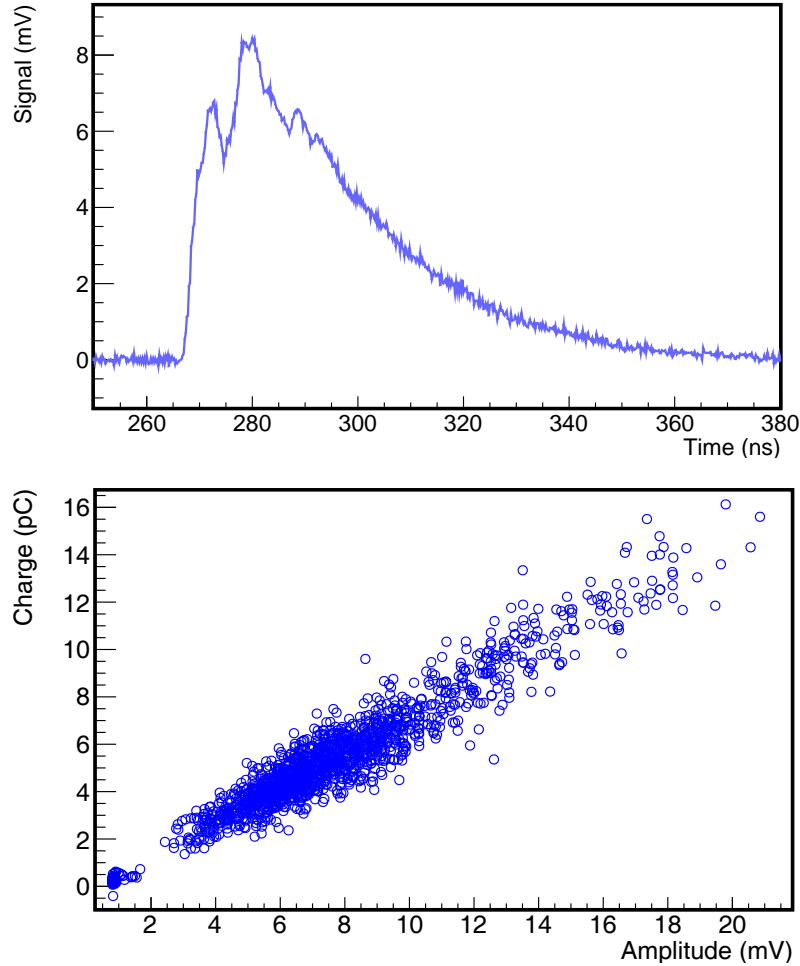


**Figure 6.9:** (Top) example muon signal measured a 2 m on the scintillator strip. The arriving photons are time distributed. (Bottom) signal charge as a function of its amplitude for muons measured at 2 m on the scintillator strip.

we show the SiPM mean charge in a time line. The gain remained stable during the whole acquisition within a fluctuation of less than 1%.

In Fig. 6.11, we show the number of PEs in charge and amplitude as a function of the position on the strip, along with the attenuation curves fitted with equation 5.1. The number of PEs in charge is estimated by dividing the muon charge by the mean charge of a single-PE. Analogously, the number of PEs in amplitude is estimated by dividing the muon signal amplitude by the mean amplitude of the single-PE. As explained before, the difference between amplitude and charge is related to the time distribution of photons reaching the optical sensor. It is worth to note that the *counter* mode, as it implements an amplitude threshold, is sensitive to the attenuation in amplitude, while the *integrator* mode is sensitive to the attenuation in charge.

### 6.3.2 Simulated muons

To generate the muon signals in a given position on the scintillator strip, we use the attenuation curve (6.11) to create a Poissonian distribution with the measured mean number of PEs at that position. We then simulate the time profile of the arriving photons using two exponential distributions with the decay times of the scintillator and optical fiber. For each photon, we generate the PE pulse with the SiPM peak generator described in 6.2.4 and we

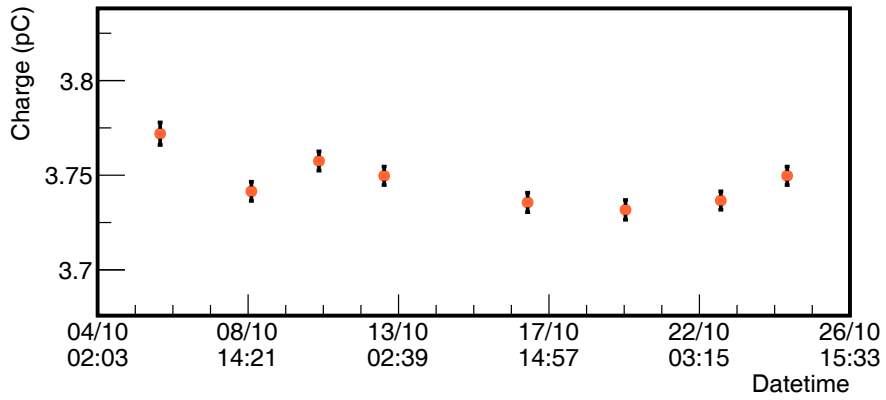


**Figure 6.10:** SiPM mean charge as a function of the date time. Each data point was obtained using a data set of 2000 dark rate pulses. The SiPM gain remain stable during the whole period.

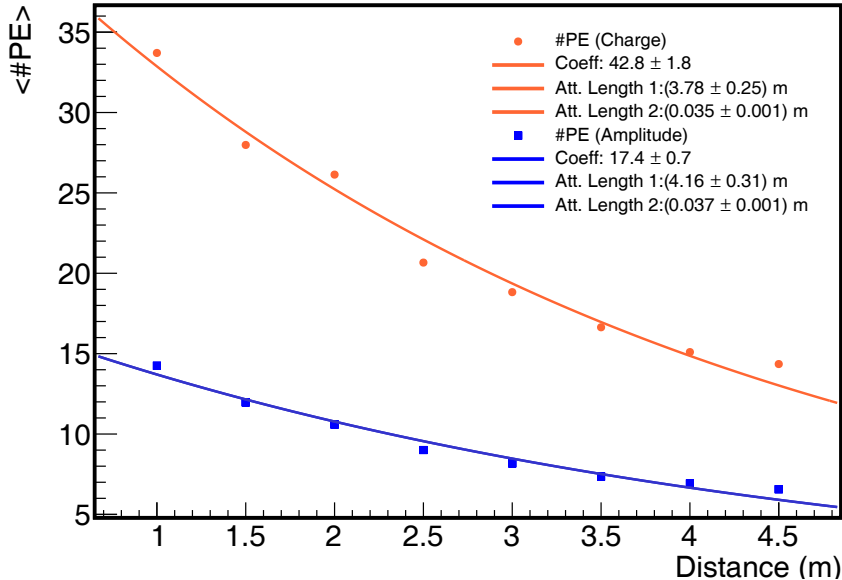


**Figure 6.11:** Mean number of photo-equivalents in charge and amplitude as a function of the trigger position. The data was fitted with the double-exponential decay function from equation 5.1. The difference between the number of PEs in amplitude and charge is produced by the decay times of the scintillator and optical-fiber.

use exponential distributions in a random generator to obtain the PE start time. By adding all PE signals, the muon signal is obtained. In the top panel of Fig. 6.12 we show an example of a simulated muon signal at 2 m on the scintillator strip. In blue, we plot the individual PEs signals and in red the muon. In Fig. 6.12 bottom panel, we display the correlation between charge and amplitude of the measured and simulated muon signal at 2 m on the scintillator strip. The laboratory data and the simulation agreement is satisfactory.

The simulations are expected to describe accurately the signal parameters relevant to the estimation of muon densities in air showers using the UMD. In this sense, one of the main features of the muon signals is the peak amplitude which has an impact on the performance of the *counter* mode since it implements an amplitude threshold. In the top panel of

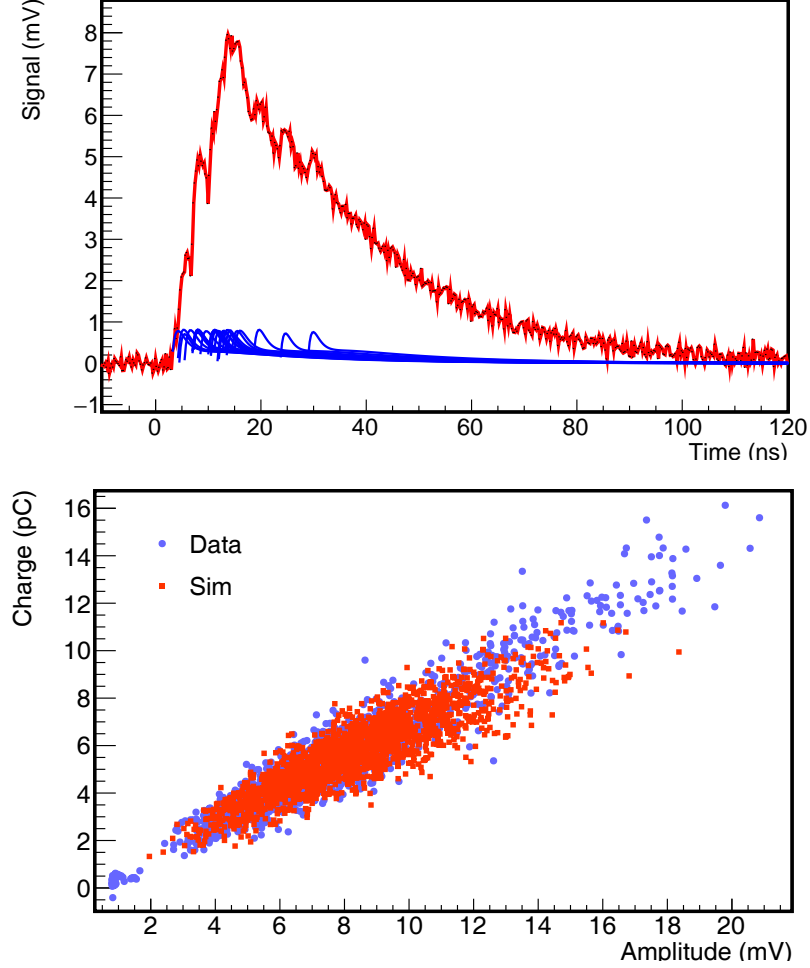


**Figure 6.12:** (Top) example of simulated muon signal at 2 m of the scintillator strips. In blue, the single-PE pulses with their time profile can be seen. In red we plot the total muon signal, which results from adding all the single-PE pulses. (Bottom) correlation between the muon signal charge and amplitude for 2000 events of both laboratory data and simulation. The simulation is quite consistent with the laboratory data.

Fig. 6.13, we show the mean and RMS of the signal amplitude at different positions on the scintillator strip, using both laboratory data and simulations. On the other hand, the muon signal charge has an impact in the *integrator* mode since in this mode, the number of muons is estimated as the ratio of the total signal charge and the mean charge of the single-muon. In the middle of 6.13, we display the mean and RMS of the signal charge at different positions on the scintillator strip for both laboratory data and simulations. Finally, the third feature we need to consider is the signal time width, which affects the signal timing (*counter* inhibition window) of both *counter* and *integrator* modes. In the bottom panel of 6.13 we show at different positions on the scintillator strip, the mean and RMS of the muon signal full width at half maximum (FWHM) using both laboratory data and simulations. It is apparent from Fig. 6.13 that there is an agreement between the laboratory data and the simulations, which denotes that the simulation provides a good description of the main features of the muon signals.

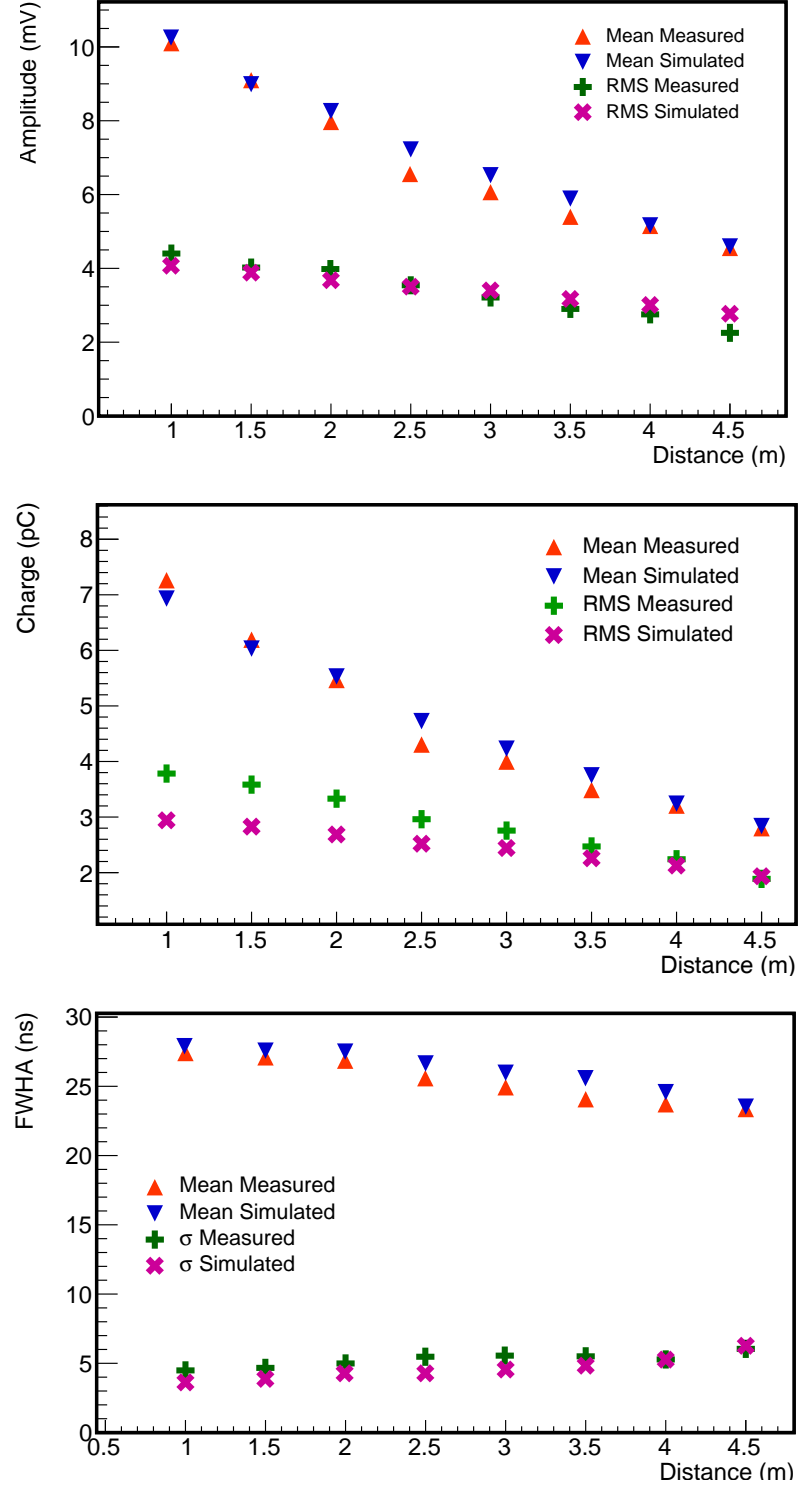


**Figure 6.13:** Main features of the muon signal at different positions on the scintillator strip. We show the means and RMS for laboratory data and simulations. We display on the top panel the muon signal charge, in the middle panel the muon signal amplitude and in the bottom, the muon signal full width at half maximum. It is apparent that in all cases there is an agreement between the experimental data and the simulations.

## 6.4 Conclusions of this chapter

In this chapter, we have developed and validated SiPM analog simulations using laboratory data. We have first achieved a single-PE simulation, which provides the SiPM analog output signal for single photons. Then, we obtained the optical-fiber attenuation curve from which we can estimate the number of PEs detected with the SiPM when a muon impinges on a scintillator strip. Using the scintillator and optical-fiber characteristic times and the number of PEs, single muon signals were simulated and validated using analog laboratory data obtained with an oscilloscope, showing a good agreement between simulations and experimental data.

We have achieved a pulse simulation that provides the SiPM output signal after a muon impinges on a scintillator strip. However, the muon analog signals are only the input of the UMD electronics [88], and at this instance, we have not yet included the *counter* or the *integrator* mode electronics. We discuss in chapter 7, the behavior of the UMD simulations after the electronic processing.

---

---

# CHAPTER 7

---

## Electronics simulation

In chapter 6, we explained how the SiPM signal is simulated for both PE and muon pulses. This SiPM signal is the input to the electronics of both *counter* and *integrator* modes. In this chapter, we describe how the electronics are simulated and the simulation implementation in the Auger Offline software.

Firstly, we describe in section 7.1 the read-out electronics of the *counter* mode and its transfer functions. The CITIROC pre-amplifier and fast-shaper are modeled as a low-pass filter and a practical differentiator respectively. Then, the discriminator and FPGA are simulated to generate binary traces. We use the laboratory data presented in section 4.4, to validate the simulation of the *counter* mode electronics. Secondly, we present the simulation of the *integrator* mode electronics in section 7.2 for which we approximated the transfer functions of the read-out electronics as low-pass filters. We used the laboratory data presented in section 5.1 to validate this part of the simulation. Finally we comment, in section 7.3, the implementation of the AMIGA SiPM and electronics simulations in Offline. Also, we briefly discuss how the simulation modules can be set up to attain different run modes.

### 7.1 Counter mode simulation

As we explained in section 3.6, the electronics of the *counter* mode consists of two 32-channel ASICs (Weeroc CITIROC [87]) and an FPGA [115]. To process the SiPMs pulses into binary traces we use the trigger channel of the CITIROCs, which handles the 64 SiPM signals individually. At the input of the trigger channel, the signal is first processed with a pre-amplifier followed by a fast-shaper and a discriminator. We simulate the pre-amplifier as a 10 MHz active low-pass filter, with an amplification factor of  $\times 10$ , which is the ASIC configuration implemented in the UMD electronics. The fast-shaper is simulated as a practical differentiator with a characteristic time of 15 ns and a maximum gain of  $\sim \times 18$  [116]. We then tuned the transfer functions parameters to obtain the best representation of laboratory data used to validate the simulations (presented in section 4.4). We describe in the following section the models used in the *counter* mode simulation, and its validation with laboratory data.

#### 7.1.1 Model and transfer functions

As we mentioned before, we simulate the pre-amplifier as a low-pass filter and the fast-shaper as a practical differentiator. In the top panels of Fig. 7.1 we show the model corresponding to the pre-amplifier (left) and the fast-shaper (right). The circuit components were

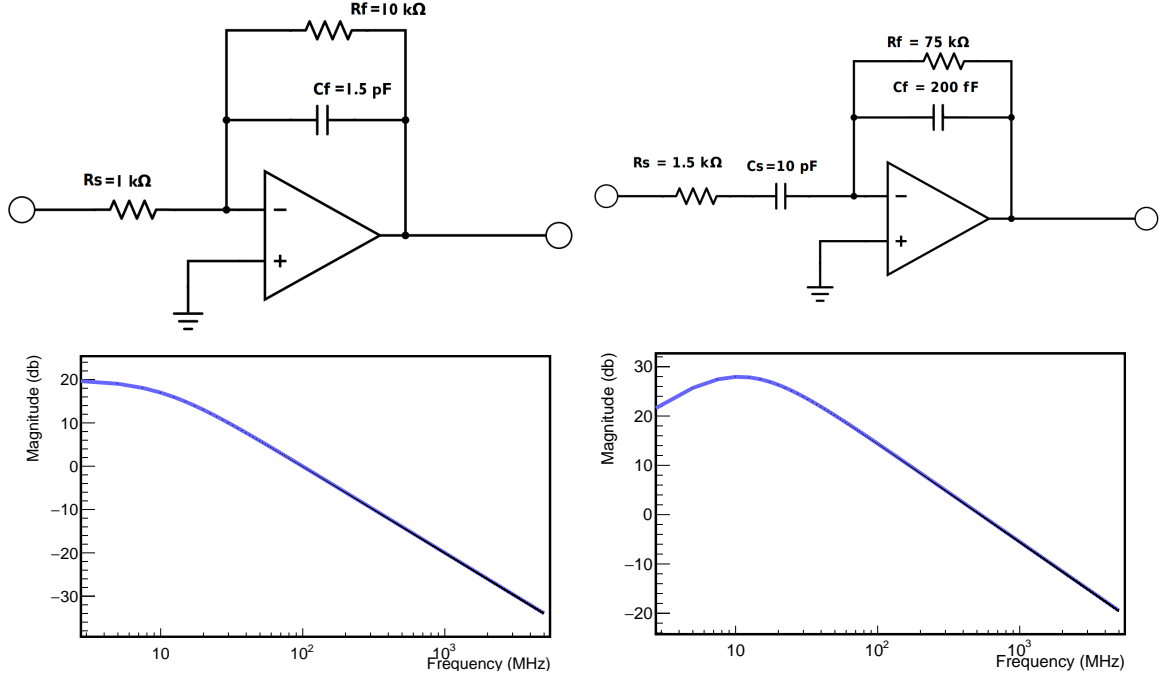


**Figure 7.1:** (Top) Proposed models for the CITIROC pre-amplifier (left) and fast-shaper (right) [116]. The pre-amplifier is simulated as an active low-pass filter with a frequency cut-off of 10 MHz and an amplification factor of  $\times 10$ . The fast-shaper is simulated as a practical differentiator with a characteristic time of 15 ns and a maximum gain of  $\sim \times 18$ . The circuit resistors and capacitors were chosen to match these features. (Bottom) transfer function magnitude in dB as a function of the signal frequency. In the left panel, we show the transfer for the pre-amplifier deduced in equation 7.2. The frequency cutoff of 10 MHz and an amplification factor of  $\times 10$  is obtained, as desired. In the right panel, we show the magnitude of the fast-shaper transfer as deduced in equation 7.6. In this case, a maximum amplification factor of  $\sim \times 18$  and a frequency of 10 MHz was obtained.

selected to obtain a low-pass filter with a frequency cutoff of 10 MHz and an amplification factor of  $\times 10$  in the first case, and a shaping time of 15 ns with a maximum gain of  $\sim \times 18$ , for the second case. From these models, the transfer functions to implement in the simulation were calculated. To convolute the electronics transfer with the SiPM signal we follow the method explained in 6.2.1, for which we need to separate the transfer into their real and imaginary parts. Concerning the pre-amplifier, the transfer function of an active low-pass filter can be written as

$$\begin{aligned} H(s) &= k \frac{1}{1 + \tau s} = k \frac{1}{1 + i\omega\tau} \\ &= k \frac{1 - i\omega\tau}{1 + (\omega\tau)^2} \end{aligned} \tag{7.1}$$

where  $\tau = R_f C_f$  is the circuit characteristic time and  $k = -\frac{R_f}{R_s}$  is the amplification factor or gain. Then, it is obtained

$$\begin{aligned}
Re[H(s)] &= k \frac{1}{1 + (\omega\tau)^2} \\
Im[H(s)] &= -k \frac{\omega\tau}{1 + (\omega\tau)^2} \\
|H(\omega)| &= \frac{|k|}{1 + (\omega\tau)^2} \sqrt{1 + (\omega\tau)^2} = |k| \sqrt{\frac{1 + (\omega\tau)^2}{(1 + (\omega\tau)^2)^2}} \\
|H(\omega)| &= \frac{|k|}{\sqrt{1 + (\omega\tau)^2}}
\end{aligned} \tag{7.2}$$

For the fast-shaper, we can write the transfer of a practical differentiator as:

$$\begin{aligned}
H(s) &= -\frac{R_f(sC_s)}{(1 + sC_fR_f)(1 + sC_sR_s)} \\
&= -\frac{R_f(i\omega C_s)}{(1 + i\omega C_f R_f)(1 + i\omega C_s R_s)}
\end{aligned} \tag{7.3}$$

Then,

$$\begin{aligned}
H(\omega) &= -\frac{R_f(i\omega C_s)}{(1 + i\omega C_f R_f)(1 + i\omega C_s R_s)} \\
&= -\frac{R_f}{R_s} \frac{(i\omega\tau)}{(1 + i\omega\tau)^2} = -k \frac{(i\omega\tau)}{(1 + i\omega\tau)^2},
\end{aligned} \tag{7.4}$$

where  $\tau = C_f R_f = C_s R_s$ , and  $k = \frac{R_f}{R_s}$ . Then, we can write:

$$\begin{aligned}
H(\omega) &= -k \frac{(i\omega\tau)}{(1 - (\omega\tau)^2 + 2i\omega\tau)} \\
&= -k \frac{(i\omega\tau)(1 - (\omega\tau)^2 - i2\omega\tau)}{(1 - (\omega\tau)^2)^2 + (2\omega\tau)^2} \\
&= -k \frac{2(\omega\tau)^2 + i\omega\tau(1 - (\omega\tau)^2)}{(1 - (\omega\tau)^2)^2 + (2\omega\tau)^2} \\
&= -k \frac{2(\omega\tau)^2 + i\omega\tau(1 - (\omega\tau)^2)}{1 - 2(\omega\tau)^2 + (\omega\tau)^4 + 4(\omega\tau)^2} \\
&= -k \frac{2(\omega\tau)^2 + i\omega\tau(1 - (\omega\tau)^2)}{(1 + (\omega\tau)^2)^2}
\end{aligned} \tag{7.5}$$

If we split the equations into their real and imaginary parts, we obtain

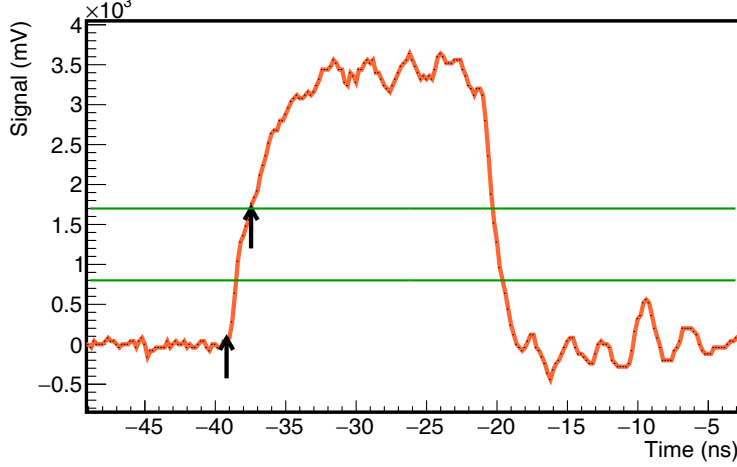


**Figure 7.2:** Example signal at the discriminator output. The black arrows show the limits within which the rise time was estimated. The green lines show the 0.8 V and 1.7 V levels)

$$\begin{aligned}
 Re[H(\omega)] &= -k \frac{2(\omega\tau)^2}{(1 + (\omega\tau)^2)^2} \\
 Im[H(\omega)] &= -k \frac{\omega\tau(1 - (\omega\tau)^2)}{(1 + (\omega\tau)^2)^2} \\
 \implies |H(\omega)| &= k \frac{\omega\tau}{1 + (\omega\tau)^2}
 \end{aligned} \tag{7.6}$$

In the bottom panels of Fig. 7.1 we show the magnitude of the transfers for the pre-amplifier (left) and the fast-shaper (right). An amplification factor of  $\times 10$  and frequency cutoff of 10 MHz was obtained for the pre-amplifier. For the fast-shaper, we obtained a maximum amplification of  $\sim \times 18$  at 10 MHz.

The fast-shaper output is processed by a discriminator (also integrated into the CITIROC) and then sampled with an FPGA. As a rough approximation, the discriminator outputs a signal of 3.3 V if the fast-shaper is above the discriminator threshold and 0 V otherwise. In more detail, the discriminator has a typical rise and fall time that affects the signal sampling. The FPGA outputs a “1” if the discriminator signal is above 1.7 V and a “0” if it is below 0.8 V. If one of the FPGA flip-flops is clocked when the discriminator signal is between 0.8 V and 1.7 V then the FPGA output is undetermined. To tune the simulation to this behavior, we obtained a data set of signals after at the discriminator output with an oscilloscope. In Fig. 7.2, we show an example of this output, where the signal rise time, relevant to the FPGA sampling, are indicated with black arrows. We assumed that if the FPGA samples during this rise time, then a “0” is output. To include this in the simulation we have obtained the rise time of 1000 signals as in Fig. 7.2. To this aim, we implemented an algorithm that locates the start time when the signal is above  $2\sigma$  from the baseline. Then, it looks for the discriminator signal to be above 1.7 V and uses a first order interpolation to find the 1.7 V level. We obtained a mean rise time, which is calculated as the difference between the start time and the 1.7 V level, of  $(1.51 \pm 0.01)$  ns.

We simulate the last step of the *counter* mode electronics, which consist in the discriminator and the FPGA, by generating a 3.3 V signal if the fast-shaper is above the discriminator

threshold during more than 1.51 ns and generating a signal of 0 V otherwise. Finally, we output a “1” in the binary trace if the resulting signal is 3.3 V and a “0” if it is 0 V.

### 7.1.2 Validation of the *counter* mode simulation

After implementing the transfer functions of the *counter* mode, we can proceed to simulate dark-rate curves (using the crosstalk probability obtained in 6.1), which is of interest since it lays the ground of the SiPM calibration presented in [88]. We compare, in the top panel of Fig. 7.3, the simulated dark-rate curve with the curve measured in the laboratory (as shown in section 4.1). We are able to simulate the calibration curve with good accuracy, obtaining similar values to the laboratory data for both PEs and crosstalk. It is worth noticing that in order to obtain a “1” in the FPGA output the fast-shaper signal needs to be over the discriminator threshold during more than 1.51 ns (see 7.1.1). To study the impact of the discriminator rise time on the SiPM calibration, we compare the single-PE peak directly obtained after the fast-shaper with the value obtained in the simulated calibration. In the middle panel of Fig. 7.3, we show the histogram of the single-PE amplitude at the fast-shaper output, where we obtained a mean peak amplitude of  $(35.39 \pm 0.04)$  mV. The single-PE amplitude obtained from the calibration (by fitting the derivative of the dark-rate curve) is  $(24.3 \pm 0.3)$  DAC counts. Since each DAC step equals to 1.3 mV [87], the amplitude obtained is  $(31.6 \pm 0.4)$  mV. Therefore, in this case, the effect of the discriminator rise time produces a bias in the estimation of the single-PE amplitude of approximately 11%.

Using the *counter* mode simulation, we can also generate binary traces. An example of a simulated single-muon is shown in the bottom panel of Fig. 7.3. We simulate the muon signal as explained in section 6.3.2, which is the input of the electronics. We display the output after the pre-amplifier and the fast-shaper, the discriminator response and the FPGA sampling. The fast-shaper undershooting can also be seen, which has no effect in the muon detector performance.

To further validate the *counter* mode simulations, we compare the two main features of the binary traces relevant to the UMD performance: the signal width and the muon detection efficiency. To this aim, we used the laboratory data presented in 4.4 and simulations of single-muon signals at different positions on the scintillator strip.

In the top panel of Fig. 7.4 the counting efficiency is shown at different positions of the scintillator strip using a discriminator threshold of 2.5 and 3.5 PE as we explained in section 4.4.2. The efficiency was estimated using laboratory data, simulations and a Poissonian prediction based on the measured number of PEs as a function of the position on the strip (see section 6.3.1). This prediction consists of integrating a Poissonian distribution between the discriminator threshold (2.5 or 3.5 PE) and infinity, where the mean number of PEs is the measured at each position on the strip (see Fig. 6.11). The Poissonian prediction shows the efficiency loss produced by muon signals with less than 2.5 PE (or 3.5 PE), which is the *counter* mode threshold. Therefore, the agreement between data and prediction denotes that there is not a significant efficiency loss in the signal processing or in the reconstruction analysis (as discussed in section 4.4.1). Furthermore, the binary channel simulations provide an accurate description of the *counter* mode efficiency.

In Fig. 7.4 bottom panel the signal width at different positions on the scintillator strip is shown, both with laboratory (as in section 4.4) and simulated data and discriminator thresholds of 2.5 and 3.5 PE. We show at each position on the scintillator strip the mean value and standard deviation of the width distribution of single-muon signals. The simulation is compatible with the laboratory data, which implies that this simulation provides an accurate description of the *counter* mode performance.

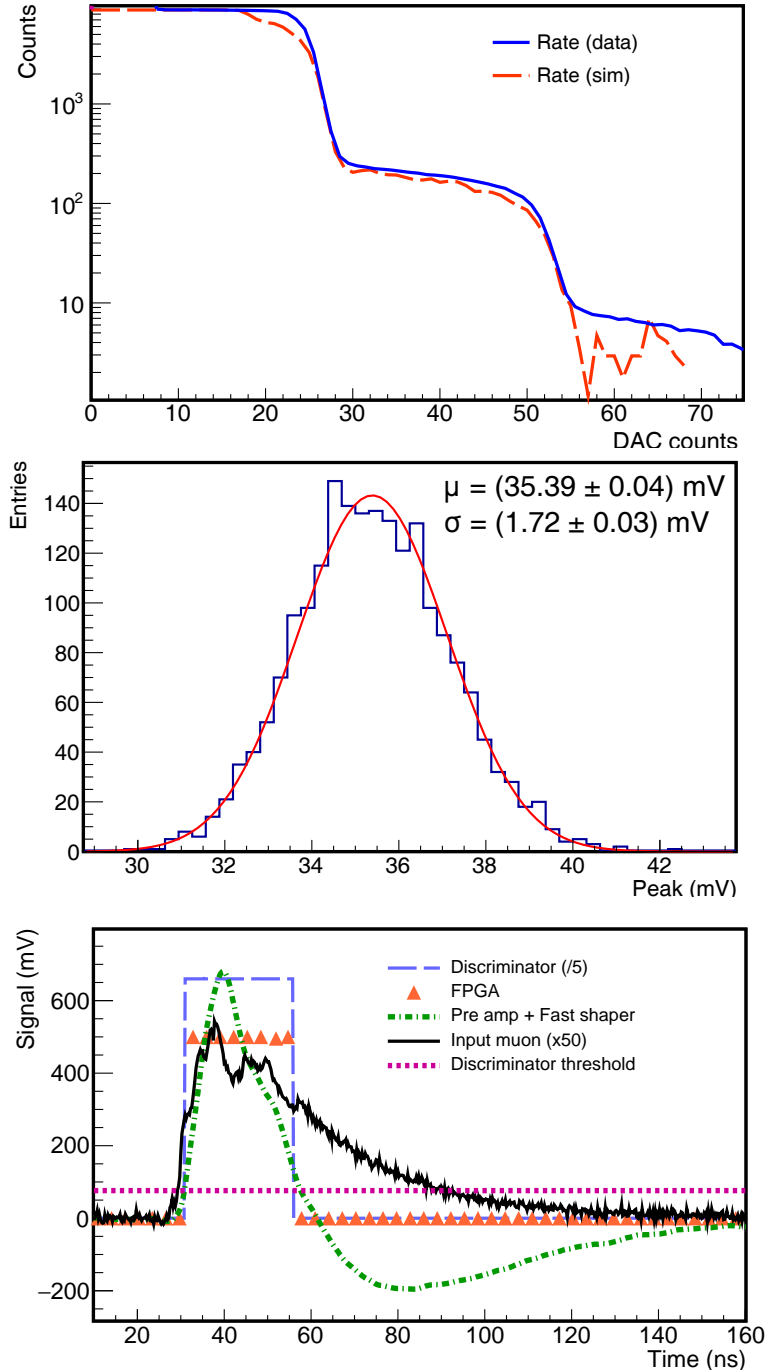


**Figure 7.3:** (Top) dark-rate curves used to calibrate the SiPMs. We show the curves obtained using laboratory data and the *counter* mode simulation. The single-PE amplitude obtained with the simulation is  $(24.3 \pm 0.3)$  DAC counts ( $(31.6 \pm 0.4)$  mV). (Middle) histogram of the signal maximum amplitude at the fast-shaper output for single-PE events. The peak amplitude obtained is  $(35.39 \pm 0.04)$  mV. (Bottom) simulated single-muon trace in the *counter* mode. The signal from the SiPM and the discriminator pulse are re-scaled for illustration. The FPGA outputs a “1”-bit in the binary trace when the fast-shaper output is above the discriminator threshold during more than 1.51 ns.

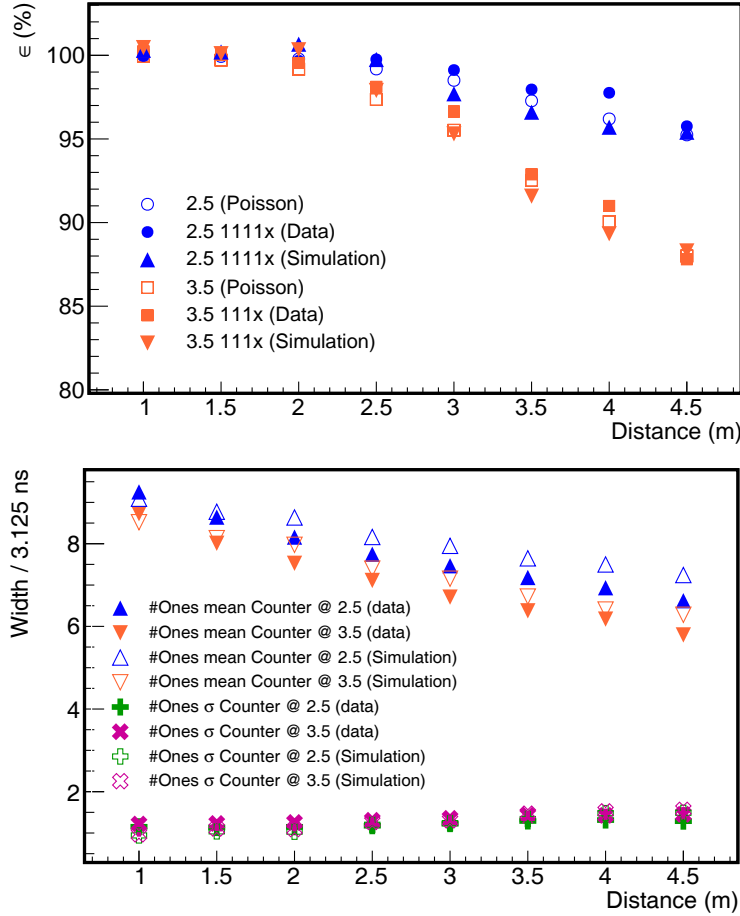


**Figure 7.4:** (Top) Efficiency as a function of the position on the scintillator strip estimated from laboratory data, simulations, and a Poissonian prediction using a discriminator threshold of 2.5 and 3.5 PE. (Bottom) mean signal width over sample time and  $\sigma$  in the *counter* mode as a function of the position on the scintillator strip with both laboratory and simulated data of single muons. The signal widths were obtained also with two different discriminator thresholds: 2.5 and 3.5 PE.

## 7.2 Integrator mode simulation

As we explained in section 3.6, the *integrator* mode electronics, first analogically sums in two steps of adders all 64 SiPM signals and then amplifies the result with a low- and a high-gain amplifier. The amplifier outputs are sampled with an ADC at a speed of 160 MHz, and an ADC step of 0.12207 mV into two traces of 1024 samples. In Fig. 7.5, we show a diagram of the *integrator* mode steps. The first step consists of four adders, each one sums the signal of 16 SiPMs, thus at the output of the first step, four analog signals are obtained. The second step consists of one adder, that sums these four signals into one. The result is amplified in the third step and then sampled with the ADCs.

### 7.2.1 Model and transfer functions

To simulate each of the electronics blocks, we need the component transfer functions. In this case, since the electronics are not integrated into an ASIC, we were able to obtain the components transfers using a SPICE [117] simulation. We fitted the simulated data with the transfer function of a low-pass filter as in equation 7.2 to obtain a simplified transfer for implementing in the electronics simulation. In Fig. 7.6 we show the results of the SPICE

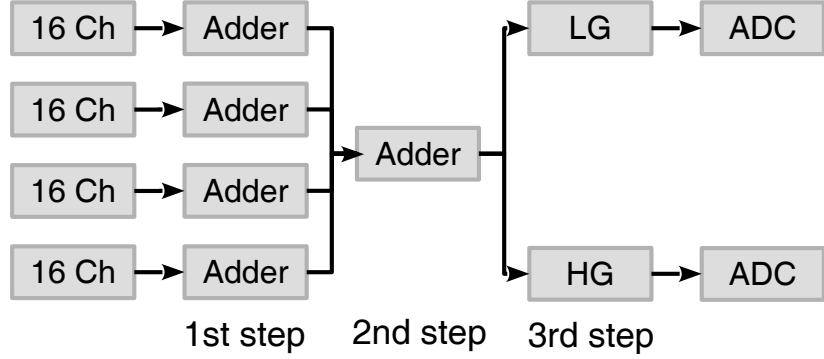


**Figure 7.5:** Schematics of the *integrator* mode electronics. The 64 SiPM signals are analogically added up with two steps of adders, and the result is amplified with a low- and high-gain amplifiers. Amplifier outputs are sampled with two ADCs.

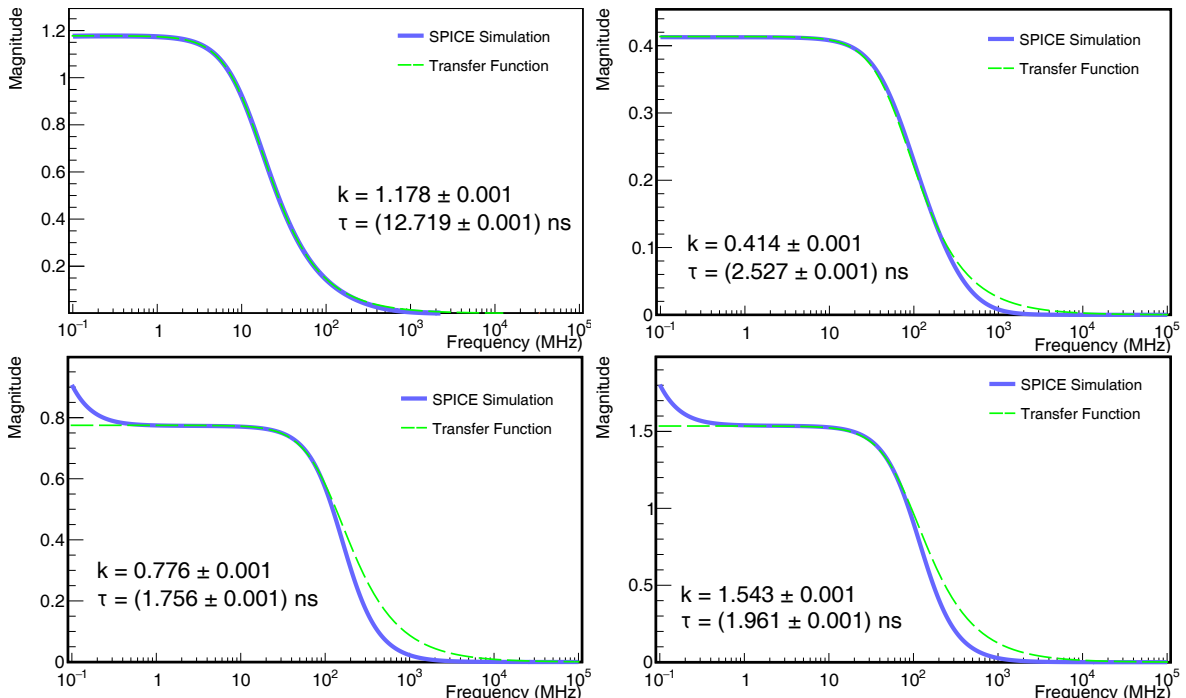


**Figure 7.6:** Transfer functions of the *integrator* mode electronics. The transfers were fit with the of a low-pass filter as described in equation 7.2. (Top) transfer functions of the adders in the *integrator* mode electronics. In the left (right) panel we show the transfer function corresponding to the adders of the first (second) block. The frequency cutoff of the first step is  $\sim 10$  MHz, while the frequency cutoff of the second step is  $\sim 100$  MHz. This implies that the signal timing is determined by the first transfer in the electronics. (Bottom) transfer functions of the low-gain (high-gain) amplifier. In both cases, the frequency cutoff is  $\sim 100$  MHz, and the difference lays on the amplification factor.

simulation and the fits. In the top left (right) panel, the transfer for the adders in the first (second) step is shown. In the bottom left (right) panel the transfer of the low-gain (high-gain) amplifier is shown. If we consider the components cutoff frequency to be the frequency for which the output of the circuit is -3 dB (or falls 30% in magnitude) of the nominal pass-band value, it is apparent that the first step of adders determines the signal timing. As we show in Fig. 7.6, the adders in the first step introduce a frequency cutoff of  $\sim 10$  MHz, whereas the other steps introduce a frequency cutoff of  $\sim 100$  MHz. In this sense, the electronics response after the first step of adders is rather flat in frequency.

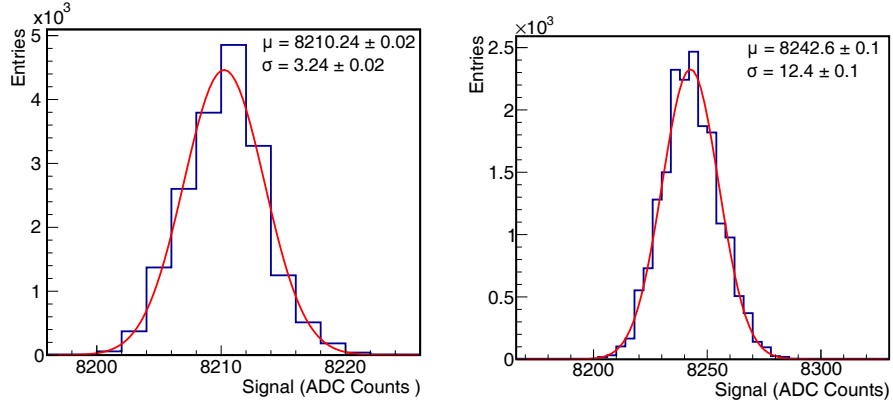


**Figure 7.7:** Baseline histograms of the low- (left) and high-gain (right) channels. The fit result units are ADC counts, in all cases.

The final step of the *integrator* mode simulation is the ADCs. To simulate the ADC sampling we group the amplifier outputs in bins of 6.25 ns, and we extract the maximum amplitude reached in each bin. We then obtain the ADC counts per sample by diving the signal amplitude by the ADC step, which is 0.12207 mV/bit.

### 7.2.2 Validation of the *integrator* mode simulation

An important characteristic of the ADC channel is the baseline fluctuation due to the SiPMs dark rate, as explained in section 5.1.2, which may have a significant impact on the signal charge estimations. For this reason, we included these fluctuations by analyzing the *integrator* mode baseline. In Fig. 7.7, we show the baselines histograms for the low- (left) and high-gain (right) channels, from which the signal offset and baseline fluctuation are obtained. To implement the baseline offsets and fluctuations in the simulation we used a random generator with a Gaussian distribution in which the parameters are extracted from fits as shown in Fig. 7.7.

To illustrate the behavior of the *integrator* mode simulation, we show in Fig. 7.8 an example of a muon signal at 2 m from the scintillator strip with laboratory data (top) and simulations (bottom). In the simulated trace, we show the muon analog signal and the output after the ADCs. It is apparent that the baseline fluctuations were also simulated. The expected agreement in the overall features is quite satisfying.

To estimate the number of muons with the ADC channel, we compute the signal charge and divided it by the mean charge of a single muon. For this reason, the main feature in the *integrator* mode relevant to the UMD performance is the signal charge and its fluctuation. Therefore, the detector simulation is expected to provide a good description of this feature. In the top panel of Fig. 7.9 we show the mean charge attenuation as a function of the position on the scintillator strip, along with the charge RMS as presented in section 5.1.2. We show for comparison, the results obtained with the simulation. The *integrator* mode simulation describes accurately the laboratory data.

Another feature to consider is the detector saturation which determines the upper limit of the UMD detection range. We show in the bottom panel of Fig. 7.9 the signal charge in the simulation as a function of the number of muons simultaneously injected. We determine the position on the scintillator strip where the muon is injected with a uniform random generator which provides values between 1 m and 4 m and we simulate the muon signal as explained in section 6.3. We identified the saturation point where the signal charge starts to lose linearity with respect to the number of injected muons. The high-gain channel starts to

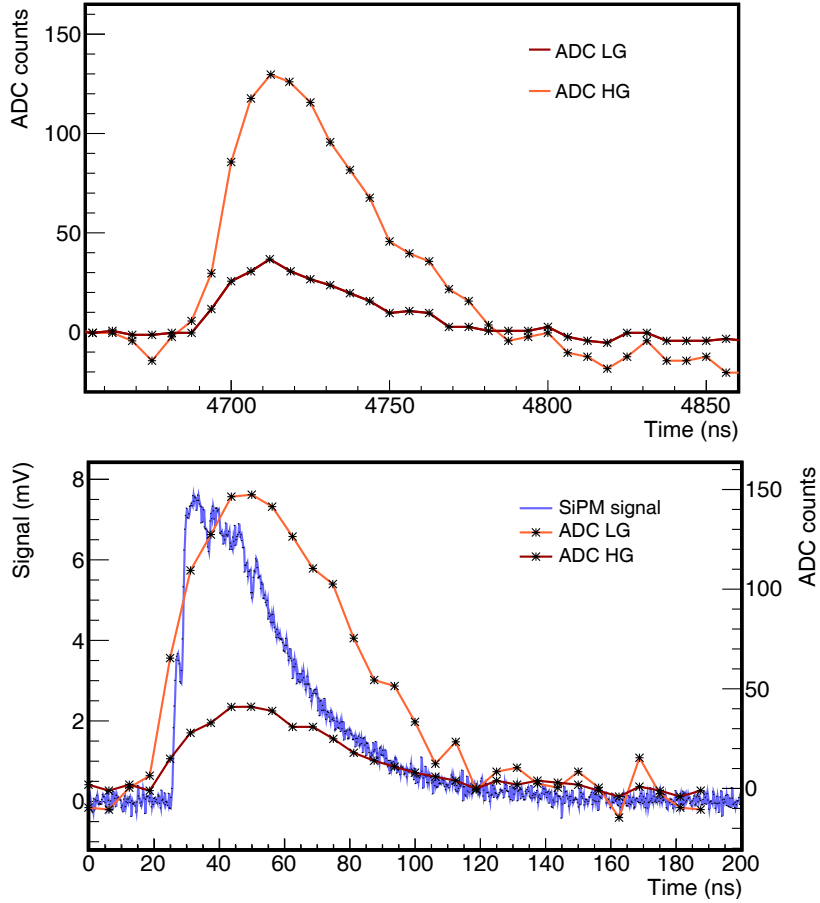


**Figure 7.8:** (Top) example ADC channel traces measured at 2 m on the scintillator strip. The low- and high-gain traces are displayed. (Bottom) example of simulated ADC traces at 2 m on the scintillator strip. The muon input signal, which corresponds to the SiPM analog signal is displayed, along with the ADC outputs.

saturate at  $\sim$  simultaneous 80 muons, while the low-gain channel starts to saturate at  $\sim$  300 muons. Note that this is a rough estimation as we did not introduce the time profile of the arriving muons. Also the number of PEs per muon is estimated using only laboratory data and the actual saturation number per detection position will be 3 times larger since there are  $10\text{ m}^2$  modules per position. We discuss the ADC channel saturation in detailed in chapter 8.

### 7.3 Implementation in Offline

In the previous sections, we have described how the SiPM simulations were developed, and how these were validated with laboratory data. In this section, we show how the SiPM simulations are implemented in the Auger Offline software [110].

#### 7.3.1 UMD SiPM simulations

In previous versions of the Offline framework, the AMIGA UMD modules simulations would only run with PMTs as photodetectors. Since there are still analysis ongoing with PMT data, we implemented the SiPM simulation without losing compatibility with PMTs. To this aim, a new attribute was created at `Mdet::Module` level to use either PMTs or SiPMs in

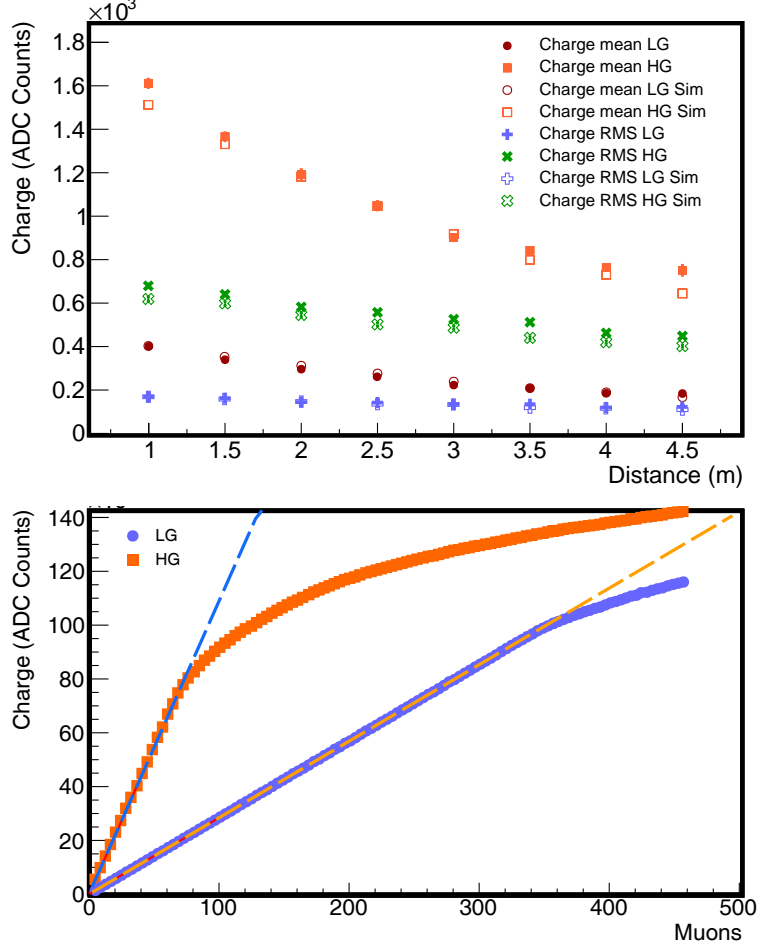


**Figure 7.9:** (Top) signal charge as a function of the position on the scintillator strip. We show the signal mean charge and RMS obtained using laboratory data as we explained in section 5.1.2. We also display the result using the *integrator* mode simulation. The simulation and data are consistent. (Bottom) signal charge of simulated data as a function of the number of injected muons. The high-gain (low-gain) channel starts to lose linearity when  $\sim 80$  muons ( $\sim 300$  muons) are injected simultaneously.

the AMIGA modules. All SiPM new attributes and classes are implemented in the `MDetector` in the same way as PMTs.

In the current version of Offline, the UMD simulations are only compatible with Geant4 9 [118] libraries. However, efforts are being made to achieve compatibility with Geant4 10 libraries. In this version, the parametrization of the PE-attenuation curve is no longer used (see section 6.3.1), and scintillators and optical fibers are simulated from first principles. However, the version compatible with Geant4 10 has not yet been tested and tuned. Nevertheless, the SiPM simulation is compatible with the two versions of Geant4 libraries. In Fig. 7.10 we show two module sequences, which run with the different version of Geant4 libraries and how the modules should be set up. In the simulation compatible with Geant4 10, the `UnderGrindInjectorAG` and `EdepSimulatorAG` modules are no longer used, since the scintillator simulation is included in the `G4StationSimulator` module. The `MdCounterSimulatorAG` has to be configured to run with each version of the `ModuleSequence` through the `simType` attribute. Independently of the `ModuleSequence` and the Geant4 libraries, the `MModelConfig.xml.in` can be configured to use either PMT or SiPM with the `phohtoDetector`

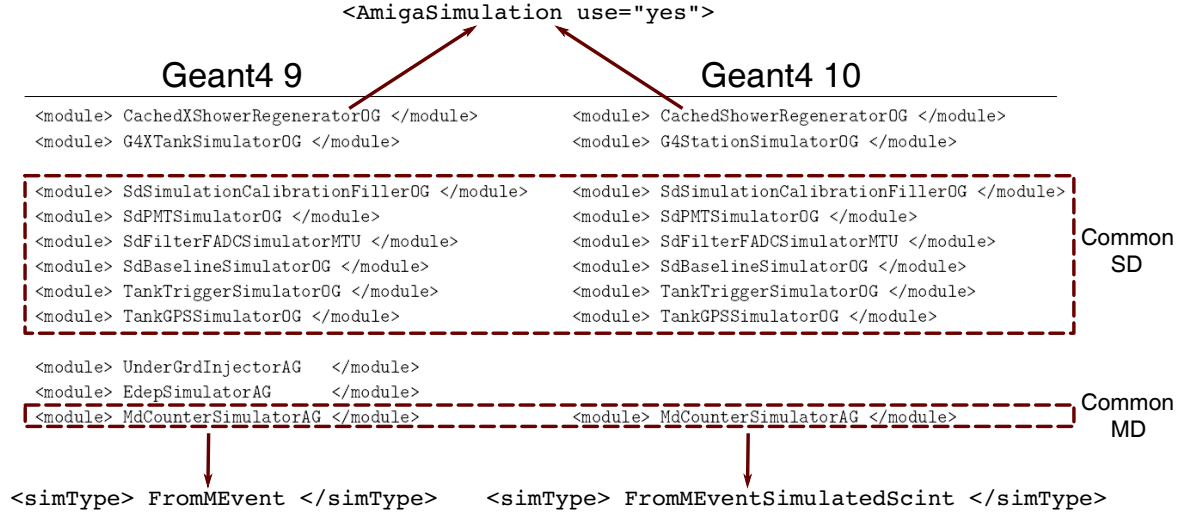


**Figure 7.10:** Module sequences compatible with the Geant4 9 (left) and Geant4 10 (right) libraries.

attribute. The `MdCounterSimulatorAG` module uses this attribute to run with PMT or the SiPMs and it is prepared to run with both version of the Geant4 libraries.

In the `MdCounterSimulatorAG` module, new attributes to configure the simulation run were created. The *integratorSimType* allows to set up the ADC channel simulations in a slow or fast mode. In the slow mode, each transfer block is applied step by step, while in the fast mode all transfer blocks are applied in one iteration improving the performance. The *injectNoiseBinary* attribute has been created to simulate the binary channel noise as described in section 4.3. If this option is on, the simulation injects noise randomly (with a probability of 5.8%) in the binary traces. This noise consists of sequences of "1"s, whose width is a Gaussian fluctuation of the mean width (5.6 samples) of noise signals. Finally the *includeBaseLineFluctuationsIntegrator* attribute allows to introduce the baseline fluctuations in the *integrator* mode, as explained in 7.2.2. The SiPM simulation is available in the Offline trunk from revision 32430.

To implement the SiPM simulations in Offline, we have simulated all the electronics steps in one. To this aim, instead of convoluting each of the transfer functions steps by step, we convolute successive transfer functions at ones. This can be done as:

$$f_{out}(\omega) = f_{in}(\omega) H_1(\omega) H_2(\omega)$$

$$V_{out} = \mathcal{F}^{-1}(f_{in}(\omega) H_1(\omega) H_2(\omega))$$

Then, in Fourier space, we split all functions into their real and imaginary parts:

$$Re[f_{out}(\omega)] = Re[f_{in}(\omega)]Re[H_1(\omega)] - Im[f_{in}(\omega)]Im[H_1(\omega)]$$

$$Im[f_{out}(\omega)] = Re[f_{in}(\omega)]Im[H_1(\omega)] + Im[f_{in}(\omega)]Re[H_1(\omega)]$$

And if we convolute more than one transfer:

$$Re[f_{out}(\omega)] = Re[f_{in}(\omega)]Re[H_1(\omega) H_2(\omega)] - Im[f_{in}(\omega)]Im[H_1(\omega) H_2(\omega)]$$

For  $H_1(\omega) H_2(\omega)$ :

$$Re[H_1(\omega) H_2(\omega)] = Re[H_1(\omega)]Re[H_2(\omega)] - Im[H_1(\omega)]Im[H_2(\omega)]$$

$$Im[H_1(\omega) H_2(\omega)] = Re[H_1(\omega)]Im[H_2(\omega)] + Im[H_1(\omega)]Re[H_2(\omega)]$$

Then,

$$\begin{aligned} \text{Re}[f_{out}(\omega)] &= \text{Re}[f_{in}(\omega)]\text{Re}[H_1(\omega)H_2(\omega)] - \text{Im}[f_{in}(\omega)]\text{Im}[H_1(\omega)H_2(\omega)] \\ &= \text{Re}[f_{in}(\omega)](\text{Re}[H_1(\omega)]\text{Re}[H_2(\omega)] - \text{Im}[H_1(\omega)]\text{Im}[H_2(\omega)]) \\ &\quad - \text{Im}[f_{in}(\omega)](\text{Re}[H_1(\omega)]\text{Im}[H_2(\omega)] + \text{Im}[H_1(\omega)]\text{Re}[H_2(\omega)]) \end{aligned}$$

And

$$\begin{aligned} \text{Im}[f_{out}(\omega)] &= \text{Re}[f_{in}(\omega)]\text{Im}[H_1(\omega)H_2(\omega)] + \text{Im}[f_{in}(\omega)]\text{Re}[H_1(\omega)H_2(\omega)] \\ &= \text{Re}[f_{in}(\omega)](\text{Re}[H_1(\omega)]\text{Im}[H_2(\omega)] + \text{Im}[H_1(\omega)]\text{Re}[H_2(\omega)]) \\ &\quad + \text{Im}[f_{in}(\omega)](\text{Re}[H_1(\omega)]\text{Re}[H_2(\omega)] - \text{Im}[H_1(\omega)]\text{Im}[H_2(\omega)]) \end{aligned}$$

Using the polar form, where:

$$H_1(\omega) = |z| \exp i\phi = M[H_1(\omega)] \exp i\Phi[H_1(\omega)]$$

It is obtained:

$$\begin{aligned} M[f_{out}(\omega)] &= M[f_{in}(\omega)]M[H_1(\omega)H_2(\omega)] \\ M[f_{out}(\omega)] &= M[f_{in}(\omega)]M[H_1(\omega)]M[H_2(\omega)] \\ \Phi[f_{out}(\omega)] &= \Phi[f_{in}(\omega)] + \Phi[H_1(\omega)H_2(\omega)] \\ \Phi[f_{out}(\omega)] &= \Phi[f_{in}(\omega)] + \Phi[H_1(\omega)] + \Phi[H_2(\omega)] \end{aligned}$$

Using this simplification we convolute the transfer functions of the *counter* mode pre-amplifier and fast-shaper in one step. For the *integrator* mode, we first add the signal of the 64 SiPMs and then, we convolute the transfer of all blocks at once.

### 7.3.2 The UMD component in the EventBrowser

As the production phase of the AMIGA underground muon detector has recently started, it is important to improve the access to the UMD data within the Auger Offline software [110]. A pending task was the integration of the underground muon detector in the Event Browser [119], the events visualization GUI<sup>1</sup> of Offline. To this end, a new UMD tab, similar to the SD tab [120], has been created. This tab facilitates access to the raw and reconstructed UMD data from Advanced Data Summary Trees (ADSTs [120]). The new tab is activated when there is a UMD event associated to its respective SD event. Furthermore, the tab is only enabled when the UMD event is not empty (i.e.: raw traces are found in the event).

In data from the engineering array, AMIGA modules may be equipped with an array of 64 SiPMs or with a 64 channel multi-anode PMT (see 3.6.3). In both scenarios, the modules may work simultaneously as a *counter* and as an *integrator* 3.6. The Event Browser is compatible with both the SiPM modules and the PMT modules.

#### General view

In Fig. 7.11 an example of the general view of the UMD tab is shown (Auger ID: 160915817600). The screen is divided in four main panels:

---

<sup>1</sup>Graphic User Interface

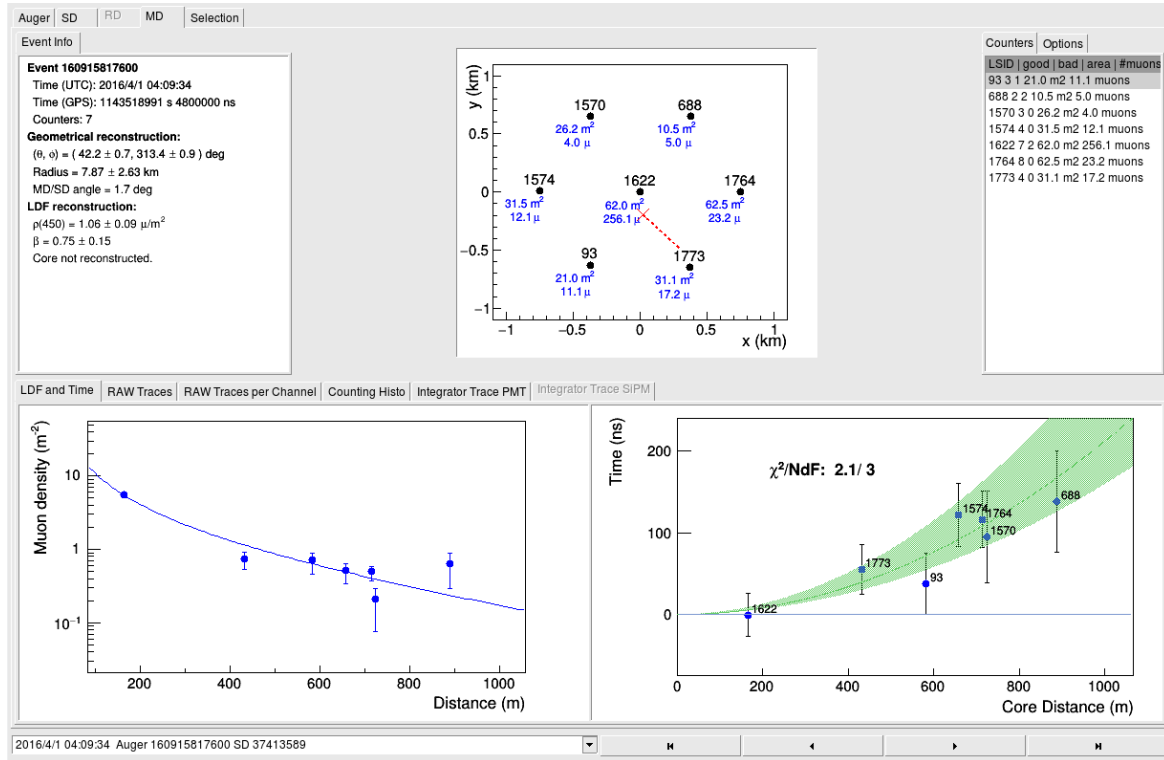


**Figure 7.11:** The UMD tab for an example event (Auger ID 160915817600), see description in the text. Top left panel: the event and reconstruction summary. Top middle panel: the SD stations map. Top right panel: *counter* list tab and options tab. Bottom panel: the user can switch between different features by selecting the sub-tabs.

- Top left panel - the event information that includes the reconstruction data (if available) along with the event general information.
- Top middle panel - the station map where the muon detector associated WCD and the shower core position are displayed.
- Top right panel - the *counter* list tab, showing the module status and the number of muons per counter, and the options tab.
- Bottom panel - the user can switch between different features of the reconstructed and raw data by selecting the sub tabs. These features are:
  - Time residuals and lateral distribution function (LDF).
  - Raw binary traces.
  - Raw binary traces per channel.
  - Counting histograms.
  - ADC traces.

At the bottom of the Event Browser, the event selector remains available. In the case that an event with no UMD information is selected while the UMD tab is active, the application switches automatically to the Auger tab and disables the UMD tab.

### Event information, stations map and list

The Event Info panel shows the event ID and the time stamps in tandem with the parameters fitted in the UMD reconstruction (if available). If the Muon Lateral Distribution Function (MLDF) [121] or/and the geometrical reconstruction [101] were not performed, a label indicating this would be displayed. For the geometrical reconstruction, the zenith ( $\theta$ ) and azimuth ( $\phi$ ) angles, the radius of curvature of the shower front and the angle between the SD and the UMD reconstructed axes (MD/SD angle) are shown. In the LDF section, the muon density at 450 m ( $\rho_{450}$ ), the LDF slope ( $\beta$ ), the core position (x,y) and the distance between the reconstructed SD and UMD core positions ( $\Delta x, \Delta y$ ) are displayed. If the radius of curvature or the MLDF slope was fixed during the reconstruction, errors would not be displayed and a *fixed* label would be shown instead. The example in Fig. 7.11 shows an event with a fitted  $\beta$  and radius of curvature.

In the top middle panel, the station map is displayed. Currently, only the deployed engineering array is shown. If a station has no associated *counter* (due to an error in the WCD acquisition), a gray marker is displayed; otherwise, a black marker is shown. Along with the marker and the station number, the *counter* effective area and the number of muons are displayed in blue. If a *counter* is saturated, a low limit for the number of muons along with a *saturated* label is shown. In red, the core position and the shower axis from the UMD reconstruction are shown if available; otherwise, the core position and shower axis from the SD reconstruction are displayed.

In the top right panel, the *counter* list can be found. Each line shows the *counter* ID, the number of *good* modules (not rejected), the number of *bad* modules (rejected), the effective area of the *counter* and the number of muons (or the lower limit with a saturation label if the *counter* is saturated).

### LDF and time residuals

In the bottom panel, the LDF and Time tab is selected by default. In the left panel, the reconstructed MLDF is plotted along with the data points corresponding to the density of muons ( $\rho_\mu$ ) measured by each muon detector. Details concerning the MLDF reconstruction can be found in [121]. If the MLDF reconstruction was not performed, a label indicating this would be shown.

In the right panel, the time residuals are plotted only if the geometrical reconstruction was performed. This residuals plot contains a point for each UMD *counter* included in the geometrical reconstruction. The X coordinate is the distance from the *counter* to the UMD axis. The time observable used in the UMD is the median arrival time of the muons at each *counter* ( $t_{50}$ ) [101]. A time residual is the difference between the  $t_{50}$  of each *counter* and the arrival time of a plane or spherical shower front. The user can switch between the two visualizations with a radio button in the options tab. The first option shows the time residuals relative to a plane shower front oriented with the UMD axis. In blue, the plane front is plotted. In green, the fitted spherical plane is also displayed. During the reconstruction, the curvature radius might be set free or fixed; if the curvature radius was free, a band error around the spherical shower front is also plotted. If the curvature option is selected, the time residuals are plotted relative to the spherical front. In blue, the spherical front is shown. Finally, the  $\chi^2$  and the number of degrees of freedom of the geometrical fit are always displayed.

### Traces

Along with the LDF tab, the traces tabs display the traces for all modules of a muon detector. When a station is selected from the *counter* list, each tab displays a different module attribute.

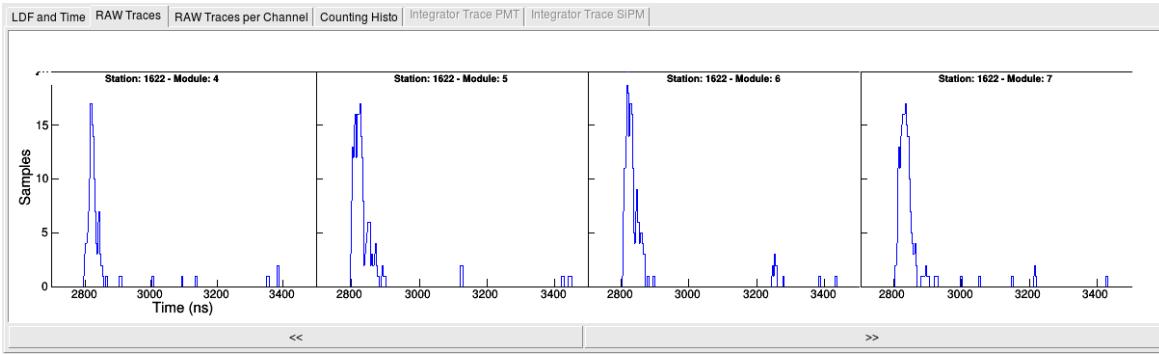


**Figure 7.12:** Raw traces tab. The 64 binary traces collapsed on the X axis. In each time bin (of 3.125 ns) a maximum of 64 samples (one per channel) can be obtained.

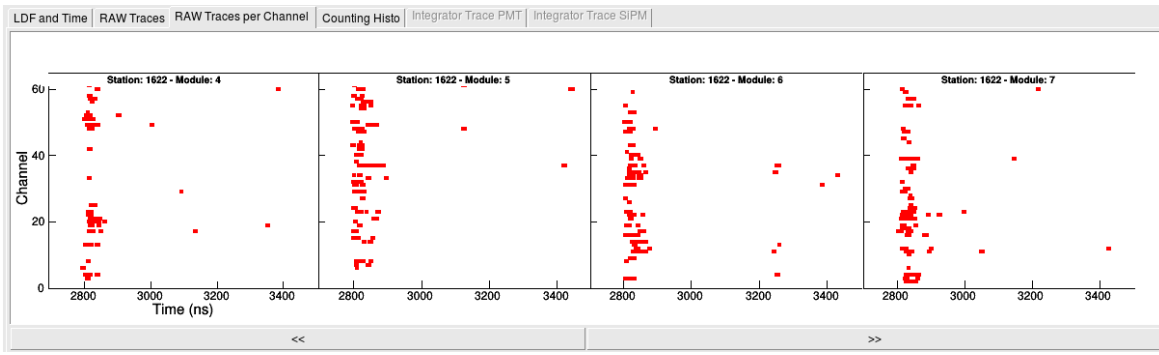


**Figure 7.13:** Raw binary traces per channel. Each line on the Y-axis corresponds to one channel. If in the corresponding time bin a positive sample in the trace is found, a red marker is plotted. The raw traces (Fig. 7.12) are the projection on the X-axis of these plots.

At the bottom of the panel, the navigation arrows can be found. A maximum of four modules is displayed simultaneously. With the navigation arrows, the user can surf the different modules, if there are more than four of them available in the selected station. If a module is rejected, the module attributes are not shown.

The first attribute is the raw trace (Fig. 7.12). For each module, the number of channels with positive samples is shown. The traces length are 1024 (2048) bits for the PMT (SiPM) electronics. The sampling rate of the electronics is 3.125 ns [115]. The traces are synchronized to the SD station to assign a GPS time stamp [101].

On Fig. 7.13, an example of the raw binary traces per channel is shown. Each row on the Y-axis corresponds to one of the 64 detector scintillator strips. For each positive sample in the trace, a red marker is plotted. The raw traces (Fig. 7.12) are the projection on the X-axis of these graphs. This feature can be used to easily detect problems in individual channels.

The third attribute is the counting histogram (Fig. 7.14). The counting histogram is the result of applying the counting strategy to the raw data (Fig. 7.12) (see section 4.4.1). The time bin size corresponds to the inhibition window used in the reconstruction [119]. A maximum of 64 entries can be obtained in each time bin. In this case, the module would be saturated.

The last two tabs display the *integrator* traces. Both PMT and SiPM electronics may have an *integrator* mode. Only one of these tabs can be accessed at the time. The *integrator* traces are enabled/disable according to if they are available or not in each module. To access this feature, it is needed to use a CDAS version above v5r8 during the reconstruction. An example of the SiPM traces can be found in Fig. 7.15. The SiPM modules have a low- and a high-gain output, while for the PMT modules only one output is available. The traces lengths are 1024 and 512 bins respectively and the sampling time is 6.25 ns. If a counter with

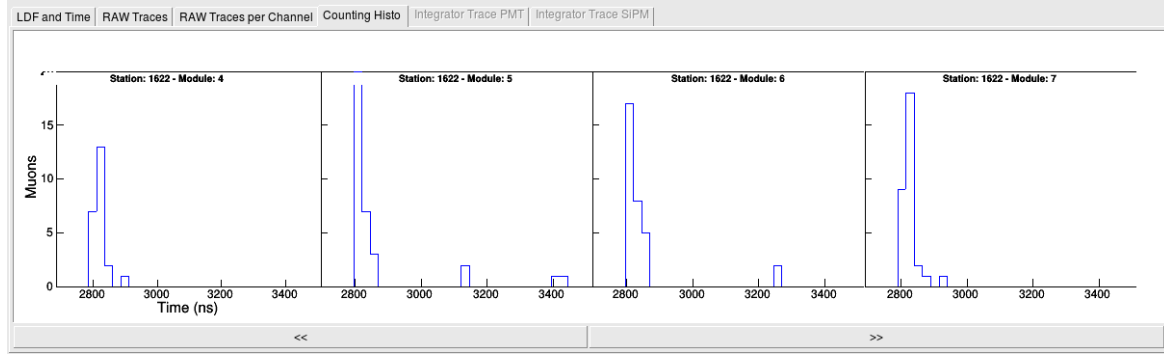


**Figure 7.14:** Counting histograms. The counting histogram is the result of applying the counting strategy to the raw traces (see Fig. 7.12) [121].

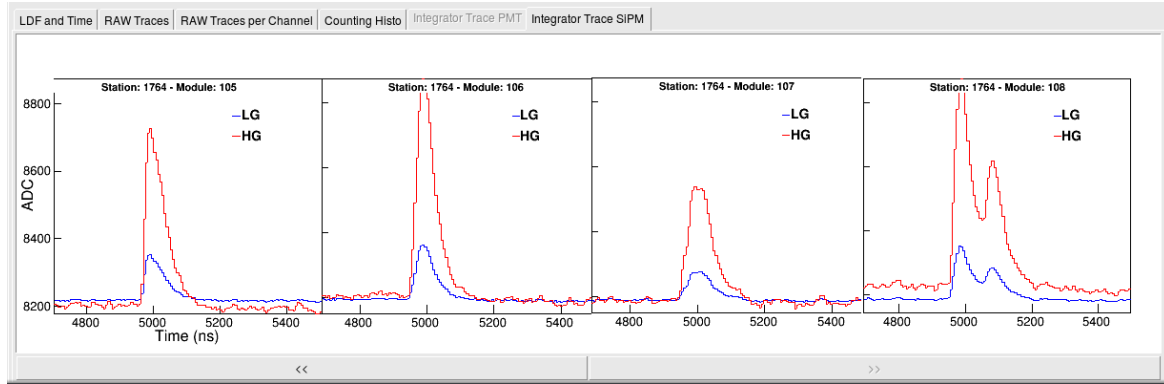


**Figure 7.15:** Integrator mode traces. An example of modules with SiPM is shown. In this case, the low- and a high-gain traces are available.

no SiPM is selected while the SiPM *integrator* traces tab is active, the application switches automatically to the LDF and time residuals tab.

### SD/MD combined view

In the options tab at the top left of the UMD window, a check box to enable/disable an SD/MD combined view can be found. When this check box is activated, the plots are updated to display the SD information along with the MD. An example is displayed in Fig. 7.16. First of all, the map shows the SD stations timing in color code and the signal intensity corresponding to the marker size. For the LDF plot, the SD markers are shown with the LDF fit. The vertical axis shows the measured signals at the corresponding UMD and SD stations. In addition, in the time residuals plot, the SD times referred to the UMD shower front, are plotted. For some outlier events, the SD and UMD markers might be far apart. This feature will allow the visual identification of such anomalous events. Finally, in the raw traces tab and in the counting histograms tab, the average WCD trace (average from the 3 PMTs) is displayed in red. The combined view of the counting histogram tab can be found in Fig. 7.17.

## 7.4 Conclusions of this chapter

In this chapter, we have achieved the simulation of the SiPM output signal including the electronics response. The transfer functions of both *counter* and *integrator* modes were described and applied to analog simulated signals to obtain digital outputs. Data acquired

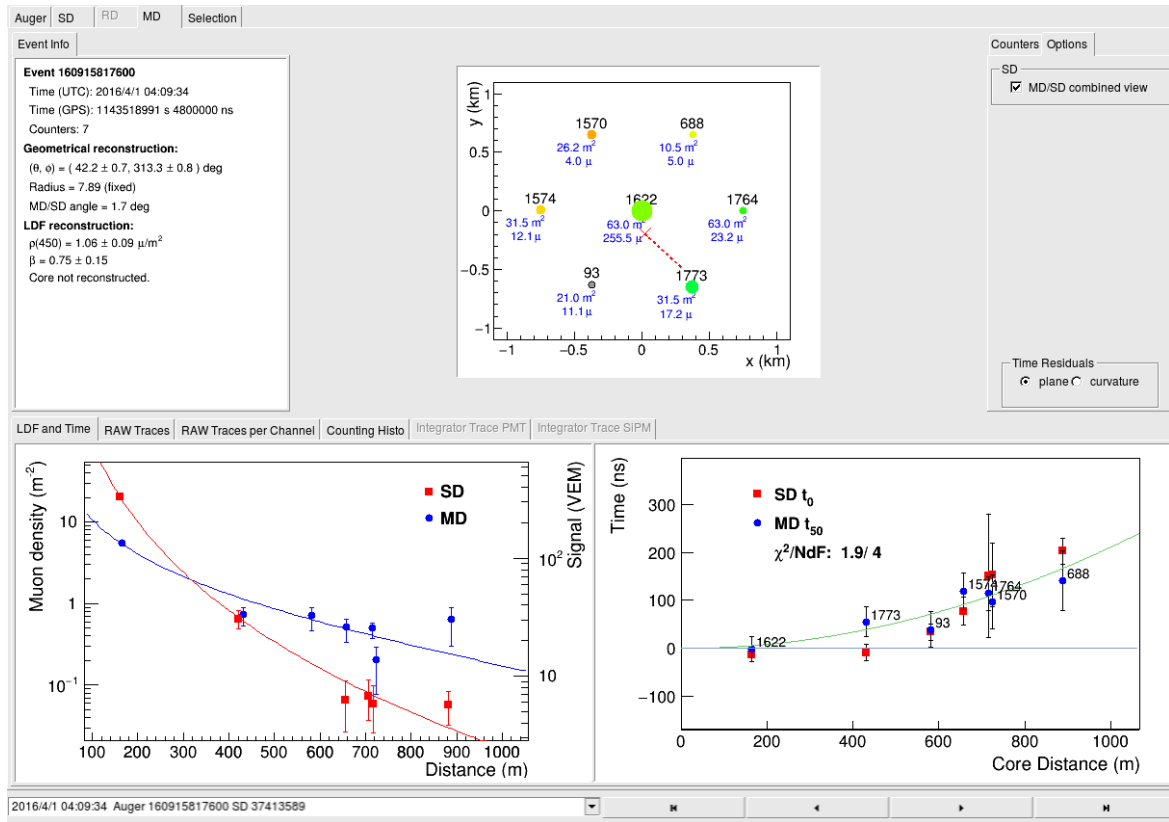


**Figure 7.16:** An example of the combined view. The SD map, LDF, time residuals, and average traces are displayed in tandem with the UMD information. This visualization can be activated or deactivated through the check box in the options tab.

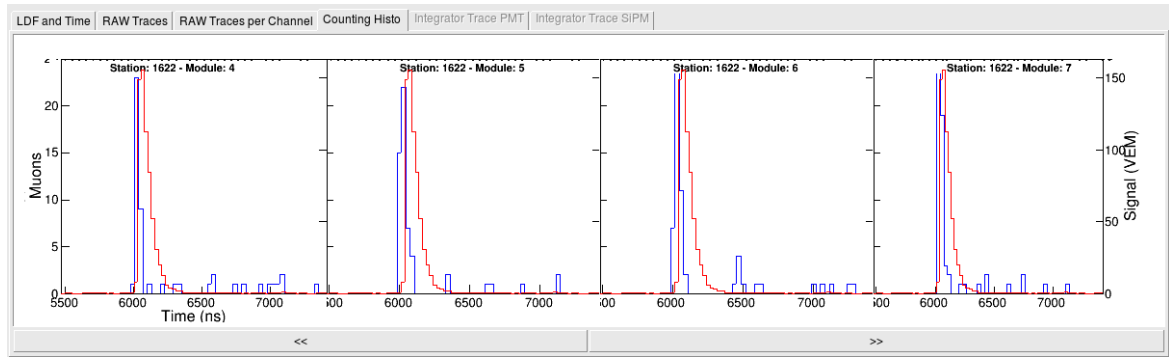


**Figure 7.17:** Example of the combined view for the counting histograms. In red, the WCD average trace is plotted.

with the standard AMIGA electronics kit was used to validate these simulations. We have proven that simulation and laboratory data are compatible.

We also described the implementation of the SiPM simulation in the `Offline` software. New attributes were created to configure the simulation run. Also, the integration of the UMD in the `Offline` Event Browser has been presented. With the new UMD tab, users can visualize different features of the UMD event reconstruction. These software upgrades will be used by the whole Collaboration when simulating the underground muon detector.

---

---

# CHAPTER 8

---

## UMD optimization and Proton-Iron discrimination

To estimate the muon content of extensive air showers with the underground muon detector, it is necessary to understand and correct any reconstruction bias. This work has been previously performed with PMT simulations [109]. However, since SiPMs perform very differently from PMTs (see section 3.6.3), this analysis has to be repeated for UMD modules with SiPMs. To this aim, we have used sets of simulated air showers available in the KIT cluster and the Auger `Offline` framework, where we recently implemented SiPM simulations (see chapters 6 and 7).

In section 8.1, we briefly describe the simulation library and configuration used in the analysis in this chapter. In section 8.2, we describe the bias sources in the *counter* mode, and we quantify them using shower simulations. We then propose and test a correction to achieve an unbiased reconstruction within this working mode.

In section 8.3, we discuss the angular dependence of the signal charge in the *integrator* mode and test the calibration of the ADC channel. The resolution and saturation of both modes are analyzed in detail in section 8.4, where we define working ranges for each. In section 8.5, we reconstruct the muon content of air showers using the *counter* and *integrator* modes separately and, also, combining both. Finally, we briefly discuss the discrimination power of the UMD for proton- and iron-like primary cosmic rays using different approaches.

### 8.1 The simulation library

Since it is not possible to study the signals produced by air showers in the muon detector with a laboratory setup, we used air shower simulations to attain a better understanding of the detector effects on the estimation of the number of particles impinging on the muon detector. Monte-Carlo simulations of extensive air showers and their corresponding detector responses are crucial tools to verify reconstruction methods of physical shower quantities from the observed detector signals. Furthermore, the theoretical predictions used to interpret the experimental data are attained via simulations. In this chapter, we have used simulated air showers generated with the COsmic Ray Simulations for KAscade (CORSIKA) software [122]. Libraries of air showers simulated with different hadronic interaction models are already available in the KIT cluster for proton and iron primary cosmic rays with different energies and geometries.

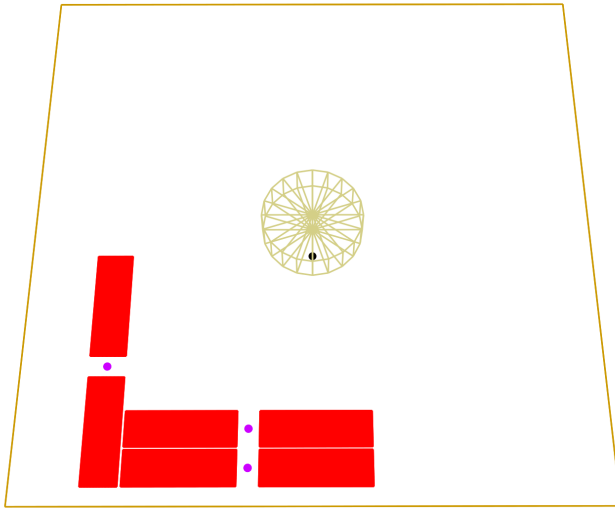


**Figure 8.1:** Schematic of one station setup in the simulation run. The WCD and the three  $10\text{ m}^2$  modules of the muon detector are displayed.

For the purpose of this work, we have used air showers simulated with the hadronic model EPOS-LHC, since, from the available libraries, this is the model that best describes the muon content of air showers<sup>1</sup>. Each air shower is simulated for a given energy, type of primary cosmic ray, and geometry. The axis of air showers is defined by a zenith angle ( $\theta$ ), which is the inclination angle of the shower axis with respect to the upwards pointing z-axis and by the azimuth angle ( $\varphi$ ) defined as the direction of the shower on the ground plane. Showers produced by primary cosmic rays with fixed energies of  $10^{17}\text{ eV}$ ,  $10^{17.5}\text{ eV}$ ,  $10^{18}\text{ eV}$  and  $10^{18.5}\text{ eV}$  and fixed zenith angles of  $0^\circ$ ,  $12^\circ$ ,  $22^\circ$ ,  $32^\circ$ ,  $38^\circ$  and  $48^\circ$  were used. The azimuth angle of the shower axis was uniformly distributed.

SD and UMD responses are simulated with the `Offline` framework [110]. We use the revision number r29804 of the trunk in the subversion repository since SiPM simulations have not yet been implemented in any official release. For each energy-z zenith angle bin, we have used 120 simulated CORSIKA showers. To improve statistics, each shower is injected ten times inside an array of WCDs, which are distributed on a triangular grid with a 750 m spacing. Next to each WCD, a  $30\text{ m}^2$  muon detector, which consists of three  $10\text{ m}^2$  modules, is buried at a soil depth of 2.3 m. A schematic of the WCD and the muon detector at each position of the grid is shown in Fig. 8.1. In each simulation run, the shower is injected randomly at different positions of the array, so the position of the shower core is uniformly distributed.

---

<sup>1</sup>However, it is not the best in describing the timing of shower signals [123].

## 8.2 Counter mode optimization

In this section, we describe the bias sources in the *counter* mode, quantify these biases using shower simulations in the *Offline* framework, and propose a correction to remove them. We use vertical proton and iron showers ( $\theta = 0^\circ$ ) to analyze the impact of the choice of the inhibition window on the reconstruction bias and to describe the effects of the soil in the estimation of the shower muon content. Then, we analyze the dependency of the reconstruction bias on the shower axis using proton and iron shower simulations with energies of  $10^{17}$  eV,  $10^{17.5}$  eV,  $10^{18}$  eV and  $10^{18.5}$  eV and fixed zenith angles of  $0^\circ, 12^\circ, 22^\circ, 32^\circ, 38^\circ$  and  $48^\circ$ .

### 8.2.1 Bias sources

We have identified two types of biases in the *counter* mode: the first related to the timing of particles in the shower and the second related to the shower geometry. Before analyzing these effects with simulated data, we present a brief description of each.

#### Pile-up

As presented in section 4.4.1, to reconstruct the number of muons with the *counter* mode, we need to define an inhibition window to avoid counting the same muon more than once. However, if two particles reach the same scintillator strip within this window, the second particle will not be detected and the number of muons in the shower will be under-estimated. We refer to this effect as muon “pile-up”. Given 64 strips hit by  $k$  muons, the probability of missing the  $k+1$  muon within the same inhibition window is  $\frac{k}{64}$ . It is apparent how the probability of under-counting depends on the number of impinging particles. However, this can be considered in the reconstruction with a maximum-likelihood approach assuming a binomial distribution [108]. In a  $6.4 \mu\text{s}$  trace and assuming an inhibition window of 37.5 ns (see section 4.4.1), we have  $\frac{6.4 \mu\text{s}}{37.5 \text{ ns}} \sim 170$  windows. For a window  $w_i$  and 64 scintillator strips, if we count  $k_i$  muons in  $w_i$ , then the true number of muons in this windows is estimated by

$$\hat{\mu}_i = -64 \ln \left( 1 - \frac{k_i}{64} \right). \quad (8.1)$$

The total number of muons is estimated by summing over all time windows

$$\hat{\mu} = -64 \sum_{i=1}^{170} \ln \left( 1 - \frac{k_i}{64} \right). \quad (8.2)$$

#### Corner clipping muons

Corner clipping muons are a source of bias in the *counter* mode since they may produce under- or over-counting. These are muons that deposit energy in more than one scintillator strip and therefore might be interpreted as 0 (not enough energy in either channel), 1 (enough energy in a single channel) or 2 (enough energy in both channels) muons. The frequency of corner clipping depends on the direction of the shower axis as we illustrate in Fig. 8.2, where a frontal view of two scintillator strips is displayed in the left panel and a schematic of a whole module is displayed in the right panel. The reconstruction bias is determined by the muon inclination angle (which is relative to the zenith angle of the shower axis ( $\theta$ ) with respect to the upwards pointing z-axis) and to the difference in azimuth ( $\Delta\varphi_m = \varphi - \varphi_m$ ) between the direction of the shower and the orientation of the module in the ground plane. A muon can only pass through two neighboring strips if both  $\theta$  and  $\Delta\varphi_m$  are distinct from

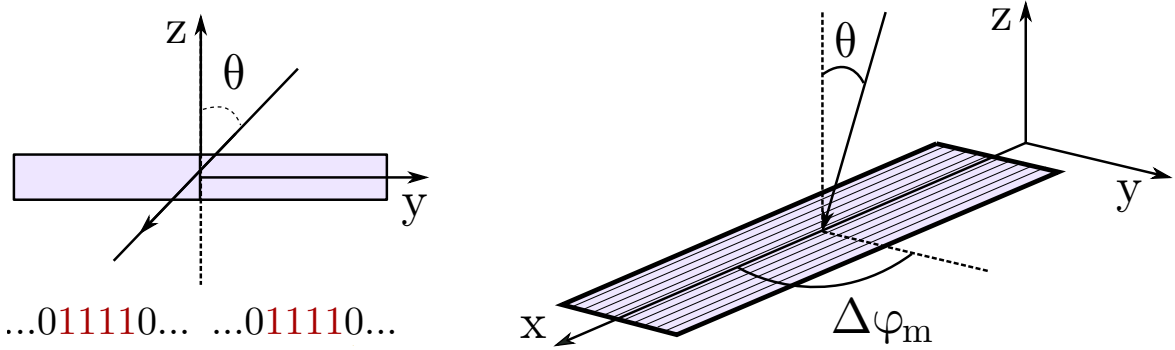


**Figure 8.2:** (Left) schematic of frontal view of two scintillator strips and an impinging muon depositing energy in both. We also show an example of the binary output of the *counter* mode for this event. (Right) schematic of the geometric dependency of corner clipping muons. The probability of finding the muon signal in two adjacent strips depends both on the zenith angle of the shower axis ( $\theta$ ) and on the difference between the azimuth angle of the shower axis and the orientation of the UMD module ( $\Delta\phi_m$ )

zero as illustrated in Fig. 8.2. Maximal corner clipping occurs for  $\Delta\phi_m = 90^\circ$ , i.e. when the muon momentum is perpendicular to the orientation of the scintillator strips, and increases with  $\theta$ .

### Knock-on electrons

When a muon propagates through the soil and reaches the muon detector, it transfers energy to the medium mainly via ionization [124, 125]. As a result, knock-on electrons are emitted from atoms of the soil. When these electrons impinge on the muon detector, they produce signals similar to those of muons. A (non-typical) example is illustrated in Table 8.1, obtained from a vertical ( $\theta = 0^\circ$ ) proton shower simulated with an energy of  $10^{18}$  eV. In this particular event, only one muon impinged on the detector and deposited energy in two scintillator strips producing over-counting. Furthermore, three other scintillator strips had signal from electrons, which produced two over-counts. The electron on the scintillator strip with Id. 52 produced a signal in the detector but this was rejected by the counting strategy since it did not meet the  $1111x$  criteria (see section 4.4.1). As a result, despite only one muon reaching the detector, four muons were counted. We have chosen this example to illustrate the effect of knock-on electrons from the soil. However, this is not a typical scenario, since electrons from the soil tend to leave a smaller amount of deposit energy (if any) and produce signals that are rejected by the counting strategy. These electrons have a bigger impact on the *integrator* mode since in this case the signals from the 64 scintillator strips are summed. This leads to signals with higher charge than those measured in the laboratory. We discuss this in further detail in section 8.4.

In the *Offline* software, it is possible to set the simulation run to inject only muons in the underground muon detector. This feature is useful to understand the impact of electrons from the soil on the reconstruction. To this aim, we have simulated proton showers with an energy of  $10^{18}$  eV and zenith angles of  $0^\circ$ ,  $12^\circ$ ,  $32^\circ$ , and  $48^\circ$ . We have run simulations with two configurations: injecting all particles and injecting only muons. To illustrate the effects of electrons in the reconstruction we analyzed the reconstruction bias

$$\left( \frac{N_\mu^{\text{Rec}} - N_\mu^{\text{MC}}}{N_\mu^{\text{MC}}} \right), \quad (8.3)$$

Scintillator Id	Particle	Energy deposit (MeV)	Binary trace (cropped)
26	$e^-$	3.09	
26	$e^-$	1.99	...00011111111000...
26	$e^-$	1.90	
27	$e^-$	1.89	...00001111111000...
50	$\mu^-$	1.63	...00011111110000...
51	$\mu^-$	0.32	...00011111110000...
52	$e^-$	0.01	...000000100000000...

**Table 8.1:** Particles that deposit energy in a UMD module for a proton vertical shower with energy  $10^{18}$  eV.

where  $N_\mu^{Rec}$  is the number of muons reconstructed with the muon detector and  $N_\mu^{MC}$  is the number of muons in the Monte-Carlo simulation, which we normally refer to as the number of injected muons. In Fig. 8.3, we show the reconstruction bias as a function of the distance of the muon detector to the shower core (extracted from the SD reconstruction) for  $\theta = 0^\circ$ ,  $\theta = 12^\circ$ ,  $\theta = 32^\circ$ , and  $\theta = 48^\circ$ . It is apparent how the over-counting increases with the zenith angle, which is expected since the probability of having corner clipping muons also increases with the zenith angle, as explained before. When injecting only muons, the over-counting is produced by corner clipping muons; however, when injecting all particles, the bias is produced by both corner clipping muons and electrons from the soil. The results in Fig. 8.3 show that each of these effects contributes to approximately half of the total bias. In section 8.2.1 we quantify the reconstruction bias as a function of the distance to the shower axis.

### 8.2.2 Inhibition window selection

When counting muons in the field, several effects need to be considered that can not be measured in the laboratory. First of all, in the laboratory, we only have access to single-muon events from background, while in the field we intend to measure muons of extensive air showers. The muon pile-up is only relevant when detecting a higher number of particles. Furthermore, the light-output per impinging muon is higher when the detector is underground since knock-on particles emitted by atoms in the soil deposit energy in the scintillator strips. For this reason, it is necessary to review the selected counting strategy, particularly, to tune the inhibition window and avoid under-counting due to pile-up and over-counting due to wider signals. To this aim, we have used vertical ( $\theta = 0^\circ$ ) proton and iron showers with energies of  $10^{18}$  eV and  $10^{18.5}$  eV in the `Offline` software to assess the reconstruction bias when the effects of corner clipping muons are minimal.

To understand the impact of the choice of the inhibition window on the reconstruction bias, we have tested three window sizes in the simulated data: 31.5 ns, 37.5 ns, and 44 ns. In Fig. 8.4, we present the reconstruction bias (previously defined in equation 8.3) as a function of the injected number of muons (top panels) and as a function of the distance to the shower core extracted from the SD reconstruction (bottom panels) for proton (left panels) and iron (right panels) showers with an energy of  $10^{18}$  eV. The same result for an energy of  $10^{18.5}$  eV is shown in Fig. 8.5. It is apparent that when the energy of the primary cosmic ray is increased, the detector saturates further from the shower core, which is expected considering that the number of muons in air showers grows exponentially with the energy of the primary cosmic ray. It is also worth noting that the detector saturates closer from the core for iron primaries

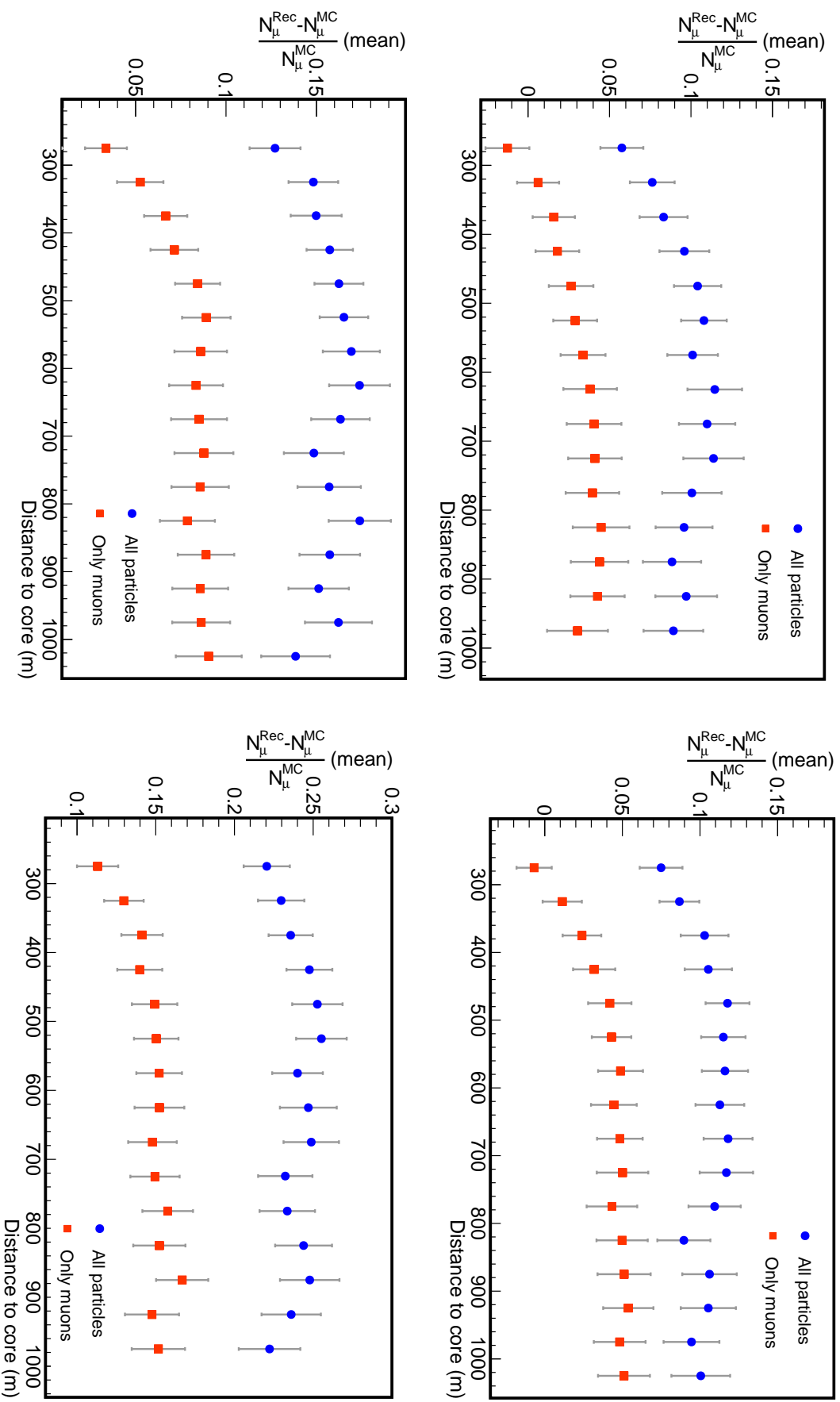


**Figure 8.3:** Reconstruction bias with the *counter* mode as a function of the distance to the shower core (extracted from the SD reconstruction) for air shower simulations with an energy of  $10^{18}$  eV and zenith angles of  $0^\circ$  (top-left),  $12^\circ$  (top-right),  $32^\circ$  (bottom-left), and  $48^\circ$  (bottom-right). We show the result for simulations in which only muons were injected in the muon detector and for simulation in which all particles (including electrons from the soil) were injected.

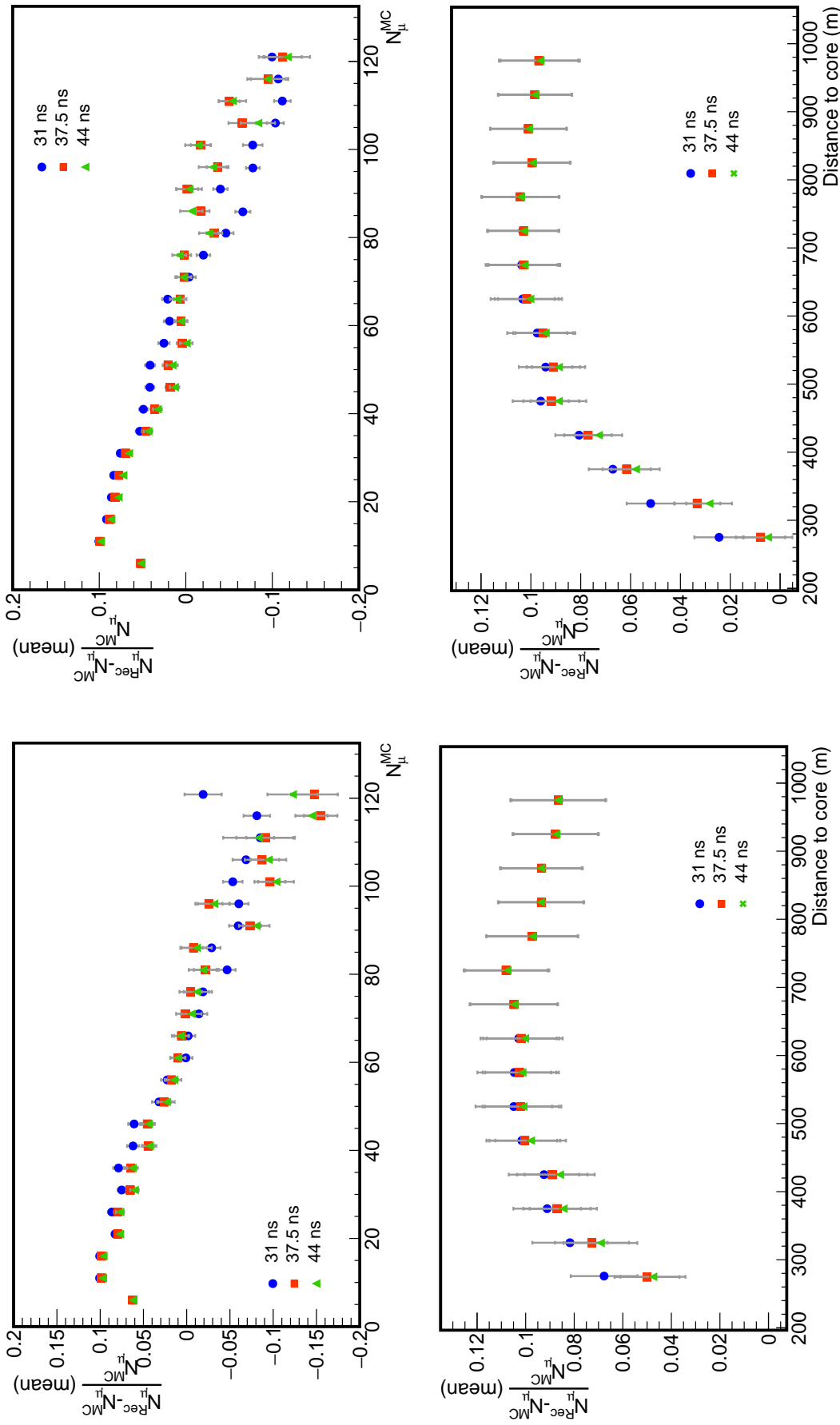


**Figure 8.4:** Reconstruction bias with the *counter* mode as a function of the number of injected muons (top panels) and as a function of the distance to the shower core extracted from the SD reconstruction (bottom panels) for proton (left panels) and iron (right panels) showers with an energy of  $10^{18}$  eV. To analyze the impact on the inhibition window in the reconstruction bias we show the results after reconstructing the simulated data with three inhibition windows: 31 ns, 37.5 ns and 44 ns.

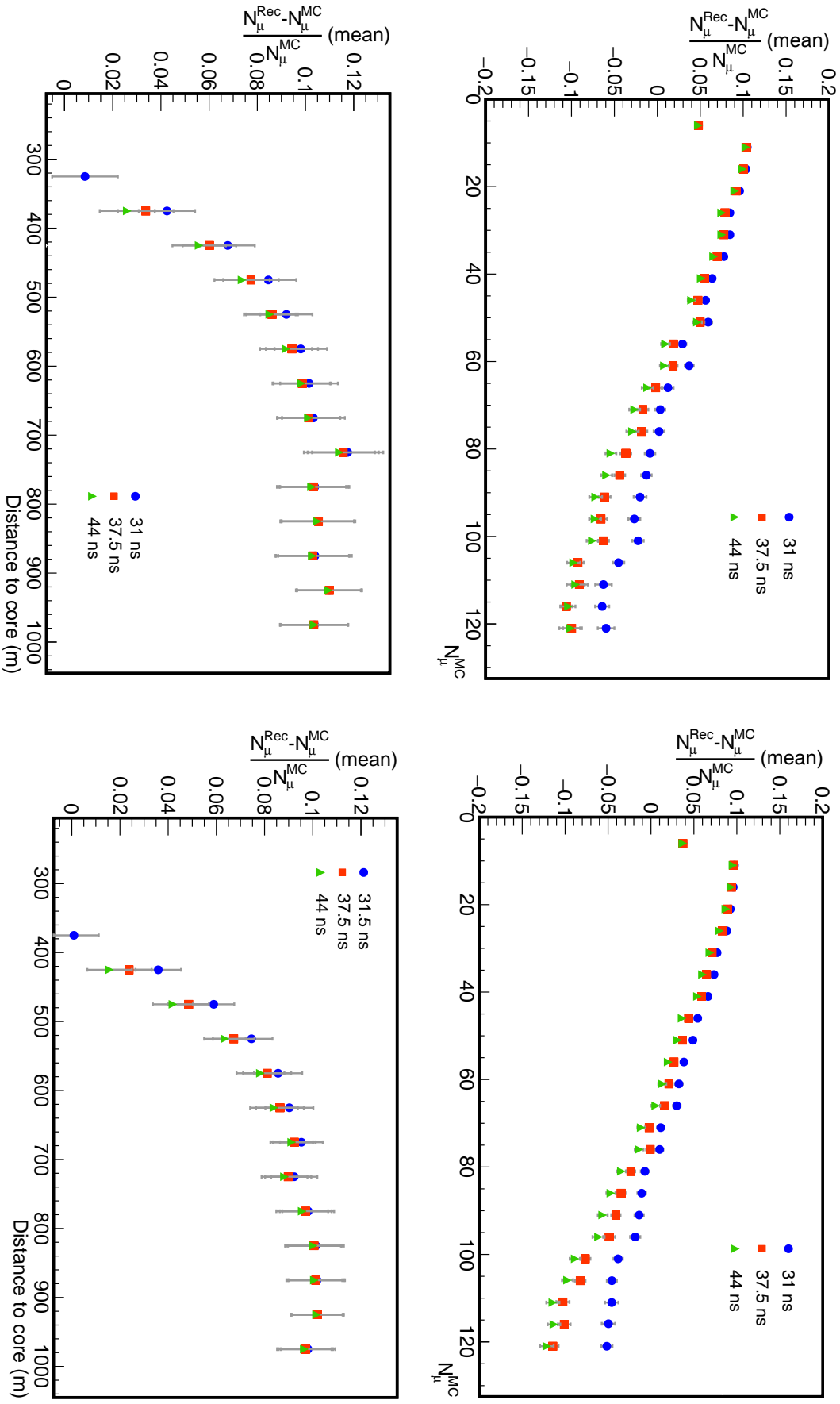


**Figure 8.5:** Reconstruction bias with the *counter* mode as a function of the number of injected muons (top panels) and as a function of the distance to the shower core extracted from the SD reconstruction (bottom panel) for proton (left panels) and iron (right panels) showers with an energy of  $10^{18}$  eV. To analyze the impact on the inhibition window in the reconstruction bias we show the results after reconstructing the simulated data with three inhibition windows: 31 ns, 37.5 ns and 44 ns.

than for proton. This is also expected since iron showers have a higher muon content as explained in section 1.3.

In the *counter* mode, the reconstruction bias is produced by both muon over-counting (due to corner clipping muons, electrons from the soil and wide muon signals) and muon under-counting (mainly due to particle pile-up). The pile-up probability increases with the number of muons and as it is shown in Fig. 8.4 and 8.5 as does the bias. Since there is no clear improvement by selecting a different inhibition window from the one previously determined, the window used in the reconstruction with the *counter* mode was finally set to 37.5 ns (as explained in section 4.4.1).

### 8.2.3 Geometric correction

As shown in Fig. 8.2, a particle that impinges on more than one scintillator strip may lead to under- or over-counting. This leads to a reconstruction bias, whose magnitude depends on the direction of the particles impinging on the detector, which in turn depends on the orientation of the shower axis. Therefore, the dependency of the bias on both azimuth and zenith angles of the shower axis must be studied. Since the reconstruction of the shower geometry with the UMD is achievable but still under development [101], we extract the geometry of the air shower from the SD [45, 46] reconstruction. Proton and iron showers with energies of  $10^{17}$  eV,  $10^{17.5}$  eV,  $10^{18}$  eV, and  $10^{18.5}$  eV and zenith angles of  $0^\circ$ ,  $12^\circ$ ,  $22^\circ$ ,  $32^\circ$ ,  $38^\circ$ , and  $48^\circ$  were used. In the top panel of Fig. 8.6, we show the reconstruction bias in the *counter* mode as a function of the difference ( $\Delta\varphi_m$ ) between the azimuth angle of the shower axis extracted from the SD reconstruction ( $\varphi_{SD}$ ) and the module orientation ( $\varphi_m$ ) for different zenith angles. It is apparent, how the bias increases with the zenith angle and reaches its maximum when  $\Delta\varphi_m = (n + \frac{1}{2})\pi$ , as explained in section 8.2.1. Also noted is that over-counting is clearly the dominant feature probably due to both large PE signals and the detection efficiency involved.

To achieve a bias correction we have fit the reconstruction bias as a linear function of  $|\sin \Delta\varphi_m|$ ,

$$f_{clip}(\theta, \Delta\varphi_m) = a(\theta) + b(\theta) |\sin \Delta\varphi_m|, \quad (8.4)$$

where  $\Delta\varphi_m = \varphi_{SD} - \varphi_m$  and the  $a(\theta)$  and  $b(\theta)$  functions were parametrized using a phenomenological approach as in [109],

$$\begin{aligned} a(\theta) &= a_0 + a_1(1 + a_2 \cos \theta) \sin \theta \quad \text{and} \\ b(\theta) &= b_0(1 + b_1 \cos \theta) \sin \theta \end{aligned} \quad (8.5)$$

In the middle panel of Fig. 8.6 we show the parametrization of the  $a(\theta)$  and  $b(\theta)$  functions obtained by fitting the biases in Fig. 8.6 with equation 8.4. We used equations 8.5 to fit the  $a(\theta)$  and  $b(\theta)$  functions and obtained the best fits of the parameters,

$$\begin{aligned} a_0 &= 0.090 \pm 0.001 & b_0 &= 0.583 \pm 0.015 \\ a_1 &= 0.102 \pm 0.011 & b_1 &= -0.738 \pm 0.014 \\ a_2 &= -1.298 \pm 0.034 \end{aligned} \quad (8.6)$$

With the  $f_{clip}$  parametrization we can now correct the biases in the *counter* mode using the information of the shower geometry reconstructed with the SD as

$$N_{Rec}^{corr}(\theta, \Delta\varphi_m) = \frac{N_{Rec}}{1 + f_{clip}(\theta, \Delta\varphi_m)} \quad (8.7)$$

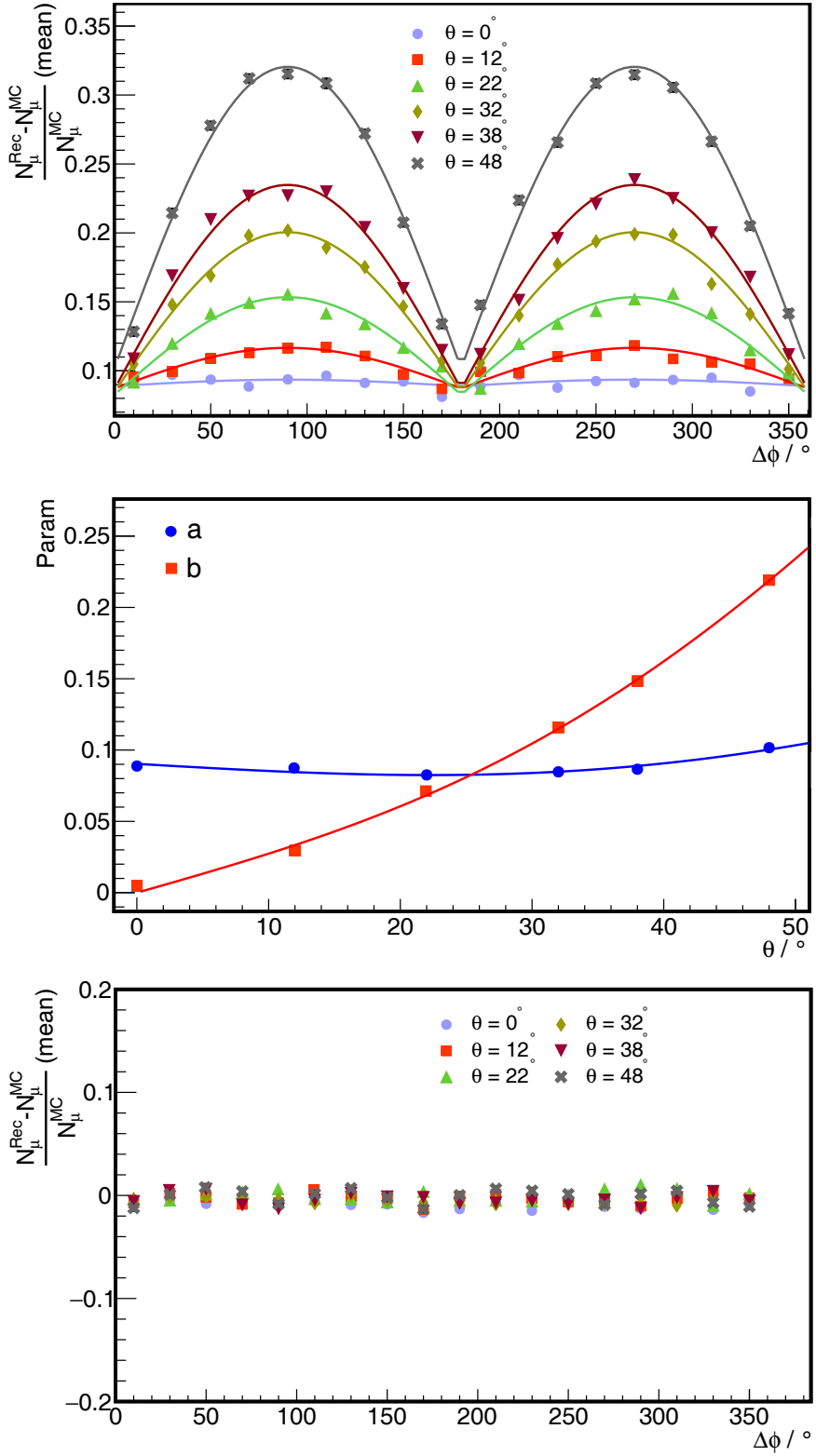


**Figure 8.6:** Geometry dependence of the reconstruction bias using proton and iron showers with energies of  $10^{17}$  eV,  $10^{17.5}$  eV,  $10^{18}$  eV,  $10^{18.5}$  eV and zenith angles of  $0^\circ, 12^\circ, 22^\circ, 32^\circ, 38^\circ$  and  $48^\circ$ . (Top) Reconstruction bias as a function of the difference between the azimuth angle of the shower axis extracted from the SD reconstruction and the UMD module orientation ( $\Delta\varphi_m$ ) for different zenith angles ( $\theta$ ). The biases were fitted using equation 8.4. (Middle)  $a(\theta)$  and  $b(\theta)$  functions of the bias parametrization fitted with equations 8.5. (Bottom) Reconstruction bias as a function of the difference between the azimuth angle of the shower axis and the UMD module orientation ( $\Delta\varphi_m$ ) for different zenith angles ( $\theta$ ) after implementing the geometry correction.

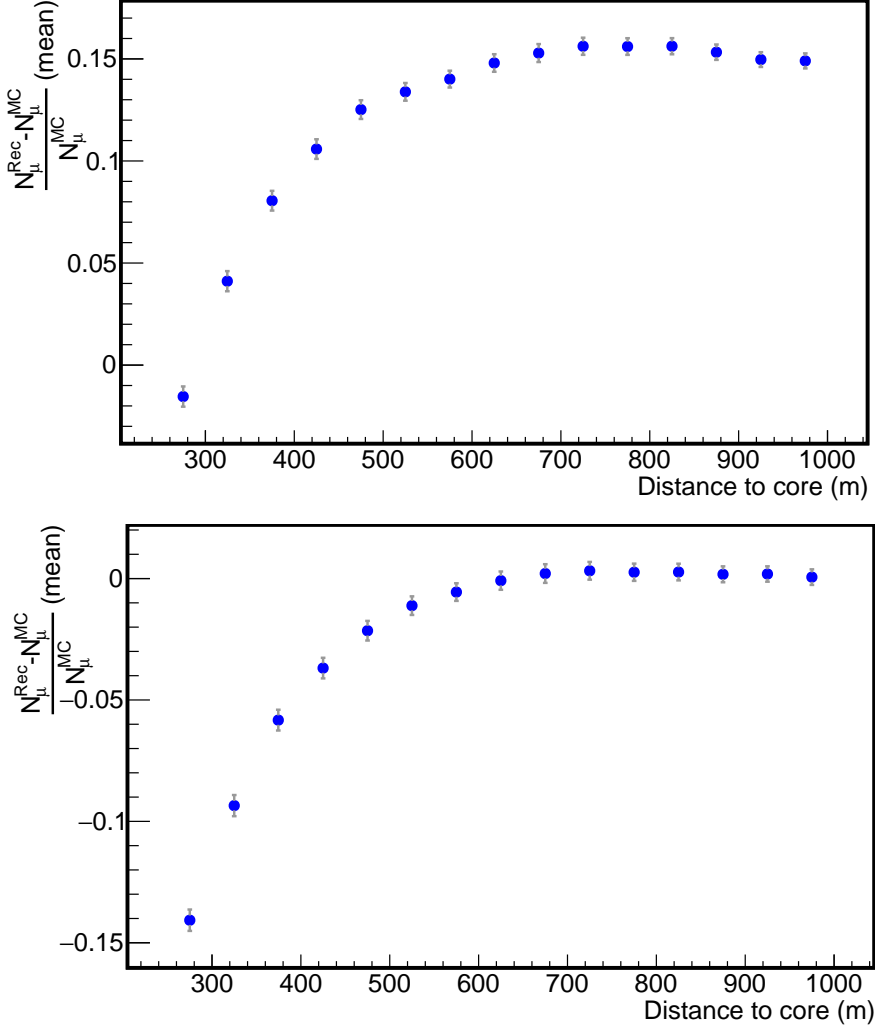


**Figure 8.7:** Reconstruction bias with the *Counter* mode as a function of the distance to the shower core before (top panel) and after (bottom panel) the correction. The data set is the same as in Fig. 8.6

To test the new reconstruction, we repeated the analysis shown in the top panel of Fig. 8.6, introducing the bias correction. We display the result in the bottom panel of Fig. 8.6. After the correction, the bias dependence on the direction of the shower axis is removed and the reconstruction bias is reduced to less than 2% (depending on the energy-z zenith angle bin).

To finally illustrate the effectiveness of the correction, we show in Fig. 8.7 the reconstruction bias in the *counter* mode as a function of the distance to the shower core before (top panel) and after (bottom panel) the correction. We have used the same data set as in Fig. 8.6, each data point includes events of all zenith angles, energies, and primaries. After applying the correction, the reconstruction bias is reduced from  $\sim 15\%$  to  $\sim 0\%$ .

### 8.3 Integrator mode optimization

In the same way we optimized the reconstruction of the *counter* mode to remove the detector bias, we performed a similar analysis for the *integrator* mode to attain an unbiased estimation of the muon content in air showers.

### 8.3.1 Geometry dependence

Since in the *integrator* mode the signal of the 64 strips is summed, corner clipping muons do not have any impact on this mode; the energy deposit in the detector is the same regardless in how many strips a particle leaves energy. The amount of light produced in the scintillator (which propagates to SiPMs, and to the signal charge in the ADC channel) depends on this energy deposit, which increases as the trace length of the particle in the detector increases. It can be inferred, from the left panel of Fig. 8.2 that the mean energy deposit in the scintillators is

$$\langle E_{\text{deposit}} \rangle = \frac{2.25 \text{ MeV}}{\cos \theta}, \quad (8.8)$$

where 2.25 MeV is the mean energy deposit left by a charged particle in 1 cm of scintillator. To achieve a uniform response in the *integrator* mode we correct the signal charge by the track length, i.e.  $\cos \theta$  with  $\theta \leq 48^\circ$ . In Fig. 8.8 we show the ratio of the mean charge ( $\overline{Q_\theta}$ ) and mean charge of vertical showers ( $\overline{Q_0}$ ) as a function of  $\frac{1}{\cos \theta}$  before (top panel) and after (bottom panel) the correction for events with 20 muons. The charge dependency to the zenith angle is removed after the correction.

### 8.3.2 Calibration in simulation

To test the calibration of the *integrator* mode we have used proton and iron showers with energies of  $10^{17}$  eV,  $10^{17.5}$  eV,  $10^{18}$  eV,  $10^{18.5}$  eV and zenith angles of  $0^\circ$ ,  $12^\circ$ ,  $22^\circ$ ,  $32^\circ$ ,  $38^\circ$  and  $48^\circ$ . To reconstruct the number of muons we need to estimate the mean charge of a single muon as explained in chapter 5. We have performed a calibration in a similar way as we intend to do it in the field. Firstly, we estimated the mean charge value for single muons using the whole shower information as in section 5.2. We refer to this calibration as T3 calibration. The result is displayed in top panels of Fig. 8.9 for the low- (left) and high-gain (right) channels where we plotted the charge in the ADC channels as a function of the reconstructed number of muons in the binary channel (*counter* mode). It is quite noticeable the agreement between the calibration line and the mean values (red squares). Secondly, we built charge histograms for events with only one reconstructed muon in the binary channel, which are displayed in the bottom panels of Fig. 8.9. To obtain the mean charge of a single muon, we fitted the histogram with a log-normal-like function (as explained in section 5.3.3) and we computed the histogram average and median (50% quantile). We also performed a direct mean computing. The results are displayed in Fig. 8.9 bottom panels. Extracting the mean using the log-normal fit or computing the average leads to the same results.

A selection between T3 and charge histogram calibrations will be performed, in the following section base on the detector bias and saturation.

### 8.3.3 Bias and saturation

To test the above-mentioned calibrations, we show in the top panel of Fig. 8.10 the reconstruction bias in the *integrator* mode as a function of the distance to the shower core extracted from the SD reconstruction for the same data set used in section 8.3.2. It is apparent that the T3 calibration (extracted using the whole shower event) is unbiased while the calibration obtained from the charge histograms is not. Therefore, we use the T3 calibration in the subsequent analysis of this chapter. It is also worth to note that the high-gain channel saturates at around 300 m from the shower core, while the low-gain does not seem to saturated in the displayed range.

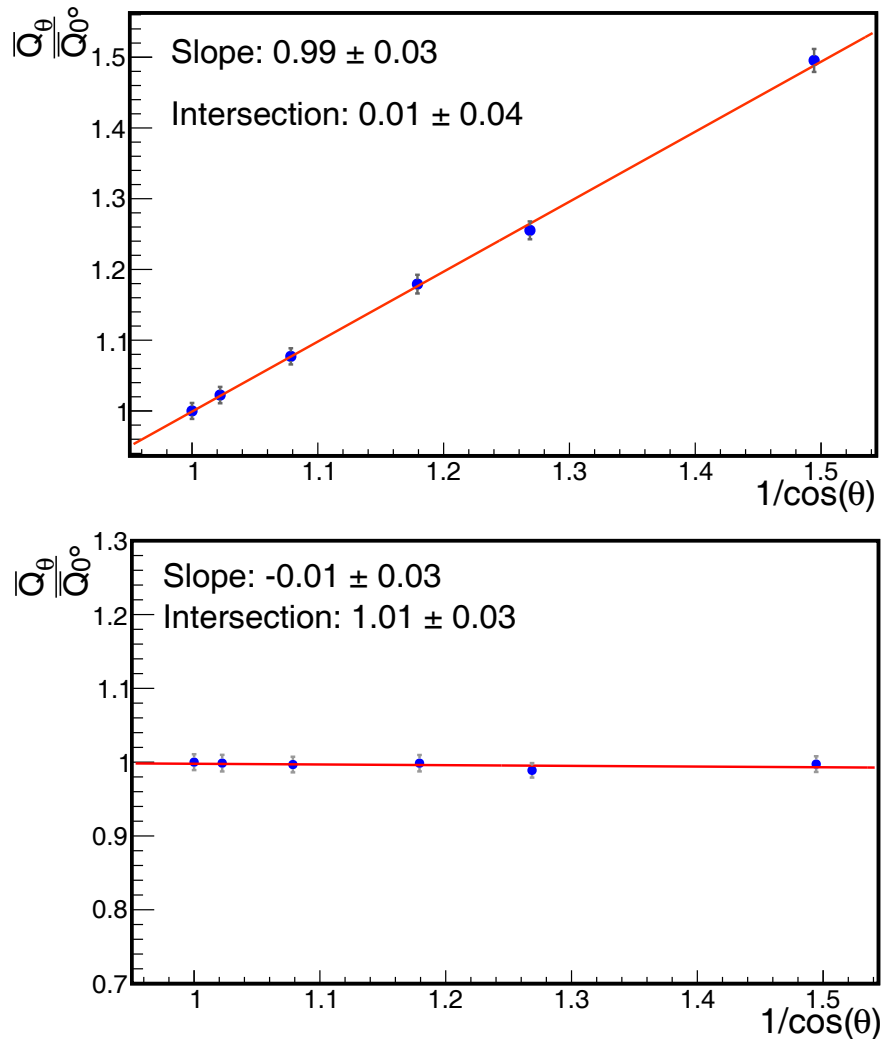


**Figure 8.8:** Ratio of the mean charge ( $\bar{Q}_\theta$ ) and mean charge of vertical showers ( $\bar{Q}_0$ ) as a function of  $\frac{1}{\cos \theta}$  before (top panel) and after (bottom panel) the correction, which removes the angular dependence.

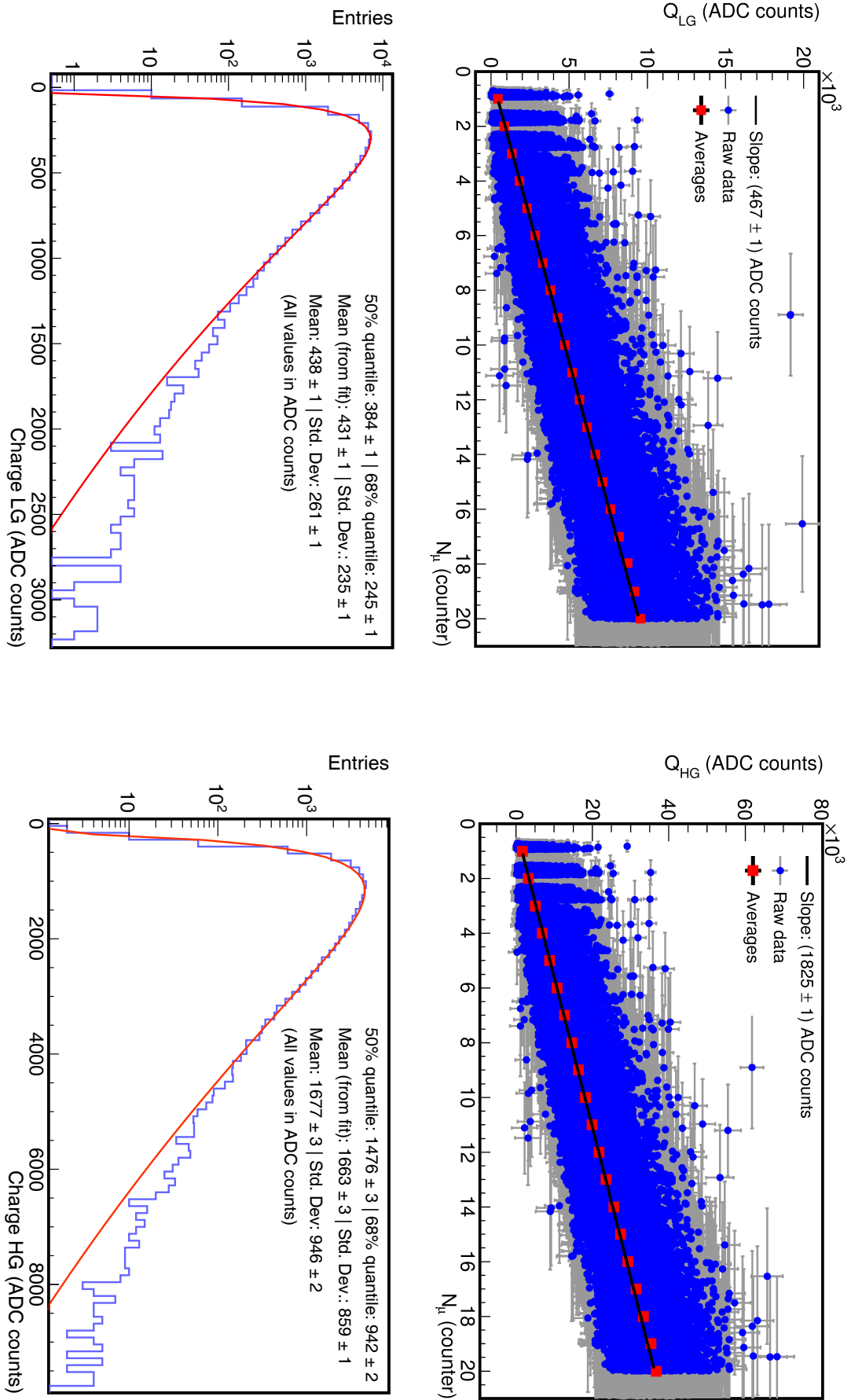


**Figure 8.9:** (Top) Signal charge in the *integrator* mode as a function of the number of reconstructed muons in the *counter* mode for the low- (left) and high-gain (right) channels. The mean charge per muon is obtained with a linear fit. (Bottom) charge histograms for  $N_\mu = 1$ . The calibration using the histograms were achieved with three different methods: the median (50% quantile), fitting a log-normal-like function and computing the charge average.

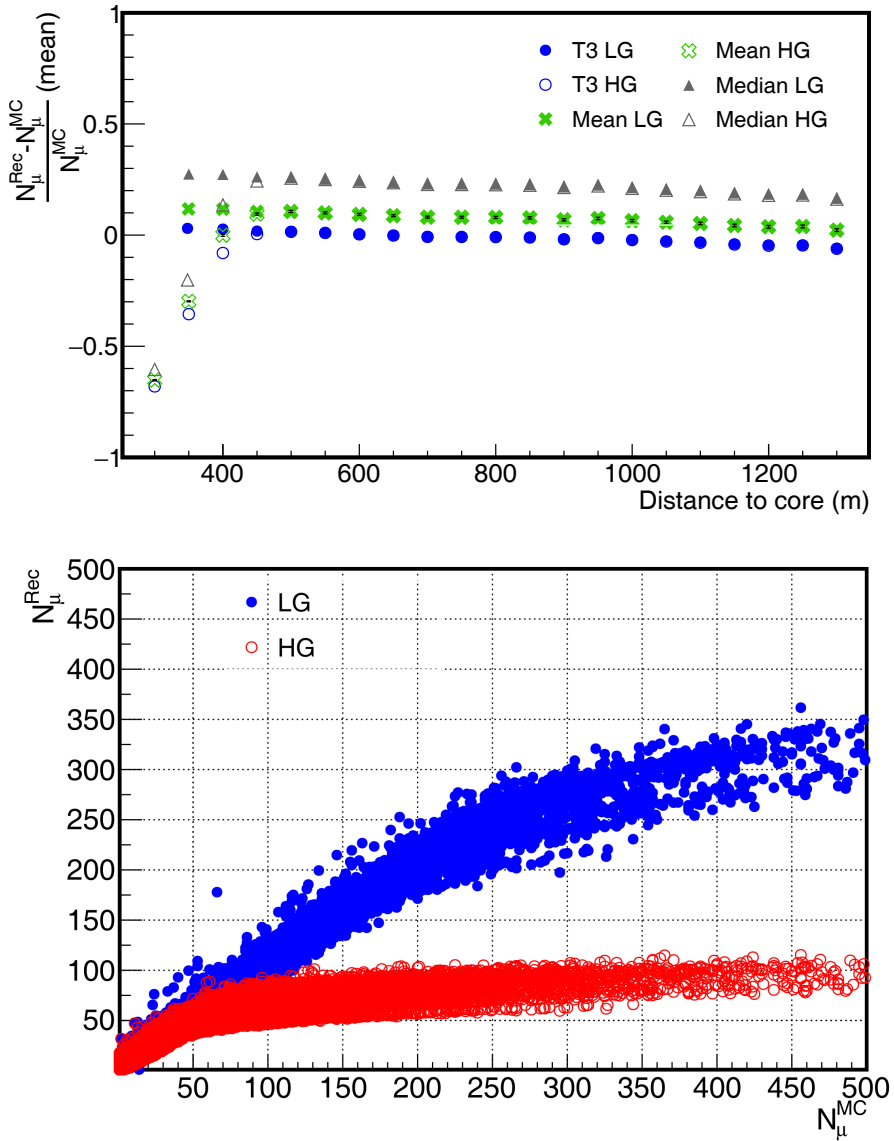


**Figure 8.10:** (Top) Reconstruction bias as a function of the distance to the shower core for the low- and high-gain channels and different calibration outputs. (Bottom) Number of reconstructed muons with the *integrator* mode and the low-/high-gain channel as a function of the number of injected muons.

In the bottom panel of Fig. 8.10, we show the number of reconstructed muons as a function of the number of injected muons for the low- and high-gain channels. The saturation at the low-gain channel is reached at  $\sim 250$  muons, while at high-gain it is reached at  $\sim 60$  muons. We have shown in section 8.2.1 that when injecting one muon, a bunch of knock-on electrons from the soil may also leave a fair amount of energy in the scintillator. Furthermore, in the laboratory, we mainly measure vertical muons, while in the simulation we are considering showers up to  $\theta = 48^\circ$ . For these reasons, the light-output per muon in the field is expected to be higher than the light-output measured in the laboratory, and therefore, the detector deployed underground is expected to saturate with a lower number of muons. We discuss in the next section the saturation point at different energies as a function of the distance to the shower core.

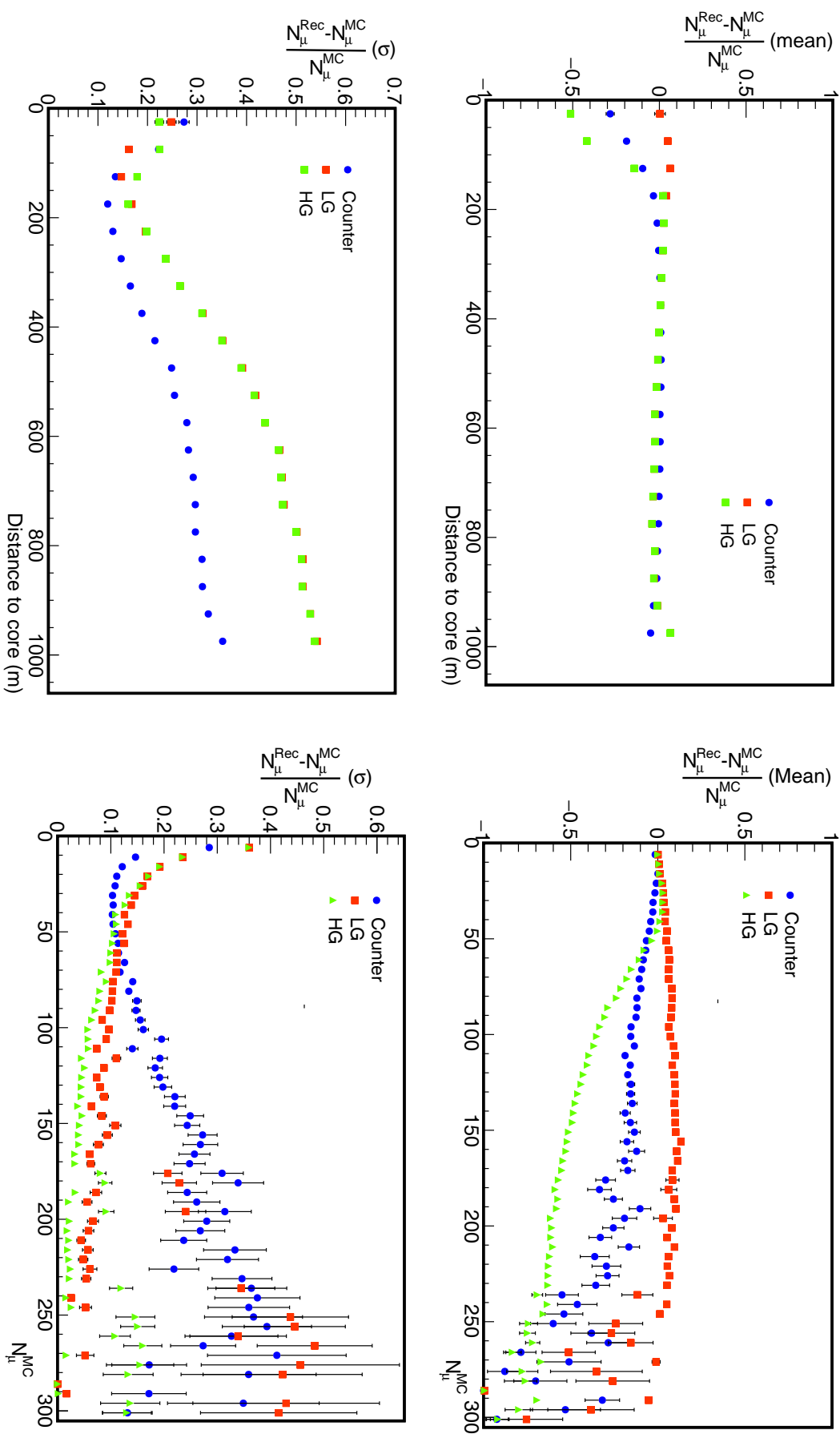


**Figure 8.11:** Reconstruction bias (top panels) and fluctuations (bottom panels) as a function of the distance to the shower core extracted from the SD reconstruction (left panels) and the number of injected muons (right panels) for proton and iron shower with an energy of  $10^{17.5}$  eV and zenith angles of  $0^\circ, 12^\circ, 22^\circ, 32^\circ, 38^\circ, 48^\circ$ . We show the results obtained using the *counter* mode and the low- and high-gain channels of the *integrator* mode.

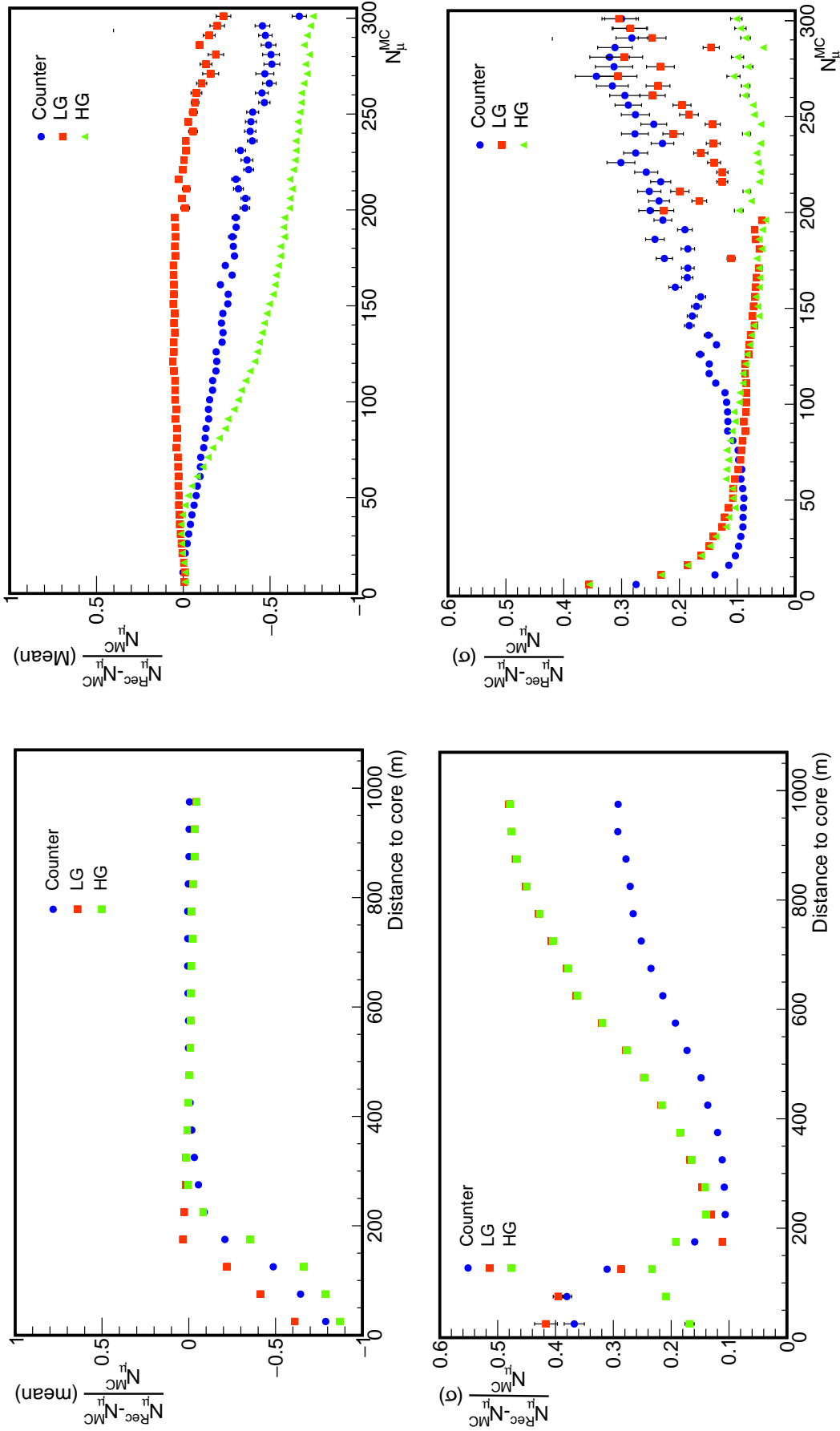
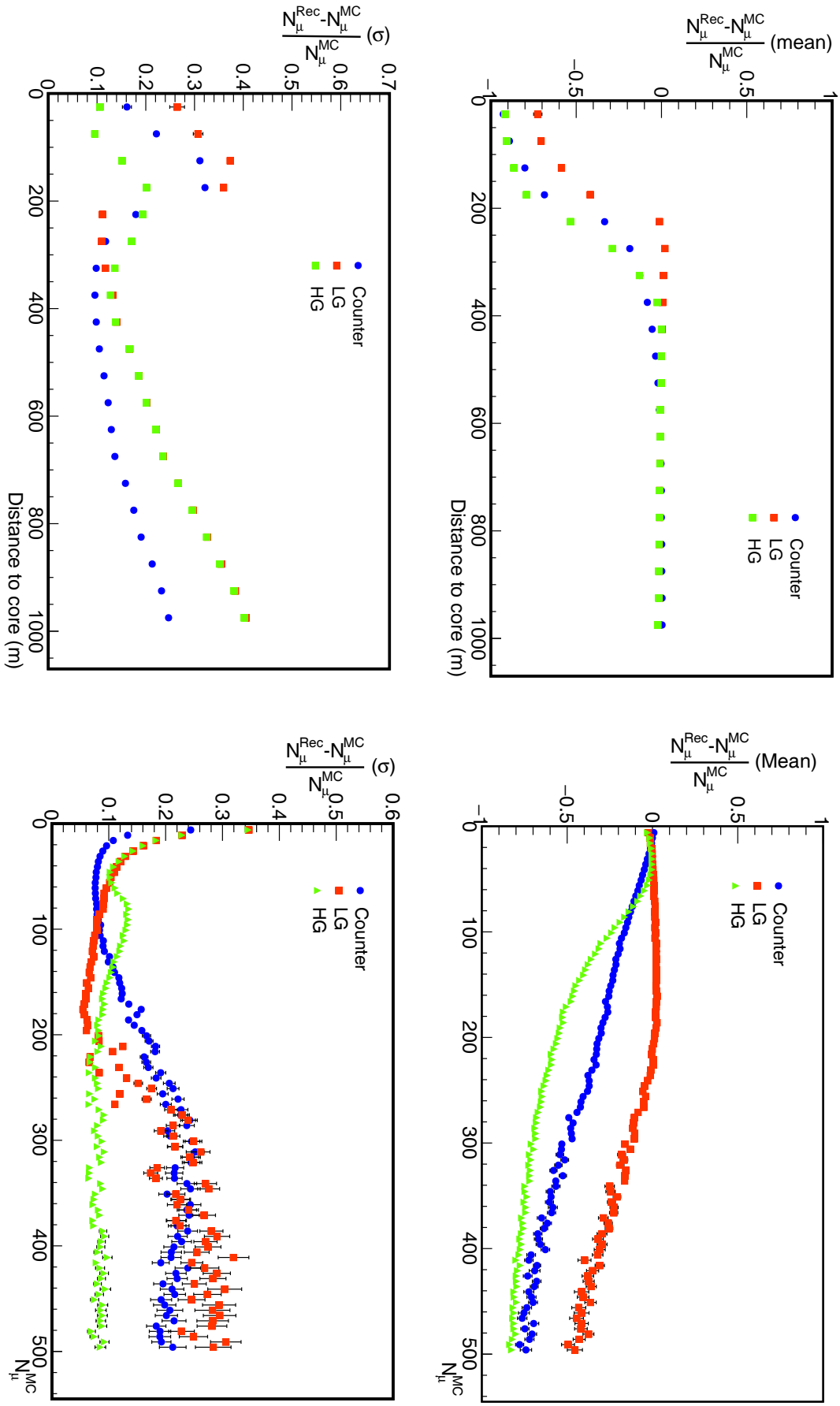


Figure 8.12: Reconstruction bias (top panels) and fluctuations (bottom panels) as a function of the distance to the shower core extracted from the SD reconstruction (left panels) and the number of injected muons (right panels) for proton and iron shower with an energy of  $10^{18}$  eV and zenith angles of  $0^\circ, 12^\circ, 22^\circ, 32^\circ, 38^\circ, 48^\circ$ . We show the results obtained using the *counter* mode and the low- and high-gain channels of the *integrator* mode.



**Figure 8.13:** Reconstruction bias (top panels) and fluctuations (bottom panels) as a function of the distance to the shower core extracted from the SD reconstruction (left panels) and the number of injected muons (right panels) for proton and iron shower with an energy of  $10^{18.5}$  eV and zenith angles of  $0^\circ, 12^\circ, 22^\circ, 32^\circ, 38^\circ, 48^\circ$ . We show the results obtained using the *counter* mode and the low- and high-gain channels of the *integrator* mode.

## 8.4 Counter and integrator modes range and resolution

To finally assess the resolution and working range of the *counter* and *integrator* modes we computed the bias and its standard deviation  $\sigma$  (herein addressed as fluctuations) as a function of the distance to the shower core and of the number of injected muons. We have performed the analysis for different energy bins:  $10^{17.5}$  eV (Fig. 8.11),  $10^{18}$  eV (Fig. 8.12), and  $10^{18.5}$  eV (Fig. 8.13). The muon content increases with the energy and therefore, the detector can measure closer to the shower core without saturation as the energy decreases. The binary channel tends to saturate at the same point as the high-gain channel (around 50~60 muons), but with smaller fluctuations in its working range. When the binary channel starts to saturate, the behavior of the low-gain channel is improved in both its reconstruction bias and fluctuations. It is also worth to note that the working range of both modes depend on the energy unless we set limits on the number of muons and not on the distance to the shower core.

## 8.5 Proton-Iron discrimination

To evaluate the UMD potential for performing studies on the composition of primary cosmic rays, we have obtained the muon densities at an optimal distance from the shower core ( $\rho_{450}$  [126, 127]), which is an observable sensitive to the mass of the primary cosmic ray (see section 1.3). To analyze the discrimination power of the UMD for proton and iron primaries, we have fitted the simulated data with a muon lateral-distribution function (MLDF) parametrized by a KASKADE-Grande-like function [128],

$$\begin{aligned} \rho_\mu(r) &= A_\mu \frac{f_\mu(r)}{f_\mu(r_{opt})}, \quad \text{with} \\ f_\mu(r) &= \left(\frac{r}{r^*}\right)^{-\alpha} \left(1 + \frac{r}{r^*}\right)^{-\beta} \left(1 + \left(\frac{r}{10r^*}\right)^2\right)^{-\gamma} \end{aligned} \quad (8.9)$$

where  $r^* = 150$  m,  $r_{opt} = 450$  m,  $\alpha = 1$  and  $\gamma = 1.85$  are fixed [53, 126], while  $\beta$  and  $A_\mu = \rho_{450}$  are free parameters.

We have performed the fits using only the *counter* mode data, the *integrator* mode data and combining both. To combine the modes, we used the reconstruction bias plots in section 8.4 to define a working range as a function of the energy of the primary cosmic ray. We have used the integrator mode when the counter mode starts to saturate, this is for energies of  $10^{17.5}$  eV, 200 m,  $10^{18}$  eV, 250 m, and  $10^{18.5}$  eV, 500 m. In Fig. 8.14 we present an example of a simulated event, where we display the muon densities obtained with the muon detector as a function of the distance to the shower core and the corresponding MLDF fit. The data points and fits obtained with both working modes and with the combined approach are displayed.

After fitting the MLDF, we extract the  $\rho_{450}$  parameters and built histograms for each primary, energy and zenith angle. In Fig. 8.15 we show an example histogram with the *integrator* mode for proton and iron primaries with an energy of  $10^{18.5}$  eV and  $\theta = 0^\circ$ . The separation in the distribution of  $\rho_{450}$  for both primaries is apparent. We have also estimated the merit factor for proton-iron discrimination as

$$MF = \frac{\left| \overline{\rho_{450}^i} - \overline{\rho_{450}^p} \right|}{\sqrt{\sigma_{\rho_{450}^i}^2 + \sigma_{\rho_{450}^p}^2}}, \quad (8.10)$$

where i refers to iron and p to proton.

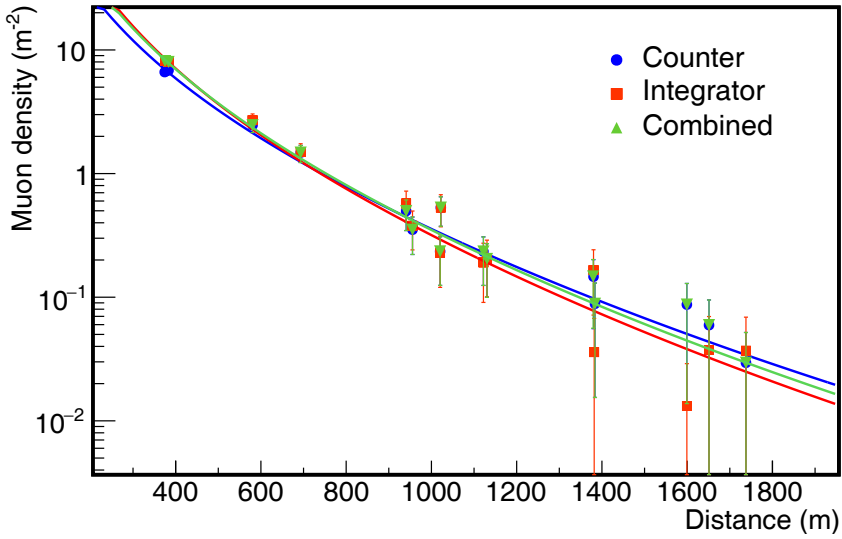


**Figure 8.14:** Example of muon densities obtained with the UMD as a function of the distance to the shower core with the corresponding MLDF fit using the *counter* and *integrator* modes and combining both. From each of the MLDF fits we obtained  $\rho_{450} = (4.4 \pm 0.2) \text{ m}^{-2}$ ,  $\rho_{450} = (5.0 \pm 0.2) \text{ m}^{-2}$ , and  $\rho_{450} = (5.0 \pm 0.2) \text{ m}^{-2}$  for the *counter*, *integrator* and combined data, respectively.

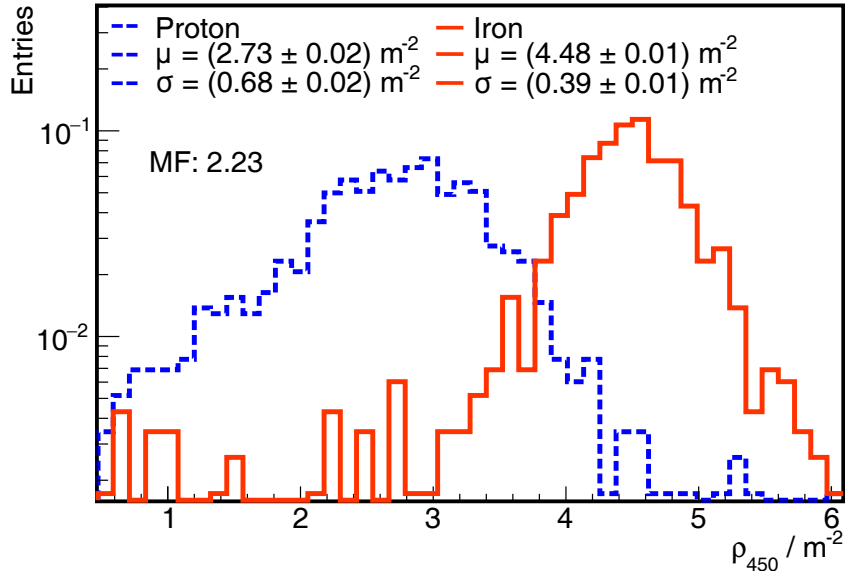


**Figure 8.15:** Example of  $\rho_{450}$  distributions obtained with the *integrator* mode for proton and iron primaries with an energy of  $10^{18.5} \text{ eV}$  and zenith angle of  $0^\circ$ .

Defining a working range for each mode is a rough approach only useful to attain a general idea of the detector performance, and a more robust analysis is needed to maximize the discrimination power of the UMD. A way to combine the *counter* and *integrator* modes without defining a range, and depending only on event-by-event data should be attempted [89].

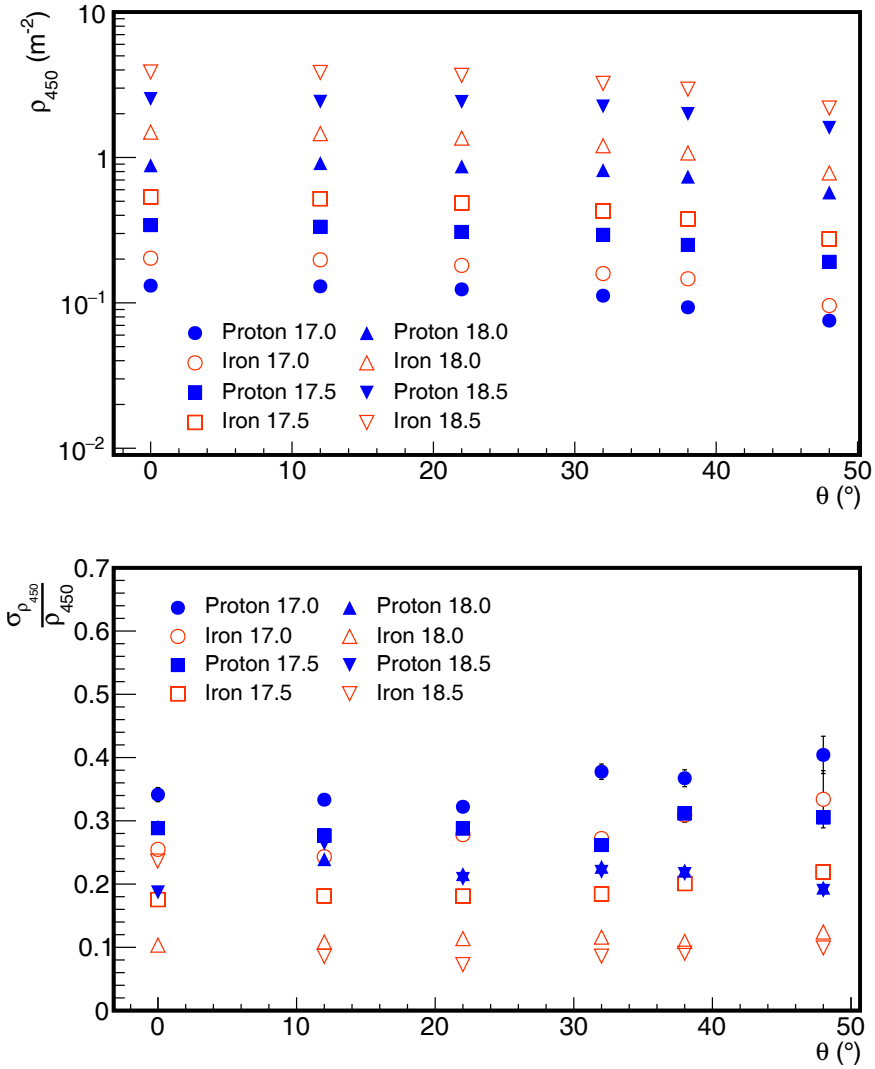


**Figure 8.16:** Muon density (top) and relative fluctuation (bottom) for proton and iron primaries and energies of  $10^{17}$  eV,  $10^{17.5}$  eV,  $10^{18}$  eV and  $10^{18.5}$  eV as a function of the zenith angle obtained with the *counter* mode.

### 8.5.1 Muon densities

To obtain the merit factor for each energy and zenith angle we have first computed the mean  $\rho_{450}$  and  $\sigma_{450}$  using the *counter* and *integrator* modes, and, also, combining the two modes. The results are shown in Fig. 8.16, 8.17 and 8.18 respectively. It is apparent that when increasing the zenith angle, the shower particles get attenuated and, therefore, the muon content decreases. In these results, it is also apparent how the muon content increases with the energy and the number of nucleons as expected from the Heitler model explained in section 1.3.

Since the *counter* mode is designed to measure low-muon densities while the *integrator* mode has been designed to measure high-muon densities, the integrator performance is best in scenarios with an increasing number of muons, such as higher energies, higher number of nucleons in the primary cosmic ray and vertical showers. Is apparent how relative fluctuations in the *integrator* mode are significantly higher than in the *counter* mode for proton showers of lower energy since these have a lower muon content.

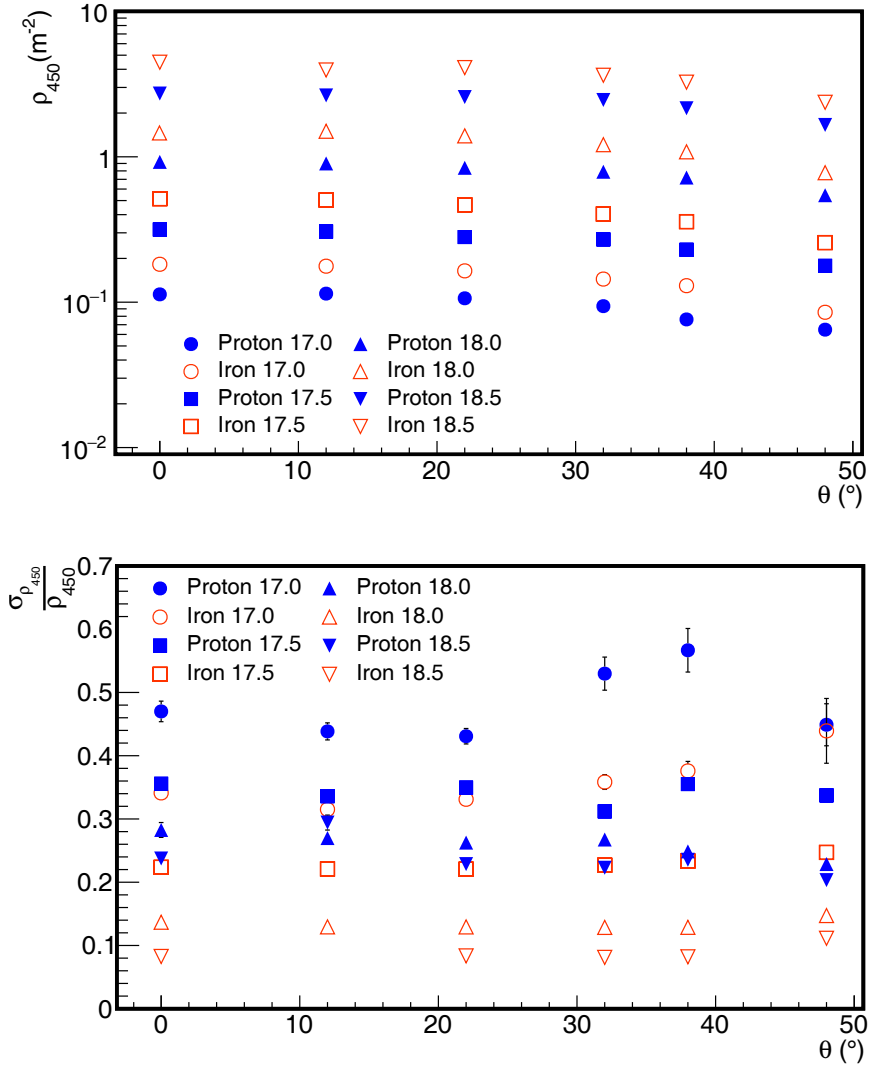


**Figure 8.17:** Muon density (top) and relative fluctuation (bottom) for proton and iron primaries and energies of  $10^{17}$  eV,  $10^{17.5}$  eV,  $10^{18}$  eV and  $10^{18.5}$  eV as a function of the zenith angle obtained with the *integrator* mode.

### 8.5.2 Merit factor

Using the results in section 8.5.1, we estimated the merit factor for proton-iron separation using the *counter* mode, the *integrator* mode and combining both. In Fig. 8.19 the results for energies  $10^{17}$  eV,  $10^{17.5}$  eV,  $10^{18}$  eV,  $10^{18.5}$  eV are shown. The merit factor increases with the energy and decreases with the zenith angles. For  $E = 10^{17}$  eV the result obtained is similar to the one using only the *counter* mode since in this case, we do not reach the saturation point of the binary channel, and therefore, a different approach is needed to include the *integrator* mode data). In the other energy bins, a small but systematic improvement using the combined data seems to occur. It is also worth to note that for the highest energy bin, the *integrator* mode tends to provide an improved discrimination than the *counter* mode due to the high muon content for which the *counter* mode is mostly saturated.

We have performed an analysis to attain a general idea of the UMD behavior. Further improvements can be performed, such as combining the data from both modes in a more

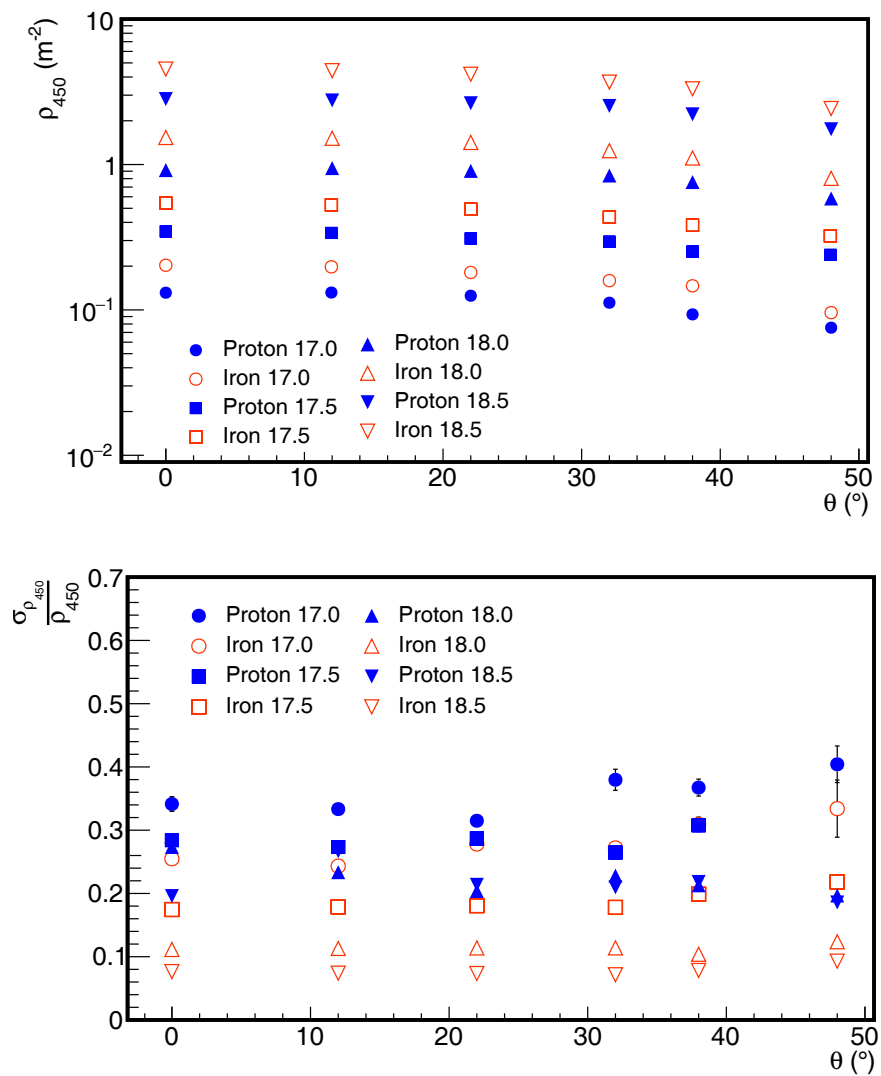


**Figure 8.18:** Muon density (top) and relative fluctuation (bottom) for proton and iron primaries and energies of  $10^{17}$  eV,  $10^{17.5}$  eV,  $10^{18}$  eV and  $10^{18.5}$  eV as a function of the zenith angle obtained combining the *counter* and *integrator* modes.

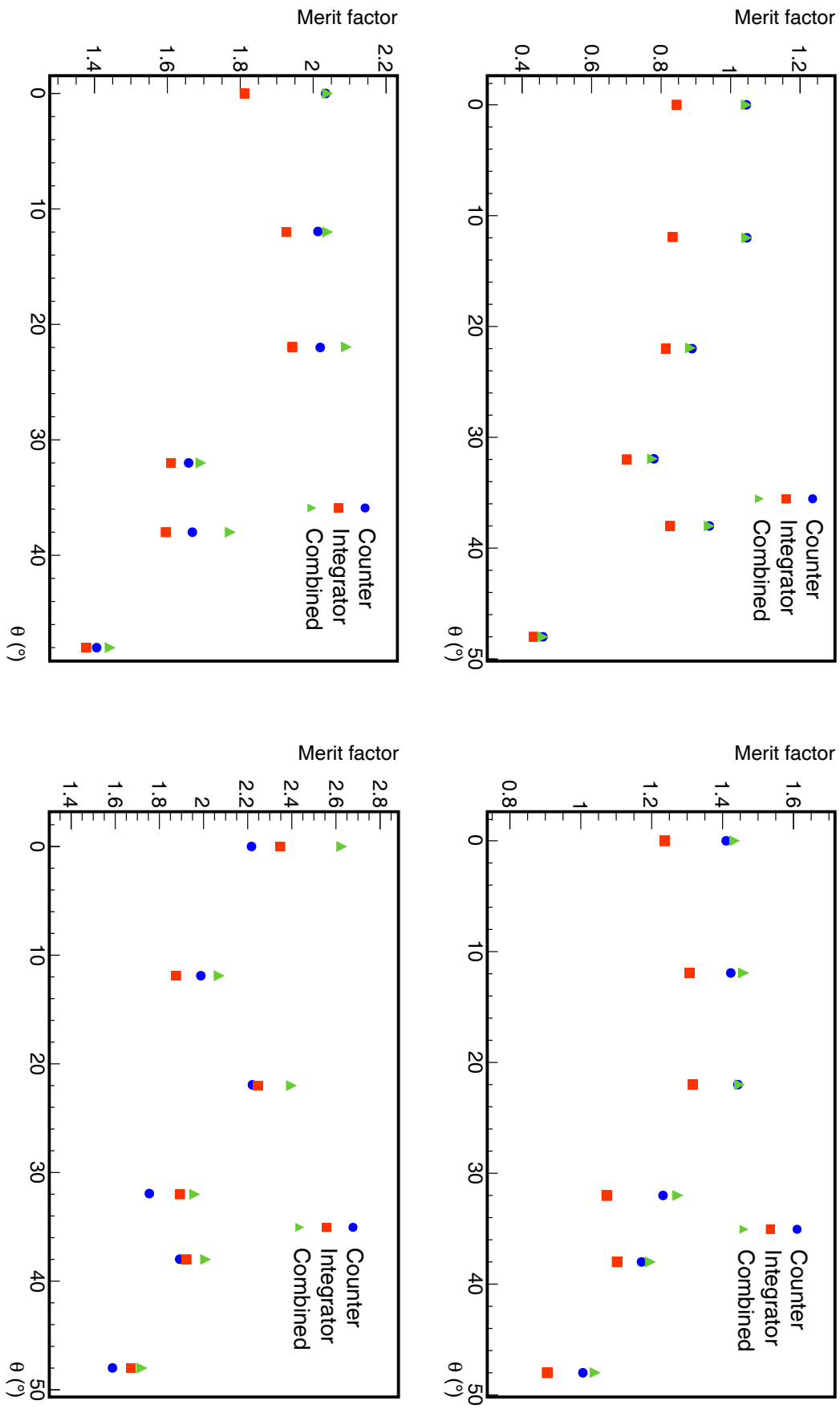


Figure 8.19: Merit factor as a function of the zenith angle for proton-iron discrimination in showers with energy  $10^{17}$  eV,  $10^{17.5}$  eV,  $10^{18}$  eV and  $10^{18.5}$  eV, using separately the *counter* and *integrator* modes and combining both.

robust way, as well as improving the measurements closer to the shower core by recovering the saturated traces of the *integrator* mode (as done with the SD traces [129]).

The merit factors estimates at 1.0 EeV energies and above are quite satisfying. Also shown is the reliability of the coherent results from the *integrator* and *counter* modes (cross checks between the two modes should certainly help towards achieving a more robust research). Lower energies might be better explored with the AMIGA 433 m array.

## 8.6 Conclusions of this chapter

In this chapter, we have analyzed the sources of reconstruction bias in the UMD and propose corrections to achieve an unbiased reconstruction using simulations with the Auger Offline framework. The correction effectively removes most of the bias in the *counter* mode until its saturation point.

We have also tested the calibration of the *integrator* mode with simulations, and we have shown that the calibration achieved with shower events leads to an unbiased reconstruction. We have also shown that the low-gain channel starts to saturate at approximately 250 muons, and its resolution becomes smaller than the *counter* mode at approximately 100 muons.

We have estimated the reconstructed muon densities with the *counter* and *integrator* modes and combining both detectors, showing that the muon content is attenuated for increasing zenith angles. To combine the data, we have defined a working range as a function of the shower energy, in which we start using the *integrator* mode at the distance to the shower core where the *counter* mode starts to saturate. With this analysis, we have shown that there is systematic improvement when using the combined data as compared with using either of the modes independently.

We have performed merit factor evaluations for energies from 0.1 EeV (the realm of the SD-433 array) onward. The merit factors for energies above 1.0 EeV are quite good which is very encouraging for studying the ankle region, the main purpose of the SD-750 array.



---

---

# CHAPTER 9

---

## Summary and conclusions

The number of muons in extensive air showers is a crucial observable for determining the composition of primary cosmic rays at the highest energies. This is one of the main motivations of AugerPrime, the upgrade of the Pierre Auger Observatory. The AMIGA underground muon detector (UMD) is an essential part of this upgrade. It consists of buried segmented scintillation detectors with embedded wavelength-shifting optical fibers and silicon photo-multipliers (SiPMs). It will allow for direct measurements of muon densities on a shower-by-shower basis. To enhance its dynamic range, two operation modes are integrated into the UMD electronics: the *counter* mode and the *integrator* mode, each designed to measure low- and high-muon densities, respectively with a significant overlap region.

In this thesis work, we have thoroughly studied both working modes and accomplished an optimized UMD calibration and an uncertainties control towards a most reliable event reconstruction. These achievements entail both laboratory and field data analyses which include detector performance and stability. Furthermore, SiPM simulations along with simulations of the read-out electronics of both working modes were developed, validated, and implemented in the Auger data analysis and simulation software (*Offline*). Without such a simulation framework no composition analyses could be performed. These simulation were used to analyze the UMD power to discriminate between proton and iron cosmic-ray primaries.

The UMD production phase has already started and the full AMIGA array is expected to be completed by 2020. In this context, the tools and methods developed and validated are of significant importance for future analyses performed with the underground muon detector of AugerPrime. Details of the achievements now follow.

### ***Counter mode performance and muon counting strategy***

We have probed the robustness of the SiPM calibration both in the laboratory and in the field. We have also evaluated the performance of the temperature compensation mechanism of SiPMs and shown, in a prototype module, that the dependence of the gain with the temperature is reduced by a factor of 20 with this mechanism.

The impact of different muon counting strategies on the noise over signal ratio was addressed with a systematic study to attain the final counting strategy for the *counter* mode. Laboratory measurements with four scintillator strips identical to those in the Observatory UMD were presented. Using a muon telescope to trigger events, measurements at 2.5 and 3.5 PE discrimination level were performed. First of all, the muon and background signals

were characterized. Two different sources of noise were acknowledged: the SiPM dark rate and the optical-fiber noise. The SiPM dark rate, which is present at the 2.5 PE discrimination level (not at 3.5 PE), was found to be distinguishable in width from the muon signal. Therefore, it may be rejected by choosing a proper counting strategy. The optical-fiber noise, although present at both 2.5 and 3.5 PE discrimination levels, is less frequent and cannot be separated from muons.

For the counting strategies 1111x and 1x the total noise expected at the field is 5.5% at 2.5 PEs and 5.7% at 3.5 PEs if the whole trace length is used ( $6.4 \mu\text{s}$ ) with an efficiency of  $(98.5 \pm 0.3)\%$  and  $(98.7 \pm 0.5)\%$  (respectively) for  $10 \text{ m}^2$  modules. Also, data from the module with Id 108, at the station with Id 1764, was analyzed. The results of the background in the field are consistent with the results from the laboratory. Finally, if the trace length is reduced to  $1 \mu\text{s}$ , a counting strategy of 1x and a 2.5 PE discriminator threshold might be enough to cope with the noise (which would be reduced to  $\sim 2.3\%$ ).

By analyzing the attenuation curve of optical fibers, it was shown that the amplitude cut of 2.5 PE introduced in the binary channels will not lead to any significant signal loss in the ADC channel (*integrator mode*). Further to this and to minimize the impact of potential issues such as materials aging and undershooting, the decision was made of setting the discriminator threshold at 2.5 PE for the AMIGA array.

A further parameter that was studied and fixed was the counter inhibition window of 12 samples, which will contain more than 99% of the signals. Larger/shorter inhibition windows might lead to the under-/over-counting of muons.

These systematic analyses led towards choosing the counting strategy, PE threshold, and inhibition window so as to achieve a suitable noise reduction with a high signal efficiency. These choices set the analysis framework for AMIGA.

### ***Integrator mode performance and calibration***

Laboratory measurements with four scintillator strips identical to those in the AMIGA modules were presented. Using a muon telescope to trigger events, one- and four-muon signals were obtained in order to characterize the ADC traces of the *integrator mode*. First of all, the signal timing was analyzed; the delay between the binary and ADC trace was found to be  $(170.62 \pm 0.03) \text{ ns}$  with a relative offset of 3 ns ( $\sim$  half of the ADC sampling time). This result implies that it is possible to determine when a particle impinges on the detector with the binary traces and thus search for the associated ADC trace. This coincidence feature is useful to calibrate the ADC channels due to the random large fluctuations introduced by the SiPM dark rate and thus leads to a single muon calibration. Also, one-muon signals were obtained from the field to compare with laboratory data. The analyses clearly showed that the relevant features of the signal shape, timing, and charge are similar within both data sets.

An online calibration for the ADC channel of the AMIGA muon detector has also been proposed and discussed, based on single-muon signals from background data. To this aim, we extracted T1 events from a test module in the Observatory. As in the laboratory, we characterized the signal timing of both binary and ADC channels, and determined that the delay between the binary-trace start time and the bin of the maximum signal amplitude in the ADC is stable within a 7.25 ns mean fluctuation, which is similar to the sample time of the ADC (6.25 ns). We identified particles in the *integrator* if in coincidence with a *counter* signal. This identified particle sets the start time of the integration window of the ADC trace. We optimized this analysis to obtain a charge histogram of the single-muon signal, from which the mean charge and variance of a single-muon can be extracted. We have also presented a method to remove noise signals that may bias the calibration. We showed that

this online calibration is stable within the analyzed period of time (08-2019 to 02-2019) with a fluctuation in the mean muon charge of less than 4%. Furthermore, it has been proven that this calibration is robust when changing the counting strategy used to determine when a muon impinged on the detector. To implement the online calibration in the field, it is only necessary to tune the latch bin of the binary channel (used to find the muon signal) in each of the AMIGA modules, since different cable lengths produce different delays in the signal start times. The delay between the start time of the binary trace and the maximum signal amplitude in the ADC channel is uniform among all modules.

We have also presented an offline calibration and, moreover, an error model with one free parameter was assessed. By comparing the ADC charge with the number of muons ( $N$ ) estimated with the binary channel, the mean charge per muon was obtained. The signal charge in the ADC channel (in term of mean values) varies quite linearly with the number of muons, as expected. An average ratio between the high- and low-gain channels of 3.96 (with less than 1% fluctuation) was obtained. As expected, relative fluctuation for the  $5\text{ m}^2$  modules is lower than for the  $10\text{ m}^2$  modules. For  $N = 1$ , the average relative uncertainty is 0.52 for the  $5\text{ m}^2$  and 0.61 for the  $10\text{ m}^2$ . Also, the light output for the  $5\text{ m}^2$  is 22% higher than for the  $10\text{ m}^2$  modules. It was observed that the uncertainties expected when estimating the shower muon density are dominated by the Poissonian fluctuation in the whole range: for  $N = 1$ , the integrator resolution is just  $\sim 20\%$  higher than an ideal Poissonian detector. This result is encouraging since it means that the overlap region between *integrator* and *counter* modes is significant, allowing a cross-check with these two detector modes.

Finally, we have corroborated the consistency of the online and offline calibrations, obtaining a difference in the result of less than 3%.

Tests are currently performed to implement the online calibration in the AMIGA electronics, both in the laboratory and in a test module deployed in the field. The electronics software has already been modified to extract the calibration data from T1 events, which will be soon validated. Analyses to optimize the calibration parameters (such as the window size for searching muon signal) is also ongoing. Preliminary results from both laboratory and field are promising, showing agreement with previous offline results.

### **SiPM simulations development and implementation in the Offline software**

In this work, we have developed and validated the SiPM simulations for the UMD using laboratory data. Firstly, we achieved a single-PE simulation by setting the correct parametrization from the SiPM analog output for single-PE signals. Secondly, we obtained the optical-fiber attenuation curve from which we can estimate the number of PEs detected with the SiPM when a muon impinges on a scintillator strip. Using the scintillator and optical-fiber characteristic times and the number of PEs, single-muon signals were simulated and validated using analog laboratory data obtained with an oscilloscope, showing a good agreement between simulations and experimental data.

After achieving the simulation of the SiPM output signal, we included the electronics response. The transfer functions of both *counter* and *integrator* modes were described and applied to analog simulated signals to obtain digital outputs. Data acquired with the standard AMIGA electronics kit was used to validate these simulations. We have proven that simulation and laboratory data are compatible.

Finally, we described the implementation of the SiPM simulation in the Offline software. New attributes were created to configure the simulation run. Also, the integration of the UMD in the Offline Event Browser has been presented. With the new MD tab, users can visualize different features of the UMD event reconstruction.

In short, end-to-end simulations for both *integrator* and *counter* modes have been performed and included in the official Auger Offline software.

### **Counter and integrator mode optimization**

To assess the reconstruction of muon densities in extensive air showers, we analyzed the reconstruction bias in the UMD and propose corrections to achieve an unbiased reconstruction. In the *counter* mode, we acknowledged two types of bias sources. The first one, as above-mentioned, depends on the timing of the particles in the air shower and on the choice of the inhibition window. When more than one muon impinges on the same scintillator strip within an inhibition window, under-counting occurs in the *counter* mode. This bias can be improved by a judicious choice of an inhibition windows and with a statistical correction. The second kind of bias depends on the shower geometry and it is produced by corner clipping muons and electrons emitted by atoms in the soil. Correction of these effects was achieved using simulations with the Auger Offline framework. The correction effectively removes most of the bias in the *counter* mode until its saturation point.

We have also tested the calibration of the *integrator* mode with simulations, and we have shown that the calibration achieved with shower events leads to an unbiased reconstruction. We have also shown that the low-gain channel starts to saturate at approximately 250 muons, and its resolution becomes smaller than the *counter* mode at approximately 100 muons for a single  $10\text{ m}^2$  (there are three per UMD position).

We have estimated the reconstructed muon densities with the *counter* and *integrator* modes and combining both detectors, showing that the muon content is attenuated for increasing zenith angles (reduced detection area in the shower plane). To combine the data, we have defined a working range as a function of the shower energy, in which we start using the *integrator* mode at the distance to the shower core where the *counter* mode starts to saturate. With this analysis, we have shown that there is a systematic improvement when using the combined data as compared with using either of the modes independently.

We have performed merit factor evaluations for energies from 0.1 EeV (the realm of the SD-433 array) onward. The merit factors for energies above 1.0 EeV are quite good what is very encouraging for studying the ankle region, the main purpose of the SD-750 array.

---

---

## APPENDIX A

---

# Deconvolution algorithm in ROOT

### Implementation in ROOT

For the analysis described in this work, we implemented a deconvolution algorithm based on ROOT libraries [130]. The following algorithm is a simplified example, in which we use the transfer function of a low-pass filter (described in section 7.1.1). We present the transfer function of the actual amplifier used to extract the SiPM dark rate in section 6.2.2.

```
//Define transfer function
//Real Part
TF1 *transferRe = new TF1 ("transferRe","10/(1+(x*TMath::TwoPi()*0.0159)^2)",
0,5000); //Transfer RE for Pre Amp in MHz

//Imaginary Part
TF1 *transferIm = new TF1 ("transferIm","(-10*(x*TMath::TwoPi())*0.0159/
(1+(x*TMath::TwoPi())^2))",0,5000); //Transfer IM for Pre Amp in MHz

//Number of datapoints per adquisition
Int_t N = 2501;
//Input dataset
Double_t *in = new Double_t[N];
//Output after Anti-Transform
Double_t *out = new Double_t[N];
//Real part of the transformation
Double_t *re = new Double_t[N];
//Imaginary part of the transformation
Double_t *im = new Double_t[N];
//time scale for XAxis in time space
Double_t *timesArray = new Double_t[N];
//Frequency scale for XAxis in frequency space
Double_t *frecuencias = new Double_t[N];

// microSeconds to match input of transfer function (MHz).
//This is the oscilloscope time resolution which in this case is 0.25 ns
//or sample frequency = 4 GHz
Double_t timeInterval = 0.00025; //in microS
for(int h = 0; h < N; h++){
//put file input in a static array
in[h] = signal.at(h);
timesArray[h] = h*timeInterval;// in microSeconds
//Frequency step in MHz. Needs N for normalization
frecuencias[h] = h/(timeInterval*N);
```

```

}

// R2C: real to complex conversion
TVirtualFFT *fftr2c = TVirtualFFT::FFT(1, &N, "R2C", 1, 4);
fftr2c->SetPoints();
fftr2c->Transform();

// By doing the manual DFT:
/* for (Int_t i=0; i<N; i++){
reTMP=0;
imTMP=0;
for (Int_t j=0; j<N; j++){
reTMP += TMath::Cos(TMath::TwoPi()*j/N*i)*signal.at(j);
imTMP += TMath::Sin(TMath::TwoPi()*j/N*i)*signal.at(j);
}

*/
// the same results are obtained

//Temporary array to store the output of the transform in Fourier space
Double_t reTMP, imTMP;

vector <Double_t> magnitud;
vector <Double_t> phase;

for (Int_t i=0; i<N; i++){
fftr2c->GetPointComplex(i, reTMP, imTMP);
re[i] = reTMP/N; //normalization
im[i] = imTMP/N; //normalization
//No need to calculate magnitude, but here it is.
magnitud.push_back(pow(pow(reTMP/N,2) + pow(imTMP/N,2),0.5));
//No need to calculate phase, but here it is.
phase.push_back(atan2(imTMP/N,reTMP/N));
}

//Now let's make a backward transform:
//Complex to real conversion
TVirtualFFT *fft_back = TVirtualFFT::FFT(1, &N, "C2R", 5, 1);

for(int h = 0; h < N; h++){
re[h] = (re[h]*transferFunctionRe->Eval(frecuencias[h])-  

im[h]*transferFunctionIm->Eval(frecuencias[h]));
im[h] = (re[h]*transferFunctionIm->Eval(frecuencias[h])+  

im[h]*transferFunctionRe->Eval(frecuencias[h]));
}

fft_back->SetPointsComplex(re,in);
fft_back->Transform();
//Signal in time after anti transform. Only real values
Double_t *out = fft_back->GetPointsReal();

```

---

# Bibliography

- [1] V. Hess, Penetrating radiation in seven free balloon flights, *Phys. Z.* 13 (1912) 1804.
- [2] R. A. Millikan, High frequency rays of cosmic origin, *Science* 62 (1612) (1925) 445–448. [arXiv:https://science.sciencemag.org/content/62/1612/445.full.pdf](https://science.sciencemag.org/content/62/1612/445.full.pdf), doi:10.1126/science.62.1612.445.  
URL <https://science.sciencemag.org/content/62/1612/445>
- [3] S. H. Neddermeyer, C. D. Anderson, Note on the nature of cosmic-ray particles, *Phys. Rev.* 51 (1937). doi:10.1103/PhysRev.51.884.
- [4] Auger, P., et al., Extension et pouvoir pénétrant des grandes gerbes de rayons cosmiques, *Comptes rendus Physique* 208 (1939) 1641. doi:10.1103/PhysRev.51.884.
- [5] P. Blasi, The Origin of Galactic Cosmic Rays, *Astron. Astrophys. Rev.* 21 (2013) 70. arXiv:1311.7346, doi:10.1007/s00159-013-0070-7.
- [6] R. Aloisio, Acceleration and propagation of ultra high energy cosmic rays, *PTEP* 2017 (12) (2017) 12A102. arXiv:1707.08471, doi:10.1093/ptep/ptx115.
- [7] M. T. Dova, Ultra-High Energy Cosmic Rays, in: Proceedings, 7th CERN–Latin-American School of High-Energy Physics (CLASHEP2013): Arequipa, Peru, March 6–19, 2013, 2015, pp. 169–190. arXiv:1604.07584, doi:10.5170/CERN-2015-001.169.
- [8] A. Aab, et al., Pierre Auger, Observation of a Large-scale Anisotropy in the Arrival Directions of Cosmic Rays above  $8 \times 10^{18}$  eV, *Science* 357 (6537) (2017) 1266–1270. arXiv:1709.07321, doi:10.1126/science.aan4338.
- [9] M. G. Baring, Diffusive shock acceleration: The Fermi mechanism, in: Very high-energy phenomena in the universe. Proceedings, 32nd Rencontres de Moriond, Les Arcs, France, January 18–25, 1997, 1997, pp. 97–106. arXiv:astro-ph/9711177.
- [10] K. Greisen, End to the cosmic ray spectrum?, *Phys. Rev. Lett.* 16 (1966) 748–750. doi:10.1103/PhysRevLett.16.748.
- [11] G. T. Zatsepin, V. A. Kuzmin, Upper limit of the spectrum of cosmic rays, *JETP Lett.* 4 (1966) 78–80, [Pisma Zh. Eksp. Teor. Fiz. 4, 114 (1966)].
- [12] J. Linsley, Evidence for a primary cosmic-ray particle with energy  $10^{20}$  ev, *Phys. Rev. Lett.* 10 (1963) 146–148. doi:10.1103/PhysRevLett.10.146.  
URL <https://link.aps.org/doi/10.1103/PhysRevLett.10.146>

- [13] D. J. Bird, et al., Detection of a cosmic ray with measured energy well beyond the expected spectral cutoff due to cosmic microwave radiation, *Astrophys. J.* 441 (1995) 144–150. [arXiv:astro-ph/9410067](https://arxiv.org/abs/astro-ph/9410067), doi:10.1086/175344.
- [14] M. Takeda, N. Sakaki, K. H. et al., [Energy determination in the akeno giant air shower array experiment](#), *Astroparticle Physics* 19 (4) (2003) 447 – 462. doi:[https://doi.org/10.1016/S0927-6505\(02\)00243-8](https://doi.org/10.1016/S0927-6505(02)00243-8).  
URL <http://www.sciencedirect.com/science/article/pii/S0927650502002438>
- [15] M. A. Lawrence, R. J. O. Reid, A. A. Watson, [The cosmic ray energy spectrum above  \$4 \times 10^{17}\$ ev as measured by the haverah park array](#), *Journal of Physics G: Nuclear and Particle Physics* 17 (5) (1991) 733–757. doi:10.1088/0954-3899/17/5/019.  
URL <https://doi.org/10.1088%2F0954-3899%2F17%2F5%2F019>
- [16] G. A. Medina-Tanco, The Energy spectrum observed by the AGASA experiment and the spatial distribution of the sources of ultrahigh-energy cosmic rays, *Astrophys. J.* 510 (1999) L91. [arXiv:astro-ph/9810366](https://arxiv.org/abs/astro-ph/9810366), doi:10.1086/311814.
- [17] A. Aab *et al.* (Pierre Auger Collab.), The Pierre Auger Cosmic Ray Observatory, *Nucl. Instrum. Meth. A* 798 (2015) 172–213. [arXiv:astro-ph.IM/1502.01323](https://arxiv.org/abs/astro-ph.IM/1502.01323), doi:10.1016/j.nima.2015.06.058.
- [18] W. F. Hanlon, [Recent results from the telescope array project](#), *Nuclear and Particle Physics Proceedings* 279-281 (2016) 15 – 22, proceedings of the 9th Cosmic Ray International Seminar. doi:<https://doi.org/10.1016/j.nuclphysbps.2016.10.004>.  
URL <http://www.sciencedirect.com/science/article/pii/S2405601416301857>
- [19] K. H. Kampert, et al., KASCADE Grande, Cosmic rays in the ‘knee’-region - recent results from KASCADE, *Acta Phys. Polon. B* 35 (2004) 1799–1812. [arXiv:astro-ph/0405608](https://arxiv.org/abs/astro-ph/0405608).
- [20] G. Giacinti, M. Kachelriess, D. V. Semikoz, G. Sigl, Cosmic Ray Anisotropy as Signature for the Transition from Galactic to Extragalactic Cosmic Rays, *JCAP* 1207 (2012) 031. [arXiv:1112.5599](https://arxiv.org/abs/1112.5599), doi:10.1088/1475-7516/2012/07/031.
- [21] W. D. Apel, et al., KASCADE Grande, Kneelike structure in the spectrum of the heavy component of cosmic rays observed with KASCADE-Grande, *Phys. Rev. Lett.* 107 (2011) 171104. [arXiv:1107.5885](https://arxiv.org/abs/1107.5885), doi:10.1103/PhysRevLett.107.171104.
- [22] M. Unger, Cosmic Rays above the Knee (2008)[arXiv:0812.2763](https://arxiv.org/abs/0812.2763).
- [23] Particle Data Group, [Review of particle physics](#), *Phys. Rev. D* 98 (2018) 030001. doi:10.1103/PhysRevD.98.030001.  
URL <https://link.aps.org/doi/10.1103/PhysRevD.98.030001>
- [24] R. Alves Batista, M. Erdmann, C. Evoli, K. H. Kampert, D. Kuempel, G. Müller, G. Sigl, A. van Vliet, D. Walz, T. Winchen, CRPropa: a public framework to propagate UHECRs in the universe, *EPJ Web Conf.* 99 (2015) 13004. [arXiv:1411.2259](https://arxiv.org/abs/1411.2259), doi:10.1051/epjconf/20159913004.
- [25] J. W. Cronin, [The highest-energy cosmic rays](#), *Nuclear Physics B - Proceedings Supplements* 138 (2005) 465 – 491, proceedings of the Eighth International Workshop on Topics in Astroparticle and Underground Physics. doi:<https://doi.org/10.1016/j.nuclphysbps.2004.11.107>.  
URL <http://www.sciencedirect.com/science/article/pii/S0920563204006723>

- [26] M. Unger for the Pierre Auger Collaboration, Pierre Auger, Highlights from the Pierre Auger Observatory, PoS ICRC2017 (2018) 1102, [35,1102(2017)]. [arXiv:1710.09478](https://arxiv.org/abs/1710.09478), [doi:10.22323/1.301.1102](https://doi.org/10.22323/1.301.1102).
- [27] V. Verzi, D. Ivanov, Y. Tsunesada, Measurement of Energy Spectrum of Ultra-High Energy Cosmic Rays, PTEP 2017 (12) (2017) 12A103. [arXiv:1705.09111](https://arxiv.org/abs/1705.09111), [doi:10.1093/ptep/ptx082](https://doi.org/10.1093/ptep/ptx082).
- [28] R. Aloisio, V. Berezinsky, S. Grigorjeva, [Analytic calculations of the spectra of ultra-high energy cosmic ray nuclei. i. the case of cmb radiation](#), Astroparticle Physics 41 (2013) 73–93. [doi:10.1016/j.astropartphys.2012.07.010](https://doi.org/10.1016/j.astropartphys.2012.07.010)  
URL <http://dx.doi.org/10.1016/j.astropartphys.2012.07.010>
- [29] R. Aloisio, V. Berezinsky, S. Grigorjeva, [Analytic calculations of the spectra of ultra-high energy cosmic ray nuclei. ii. the general case of background radiation](#), Astroparticle Physics 41 (2013) 94–107. [doi:10.1016/j.astropartphys.2012.06.003](https://doi.org/10.1016/j.astropartphys.2012.06.003)  
URL <http://dx.doi.org/10.1016/j.astropartphys.2012.06.003>
- [30] D. Ivanov, Telescope-Array, Pierre Auger, Report of the Telescope Array - Pierre Auger Observatory Working Group on Energy Spectrum, PoS ICRC2017 (2018) 498. [doi:10.22323/1.301.0498](https://doi.org/10.22323/1.301.0498).
- [31] Oliver Deligny for the Pierre Auger Collaboration, Pierre Auger, The energy spectrum of ultra-high energy cosmic rays measured at the pierre auger observatory and at the telescope array, PoS ICRC2019 (2019) 234.
- [32] A. Watson, The mass composition of cosmic rays above 1017 ev, Nuclear Physics B - Proceedings Supplements 136 (2004) 290–300. [doi:10.1016/j.nuclphysbps.2004.10.066](https://doi.org/10.1016/j.nuclphysbps.2004.10.066).
- [33] K.-H. Kampert, M. Unger, Measurements of the Cosmic Ray Composition with Air Shower Experiments, Astropart. Phys. 35 (2012) 660–678. [arXiv:1201.0018](https://arxiv.org/abs/1201.0018), [doi:10.1016/j.astropartphys.2012.02.004](https://doi.org/10.1016/j.astropartphys.2012.02.004).
- [34] A. Haungs, H. Rebel, M. Roth, Energy spectrum and mass composition of high-energy cosmic rays, Reports on Progress in Physics 66 (2003) 1145. [doi:10.1088/0034-4885/66/7/202](https://doi.org/10.1088/0034-4885/66/7/202).
- [35] J. Matthews, A Heitler model of extensive air showers, Astropart. Phys. 22 (2005) 387–397. [doi:10.1016/j.astropartphys.2004.09.003](https://doi.org/10.1016/j.astropartphys.2004.09.003).
- [36] J. Alvarez-Muñiz, R. Engel, T. K. Gaisser, J. A. Ortiz, T. Stanev, [Hybrid simulations of extensive air showers](#), Physical Review D 66 (3) (2002). [doi:10.1103/physrevd.66.033011](https://doi.org/10.1103/physrevd.66.033011)  
URL <http://dx.doi.org/10.1103/PhysRevD.66.033011>
- [37] R. Engel, D. Heck, T. Pierog, [Extensive air showers and hadronic interactions at high energy](#), Annual Review of Nuclear and Particle Science 61 (1) (2011) 467–489. [arXiv:https://doi.org/10.1146/annurev.nucl.012809.104544](https://arxiv.org/abs/https://doi.org/10.1146/annurev.nucl.012809.104544), [doi:10.1146/annurev.nucl.012809.104544](https://doi.org/10.1146/annurev.nucl.012809.104544)  
URL <https://doi.org/10.1146/annurev.nucl.012809.104544>
- [38] J. Abraham *et al.* (Pierre Auger Collab.), Properties and performance of the prototype instrument for the pierre auger observatory, Nucl. Instrum. Meth. A523 (1-2) (2004) 50 – 95. [doi:DOI:10.1016/j.nima.2003.12.012](https://doi.org/10.1016/j.nima.2003.12.012)

- [39] P. Privitera, [The pierre auger observatory](#), Nuclear Physics B - Proceedings Supplements 110 (2002) 487 – 490. [doi:  
https://doi.org/10.1016/S0920-5632\(02\)01543-8](https://doi.org/10.1016/S0920-5632(02)01543-8).  
URL <http://www.sciencedirect.com/science/article/pii/S0920563202015438>
- [40] I. Allekotte *et al.* (Pierre Auger Collab.), The Surface Detector System of the Pierre Auger Observatory, Nucl. Instrum. Meth. A586 (2007) 409–420. [arXiv:  
astro-ph/0712.2832](https://arxiv.org/abs/astro-ph/0712.2832), [doi:  
10.1016/j.nima.2007.12.016](https://doi.org/10.1016/j.nima.2007.12.016).
- [41] F. Arqueros, F. et al., Pierre Auger, [The Central laser facility at the Pierre Auger Observatory](#), 2005. [arXiv:  
astro-ph/0507334](https://arxiv.org/abs/astro-ph/0507334).  
URL [http://lss.fnal.gov/cgi-bin/find\\_paper.pl?conf=05-291-E-TD](http://lss.fnal.gov/cgi-bin/find_paper.pl?conf=05-291-E-TD)
- [42] J. Abraham *et al.* (Pierre Auger Collab.), Properties and performance of the prototype instrument for the pierre auger observatory, Nucl. Instrum. Meth. A523 (1-2) (2004) 50 – 95. [doi:  
DOI:10.1016/j.nima.2003.12.012](https://doi.org/10.1016/j.nima.2003.12.012).
- [43] M. Unger, Pierre Auger, Mass sensitive observables of the pierre auger observatory, EPJ Web of Conferences 53 (2013) 04009–. [doi:  
10.1051/epjconf/20135304009](https://doi.org/10.1051/epjconf/20135304009).
- [44] E. M. Holt, Combined detection of muons and radio emission of cosmic-ray air showers, Ph.D. thesis, Karlsruher Institut für Technologie (KIT), 51.03.04; LK 01 (2018). [doi:  
10.5445/IR/1000083318](https://doi.org/10.5445/IR/1000083318).
- [45] C. Bonifazi, [The angular resolution of the pierre auger observatory](#), Nuclear Physics B - Proceedings Supplements 190 (2009) 20 – 25, proceedings of the Cosmic Ray International Seminars. [doi:  
https://doi.org/10.1016/j.nuclphysbps.2009.03.063](https://doi.org/10.1016/j.nuclphysbps.2009.03.063).  
URL <http://www.sciencedirect.com/science/article/pii/S0920563209003028>
- [46] C. Bonifazi, A. Letessier-Selvon, E. Santos, [A model for the time uncertainty measurements in the auger surface detector array](#), Astroparticle Physics 28 (6) (2008) 523 – 528. [doi:  
https://doi.org/10.1016/j.astropartphys.2007.09.007](https://doi.org/10.1016/j.astropartphys.2007.09.007).  
URL <http://www.sciencedirect.com/science/article/pii/S0927650507001338>
- [47] J. Abraham *et al.* (Pierre Auger Collab.), Trigger and aperture of the surface detector array of the Pierre Auger Observatory, Nucl. Instrum. Meth. A613 (2010) 29–39.
- [48] J. Abraham *et al.* (Pierre Auger Collab.), The fluorescence detector of the Pierre Auger Observatory, Nucl. Instrum. Meth. A620 (2010) 227 – 251.
- [49] E. Holt for the Pierre Auger Collaboration, Recent Results of the Auger Engineering Radio Array (AERA) (2017) 105–112[PoSICRC2017,492(2018)]. [doi:  
10.22323/1.301.0492](https://doi.org/10.22323/1.301.0492).
- [50] C. Medina et al., enhancing the pierre auger observatory to the 1017–1018.5ev range: Capabilities of an infill surface array (2006) 302–311.
- [51] A. Etchegoyen, Amiga, auger muons and infill for the ground array, Proceedings of the 30th International Cosmic Ray Conference, ICRC 2007 5 (2008) 1191–1194.
- [52] N. Gonzalez et al., Reconstruction performance of simulated events with the SD-433: a WCD+UMD analysis, Pierre Auger internal note (2019) GAP2019\_036.
- [53] A. D. Supanitsky, A. Etchegoyen, G. Medina-Tanco, I. Allekotte, M. G. Berisso, M. C. Medina, Underground Muon Counters as a Tool for Composition Analyses, Astropart. Phys. 29 (2008) 461–470. [arXiv:  
0804.1068](https://arxiv.org/abs/0804.1068), [doi:  
10.1016/j.astropartphys.2008.05.003](https://doi.org/10.1016/j.astropartphys.2008.05.003).

- [54] A. Aab, et al., Pierre Auger, Prototype muon detectors for the AMIGA component of the Pierre Auger Observatory, *JINST* 11 (02) (2016) P02012. [arXiv:1605.01625](https://arxiv.org/abs/1605.01625), doi:[10.1088/1748-0221/11/02/P02012](https://doi.org/10.1088/1748-0221/11/02/P02012).
- [55] T. H.-J. Mathes for the Pierre Auger Collaboration, The HEAT telescopes of the Pierre Auger Observatory: Status and first data, in: Proceedings, 32nd International Cosmic Ray Conference (ICRC 2011): Beijing, China, August 11-18, 2011, Vol. 3, 2011, p. 153. doi:[10.7529/ICRC2011/V03/0761](https://doi.org/10.7529/ICRC2011/V03/0761).
- [56] Kahn F. et al, Radiation from cosmic ray air showers, in: *Proc. R. Soc. Lond. A*, Vol. 289, 1997, p. 1417. doi:<http://doi.org/10.1098/rspa.1966.0007>.
- [57] J. Abraham *et al.* (Pierre Auger Collab.), Measurement of the energy spectrum of cosmic rays above  $10^{18}$  eV using the Pierre Auger Observatory, *Phys. Lett. B* 685 (4-5) (2010) 239 – 246. doi:[10.1016/j.physletb.2010.02.013](https://doi.org/10.1016/j.physletb.2010.02.013).
- [58] M. Settimi (Pierre Auger Collab.), An update on a search for ultra-high energy photons using the Pierre Auger Observatory, in: Proc. 32nd Int. Cosmic Ray Conf., Beijing, China, 2011.
- [59] P. Abreu *et al.* (Pierre Auger Collab.), Ultrahigh Energy Neutrinos at the Pierre Auger Observatory, *Adv. High Energy Phys.* 2013 (2013) 708680. [arXiv:1304.1630](https://arxiv.org/abs/1304.1630), doi:[10.1155/2013/708680](https://doi.org/10.1155/2013/708680).
- [60] J. Abraham *et al.* (Pierre Auger Collab.), Measurement of the Depth of Maximum of Extensive Air Showers above  $10^{18}$  eV, *Phys. Rev. Lett.* 104 (9) (2010) 091101. doi:[10.1103/PhysRevLett.104.091101](https://doi.org/10.1103/PhysRevLett.104.091101).
- [61] The Pierre Auger Collaboration, Measurement of the proton-air cross-section at  $\sqrt{s} = 57$  TeV with the Pierre Auger Observatory (2012) 341–347 [arXiv:1212.4053](https://arxiv.org/abs/1212.4053).
- [62] A. Aab *et al.* (Pierre Auger Collab.), Muons in air showers at the Pierre Auger Observatory: Mean number in highly inclined events, *Phys. Rev. D* 91 (3) (2015) 032003, [Erratum: *Phys. Rev.D*91,no.5,059901(2015)]. [arXiv:1408.1421](https://arxiv.org/abs/1408.1421), doi:[10.1103/PhysRevD.91.059901](https://doi.org/10.1103/PhysRevD.91.059901), [10.1103/PhysRevD.91.032003](https://doi.org/10.1103/PhysRevD.91.032003).
- [63] A. Aab *et al.* (Pierre Auger Collab.), The Pierre Auger Observatory Upgrade - Preliminary Design Report (2016). [arXiv:astro-ph.IM/1604.03637](https://arxiv.org/abs/astro-ph.IM/1604.03637).
- [64] K. Werner, F.-M. Liu, T. Pierog, Parton ladder splitting and the rapidity dependence of transverse momentum spectra in deuteron-gold collisions at the BNL Relativistic Heavy Ion Collider, *Phys. Rev. C: Nucl. Phys.* 74 (4) (2006) 11, <http://link.aps.org/abstract/PRC/v74/e044902>. doi:[10.1103/PhysRevC.74.044902](https://doi.org/10.1103/PhysRevC.74.044902).
- [65] T. Pierog, K. Werner, Muon Production in Extended Air Shower Simulations, *Phys. Rev. Lett.* 101 (2008) 171101. [arXiv:astro-ph/0611311](https://arxiv.org/abs/astro-ph/0611311), doi:[10.1103/PhysRevLett.101.171101](https://doi.org/10.1103/PhysRevLett.101.171101).
- [66] S. Ostapchenko, Monte Carlo treatment of hadronic interactions in enhanced Pomeron scheme: I. QGSJET-II model, *Phys. Rev. D* 83 (2011) 014018. [arXiv:1010.1869](https://arxiv.org/abs/1010.1869), doi:[10.1103/PhysRevD.83.014018](https://doi.org/10.1103/PhysRevD.83.014018).
- [67] E.-J. Ahn, R. Engel, T. K. Gaisser, P. Lipari, T. Stanev, Cosmic ray interaction event generator SIBYLL 2.1, *Phys. Rev. D* 80 (2009) 094003. [arXiv:0906.4113](https://arxiv.org/abs/0906.4113), doi:[10.1103/PhysRevD.80.094003](https://doi.org/10.1103/PhysRevD.80.094003).

- [68] A. Aab *et al.* (Pierre Auger Collab.), Depth of Maximum of Air-Shower Profiles at the Pierre Auger Observatory: Composition Implications, Phys. Rev. D (2014) [arXiv: astro-ph.HE/1409.5083](#).
- [69] J. Candia, S. Mollerach, E. Roulet, Cosmic ray spectrum and anisotropies from the knee to the second knee, JCAP 0305 (2003) 003. [arXiv:astro-ph/0302082](#), [doi:10.1088/1475-7516/2003/05/003](#).
- [70] R. Smida for the Pierre Auger Collaboration, Scintillator detectors of augerprime, in: The Pierre Auger Observatory: Contributions to the 35th International Cosmic Ray Conference (ICRC 2017), Vol. ICRC2017, 2018, p. 390. [doi:10.22323/1.301.0390](#).
- [71] A. Castellina for the Pierre Auger Collaboration, The dynamic range of the Auger-Prime Surface Detector: technical solution and physics reach, PoS ICRC2017 (2018) 397, [,161(2017)]. [doi:10.22323/1.301.0397](#).
- [72] D. Nitz for the Pierre Auger Collaboration, New electronics for the surface detectors of the pierre auger observatory, in: The Pierre Auger Observatory: Contributions to the 36th International Cosmic Ray Conference (ICRC 2019), Vol. ICRC2019, 2019, p. 370.
- [73] J. Zorn *et al.*, The first measurement with the fd operated at a reduced pmt gain, Pierre Auger internal note (2015) GAP2015\_021.
- [74] Bjarni Pont for the Pierre Auger Collaboration, A large radio detector at the pierre auger observatory – measuring the properties of cosmic rays up to the highest energies, in: The Pierre Auger Observatory: Contributions to the 36th International Cosmic Ray Conference (ICRC 2019), Vol. ICRC2019, 2019, p. 395.
- [75] A. Pla-Dalmau, A. D. Bross, V. V. Rykalin, Extruding plastic scintillator at fermilab, in: 2003 IEEE Nuclear Science Symposium. Conference Record (IEEE Cat. No.03CH37515), Vol. 1, 2003, pp. 102–104 Vol.1. [doi:10.1109/NSSMIC.2003.1352007](#).
- [76] J. Lakowicz, Principles of Fluorescence Spectroscopy, Vol. 1, 2006. [doi:10.1007/978-0-387-46312-4](#).
- [77] J. Birks, Chapter 3 - the scintillation process in organic materials—i, in: J. Birks (Ed.), The Theory and Practice of Scintillation Counting, International Series of Monographs in Electronics and Instrumentation, Pergamon, 1964, pp. 39 – 67.
- [78] S. N. Ahmed, 6 - scintillation detectors and photodetectors, in: S. N. Ahmed (Ed.), Physics and Engineering of Radiation Detection (Second Edition), second edition Edition, Elsevier, 2015, pp. 331 – 433.
- [79] M. Latino, M. Hampel, A. Almela, A. Krieger, D. Gorbeña, A. Ferrero, G. de la Vega, A. Lucero, F. Suarez, M. Videla, O. Wainberg, A. Etchegoyen, Amiga at the auger observatory: The scintillator module testing system, Journal of Instrumentation 6 (2011) P06006. [doi:10.1088/1748-0221/6/06/P06006](#).
- [80] Saint-Gobain, Scintillating optical fibers bcf-99-29amc (2016).
- [81] Federico Sánchez for the Pierre Auger Collaboration, The muon component of extensive air showers above  $10^{17.5}$  eV measured with the Pierre Auger Observatory, PoS ICRC2019 (2019) 411.

- [82] A. M. Botti for the Pierre Auger Collaboration, Pierre Auger, The AMIGA underground muon detector of the Pierre Auger Observatory - performance and event reconstruction, PoS ICRC2019 (2019) 202.
- [83] Hamamatsu Photonics K K, MPPC (Multi-Pixel Photon Counter) arrays S13361-2050 series (2018).
- [84] H. P. K. K, Photomultiplier tube assembly8 H8804 (2012).
- [85] M. Platino et al., AMIGA Silicon-Photomultipliers Front-End Tests, Auger internal note 90 (2014).
- [86] S. Dolinsky, Novel approach for calibration breakdown voltage of large area SiPM, PoS PhotoDet2012 (2012) 005. doi:[10.22323/1.158.0005](https://doi.org/10.22323/1.158.0005).
- [87] Weeroc, Datasheet - citiroc 1a v2.5 (2019).
- [88] The Pierre Auger Collaboration, Muon counting using silicon photomultipliers in the AMIGA detector of the Pierre Auger observatory, JINST 22 (2017) P03002. doi:[10.1088/1748-0221/12/03/P03002](https://doi.org/10.1088/1748-0221/12/03/P03002).
- [89] D. Veberič, Maximum-likelihood reconstruction of photon returns from simultaneous analog and photon-counting lidar measurements, Appl. Opt. 51 (2) (2012) 139–147. doi:[10.1364/AO.51.000139](https://doi.org/10.1364/AO.51.000139).  
URL <http://ao.osa.org/abstract.cfm?URI=ao-51-2-139>
- [90] Hamamatsu Photonics K K, Power supply for MPPC C11204-01 (2019).
- [91] Hamamatsu Photonics K.K, MPPC Multi-pixel photon counter S12572-010, -015C/P (2018).
- [92] B. Keilhauer, M. Will, Atmospheric monitoring and model applications at the pierre auger observatory, EPJ Web of Conferences 89 (2015) 02001. doi:[10.1051/epjconf/20158902001](https://doi.org/10.1051/epjconf/20158902001).
- [93] D. Renker, E. Lorenz, Advances in solid state photon detectors, Journal of Instrumentation 4 (04) (2009) P04004–P04004. doi:[10.1088/1748-0221/4/04/p04004](https://doi.org/10.1088/1748-0221/4/04/p04004).  
URL <https://doi.org/10.1088%2F1748-0221%2F4%2F04%2Fp04004>
- [94] R. Pagano, D. Corso, S. Lombardo, G. Valvo, D. Sanfilippo, G. Fallica, S. Libertino, Dark current in silicon photomultiplier pixels: Data and model, IEEE Transactions on Electron Devices 59 (2012) 2410–2416. doi:[10.1109/TED.2012.2205689](https://doi.org/10.1109/TED.2012.2205689).
- [95] P. K. F. Grieder, Cosmic rays at earth: Researcher's reference, manual and data book, Elsevier, Amsterdam, 2001.
- [96] S. Avvakumov et al., Spontaneous light emission from fibers in minos, Nuclear Instruments and Methods in Physics Research Section A: Accelerators, Spectrometers, Detectors and Associated Equipment 545 (1) (2005) 145 – 155. doi:<https://doi.org/10.1016/j.nima.2005.01.340>.  
URL <http://www.sciencedirect.com/science/article/pii/S0168900205005875>
- [97] Vacheret, A. et al., Characterization and Simulation of the Response of Multi Pixel Photon Counters to Low Light Levels, Nucl. Instrum. Meth. A656 (1) (2011) 69–83. arXiv:[1101.1996](https://arxiv.org/abs/1101.1996), doi:[10.1016/j.nima.2011.07.022](https://doi.org/10.1016/j.nima.2011.07.022).

- [98] W. Bludau, A. Onton, W. Heine, [Temperature dependence of the band gap of silicon](#), Journal of Applied Physics 45 (4) (1974) 1846–1848. [arXiv:https://doi.org/10.1063/1.1663501](https://arxiv.org/abs/https://doi.org/10.1063/1.1663501), [doi:10.1063/1.1663501](https://doi.org/10.1063/1.1663501).  
URL <https://doi.org/10.1063/1.1663501>
- [99] B. Wundheiler for the Pierre Auger Collaboration, The AMIGA muon counters of the Pierre Auger Observatory: performance and first data, Proceedings of the 32nd International Cosmic Ray Conference, ICRC 2011 3 (2011) 84–87. [doi:10.7529/ICRC2011-V03/0341](https://doi.org/10.7529/ICRC2011-V03/0341).
- [100] M. Platino et al., AMIGA Production Status, Presentation at Auger Analysis Meeting (2018).
- [101] D. Ravignani et al., Time distribution of the muons observed with the Muon Detector of the Pierre Auger Observatory, Pierre Auger internal note (2019) GAP2019\_013.
- [102] F. Sánchez et al., Timing studies for the prototype AMIGA detectors, Pierre Auger internal note (2016) GAP2016\_069.
- [103] M. Platino et al., [AMIGA at the Auger Observatory: the scintillator module testing system](#), Journal of Instrumentation 6 (06) (2011) P06006–P06006. [doi:10.1088/1748-0221/6/06/p06006](https://doi.org/10.1088/1748-0221/6/06/p06006)  
URL <https://doi.org/10.1088%2F1748-0221%2F6%2F06%2Fp06006>
- [104] X. Bertou *et al.* (Pierre Auger Collab.), Calibration of the surface array of the Pierre Auger Observatory, Nucl. Instrum. Meth. A568 (2006) 839–846.
- [105] M. Loeve, [Probability Theory: Third Edition](#), Dover Books on Mathematics, Dover Publications, 2017.  
URL <https://books.google.com.ar/books?id=sKvPDgAAQBAJ>
- [106] B. Wundheiler, Pierre Auger, The AMIGA Muon Counters of the Pierre Auger Observatory: Performance and Studies of the Lateral Distribution Function, PoS ICRC2015 (2016) 324. [doi:10.22323/1.236.0324](https://doi.org/10.22323/1.236.0324).
- [107] The Pierre Auger collaboration, [Reconstruction of inclined air showers detected with the pierre auger observatory](#), Journal of Cosmology and Astroparticle Physics 2014 (08) (2014) 019–019. [doi:10.1088/1475-7516/2014/08/019](https://doi.org/10.1088/1475-7516/2014/08/019).  
URL <https://doi.org/10.1088%2F1475-7516%2F2014%2F08%2F019>
- [108] D. Ravignani, A. D. Supanitsky, D. Melo, Reconstruction of air shower muon densities using segmented counters with time resolution, Astropart. Phys. 82 (2016) 108–116. [arXiv:1606.02531](https://arxiv.org/abs/1606.02531), [doi:10.1016/j.astropartphys.2016.06.001](https://doi.org/10.1016/j.astropartphys.2016.06.001).
- [109] S. Müller for the Pierre Auger Collaboration, Direct Measurement of the Muon Density in Air Showers with the Pierre Auger Observatory, EPJ Web of Conferences 210 (2019) 02013. [doi:10.1051/epjconf/201921002013](https://doi.org/10.1051/epjconf/201921002013).
- [110] S. Argirò, S. Barroso, J. Gonzalez, L. Nellen, T. Paul, T. Porter, L. P. Jr., M. Roth, R. Ulrich, D. Veberič, [The offline software framework of the pierre auger observatory](#), Nuclear Instruments and Methods in Physics Research Section A: Accelerators, Spectrometers, Detectors and Associated Equipment 580 (3) (2007) 1485 – 1496. [doi:https://doi.org/10.1016/j.nima.2007.07.010](https://doi.org/10.1016/j.nima.2007.07.010).  
URL <http://www.sciencedirect.com/science/article/pii/S0168900207014106>

- [111] Y. Katznelson, An Introduction to Harmonic Analysis, 3rd Edition, Cambridge Mathematical Library, Cambridge University Press, 2004. [doi:10.1017/CBO9781139165372](https://doi.org/10.1017/CBO9781139165372).
- [112] D. Marano, A. Grasso, Enhanced analytical model and output dynamic response of sipm-based electronic read-outs, 2016, pp. 305–308. [doi:10.1109/ICECS.2016.7841193](https://doi.org/10.1109/ICECS.2016.7841193).
- [113] J. Shlens, A tutorial on principal component analysis, *Educational* 51 (2014).
- [114] G. Ros, G. Saez-Cano, G. Medina-Tanco, A. D. Supanitsky, On the design of experiments based on plastic scintillators using geant4 simulations, *Radiation Physics and Chemistry* 153 (2018). [doi:10.1016/j.radphyschem.2018.09.021](https://doi.org/10.1016/j.radphyschem.2018.09.021).
- [115] O. Wainberg, A. Almela, M. Platino, F. Sanchez, F. Suarez, A. Lucero, M. Videla, B. Wundheiler, D. Melo, M. Hampel, A. Etchegoyen, Digital electronics for the pierre auger observatory amiga muon counters, *Journal of Instrumentation* 9 (2013). [doi:10.1088/1748-0221/9/04/T04003](https://doi.org/10.1088/1748-0221/9/04/T04003).
- [116] D. Marano, M. Belluso, G. Bonanno, S. Billotta, A. Grillo, S. Garozzo, G. Romeo, O. Catalano, G. La Rosa, G. Sottile, D. Impiombato, S. Giarrusso, Citiroc high-level analog front-end model implementation and simulations, *International Journal of Circuits, Systems and Signal Processing* 8 (2014) 276–285.
- [117] L. W. Nagel, D. Pederson, [Spice \(simulation program with integrated circuit emphasis\)](#), Tech. Rep. UCB/ERL M382, EECS Department, University of California, Berkeley (Apr 1973).  
URL <http://www2.eecs.berkeley.edu/Pubs/TechRpts/1973/22871.html>
- [118] S. Agostinelli, et al., GEANT4, *GEANT4: A Simulation toolkit*, Nucl. Instrum. Meth. A506 (2003) 250–303. [doi:10.1016/S0168-9002\(03\)01368-8](https://doi.org/10.1016/S0168-9002(03)01368-8).
- [119] F. Sánchez et al., The AMIGA extension of Auger Offline Software, *Pierre Auger internal note* (2012) GAP2012\_135.
- [120] I. Maris et al., Data summary trees and shower visualization for reconstructed auger events, *Pierre Auger internal note* (2006) GAP2006\_081.
- [121] D. Ravignani, A. D. Supanitsky, D. Melo, B. Wundheiler, A method to reconstruct the muon lateral distribution with an array of segmented counters with time resolution (2015).
- [122] D. Heck, J. Knapp, J. N. Capdevielle, G. Schatz, T. Thouw, CORSIKA: A Monte Carlo code to simulate extensive air showers (1998).
- [123] The Pierre Auger Collaboration, Inferences on mass composition and tests of hadronic interactions from 0.3 to 100 eev using the water-cherenkov detectors of the pierre auger observatory, *Physical Review D* 96 (12) (2017). [doi:10.1103/PhysRevD.96.122003](https://doi.org/10.1103/PhysRevD.96.122003).
- [124] A.N. Kalinovskii, N.V. Mokhov, Y.P. Nikitin, Passage of High Energy Particles through Matter.
- [125] D. Chirkin, W. Rhode, Muon Monte Carlo: A High-precision tool for muon propagation through matter (2004)[arXiv:hep-ph/0407075](https://arxiv.org/abs/hep-ph/0407075).

- [126] D. Ravignani, A. D. Supanitsky, A new method for reconstructing the muon lateral distribution with an array of segmented counters, *Astropart. Phys.* 65 (2015) 1–10. [arXiv:1411.7649](https://arxiv.org/abs/1411.7649), doi:[10.1016/j.astropartphys.2014.11.007](https://doi.org/10.1016/j.astropartphys.2014.11.007).
- [127] I. Maris for the Pierre Auger Collaboration, The AMIGA Infill Detector of the Pierre Auger Observatory, *Proceedings of the 32nd International Cosmic Ray Conference, ICRC 2011* 1 (2011) 267–270.
- [128] W. D. Apel, et al., The KASCADE-Grande experiment, *Nucl. Instrum. Meth. A* 620 (2010) 202–216. doi:[10.1016/j.nima.2010.03.147](https://doi.org/10.1016/j.nima.2010.03.147).
- [129] M. Aglietta et al., Recovery of saturated signals of the surface detector, *Pierre Auger internal note* (2008) GAP2008\_030.
- [130] I. Antcheva, et al., ROOT: A C++ framework for petabyte data storage, statistical analysis and visualization, *Comput. Phys. Commun.* 182 (2011) 1384–1385. doi:[10.1016/j.cpc.2011.02.008](https://doi.org/10.1016/j.cpc.2011.02.008).

---

# Acronyms

This is a list of acronyms used within this work sorted alphabetically according to the short version.

<b>ADC</b>	analog-to-digital converter
<b>AERA</b>	Auger Engineering Radio Array
<b>AMIGA</b>	Auger Muon Detectors for the Infill Ground Array
<b>APD</b>	avalanche photo diode
<b>BLS</b>	Balloon Launching Station
<b>CDAS</b>	Central Data Acquisition System
<b>CMB</b>	Cosmic Microwave Background
<b>CR</b>	cosmic ray
<b>CRS</b>	Central Radio Station
<b>DAC</b>	digital-to-analogue converter
<b>EAS</b>	extensive air shower
<b>EMA</b>	ethylene methacrylate
<b>FD</b>	Fluorescence Detector
<b>G-APD</b>	geiger mode avalanche photo diode
<b>GPS</b>	Global Positioning System
<b>GZK</b>	Greisen–Zatsepin–Kuzmin
<b>HEAT</b>	High Elevation Auger Telescopes
<b>HV</b>	high-voltage
<b>LDF</b>	lateral distribution function
<b>LPDA</b>	Logarithmic Periodic Dipole Antenna
<b>MLDF</b>	Muon Lateral Distribution Function
<b>PE</b>	photon-equivalent
<b>PMMA</b>	poly(methyl methacrylate)
<b>PMT</b>	photomultiplier tube
<b>PVC</b>	polyvinyl chloride
<b>SD</b>	Surface Detector
<b>SiPM</b>	Silicon photo-multiplexer
<b>SPMT</b>	small photomultiplier tube
<b>SSD</b>	Scintillator Surface Detector
<b>UB</b>	unified board
<b>UUB</b>	upgraded unified board
<b>UHECR</b>	ultra-high-energy cosmic ray
<b>UMD</b>	Underground Muon Detector
<b>WCD</b>	water-Cherenkov detector

**WLS** wavelength shifter

---

# List of Figures

1.1	Energy spectrum of cosmic rays with the signaling of the “knee”, the “second knee”, the “ankle” and the “spectrum suppression” [23]. . . . .	3
1.2	Average energy of protons as a function of the distance traveled through the CMB for different initial energy [25]. . . . .	4
1.3	Production of secondary particles after a primary cosmic ray interacts with the Earth’s atmosphere [34]. . . . .	5
2.1	Map of the hybrid detector at the Pierre Auger Observatory. Each black dot corresponds to one of the 1660 surface detector stations (see section 2.1.1). The 24 fluorescence detector enclosures are shown, each with a 30° field of view distributed in four buildings (see section 2.1.2). The location of the low-energy enhancements are also displayed (see section 2.2) . . . . .	10
2.2	Example of an event simultaneously measured by both the SD and the FD at the Pierre Auger Observatory [43]. Colors denote different shower times at both shower axis and ground. The size of the markers correspond to the magnitude of measured signals at the ground and of the reconstructed energy at the shower axis. Red squares illustrate the field of view of the 27 fluorescence telescopes, the viewing directions of triggered pixels are shown as gray lines. The surface detector stations are displayed as gray dots. The obtained energy and $X_{\max}$ from FD data was: $E = (4.7 \pm 0.1) \times 10^{19}$ eV and $X_{\max} = (730 \pm 3)$ g/cm <sup>2</sup> . . . . .	11
2.3	Water-Cherenkov detector at the Pierre Auger Observatory and its main components. Picture adapted from [44]. . . . .	12
2.4	Example of T3 configurations: the 3-fold T3 mode ToT2C1&3C2 is shown on the left and the 4-fold mode 2C1&3C2&4C4 on the right (see text for the definitions). C1, C2, C3, C4 indicate the first, second, third and fourth sets of neighbors, respectively, at 1.5, 3, 4.5 and 6 km from a given detector . . . . .	13
2.5	FD building at Los Leones during the day. Behind the building, there is a communication tower. The picture was taken during daytime; shutters were opened because of maintenance [17]. . . . .	14
2.6	(Left) schematics of a fluorescence telescope at the Pierre Auger Observatory [48]. (Right) picture of the telescope mirror and camera. . . . .	14

2.7	Map of the low-energy enhancements area adapted from [49]. It comprises AMIGA, HEAT, and AERA. The different AERA antennas, the SD-750 stations, the AMIGA muon detectors and HEAT field of view are shown. . . . .	15
2.8	(Left) final-layout of the AMIGA production-phase design: each WCD of the SD-750/433 array is coupled to three $10\text{ m}^2$ buried scintillator modules. (Right) a detector deployment in the field, where the tube to access the electronics and the optical sensor is seen. . . . .	16
2.9	Layout of the engineering array of AMIGA muon detectors. In the prototype phase, each $30\text{ m}^2$ muon detector was segmented in $5\text{ m}^2$ and $10\text{ m}^2$ modules. Also, two positions were equipped with extra <i>twin</i> modules to assess the detector uncertainties. Two optical sensors were tested, multipixel photomultiplier tubes and silicon photomultipliers. . . . .	17
2.10	Photograph of HEAT in tilted mode with closed shutters [55]. . . . .	17
2.11	(Left) AERA station with LPDA antenna. (Right) AERA station with butterfly antenna. . . . .	18
3.1	Estimation of the mass composition of primary cosmic-rays from the distribution of $X_{max}$ measured with the FD at the Pierre Auger Observatory [68]. The data was fitted with a superposition of four mass groups accounting for detector resolution and acceptance effects. The error bars show the combined statistical and systematic uncertainties of the mass estimates, except those related to the choice of the hadronic interaction models. The results from the different models are slightly shifted in energy for better visualization (SIBYLL-2.1 to the left and EPOS-LHC to the right) . . . . .	22
3.2	One station of the AugerPrime engineering array . . . . .	24
3.3	Picture of one side of an open SSD. . . . .	24
3.4	UMD module under construction. (Top) the optical connector with wavelength-shifting optical fibers, before polishing, is displayed. (Bottom) 64 plastic scintillator strips are shown, before closing the PVC casing. . . . .	26
3.5	Schematics of the fluorescence mechanism in organic scintillators. The incident radiation transfers energy to electrons in the material, which are promoted from the ground state $S_0$ to vibrational levels of the singlet $S_1$ . Before the electrons return to the ground state $S_0$ , they lose part of the energy absorbed and go from the vibrational levels to fundamental level of $S_1$ . Then, by emitting fluorescence photons, the electron relaxes to the ground state. Diagram adapted from [77]. . . . .	27
3.6	Diagram of mechanisms inside a plastic scintillator. Two dopants are mixed homogeneously in a plastic base. Picture adapted from [78]. . . . .	27
3.7	Piece of scintillator strip used in the UMD modules. . . . .	28
3.8	Schematic of the UMD scintillator with embedded optical fiber. Plastic scintillators emit blue photons in response to the passage of a particle. Then, the blue photons are absorbed with the WLS optical fiber and re-emitted into green photons that are propagated towards a photo-detector [79]. . . . .	28
3.9	WLS optical fiber diagram. The core and the two claddings are illustrated. . . . .	29
3.10	Schematics and pictures of muon counter photodetectors and optical connector. (Left) 8x8 multi-anode PMT. (Middle) connector for coupling the optical fibers with the photodetector. (Right) SiPM array. . . . .	29

3.11 Trace comparison between PMT (orange) and SiPM (blue) with their respective fits. The data were extracted from a prototype module (Id: 102) and a standard module (Id: 1) paired with the same station (Id: 688). Each peak displays events acquired during three months. The standard deviation for the PMT peak is $\sigma_{\text{PMT}} = (9.07 \pm 0.36)$ ns, and for the SiPM peak $\sigma_{\text{SiPM}} = (9.37 \pm 0.32)$ ns. . . . .	31
3.12 (Top) schematics of APD design. $\pi$ represents either a lightly doped p-material or intrinsic material while the superscript (+) refers to heavy doping. P-type region is rich in holes while n-type region is which in electrons. (Bottom) electric field profile of the structure shown in the top panel after applying a reverse bias voltage between $n^+$ and $p^+$ [78]. . . . .	32
3.13 Illustration of APD operation modes. . . . .	32
3.14 Schematics of the AMIGA muon detector electronics. The modules implement a <i>counter</i> and an <i>integrator</i> mode. In the <i>counter</i> mode, the output consists of 64 binary traces in which muons can be identified as sequences of "1". The <i>integrator</i> mode outputs two waveforms from which the muon number can be estimated dividing the signal charge by the mean charge of a single muon. . . . .	35
3.15 (Left) A simulated single-muon trace in the <i>counter</i> mode. The signal from the SiPM and the discriminator pulse are re-scaled for illustration. The FPGA outputs a "1"-bit in the binary trace when the fast-shaper output is above the discriminator threshold. (Right) A simulated single-muon trace in the <i>integrator</i> mode. The two ADC outputs (low- and high-gains) are shown. . . . .	36
 4.1 Schematic of the dark-rate curve as a function of an amplitude threshold (blue); its derivative (green) shows the PE amplitude spectrum. . . . .	38
4.2 Simplified schematic of the binary channel electronics relevant to the SiPM calibration. The CITIROC preamplifier, fast shaper, and discriminator are represented (section 3.6). The high-voltage (HV) is set with a Hamamatsu high-voltage source in the whole SiPM array with a 16-bit DAC. The $V_{\text{bias}}^i$ for the i-SiPM can be tuned with the CITIROC through an 8-bit DAC ( $V_1^i$ ). Analogously, the discriminator threshold can be first set with a 10-bit DAC in the whole SiPM array and the smoothly adjusted at each channel with a 4-bit DAC. . . . .	38
4.3 (Top) Dark-rate curve as a function of the discriminator threshold (blue). The first plateau (below 190 ADC counts) corresponds to the baseline while the following indicate an increasing number of PEs. The derivative of this rate curve (green) readily identifies the PE amplitude spectrum (statistical fluctuations of plateaus might produce lesser peaks). (Middle) dark-rate curves at different $V_{\text{br}}$ . It is seen how the dark rates and PE amplitudes shift towards higher values with increasing high-voltage; and (bottom) breakdown voltage, $V_{\text{br}}$ , determination for an individual SiPM. The linear extrapolation to 0 amplitude indicates the $V_{\text{br}}$ value. . . . .	39
4.4 $V_{\text{br}}^i$ histograms of CITIROC 1 (blue) and CITIROC 2 (orange). Due to the differences between the $V_{\text{br}}^i$ s it is necessary to individually set the $V_{\text{bias}}$ in each SiPM to achieve a uniform response in the whole array. Units for the fit results are volts in all cases. . . . .	40
4.5 Calibration: after breakdown voltages have been found, all SiPMs are set to the same over-voltage to assure a uniform gain. We show the dark-rate curves and 1 PE amplitude histograms before (top) and after (bottom) the calibration. Units of fit results are DAC,counts in all cases. . . . .	41
4.6 Gain, dark rate, and crosstalk as a function of the over-voltage. . . . .	42

4.7 (left) $V_{br}$ obtained from two calibration runs (August 2016 and December 2017) and (right) histogram of the differences in the obtained $V_{br}$ s. Fit results units are volts in all cases. . . . .	42
4.8 $V_{br}$ of all SiPMs deployed in the UMD engineering array. The right population corresponds to the first production batch while the left population corresponds to the second batch. . . . .	42
4.9 Results for six different calibration runs at different temperatures. The shift in the 1 PE spectrum can be observed. As a consequence of the temperature increase, the breakdown voltage increases accordingly and, therefore, the gain decreases. . . . .	43
4.10 1 PE amplitude as a function of the SiPM temperature over an eight-month period with a temperature range of $\sim 10 - 30^\circ\text{C}$ . The colors indicate the months: greenish for the coldest season and reddish to the warmest. The dotted-gray line shows 1 PE amplitude temperature dependence had there not been any temperature compensation in the front-end electronics. The almost constant 1 PE amplitude shows that the gain stabilization works at the level of $0.2\%/\text{ }^\circ\text{C}$ . . . . .	44
4.11 Temperature as a function of date time in the SiPM prototype module buried 2.3 underground (red) and at the closest weather station (blue) between November, 1st and November, 9th. The maximum variation is $\sim 26^\circ\text{C}$ at the weather station and $\sim 6^\circ\text{C}$ at the underground module. . . . .	44
4.12 Monitoring of the Hamamatsu high-voltage source at module with Id 108 of the station with Id 1764. In the top (middle) panel, the temperature and high-voltage set are shown for a one-month (year) period. The temperature modulations can be seen. The bottom panel displays the high-voltage set as a function of the temperature. The slope obtained from the linear fit is $(54.0 \pm 0.1)\text{ mV/ }^\circ\text{C}$ . . . . .	46
4.13 (Top) dark rate at 0.5 PE (left) and crosstalk (right) of a SiPM array, obtained from calibration. (Bottom) dark rate and crosstalk histograms. The rate of dark counts at 2.5 PE is estimated to be between $(103 \sim 305)\text{ Hz}$ in each SiPM. . . . .	47
4.14 Signal rate as function of the discriminator threshold for a SiPM with and without optical fiber coupled, represented by the blue and orange curve respectively. Note the rate of the SiPM without fiber falls rapidly after $\sim 3$ PE, while the rate of the SiPM with optical fiber remains close to 100 Hz. . . . .	47
4.15 CITIROC temperature and mean rate per SiPM of the module with Id 108 of the station with Id 1764 extracted from monitoring data between March, 2017 and May, 2018. In the top panel, a zoom-in of a month is shown, in which the daily modulation of the temperature and, thus, also the rate is observed. In the bottom panel, the whole data range is displayed, in which the year modulation can be seen. . . . .	48
4.16 Mean rate per channel as a function of time for 2.5 and 3.5 PE thresholds. (Top) monitoring data between December 2016 and March 2017 (December 2017 and March 2018) at 3.5 (2.5) PE. (Bottom) average rate per hour during a two-week window. The right (left) axis corresponds to the 2.5 (3.5) PE data. . . . .	49
4.17 Mean background rate per SiPM as function of the temperature of the two CITIROCs for data between December 2017 and March 2018. . . . .	50
4.18 Example of the rate as a function of the DAC level for one strip of the module with Id 108 of the station with Id 1764. The correction of the rate at 2.5 PE ( $\Delta R$ ) is estimated from the extrapolation of the rate between 4 and 7.5 PE. . . . .	51
4.19 Background rate at 2.5 and 3.5 PE after corrections in equation 4.1 and Table 4.1. After the corrections the two rates become similar. . . . .	51

- 4.20 Schematics of the laboratory setup. The four scintillator strips with optical fiber are shown. The optical fibers are coupled through an optical connector to a standard SiPM array. The signals are processed with an eKIT. Events are triggered with a muon telescope, while a T3 request is simulated with an external computer to store the events. . . . . 52
- 4.21 An example of a typical event, composed by binary traces from the 60 available channels. The muon signal is visible as sequences of positive samples in the four active channels. . . . . 53
- 4.22 (Top) Number of events per channel and time bin for a discriminator threshold of 2.5 (left) and 3.5 PE (right). Channels 2, 7, 42 and 47 are coupled to optical fibers; positive samples are accumulated around the trigger bin. Channels 4, 25, 44 and 59 have no positive samples as they were off. (Bottom) time projection of positive samples in all channels per time bin. The peak at the trigger bin can be seen, along with the background noise, which is more noticeable in the 2.5 PE threshold setup. . . . . 53
- 4.23 (Top) number of positive samples (“1”s) as a function of the signal width, defined as the distance between the first and last “1” in the  $6.4 \mu\text{s}$  trace, for 2.5 (left) and 3.5 (right) PE. (Bottom) signal width histograms. In black, the total signal of the channels with strips is shown. In red, the signal from the passive channels, corresponding to SiPM noise, is displayed. In blue, the signal from the strips outside the trigger scope can be seen. Most of the signals are located along an identity function, indicated with the red dashed line. The events away from the identity are acknowledged to be muon signals with noise away from the trigger scope. . . . . 55
- 4.24 The mean width (top) and standard deviation (bottom) of the muon signal in binary traces as a function of the trigger position for the 2.5 and 3.5 PE thresholds is displayed. The mean width of the signals decreases when moving the muon telescope towards the end of the strip, which is an effect of the optical fiber attenuation. . . . . 56
- 4.25 (Top) muon counting for 2.5 PE (left) and 3.5 PE (right) for a  $1x$  strategy. (Bottom) muon counting for 2.5 PE (left) and 3.5 PE (right) for a  $1111x$  and  $111x$  (respectively) pattern. In all cases, we used an inhibition window of 12 samples. In particular, for the 2.5 PE threshold, the background is significantly reduced when using the  $1111x$  matching pattern. . . . . 57
- 4.26 Efficiency as a function of the trigger position for the 2.5 and 3.5 PE thresholds and different matching patterns. Signal loss is produced mostly at the end of the strip when increasing the discriminator threshold or requesting a higher number of positive sample to count a muon. At the beginning of the strip, muon over-counting is observed resulting in an efficiency higher than 100%. We summarize the results for all these scenarios in Table 4.2 . . . . . 58
- 5.1 (Top) average trace as a function of the trigger position for one (left) and four (right) muons. The signal is shifted and attenuated when the trigger is moved towards the end of the strip. (Bottom) average trace of all positions for one (left) and four (right) muons. . . . . 63

- 5.2 (Top) Signal start time as a function of the trigger position on the strip. The start time of the binary and ADC channels (one and four muons) signal is shown. The start time is shifted when moving the muon telescope to the end of the strip due to the delay introduced by the photon propagation. (Bottom) difference between the channel start times ( $\Delta t$ ) as a function of the position on the strip. . . . . 64
- 5.3 (Top) signal mean width as a function of the trigger position. Due to light attenuation in the fiber, the signal becomes narrower when the trigger is moved towards the end of the scintillator strip. (Bottom) width relative fluctuations as a function of the trigger position. . . . . 65
- 5.4 Mean charge and relative RMS as a function of the position on the strip for one and four muon signals. The signal is attenuated (and the relative fluctuation increases) when moving the trigger towards the end of the strip. The fits results can be found in Table 5.1. . . . . 66
- 5.5 Top (bottom) charge histograms for one and four-muon signals low (high) gain channel. . . . . 67
- 5.6 (Top) baseline histograms for different integration windows. (Bottom) single-muon width histogram. For a mean muon width of 100 ns, the baseline spans from -400 to 400 ADC, which overlaps with MIP charge distribution. . . . . 68
- 5.7 Equation 5.2 fit for the average ADC trace of single muons. The average was obtained using 20000 laboratory events. . . . . 69
- 5.8 Results of equation 5.2 parameters as a function of the muon telescope position. At each position, fits were performed over 20000 individual events and over the average trace. The consistency between the two analysis is apparent. The signal shape is determined by parameters  $\mu$  (top left) and  $\sigma$  (top right) and remain rather constant in the whole strip. The normalization factor (bottom left) decreases as the telescopes are moved towards the end of the strip due to the light attenuation in the optical fiber. The signal start time is shifted due to the photons propagation delay as explained in section 5.1.1. The result obtained from the fits is consistent with the result in Fig. 5.2 within the sampling time of the ADC channel (6.25 ns). . . . . 71
- 5.9 Muon detector associated to the station with Id 1764. In this case, the muon detector is comprised of two twins (north and south). Each twin consists of two  $5\text{ m}^2$  modules with Ids 101, 102, 105 and 106, and two  $10\text{ m}^2$  modules with Ids modules 103, 104, 107 and 108. . . . . 72
- 5.10 (Top) signal start time by trigger type. In each channel (binary/ADC) two peaks are identified, corresponding to the T2-TH and T2-ToT triggers. (Middle) signal start time after synchronizing the traces according to the WCD timing type. (Bottom) delay between the ADC and the binary channels for the T2-TH and T2-ToT triggers. The results from the fits are summarize in Table 5.3. . . . . 73
- 5.11 Example event in module with Id 104 of the station with Id 1764. We show the muon histogram from the binary channel (top) and the ADC traces (bottom). The green (red) arrows indicate the signal start (end) times. The “muon” at 500 ns, is outside the typical shower scope and therefore, we assume it is produced by noise. . . . . 75

- 5.12  $\sigma_{\text{NS}}$  in the ADC channel as a function of the number of muons ( $N$ ) estimated with the binary channel. In the top panel, the results for  $5 \text{ m}^2$  modules are shown, for both low- and high-gain channels. In the bottom panel, the results for  $10 \text{ m}^2$  are shown. We have fitted each module data set with a  $\sigma_1 \sqrt{N}$  function. We summarized the results of the fits in Table 5.4. . . . . 76
- 5.13 Signal charge in the ADC channel as a function of  $N$  estimated with the binary traces for the module with Id 104. For each  $N$ , we plot the charge of each individual event (blue) and mean (red). From the individual events, the charge dispersion is observed. The slope of the linear fit equals to the mean charge of a single muon. . . . . 77
- 5.14 Mean charge in the ADC channel as a function of  $N$  estimated with the binary traces for all modules of the station with Id 1764. On the top (bottom) panel, the results of the low-gain (high-gain) channel are displayed. We show the mean values as a reference since the fits were performed using individual events. The fits results are summarized in Table 5.5. . . . . 78
- 5.15 Baseline histograms for all modules in the station with Id 1764. We show in the top (bottom) panel the histograms of the low-gain (high-gain) channel. The results of the Gaussian fits are summarized in Table 5.7. . . . . 81
- 5.16 Comparison between the number of muons estimated with the binary and the ADC channels. In the top (bottom) panels we display the results obtained with the low-gain (high-gain) channels, and in the left (right) panels, we show the results for the  $5$  ( $10 \text{ m}^2$ ) modules. In all cases the fits approximate an identity function. The results of the fits per module are summarized in Table 5.8. . . . . 82
- 5.17  $\sigma_s$  of the normalized low- (top panel) and high-gain (bottom panel) ADC signals as a function of the  $N$  estimated with the binary channel. We have fit the  $\sigma_1$  parameter of the error model (section 5.2.2) with a  $\sigma_1 \sqrt{N}$  function. The results of the fits are summarized in Table 5.8. . . . . 83
- 5.18 Relative uncertainties for the low- (top) and the high-gain (bottom) channels. We display the Poissonian uncertainty along with the integrator resolution and the addition in quadrature of both uncertainties. The Poissonian uncertainty dominates in the whole range. . . . . 85
- 5.19 Muon lateral distribution function reconstructed with the binary channel for an example event. The muon densities estimated with the ADC channel are also shown. . . . . 85
- 5.20 (Top) binary channel raw traces. Signal accumulation around the trigger scope is observed. Randomly distributed entries produced by background noise are also observed. (Middle) raw traces of the ADC low- and (bottom) high-gain channels. Analogously to the binary channel, accumulation of signal can be found within the shower scope, along with randomly distributed noise. A few pulses with undershoot produced by shower events were identified . . . . . 87
- 5.21 (Top) signal start time of the binary channel, defined as the first "1" in the trace. (Middle) time of the maximum signal amplitude in the ADC channel. (Bottom) difference between the binary channel start time and the maximum signal amplitude in the ADC. From the fits, it was obtained that this difference is stable with  $\sim 7.24 \text{ ns}$  fluctuation, which correspond to  $\sim 1$  sample of the ADC ( $6.25 \text{ ns}$ ). . . . . 88



5.29 (Top) delay between the binary channel start time and maximum signal amplitude time in the ADC channel. We show the means (left) and standard deviations (right) of the delays for all the UMD engineering array modules. The maximum difference between the modules is $\sim 4$ ns which is less than the sample time of the ADC channel. It is also apparent that this delay is stable since the mean fluctuation is $\sim 2.5\%$ . (Bottom) means (left) and standard deviations (right) of the binary trace start time. The T2-ToT and T2-TH triggers are distinguishable. In this case, the maximum difference in the start time of two modules is $\sim 40$ ns ( $\sim 13$ sample times of the binary channel). Therefore, we need to optimize the calibration for each module in the UMD engineering array to compensate for these differences. . . . .	98
5.30 Offline calibration using shower events for the module with Id 101 of the station with Id 93. We present the results for the low- (top) and high-gain channels. The fit results are consistent with the results obtained using the online calibration summarized in Table 5.9 . . . . .	99
5.31 Charge histograms of the low-gain channel obtained in the laboratory analyzing T3 events (top) and the charge extracted with the calibration algorithm implemented in the electronics (bottom). . . . .	100
5.32 Charge histograms obtained using the calibration algorithm implemented in the UMD electronics and deployed in the module with Id 101 in the station with Id 93. . . . .	101
 6.1 Schematics of the laboratory setups. A scintillator strip with optical fiber is shown. The optical fiber is coupled via an optical connector to a standard AMIGA SiPM. The signals are processed with an inverter amplifier (Gali 84+). A muon telescope is used to trigger the events, which are acquired with an oscilloscope. . . . .	104
6.2 (Top) PE as a function of the $V_{bias}$ . By extrapolating the curve to 0, the $V_{br}$ is obtained. (Bottom) dark-rate curve as a function of the discriminator threshold acquired with $V_{ov} = 3.5$ V. The dark rate obtained at 0.5 PE level is 650 kHz and the crosstalk probability is 2.2%. . . . .	105
6.3 (Top) dark-rate pulses measured with an oscilloscope. We can clearly identify the afterpulses, along with the different PE peaks produced by crosstalk within the SiPM inner-cells. (Bottom) signal charge as a function of its amplitude. The three populations correspond to one, two and three PEs signals. . . . .	106
6.4 (Top) Transfer function of the amplifier Gali 84+. (Middle) single-PE signal measured with the oscilloscope (after amplification). (Bottom) single-PE signal from SiPM (after applying the deconvolution algorithm). Similar waveforms are obtained due to the flat response of the amplifier. . . . .	108
6.5 (Top) data set of 2000 single-PE pulses extracted from dark-rate measurements after removing crosstalk and afterpulses. (Bottom) average single-PE signal (blue), obtained by averaging the data in the top panel. The model (equation 6.10) fit (red) is also shown. We summarized the fit results in Table 6.1.109	109
6.6 Baseline histogram of SiPM single-PE signals. Units of the fit results are mV. . . . .	110
6.7 (Top) example of parameter correlation when simulating uncorrelated parameters. In this case, the simulation does not match the laboratory data. (Bottom) example of correlation parameters when using PCA to include correlations between parameters in the simulation. The agreement between data and simulation can be seen. . . . .	112

- 6.8 (Top) Data set of 2000 simulated single-PE pulses obtained with the pulse generator. (Bottom) comparison between the model parameters fitted using laboratory data and simulated data. Data and simulations differ typically less than 5% . . . . . 113
- 6.9 (Top) example muon signal measured a 2 m on the scintillator strip. The arriving photons are time distributed. (Bottom) signal charge as a function of its amplitude for muons measured at 2 m on the scintillator strip. . . . . 114
- 6.10 SiPM mean charge as a function of the date time. Each data point was obtained using a data set of 2000 dark rate pulses. The SiPM gain remain stable during the whole period. . . . . 115
- 6.11 Mean number of photo-equivalents in charge and amplitude as a function of the trigger position. The data was fitted with the double-exponential decay function from equation 5.1. The difference between the number of PEs in amplitude and charge is produced by the decay times of the scintillator and optical-fiber. . . . . 115
- 6.12 (Top) example of simulated muon signal at 2 m of the scintillator strips. In blue, the single-PE pulses with their time profile can be seen. In red we plot the total muon signal, which results from adding all the single-PE pulses. (Bottom) correlation between the muon signal charge and amplitude for 2000 events of both laboratory data and simulation. The simulation is quite consistent with the laboratory data. . . . . 116
- 6.13 Main features of the muon signal at different positions on the scintillator strip. We show the means and RMS for laboratory data and simulations. We display on the top panel the muon signal charge, in the middle panel the muon signal amplitude and in the bottom, the muon signal full width at half maximum. It is apparent that in all cases there is an agreement between the experimental data and the simulations. . . . . 117
- 7.1 (Top) Proposed models for the CITIROC pre-amplifier (left) and fast-shaper (right) [116]. The pre-amplifier is simulated as an active low-pass filter with a frequency cutoff of 10 MHz and an amplification factor of  $\times 10$ . The fast-shaper is simulated as a practical differentiator with a characteristic time of 15 ns and a maximum gain of  $\sim \times 18$ . The circuit resistors and capacitors were chosen to match these features. (Bottom) transfer function magnitude in dB as a function of the signal frequency. In the left panel, we show the transfer for the pre-amplifier deduced in equation 7.2. The frequency cutoff of 10 MHz and an amplification factor of  $\times 10$  is obtained, as desired. In the right panel, we show the magnitude of the fast-shaper transfer as deduced in equation 7.6. In this case, a maximum amplification factor of  $\sim \times 18$  and a frequency of 10 MHz was obtained. . . . . 120
- 7.2 Example signal at the discriminator output. The black arrows show the limits within which the rise time was estimated. The green lines show the 0.8 V and 1.7 V levels) . . . . . 122

- 7.3 (Top) dark-rate curves used to calibrate the SiPMs. We show the curves obtained using laboratory data and the *counter* mode simulation. The single-PE amplitude obtained with the simulation is  $(24.3 \pm 0.3)$  DAC counts ( $(31.6 \pm 0.4)$  mV). (Middle) histogram of the signal maximum amplitude at the fast-shaper output for single-PE events. The peak amplitude obtained is  $(35.39 \pm 0.04)$  mV. (Bottom) simulated single-muon trace in the *counter* mode. The signal from the SiPM and the discriminator pulse are re-scaled for illustration. The FPGA outputs a “1”-bit in the binary trace when the fast-shaper output is above the discriminator threshold during more than 1.51 ns. . . . . 124
- 7.4 (Top) Efficiency as a function of the position on the scintillator strip estimated from laboratory data, simulations, and a Poissonian prediction using a discriminator threshold of 2.5 and 3.5 PE. (Bottom) mean signal width over sample time and  $\sigma$  in the *counter* mode as a function of the position on the scintillator strip with both laboratory and simulated data of single muons. The signal widths were obtained also with two different discriminator thresholds: 2.5 and 3.5 PE. . . . . 125
- 7.5 Schematics of the *integrator* mode electronics. The 64 SiPM signals are analogically added up with two steps of adders, and the result is amplified with a low- and high-gain amplifiers. Amplifier outputs are sampled with two ADCs. 126
- 7.6 Transfer functions of the *integrator* mode electronics. The transfers were fit with the of a low-pass filter as described in equation 7.2. (Top) transfer functions of the adders in the *integrator* mode electronics. In the left (right) panel we show the transfer function corresponding to the adders of the first (second) block. The frequency cutoff of the first step is  $\sim 10$  MHz, while the frequency cutoff of the second step is  $\sim 100$  MHz. This implies that the signal timing is determined by the first transfer in the electronics. (Bottom) transfer functions of the low-gain (high-gain) amplifier. In both cases, the frequency cutoff is  $\sim 100$  MHz, and the difference lays on the amplification factor. . . . . 126
- 7.7 Baseline histograms of the low- (left) and high-gain (right) channels. The fit result units are ADC counts, in all cases. . . . . 127
- 7.8 (Top) example ADC channel traces measured at 2 m on the scintillator strip. The low- and high-gain traces are displayed. (Bottom) example of simulated ADC traces at 2 m on the scintillator strip. The muon input signal, which corresponds to the SiPM analog signal is displayed, along with the ADC outputs. . . . . 128
- 7.9 (Top) signal charge as a function of the position on the scintillator strip. We show the signal mean charge and RMS obtained using laboratory data as we explained in section 5.1.2. We also display the result using the *integrator* mode simulation. The simulation and data are consistent. (Bottom) signal charge of simulated data as a function of the number of injected muons. The high-gain (low-gain) channel starts to lose linearity when  $\sim 80$  muons ( $\sim 300$  muons) are injected simultaneously. . . . . 129
- 7.10 Module sequences compatible with the Geant4 9 (left) and Geant4 10 (right) libraries. . . . . 130
- 7.11 The UMD tab for an example event (Auger ID 160915817600), see description in the text. Top left panel: the event and reconstruction summary. Top middle panel: the SD stations map. Top right panel: *counter* list tab and options tab. Bottom panel: the user can switch between different features by selecting the sub-tabs. . . . . 132

- 7.12 Raw traces tab. The 64 binary traces collapsed on the X axis. In each time bin (of 3.125 ns) a maximum of 64 samples (one per channel) can be obtained. . . . . 134
- 7.13 Raw binary traces per channel. Each line on the Y-axis corresponds to one channel. If in the corresponding time bin a positive sample in the trace is found, a red marker is plotted. The raw traces (Fig. 7.12) are the projection on the X-axis of these plots. . . . . 134
- 7.14 Counting histograms. The counting histogram is the result of applying the counting strategy to the raw traces (see Fig. 7.12) [121]. . . . . 135
- 7.15 *Integrator* mode traces. An example of modules with SiPM is shown. In this case, the low- and a high-gain traces are available. . . . . 135
- 7.16 An example of the combined view. The SD map, LDF, time residuals, and average traces are displayed in tandem with the UMD information. This visualization can be activated or deactivated through the check box in the options tab. . . . . 136
- 7.17 Example of the combined view for the counting histograms. In red, the WCD average trace is plotted. . . . . 136
- 8.1 Schematic of one station setup in the simulation run. The WCD and the three  $10\text{ m}^2$  modules of the muon detector are displayed. . . . . 138
- 8.2 (Left) schematic of frontal view of two scintillator strips and an impinging muon depositing energy in both. We also show an example of the binary output of the *counter* mode for this event. (Right) schematic of the geometric dependency of corner clipping muons. The probability of finding the muon signal in two adjacent strips depends both on the zenith angle of the shower axis ( $\theta$ ) and on the difference between the azimuth angle of the shower axis and the orientation of the UMD module ( $\Delta\varphi_m$ ) . . . . . 140
- 8.3 Reconstruction bias with the *counter* mode as a function of the distance to the shower core (extracted from the SD reconstruction) for air shower simulations with an energy of  $10^{18}$  eV and zenith angles of  $0^\circ$  (top-left),  $12^\circ$  (top-right),  $32^\circ$  (bottom-left), and  $48^\circ$  (bottom-right). We show the result for simulations in which only muons were injected in the muon detector and for simulation in which all particles (including electrons from the soil) were injected. . . . . 142
- 8.4 Reconstruction bias with the *counter* mode as a function of the number of injected muons (top panels) and as a function of the distance to the shower core extracted from the SD reconstruction (bottom panel) for proton (left panels) and iron (right panels) showers with an energy of  $10^{18}$  eV. To analyze the impact on the inhibition window in the reconstruction bias we show the results after reconstructing the simulated data with three inhibition windows: 31 ns, 37.5 ns and 44 ns. . . . . 143
- 8.5 Reconstruction bias with the *counter* mode as a function of the number of injected muons (top panels) and as a function of the distance to the shower core extracted from the SD reconstruction (bottom panel) for proton (left panels) and iron (right panels) showers with an energy of  $10^{18}$  eV. To analyze the impact on the inhibition window in the reconstruction bias we show the results after reconstructing the simulated data with three inhibition windows: 31 ns, 37.5 ns and 44 ns. . . . . 144

- 8.6 Geometry dependence of the reconstruction bias using proton and iron showers with energies of  $10^{17}$  eV,  $10^{17.5}$  eV,  $10^{18}$  eV,  $10^{18.5}$  eV and zenith angles of  $0^\circ$ ,  $12^\circ$ ,  $22^\circ$ ,  $32^\circ$ ,  $38^\circ$  and  $48^\circ$ . (Top) Reconstruction bias as a function of the difference between the azimuth angle of the shower axis extracted from the SD reconstruction and the UMD module orientation ( $\Delta\varphi_m$ ) for different zenith angles ( $\theta$ ). The biases were fitted using equation 8.4. (Middle)  $a(\theta)$  and  $b(\theta)$  functions of the bias parametrization fitted with equations 8.5. (Bottom) Reconstruction bias as a function of the difference between the azimuth angle of the shower axis and the UMD module orientation ( $\Delta\varphi_m$ ) for different zenith angles ( $\theta$ ) after implementing the geometry correction. . . . . 146
- 8.7 Reconstruction bias with the *Counter* mode as a function of the distance to the shower core before (top panel) and after (bottom panel) the correction. The data set is the same as in Fig. 8.6 . . . . . 147
- 8.8 Ratio of the mean charge ( $\overline{Q_\theta}$ ) and mean charge of vertical showers ( $\overline{Q_0}$ ) as a function of  $\frac{1}{\cos\theta}$  before (top panel) and after (bottom panel) the correction, which removes the angular dependence. . . . . 149
- 8.9 (Top) Signal charge in the *integrator* mode as a function of the number of reconstructed muons in the *counter* mode for the low- (left) and high-gain (right) channels. The mean charge per muon is obtained with a linear fit. (Bottom) charge histograms for  $N_\mu = 1$ . The calibration using the histograms were achieved with three different methods: the median (50% quantile), fitting a log-normal-like function and computing the charge average. . . . . 150
- 8.10 (Top) Reconstruction bias as a function of the distance to the shower core for the low- and high-gain channels and different calibration outputs. (Bottom) Number of reconstructed muons with the *integrator* mode and the low-/high-gain channel as a function of the number of injected muons. . . . . 151
- 8.11 Reconstruction bias (top panels) and fluctuations (bottom panels) as a function of the distance to the shower core extracted from the SD reconstruction (left panels) and the number of injected muons (right panels) for proton and iron shower with an energy of  $10^{17.5}$  eV and zenith angles of  $0^\circ$ ,  $12^\circ$ ,  $22^\circ$ ,  $32^\circ$ ,  $38^\circ$ ,  $48^\circ$ . We show the results obtained using the *counter* mode and the low- and high-gain channels of the *integrator* mode. . . . . 152
- 8.12 Reconstruction bias (top panels) and fluctuations (bottom panels) as a function of the distance to the shower core extracted from the SD reconstruction (left panels) and the number of injected muons (right panels) for proton and iron shower with an energy of  $10^{18}$  eV and zenith angles of  $0^\circ$ ,  $12^\circ$ ,  $22^\circ$ ,  $32^\circ$ ,  $38^\circ$ ,  $48^\circ$ . We show the results obtained using the *counter* mode and the low- and high-gain channels of the *integrator* mode. . . . . 153
- 8.13 Reconstruction bias (top panels) and fluctuations (bottom panels) as a function of the distance to the shower core extracted from the SD reconstruction (left panels) and the number of injected muons (right panels) for proton and iron shower with an energy of  $10^{18.5}$  eV and zenith angles of  $0^\circ$ ,  $12^\circ$ ,  $22^\circ$ ,  $32^\circ$ ,  $38^\circ$ ,  $48^\circ$ . We show the results obtained using the *counter* mode and the low- and high-gain channels of the *integrator* mode. . . . . 154
- 8.14 Example of muon densities obtained with the UMD as a function of the distance to the shower core with the corresponding MLDF fit using the *counter* and *integrator* modes and combining both. From each of the MLDF fits we obtained  $\rho_{450} = (4.4 \pm 0.2) \text{ m}^{-2}$ ,  $\rho_{450} = (5.0 \pm 0.2) \text{ m}^{-2}$ , and  $\rho_{450} = (5.0 \pm 0.2) \text{ m}^{-2}$  for the *counter*, *integrator* and combined data, respectively. . . . . 156

- 8.15 Example of  $\rho_{450}$  distributions obtained with the *integrator* mode for proton and iron primaries with an energy of  $10^{18.5}$  eV and zenith angle of  $0^\circ$ . . . . . 156
- 8.16 Muon density (top) and relative fluctuation (bottom) for proton and iron primaries and energies of  $10^{17}$  eV,  $10^{17.5}$  eV,  $10^{18}$  eV and  $10^{18.5}$  eV as a function of the zenith angle obtained with the *counter* mode. . . . . 157
- 8.17 Muon density (top) and relative fluctuation (bottom) for proton and iron primaries and energies of  $10^{17}$  eV,  $10^{17.5}$  eV,  $10^{18}$  eV and  $10^{18.5}$  eV as a function of the zenith angle obtained with the *integrator* mode. . . . . 158
- 8.18 Muon density (top) and relative fluctuation (bottom) for proton and iron primaries and energies of  $10^{17}$  eV,  $10^{17.5}$  eV,  $10^{18}$  eV and  $10^{18.5}$  eV as a function of the zenith angle obtained combining the *counter* and *integrator* modes. . . . . 159
- 8.19 Merit factor as a function of the zenith angle for proton-iron discrimination in showers with energy  $10^{17}$  eV,  $10^{17.5}$  eV,  $10^{18}$  eV and  $10^{18.5}$  eV, using separately the *counter* and *integrator* modes and combining both. . . . . 160

---

## List of Tables

4.1	Background rate results at 3.5 PE with model correction. . . . .	50
4.2	Comparison of the 2.5 and 3.5 PE threshold with different counting strategies applied to traces of $6.4\mu s$ . It is possible to achieve similar levels of background noise and efficiency for both threshold by choosing a $1111x$ ( $1x$ ) matching pattern at 2.5 (3.5) PE. The levels of noise observed in the laboratory are compatible with the results obtained in the field. . . . .	59
4.3	Comparison of the 2.5 and 3.5 PE threshold with different counting strategies for a $1\mu s$ trace. . . . .	59
5.1	Mean values obtained from parameter histograms of one and four muons. 20000 laboratory events were used. Concerning the field data, 681 single-muon signals and 121 four-muon signals were used. . . . .	69
5.2	RMS obtained from the parameter histograms of one and four muons. 20000 laboratory events were used. Concerning the field data, 681 single-muon signals and 121 four-muon signals were used. . . . .	70
5.3	Fit results for the start time histograms in Fig. 5.10. . . . .	74
5.4	Fit results for Fig. 5.12. We show the $\sigma_1$ s obtained from fitting the data with a $\sigma_1\sqrt{N}$ function, and also, we show for comparison the $\sigma_1$ extracted from the $N_1$ histogram calculated as in equation 5.3. As expected, both methods are consistent. Errors are smaller when using the fits, which indicates that the fits lead to a better estimation of the model parameter ( $\sigma_1$ ) by improving statistics.	77
5.5	Fit results of the ADC channel calibration (Fig. 5.14) for all modules in the station with Id 1764. The light-output in $5\text{ m}^2$ modules (101, 102, 105, 106) is higher than in $10\text{ m}^2$ modules (103, 104, 107, 108), which is expected due to the optical-fiber attenuation. Units of the mean charge per muon ( $\frac{\bar{Q}}{\mu}$ ) are $\frac{\text{ADC counts}}{\mu}$ . . . . .	79
5.6	Calibration summary of the station with Id 1764. We show the mean charge per muon ( $\bar{Q}_1$ ), the resolution for one muon ( $\sigma_1$ ), the relative fluctuation per muon ( $\frac{\sigma_1}{\bar{Q}_1}$ ), and the ratio between the low- and high-gain channels ( $\frac{HG}{LG}$ ) for both $5\text{ m}^2$ (101, 102, 105, 106) and $10\text{ m}^2$ modules (103, 104, 107, 108). This results are extracted from Fig. 5.12 (Table 5.4) and 5.14 (Table 5.5). Units of the mean charge per muon ( $\frac{\bar{Q}}{\mu}$ ) are $\frac{\text{ADC counts}}{\mu}$ and for the resolution ( $\sigma_1$ ), ADC counts. . . . .	79
5.7	Results of the baseline histogram fit from Fig. 5.15 for all modules in the station with Id 1764. . . . .	80

5.8	Fit results of the tests performed to validate the consistency of the offline calibration. We show the $\sigma_1$ from the error model fitted in Fig. 5.17 and the slopes fitted in Fig. 5.16. . . . .	84
5.9	Results for the charge histograms of the low- and high-gain channels presented in Fig. 5.25 with a window size of 20 samples. We show the results of both noise and signal. . . . .	92
6.1	Fit results of the model in equation 6.10. In the average column, we show the results of fitting the average single-PE signal shown in Fig. 6.5 bottom panel. In the columns $\mu$ and $\sigma$ we show the mean value and standard deviation of the histograms built by fitting the individual single-PE signals shown in the top panel of Fig. 6.5. The mean obtained by fitting the individual pulses is compatible with the results of fitting the average single-PE signal. . . . .	110
8.1	Particles that deposit energy in a UMD module for a proton vertical shower with energy $10^{18}$ eV. . . . .	141

---

# Acknowledgments

I would first like to thank my supervisors Professors Etchegoyen and Blümer, for facilitating this work and for laying the foundations of this joint German and Argentine program through which I have now passed. It has truly been a life-changing experience on many levels. To my advisor, Markus Roth, for his guidance and continuous support, for which I am truly grateful.

To all my colleagues at ITeDA who have helped me through my Ph.D., in particular to Brian and Diego who have greatly contribute to this thesis work. I would specially like to thank Federico who have been actively involved in my work, sometimes day-by-day, and guided me through many of the tasks. To the mechanics lab team for the good vibes and to the administration staff for handling all my paperwork. To my office mates, Nico, Belen, and Perlin, who made my workplace a really fun place.

To my study group, Ana Laura, Isabel, and Johan with whom I have very much enjoyed studying for the exam, and for keeping it relax when I was stressing out.

To my colleagues at KIT, with whom I have greatly enjoyed spending time with and some of whom have become very good friends. To Ewa and Sarah, my stays at Karlsruhe would not have been the same without them. To my dearest friends Darko and David, to whom I have a great love.

Marie-Christine, Frank, and Sabine deserve my sincerest gratitude for their outstanding logistical support. To Adrian and Doris for efficiently maintaining the servers, and helping me out every time I had an issue. I would also like to mention David again who greatly contributed with corrections to my writing and to Felix, Ana Laura, Isabel and Johan for translating my abstract into German. Also, to Alex for taking care of submitting this document.

To the many other colleagues and friends with whom I had meaningful contact, but are not mentioned explicitly here.

I would also like to thank Xavier for the boost of motivation he gave me at the final stretch and showing me what kind of scientist I would like to be. I also feel the need to thank the Pierre Auger Collaboration, in which I have taken my first steps into the scientific world.

I owe the deepest gratitude to my family and friends who know this work would not have been possible without their love and support. To Gatuli for keeping me company through all the sleepless nights. To Paula, who I truly love, for making my world the most exciting place and getting the best out of me.

I am truly fortunate.